Generation of Acoustic-Gravity Waves in Ionospheric HF Heating Experiments: Simulating Large-Scale Natural Heat Sources

by
Rezy Pradipta
B.S. Physics, MIT (2006)
M.S. Nuclear Science and Engineering, MIT (2007)
Submitted to the Department of Nuclear Science and Engineering
in partial fulfillment of the requirements for the degree of
Doctor of Philosophy in Nuclear Science and Engineering
at the
MASSACHUSETTS INSTITUTE OF TECHNOLOGY
September 2012

Author ....
Department of Nuclear Science and Engineering
August 29, 2012

Certified by ....
Prof. Min-Chang Lee
Former Head, PSFC Ionospheric Plasma Research Group
Thesis Supervisor

Certified by ....
Prof. Manuel Martinez-Sanchez
Department of Aeronautics and Astronautics
Thesis Supervisor

Certified by ....
Prof. Anne E. White
Department of Nuclear Science and Engineering
Thesis Supervisor

Accepted by ....
Prof. Mujid S. Kazimi
Chairman, Committee for Graduate Students
Department of Nuclear Science and Engineering

Generation of Acoustic-Gravity Waves in Ionospheric HF Heating Experiments: Simulating Large-Scale Natural Heat Sources

by

Rezy Pradipta

Submitted to the Department of Nuclear Science and Engineering
on August 29, 2012, in partial fulfillment of the
requirements for the degree of
Doctor of Philosophy in Nuclear Science and Engineering

Abstract

In this thesis, we investigate the potential role played by large-scale anomalous heat sources (e.g. prolonged heat wave events) in generating acoustic-gravity waves (AGWs) that might trigger widespread plasma turbulence in the ionospheric layer. The main hypothesis is that, the thermal gradients associated with the heat wave fronts could act as a source of powerful AGW capable of triggering ionospheric plasma turbulence over extensive areas. In our investigations, first we are going to examine a case study of the summer 2006 North American heat wave event. Our examination of GPS-derived total electron content (TEC) data over the North American sector reveals a quite noticeable increase in the level of daily plasma density fluctuations during the summer 2006 heat wave period. Comparison with the summer 2005 and summer 2007 data further confirms that the observed increase of traveling ionospheric disturbances (TIDs) during the summer 2006 heat wave period was not simply a regular seasonal phenomenon. Furthermore, a series of field experiments had been carried out at the High-frequency Active Auroral Research Program (HAARP) facility in order to physically simulate the process of AGW/TID generation by large-scale thermal gradients in the ionosphere. In these ionospheric HF heating experiments, we create some time-varying artificial thermal gradients at an altitude of 200–300 km above the Earth's surface using vertically-transmitted amplitude-modulated O-mode HF heater waves. For our experiments, a number of radio diagnostic instruments had been utilized to detect the characteristic signatures of heater-generated AGW/TID. So far, we have been able to obtain several affirmative indications that some artificial AGW/TID are indeed being radiated out from the heated plasma volume during the HAARP-AGW experiments. Based on the experimental evidence, we may conclude that it is certainly quite plausible for large-scale thermal gradients associated with severe heat wave events to generate some AGW which might induce widespread plasma turbulence far in space.

Thesis Supervisor: Prof. Min-Chang Lee
Former Head, PSFC Ionospheric Plasma Research Group

Thesis Supervisor: Prof. Manuel Martinez-Sanchez
Department of Aeronautics and Astronautics

Thesis Supervisor: Prof. Anne E. White
Department of Nuclear Science and Engineering

Acknowledgments

I would like to thank my thesis advisors/committee members: Prof. Min-Chang Lee, Prof. Manuel Martinez-Sanchez, Prof. Anne White, and earlier also Prof. Jeffrey Freidberg for their guidance, encouragement, and support.

I would also like to thank Dr. Michael Sulzer (Arecibo Observatory) for his help in setting up the Arecibo ISR for our observations; the HAARP operators (Drs. Helio Zwi, Mike McCarrick, and Dave Seafolk-Knopp) for setting up our HF heating experiments; Mr. James Secan (NWRA) for his help with the GPS & LEO satellite data at HAARP; Dr. Lee Snyder (NWRA) for his help in operating the HAARP digisonde; Prof. Brenton Watkins (UAF) for his help with the MUIR radar; Prof. Bill Bristow and Dr. Jef Spaleta (UAF) for their help with the Kodiak SuperDARN radar; Dr. Michael Nicolls and Dr. Craig Heinselman (SRI International) for their help on the Poker Flat AMISR operation; Dr. Anthea Coster and Dr. Bill Rideout (MIT Haystack Observatory) for their help on the Madrigal GPS-TEC database.

In addition, I would like to thank the Air Force Office of Scientific Research (AFOSR) for their generous and continuous support. This doctoral thesis work has been supported by the Air Force Office of Scientific Research (AFOSR) through the AFOSR grant FA9550-09-1-0391.

The Arecibo Observatory is the principal facility of the National Astronomy and Ionosphere Center, which was previously operated by the Cornell University. It is currently operated by the SRI International, Universities Space Research Association (USRA), and Universidad Metropolitana (UMET) — under a cooperative agreement with the National Science Foundation.

The High-frequency Active Auroral Research Program (HAARP) is a congressionally initiated program managed jointly by the United States Air Force and United States Navy.

Contents

List of Figures

List of Tables

Chapter 1

Introduction

To a large extent, our space plasma environment has been playing a vital role in our modern-day telecommunications and navigation systems. In general, a severe turbulence in the ionospheric plasma layer could potentially disrupt short wave radio communications and even affect the accuracy of GPS satellite navigation. It is also quite fitting to point out that certain types of plasma turbulence in the ionosphere are induced by acoustic-gravity waves (AGW). In fact, there are various known natural sources of AGWs including: volcano eruptions, earthquake, tsunami, and lightning. Major volcano eruptions, such as that of Mount St. Helens on 18 May 1980, had been found to produce some traveling ionospheric disturbances (TID) with large amplitudes [see e.g. *Roberts et al.*, 1982; *Liu et al.*, 1982]. Similarly, earthquakes and tsunamis are also known to generate intense AGW/TID that could propagate over long distance with little attenuation [see e.g. *Artru et al.*, 2004; *Artru*, 2005; *Lee et al.*, 2008]. It is therefore quite essential for us to recognize various AGW sources and perhaps to identify new ones. This thesis will investigate the potential role of large-scale anomalous heat source (e.g. heat wave events) to act as powerful source of AGW that might subsequently induce TID over an extensive area.

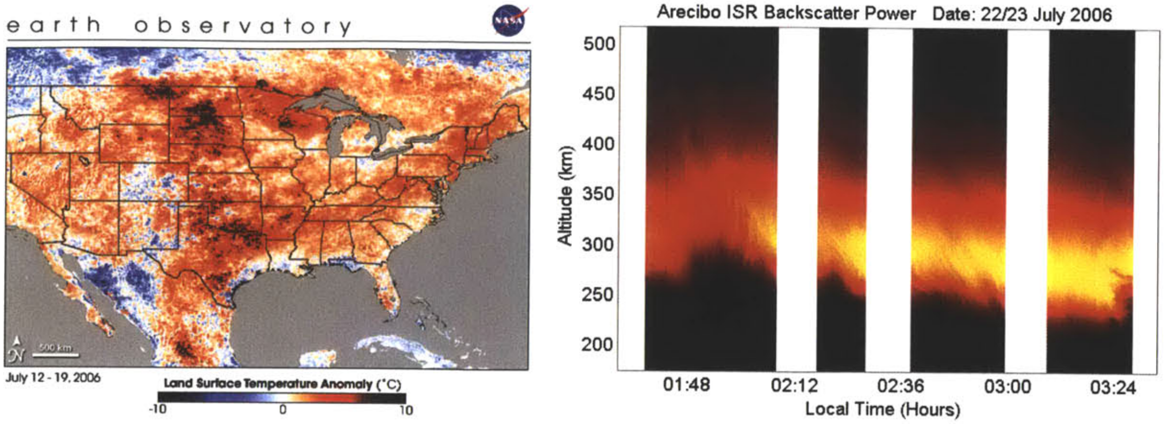

Figure 1-1: Thermal satellite imagery of the summer 2006 North American heat wave event (left). Turbulent ionospheric plasma filaments detected via ISR measurements on the night of 22/23 July 2006 at Arecibo Observatory (right). Figures taken from NASA *Earth Observatory* [2006] and *Pradipta* [MS Thesis, 2007] respectively.

1.1 Background and Overview

In our earlier report [*Pradipta*, MS Thesis 2007], we discussed at length a case study of considerably intense ionospheric plasma disturbances as detected by the Arecibo incoherent scatter radar (ISR) on the nights of 22/23 and 23/24 July 2006. Taking into consideration the geomagnetic conditions during our experiment as well as the characteristics of the observed traveling ionospheric disturbances (TID), we concluded that these ionospheric disturbances had been caused by internal gravity waves of terrestrial origin. A notable geophysical event concurrent with our radar observation of these TIDs was the summer 2006 heat wave over the mainland United States. In addition, to the best of our knowledge, there was no other major geophysical events (earthquakes, volcano eruptions, hurricanes etc.) near Puerto Rico during that time. The summer 2006 North American heat wave thus becomes the most likely source of those gravity waves. In Figure 1-1 we have a satellite imagery of the summer 2006 heat wave over North America, together with a radar imagery of turbulent plasma filaments observed over Arecibo, Puerto Rico during this heat wave period. In short, we suspect that severe heat waves covering this extensive region could potentially generate atmospheric gravity waves that will subsequently propagate upwards into the Earth's ionosphere and trigger widespread space plasma disturbances.

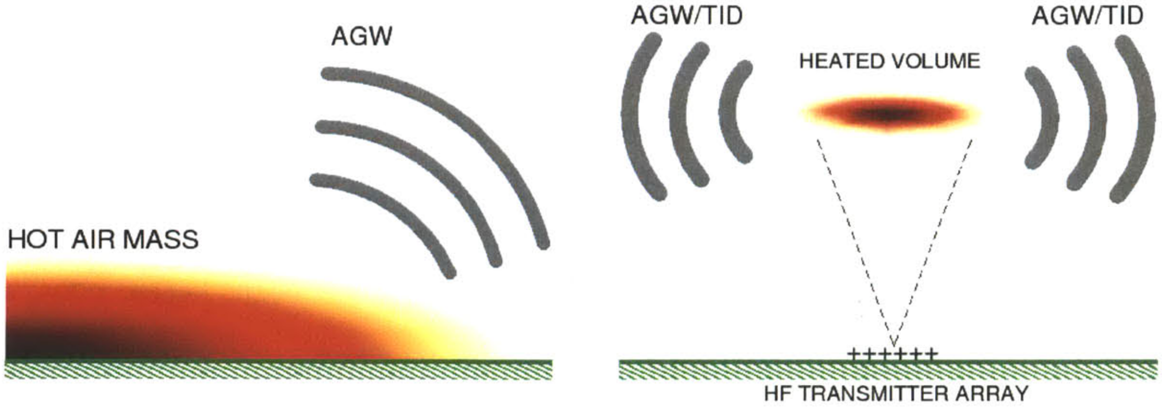

Figure 1-2: The suspected natural AGW excitation during a heat wave event (left). The basic concept of an ionospheric RF heating experiment to simulate AGW/TID excitation by large-scale thermal gradients (right). The diagrams are not to scale.

The above hypothesis therefore implies that a significant amount of ionospheric plasma disturbances are likely to be present over the mainland United States during the aforementioned heat wave period. Routine measurements of ionospheric total electron content (TEC) by the worldwide GPS receiver network should be able to provide some means to confirm this prediction. In order to investigate the possible occurrence of such TIDs, we have examined some GPS TEC data over an extended period of time covering the heat wave period. The main goal here is to establish the potential correlation between the heat waves and intense ionospheric disturbances through the case study.

Moreover, we also perform a series of field experiment to physically simulate the natural process of AGW/TID generation by large-scale thermal gradients. This field experiment is rather important because a correlation alone is generally not sufficient to assert a definitive causal relation between severe heat waves and ionospheric plasma disturbances. If the physical process of AGW/TID generation by large-scale thermal gradients can be successfully demonstrated under a reasonably controlled condition, then the experimental findings would greatly complement the correlation that we are also seeking in our case study using the GPS TEC dataset. The suspected natural mechanism as well as the basic concept of this field experiment are illustrated schematically in Figure 1-2.

In this HF heating experiment, a high-power HF radio transmitter on the ground illuminates a certain ionospheric plasma volume overhead and create artificial thermal fronts at ~250 km altitude. The transmitted power is sinusoidally varied with a modulation frequency that matches the appropriate frequency range of acoustic-gravity waves (AGW) in the upper atmosphere. Based on our working hypothesis, we can expect to have some AGW/TID being radiated out from the heated plasma volume if everything is working properly. At the same time, we are diagnosing these heater-generated artificial AGW/TID using various satellite and ground-based radio diagnostic instruments. This field experiment has been conducted at the High-frequency Active Auroral Research Program (HAARP) facility located in Gakona, Alaska (latitude 62.4° N, longitude 145° W).

In the past, the general concept and speculation regarding artificial AGW/TID generation during ionospheric HF heating experiments had actually been theorized by *Grigor'ev* [1975] and remarked by *Luhmann* [1983]. Based on the observation of rising plasma bubbles (i.e. plasma density depletion) during an ionospheric heating experiment at Arecibo [*Lee et al.*, 1998], there is some indication that the neutral temperature could be increased by the heater transmission [*Gonzalez et al.*, 2005]. However, by and large, there was relatively little experimental evidence that firmly demonstrated the actual feasibility of generating AGW/TID via ionospheric HF heating. During the Platteville heating experiment on 2 October 1970, a set of downward-traveling perturbations in the ionogram traces were observed but unfortunately natural AGW/TID cannot be ruled out [*NOAA Documentation*, 2004]. Meanwhile, some signs of ionospheric disturbances during a heating experiment at the EISCAT facility had been reported by *Blagoveshchenskaya et al.* [2005], but it was never conclusively determined whether they had actually originated from the heated region or not. It seems that there is a considerable difficulty in detecting the heater-generated AGW/TID and being able to distinguish them from the naturally-occurring ones. Indeed, a few other attempts to generate artificial AGW/TID at the HAARP facility [*Mishin et al.*, 2012] also faced some difficulty sorting out natural AGW/TID of auroral origin. To some extent, we have been successful in resolving this challenge in our experiments.

1.2 Summary of the Results

Examination of GPS TEC data over the North American sector shows a slight but quite noticeable increase in the daily RMS value of the TEC perturbation (TECP) during the summer 2006 heat wave period (15 July – 27 August 2006). An overall increase in the RMS TECP value by ~0.2 TECU above its baseline value can be seen promptly at the beginning of the heat wave period. This ~0.2 TECU increase in the RMS TECP value persisted and then gradually declined to the baseline level near the end of the heat wave period (for the detail, see Figure 2-4 in Chapter 2). Geomagnetic condition was relatively quiet throughout summer 2006, and thus any potential contribution from auroral disturbances can be ruled out. This finding indicates a very promising correlation between the occurrence of heat wave event and some increase in TID activity over the area.

During the HAARP-AGW experiments, our multi diagnostic observations have shown a number of positive indications that AGW/TID are indeed being radiated out from the heated plasma volume as a result of the modulated heating. Table 1.1 contains a comprehensive list of main findings from various diagnostic instruments used in the HAARP-AGW experiments. In order to avoid potential contamination from natural AGW/TID of auroral origin, we generally conducted the experiments during geomagnetically quiet times only. From our calculations, a propagation speed in the range of 50–150 m/s is quite typical for the heater-generated AGW/TID. The overall energy efficiency in the HAARP-AGW generation process has been estimated to be about 23%–34%. Based on some fundamental thermodynamic considerations, we have also inferred a lower bound of $T \gtrsim 1.3\,T_0 \sim 1.5\,T_0$ for the peak temperature of ions/neutrals inside the heated plasma volume.

In addition, we also formulated a simple mathematical model and performed some numerical simulations to explain a number of curious features in the experimental data. The semi-analytical fluid model of HAARP-AGW showed that the artificial AGW/TID are generated at the edge of the heated region — confirming the results of our wave kinematics analysis based on the LEO satellite observations. Meanwhile, numerical ray tracing study had also explained some of our digisonde observations quite successfully.

This thesis is organized as follows: First of all, Chapter 2 will talk about the phenomenological correlation between heat wave events and the increased level of ionospheric disturbances. Chapter 3 will describe the concept and basic setup of the HAARP-AGW experiment. Chapters 4–7 will report on the main findings from our observations using various types of radio diagnostic instruments during the HAARP-AGW experiments. Chapter 8 will talk about some results from the numerical model and simulation. Finally, in Chapter 9 we are going to have some discussion and a final conclusion on the general results of this investigation.

Table 1.1: A comprehensive summary of the various multidiagnostic observations in support of the HAARP-AGW experiments 2008–2011.

Diagnostic Instrument	Summary of Main Findings[†]
LEO satellite pass	TECP ripple pattern, more-or-less symmetrical with respect to the center of heated region
GPS satellite pass	wavelike pattern in the TECP signal, with a rather pronounced peak in Fourier frequency spectrum
HAARP digisonde	cluster of skymap echoes with large Doppler shifts at both +ve/-ve polarities; radial-outward streak of traveling disturbances in the skymap echo distribution; additional set of oblique ionogram traces that appear/disappear periodically;
MUIR radar	periodic/oscillatory time variation of LOS velocity just outside of the heated region
Kodiak SuperDARN	AGW/TID signatures in the modulated pattern of ground-scatter echoes
Poker Flat AMISR	AGW/TID signatures overhead the Poker Flat site after 2∼3 hour time delay

[†] Targeted search for affirmative indications of AGW/TID being generated as a result of the modulated ionospheric RF heating.

Additional Note:

LEO = low earth orbit
TECP = total electron content perturbation
GPS = Global Positioning System
HAARP = High-frequency Active Auroral Research Program
MUIR = Modular UHF Ionospheric Radar
LOS = line of sight
SuperDARN = Super Dual Auroral Radar Network
AGW = acoustic-gravity waves
TID = traveling ionospheric disturbances
AMISR = Advanced Modular Incoherent Scatter Radar

Chapter 2

Anomalous Large-Scale Natural Heat Source, AGW and TID

In this chapter, we are going to examine the potential increase in the intensity of ionospheric plasma disturbances during severe heat wave events. A plausible mechanism for it is the generation of acoustic-gravity waves (AGWs) by the advancing thermal fronts, which could then trigger some traveling ionospheric disturbances (TIDs) over extended areas. This possibility had been speculated based on a set of radio and optical observations of intense TIDs at the Arecibo Observatory during the summer 2006 heat wave period [*Pradipta*, MS Thesis 2007]. Here we will discuss some additional evidence that provide further verifications of the aforementioned scenario.

First, we have a set of incoherent scatter radar (ISR) data indicating that the TIDs observed over Arecibo on 21–24 July 2006 were indeed triggered by AGWs that could have survived a long propagation distance. This is necessarily the case for AGWs generated by thermal fronts on the mainland United States to be able to trigger some TIDs over the Caribbean sector. Finally, we also have some GPS TEC surveillance data over the North American sector itself. The data shows a prompt increase of TEC fluctuations during the summer 2006 heat wave event. Comparison with the summer 2005 and 2007 data reveals that the observed increase in TECP during the summer 2006 heat wave period was not a regular seasonal phenomenon.

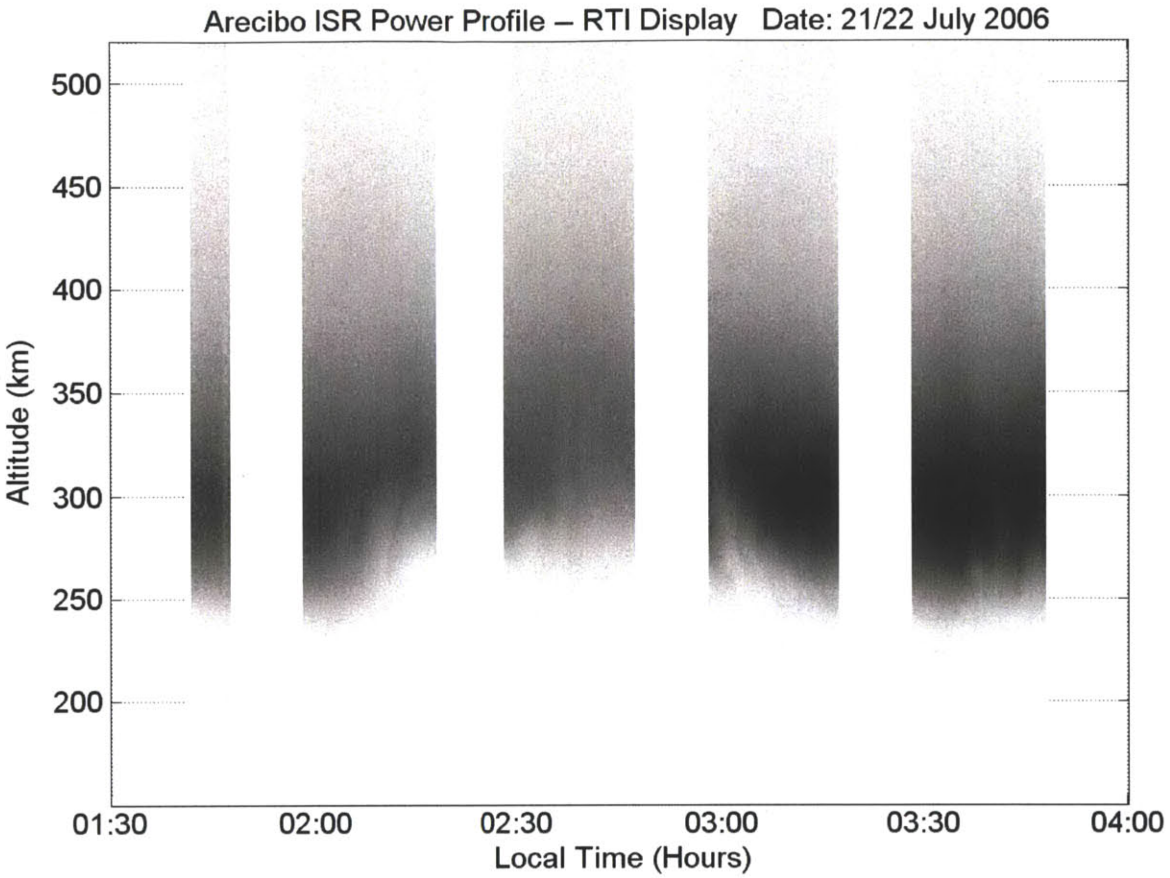

Figure 2-1: RTI plot of radar backscatter power during time period 01:30–04:00 LT on the night of 21/22 July 2006. One may recognize the presence of filament-like irregularities and an overall wavelike oscillation of the ionospheric plasma layer.

2.1 Arecibo ISR Data on 21/22 July 2006

Shown in Figure 2-1 is a range-time-intensity (RTI) plot of radar backscatter power recorded by the Arecibo ISR on the night of 21/22 July 2006. Darker color in the grayscale denotes larger backscatter power value, and vice versa. This particular dataset was not reported previously in *Pradipta* [MS Thesis, 2007] due to a lack of supporting optical airglow data on that night (very cloudy sky). For this radar observation, we operated the Arecibo ISR using a single vertical stationary beam. The backscatter power measurements give us density profile data with 600 m altitude resolution and 10 s time resolution. A series of data gaps (regular white columns of ~10 minute duration) occurred whenever the radar momentarily switched into a different mode of operation for some plasma line spectra measurements.

There are two important features that are quite apparent in this particular ISR dataset: (1) the presence of some filament-like plasma irregularities, and (2) an overall wavelike vertical displacement of the ionospheric plasma layer. We shall examine these features to gain some useful insights in our investigations.

The presence of some filament-like irregularities indicates that the vertical movement of the ionospheric plasma layer was not simply a smooth rise/descent from $\mathbf{E} \times \mathbf{B}$ drift controlled by a gradual time variation of the background electric field. The rugged structures on the bottomside ionosphere most likely had been caused by the (generalized) Rayleigh-Taylor instability seeded by some atmospheric gravity waves that are passing by [see e.g. *Nicolls and Kelley*, 2005; *Lee et al.*, 2008]. This particular feature in the data has ruled out the scenario of a simple rise/descent from $\mathbf{E} \times \mathbf{B}$ drift, and hence the apparent wavelike oscillation in this ISR dataset can be conclusively attributed as a signature of long-wavelength gravity waves.

The observed wavelike oscillation of the ionospheric plasma layer has a period of ~90 minutes, based on the time interval between a "valley" of this wavelike cycle at around 02:00 LT to the next one at around 03:30 LT. The significantly long wave period (> 1 hour) suggests that the gravity waves that had caused this vertical oscillation (~50 km displacement) must have a considerably large wavelength and could have come from far away, surviving a long propagation distance. This is the case because small-scale gravity waves of terrestrial origin would typically be dissipated at lower altitudes, and therefore cannot reach ionospheric heights [*Hines*, 1960; *Yeh and Liu*, 1972]. Furthermore, large-scale gravity waves are also able to propagate in ducted mode with relatively little attenuation [*Francis*, 1973].

This finding further motivates our current hypothesis that large thermal fronts over the mainland United States could generate gravity waves capable of reaching the Caribbeans and trigger ionospheric plasma turbulence over Arecibo. In this proposed scenario, the AGWs generated by the heat wave fronts over North America must be able to survive a long propagation distance in order to reach Arecibo and trigger some TIDs there. The characteristic signatures of long-wavelength gravity wave we observed here is therefore in support of the suspected scenario.

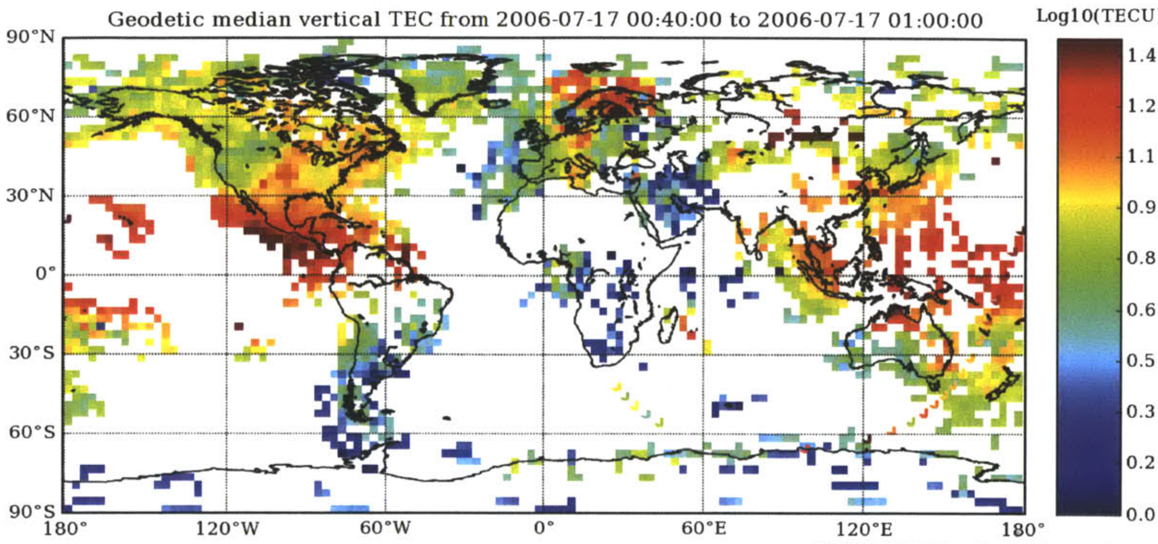

© 2009 MIT Haystack Observatory

Figure 2-2: Sample 2-D global data plot of the absolute TEC values taken from the worldwide GPS receiver network in the Madrigal database.

2.2 Worldwide GPS-Derived TEC Data

In addition to providing plausible explanations for the ionospheric plasma turbulence observed over Arecibo on 21–24 July 2006, our current hypothesis also implies a likely occurrence of some ionospheric plasma disturbances over the mainland United States itself during the summer 2006 heat wave period. Routine measurements of ionospheric total electron content (TEC) by the worldwide GPS receiver network should be able to provide an effective way to confirm this prediction. Indeed, some medium-scale TID (MSTID) was observed on 20 July 2006 [*Tsugawa et al.*, 2007] using the wide and dense GPS TEC maps over North America. To further confirm our hypothesis, we will examine some GPS TEC data over an extended period of time for a more complete picture of the phenomenon.

2.2.1 The Madrigal GPS TEC Database

A dual-frequency GPS receiver can be used to compute the value of slant TEC along the line-of-sight between the GPS satellite and the receiver [*Checcacci*, 1970]. This can be done using the differential carrier phase or the differential group delay between

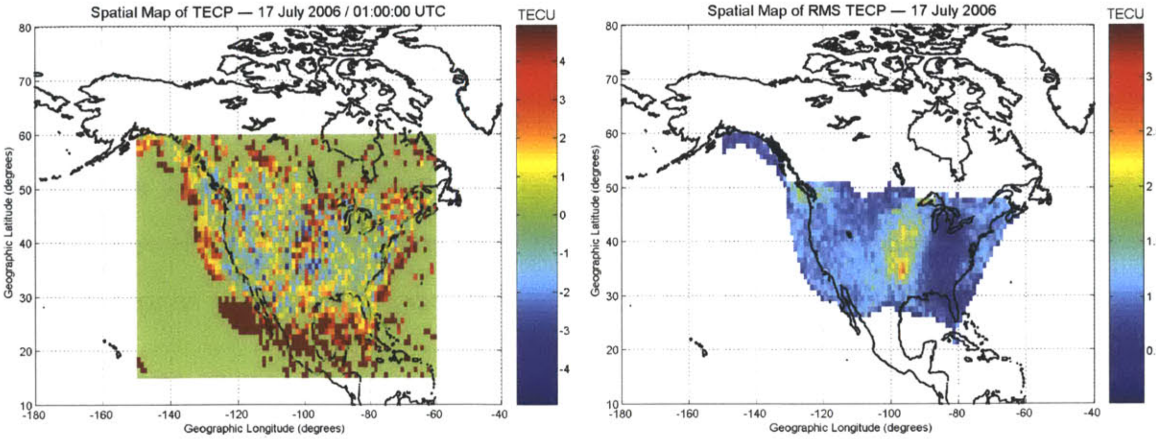

Figure 2-3: Sample 2-D maps of the TECP values over North America at certain time of the day (left) and the RMS TECP values over a 24-hour period (right).

the L1 and L2 navigation signals (at 1575.42 MHz and 1227.60 MHz, respectively). A dense network of GPS receiver stations therefore could provide a continuous monitoring of TEC values over that particular region. For our investigations, we are using the worldwide GPS TEC map from MIT Haystack Observatory's Madrigal database (accessible online at http://madrigal.haystack.mit.edu/ for public use). The vertical TEC values in this database are derived using the minimum scalloping techniques as described in *Rideout and Coster* [2006].

Shown in Figure 2-2 is a typical spatial pattern of the global TEC values at a certain time of the day. There is generally no data coverage over oceans and deserts. Likewise, blind spots are quite frequent near coastal areas or islands as well. In order to identify ionospheric disturbances and their variability, we will need to compute the net fluctuations of TEC from the absolute TEC data. The detailed procedure for calculating the TEC perturbation (TECP) is desribed in Appendix A of this thesis. Furthermore, by averaging the TECP values over a 24-hour period, we can obtain a map of daily RMS TECP values, which could serve as a quantitative measure for the intensity of ionospheric plasma disturbances over the region on that particular day. Figure 2-3 shows the representative case of TECP and RMS TECP maps calculated for the North American sector, which is the main focus in our investigation.

If there are more occurrences of ionospheric plasma disturbances over a certain region, we could reasonably expect higher RMS TECP values compared to that from a normal period. Hence, by monitoring the daily RMS TECP values continuously over the course of several months, we would be able to determine if the the level of ionospheric plasma disturbances had intensified during a specific time period. In the following section, we are going to examine the trend in RMS TECP values over North America to confirm our earlier prediction on the possible increase in ionospheric plasma disturbances during heat wave events.

2.2.2 Ionospheric Disturbances during Heat Wave Event

Using the summer 2006 data as the main subject of attention, we are going to look for some evidence indicating that there are indeed some increase in the intensity of ionopsheric disturbances during the heat wave event. We will also examine the summer 2005 and summer 2007 data as a case comparison, in order to rule out possible seasonal effects that might keep recurring every summer. For the data analysis, in addition to TECP we will also compute the differential TECP (DTECP) which is proportional to the time rate of change of TECP. More specifically, our definition for the DTECP signal is

$$\mathrm{DTECP}(t) \equiv \mathrm{TECP}(t + \Delta t) - \mathrm{TECP}(t) \tag{2.1}$$

where in our case $\Delta t = 5$ minutes is the temporal resolution of the GPS TEC data from the Madrigal database. Some further elaboration regarding the TECP and DTECP signals can be found in Appendix A of this thesis.

The result of our examination of the summer 2006 GPS TEC data over North American sector is shown in Figure 2-4. Plotted here are the daily RMS TECP and RMS DTECP values as a function of time over a specific location. We also plotted the time variation of geomagnetic K_p index to help account for any possible contamination from auroral disturbances caused by geomagnetic storms. The fact that K_p values had generally stayed below the storm threshold level indicates that geomagnetic storms probably did not have significant contribution to any patterns

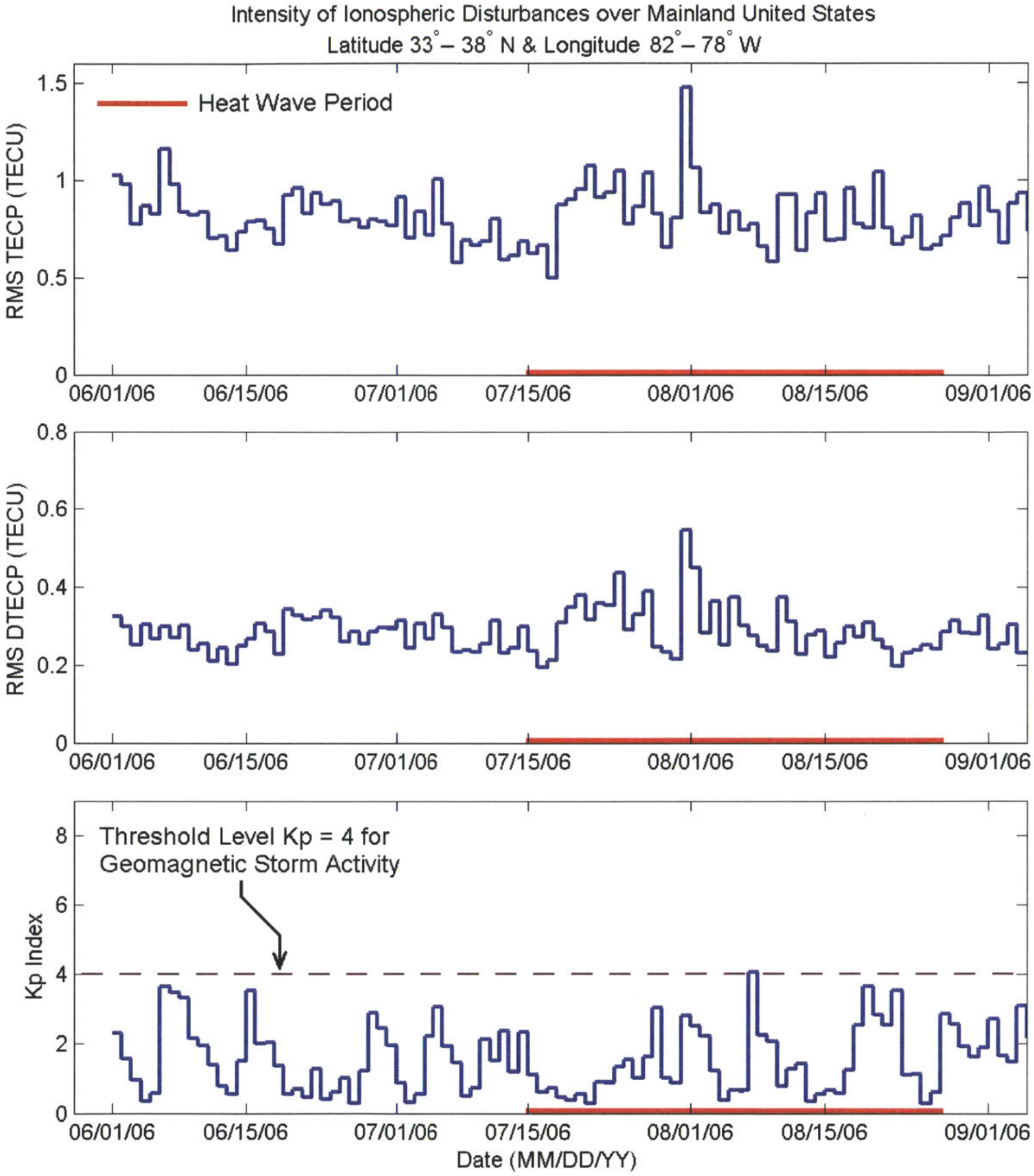

Figure 2-4: Plots of the day-averaged TECP and DTECP amplitudes over North America (around latitude 35°N & longitude 80°W) for the entire summer 2006. We have a slight but quite noticeable increase in the TID intensity over this location during the heat wave period (15 July – 27 August 2006). The K_p index had stayed below the storm level, indicating that the geomagnetic condition was generally quiet during this time period.

we are to see in the GPS TEC data.

The common consensus for the gross duration of the summer 2006 North American heat wave is 15 July – 27 August 2006 [see e.g. *Gershunov et al.*, 2009; and *Wikipedia Articles* on these topics]. The heat wave period is marked red on the time axis for all the plots shown in Figure 2-4. During the heat wave period, we can see a prompt increase in both the RMS TECP and the RMS DTECP values. The overall increase is about 0.2 TECU above the baseline for the RMS TECP, and about 0.1 TECU for the RMS DTECP. This is only a slight increase of TEC fluctuations in the absolute sense. However, the noticeable sharp rise in the beginning of the heat wave period and the gradual falloff near the end of the heat wave period certainly suggest that there is a potential correlation between the increased ionospheric disturbance and the heat wave.

Meanwhile, we also need to look at the summer 2005 and 2007 data for a case comparison. It is totally possible that the pattern we observed in the 2006 data simply happens to be a seasonal variation, not an anomaly related to the prolonged heat waves. The case comparison would therefore be useful to help eliminate this uncertainty. The results from the 2005 data are shown in Figure 2-5, while those from the 2007 data are shown in Figure 2-6. Using the 2005 and 2007 data, we shall examine the general trend in RMS TECP and RMS DTECP at the same geographical location that we selected for the summer 2006 data. The comparison period (which corresponds to the summer 2006 heat wave event) is marked orange on the time axis for all the plots in Figure 2-5 and Figure 2-6.

Overall, the geomagnetic condition in summer 2005 was somewhat more active compared to summer 2006 — but no major geomagnetic storms nonetheless. During the comparison period (around 1 August 2005), we may notice a faint sign of increased ionospheric disturbance. However, this brief bump in RMS TECP / RMS DTECP lasted much more shortly than the pattern of prompt rise and gradual decline that we found in the summer 2006 data. Meanwile, the summer 2007 data shows a very quiet geomagnetic condition throughout the entire summer, without any substantial increase in RMS TECP / RMS DTECP during the comparison period. For a more

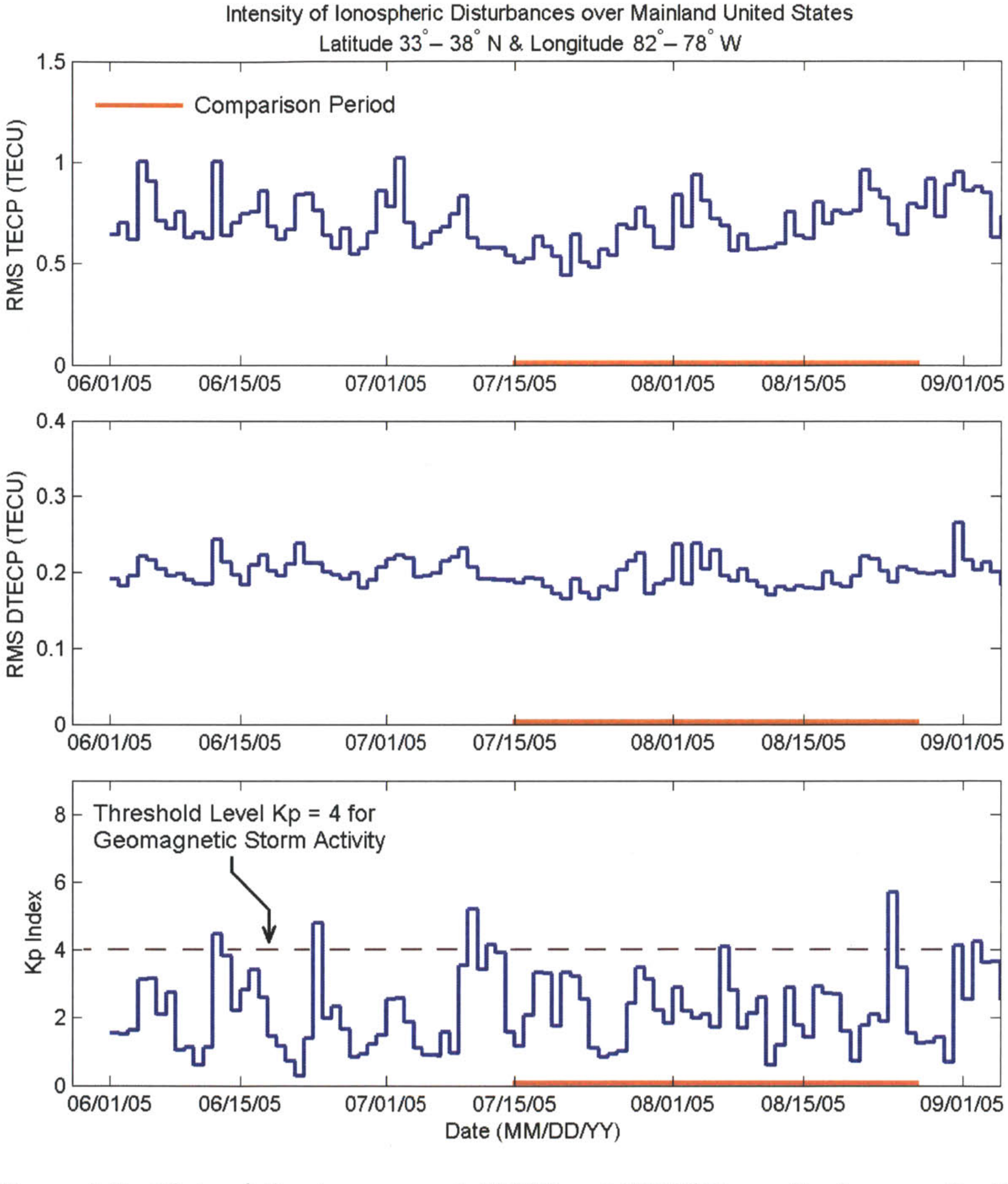

Figure 2-5: Plots of the day-averaged TECP and DTECP amplitudes over North America (around latitude 35°N & longitude 80°W) for summer 2005. In this case, we observed no prompt increase in the TID intensity within the comparison period matching the summer 2006 heat wave event.

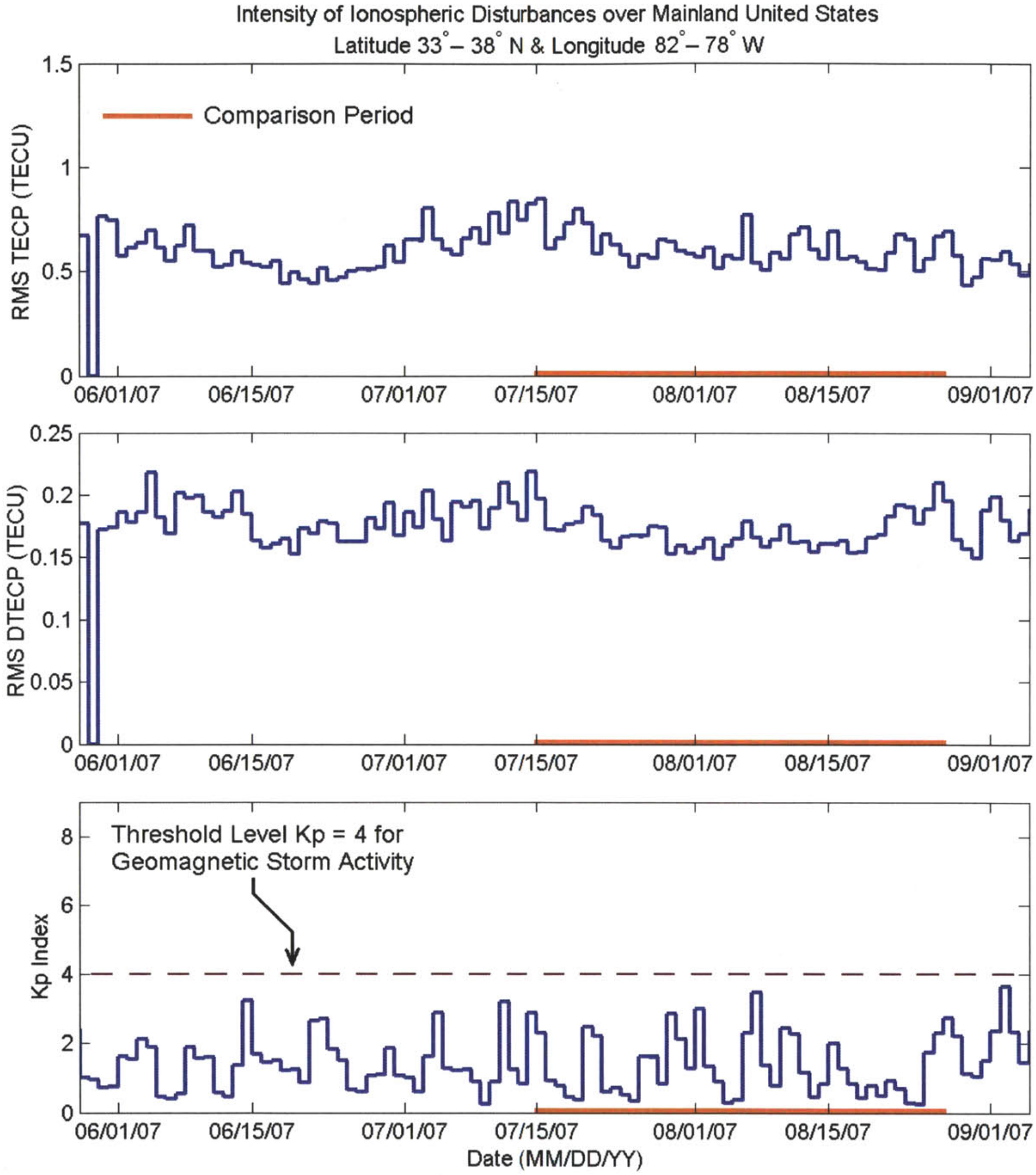

Figure 2-6: Plots of the day-averaged TECP and DTECP amplitudes over North America (around latitude 35°N & longitude 80°W) for summer 2007. There is no significant increase in the TID intensity during the comparison period like that we had observed in the 2006 data.

direct year-to-year comparison, overlaid data plots of RMS TECP and RMS DTECP from these three summers can be found in Figure 2-7. Based on the results of this case comparison, we can conclude that the pattern we observed in the summer 2006 GPS TEC data is a rather unique occurrence and not a regular seasonal variation that keeps recurring every summer.

In summary, we have examined some experimental evidence to confirm several predictions arising from the earlier speculation [*Pradipta*, MS Thesis 2007]. Our observation so far indicates that the large-scale heat wave fronts could have generated AGWs capable of triggering TIDs over extensive region. Using the Madrigal GPS TEC data, we have shown that the overall intensity of ionospheric plasma disturbances increased promptly during the summer 2006 heat wave period. In addition, through a case comparison using 2005 and 2007 data, we also demonstrate that this increase is evidently not a recurring seasonal effect.

The apparent correlation between heat wave events and higher level of ionospheric disturbances that we established using the GPS TEC data is a very promising lead. However, we would like to obtain a more direct confirmation that large-scale heat sources can indeed generate some AGW/TID. This goal might be achieved through a specially designed ionospheric HF heating experiment. In the remainder of this thesis, we will discuss about this controlled experiment where we try to simulate how large-scale natural thermal fronts (such as severe heat waves) could generate AGWs.

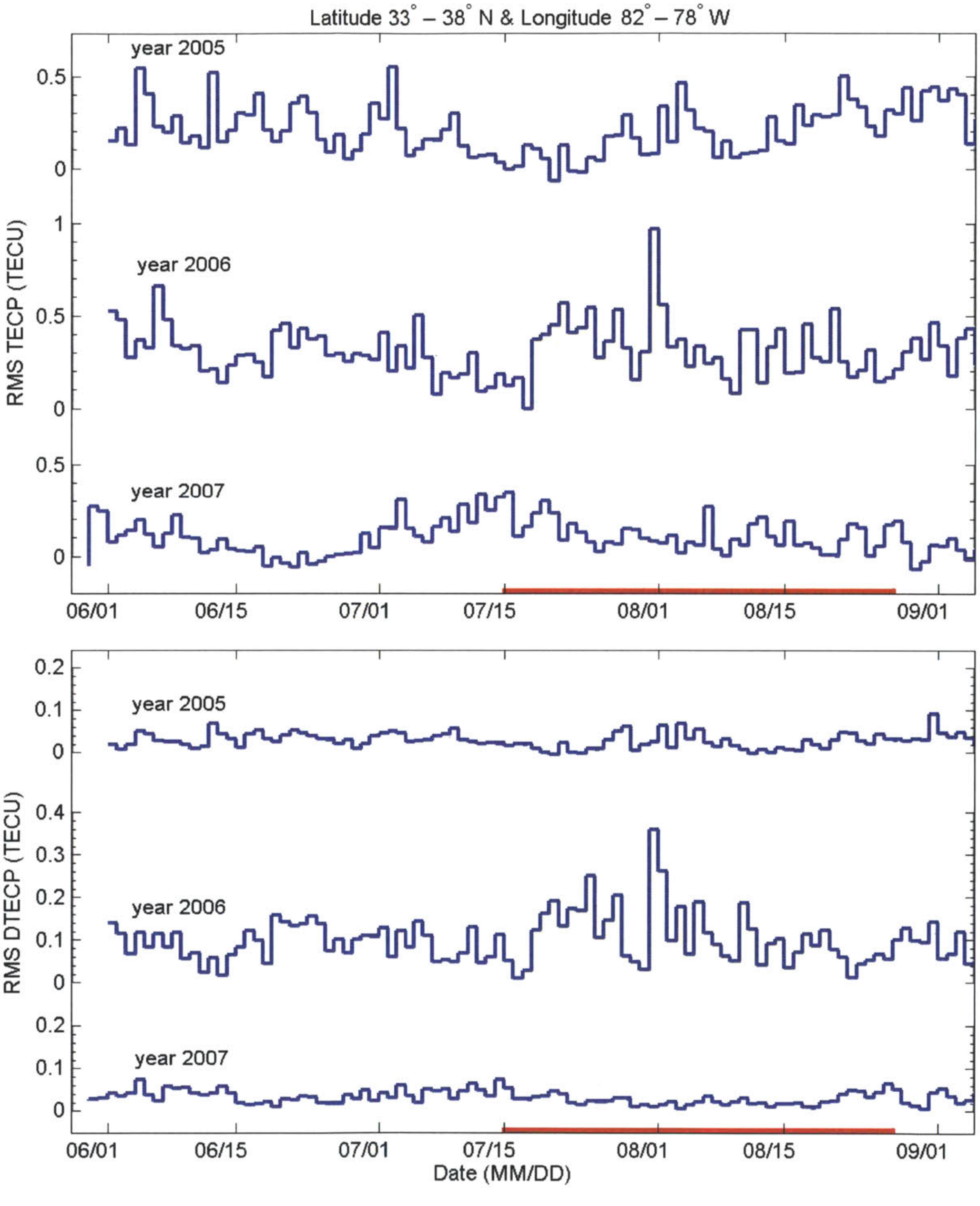

Figure 2-7: Plots of the day-averaged TECP and DTECP amplitudes over North America (around latitude 35°N & longitude 80°W) for summer 2005, 2006, and 2007. The RMS TECP data from these three summers are stacked/overlaid together with the same y-scale (similarly for the RMS DTECP data). The red marking on the time axis indicates the North American heat wave period in the summer 2006 — to be compared directly with the same time-of-year in 2005 and 2007.

Chapter 3

The HAARP-AGW Experiment

This chapter will talk about the basic concept of a field experiment that had been devised to physically simulate the generation of acoustic-gravity waves (AGWs) by anomalous large-scale natural heat source. The field experiments are conducted at the High-frequency Active Auroral Research Program (HAARP) facility located in Gakona, Alaska (latitude 62.4° N, longitude 145° W). We are going to give a general overview on this ionospheric HF heating experiment, especially about the main rationale behind the heating scheme and the prepared strategy for utilizing the available diagnostic instruments.

3.1 Generating AGW via Modulated Heating

The basic plan for the HAARP-AGW experiment is quite simple. A high-power HF transmitter on the ground will illuminate a certain plasma volume overhead, heating the ions and subsequently the neutral species as well. The transmitted HF power is modulated sinusoidally so that we will also have a sinusoidal rate of heat deposition in the heated region. The modulation frequency Ω must be properly chosen to allow for non-evanescent acoustic-gravity waves. This is going to be an overdense HF heating experiment using O-mode wave polarization, and hence the heated plasma volume would be situated around an altitude z_0 where the heater wave frequency equals the local plasma frequency. If everything goes according to plan, we expect to see

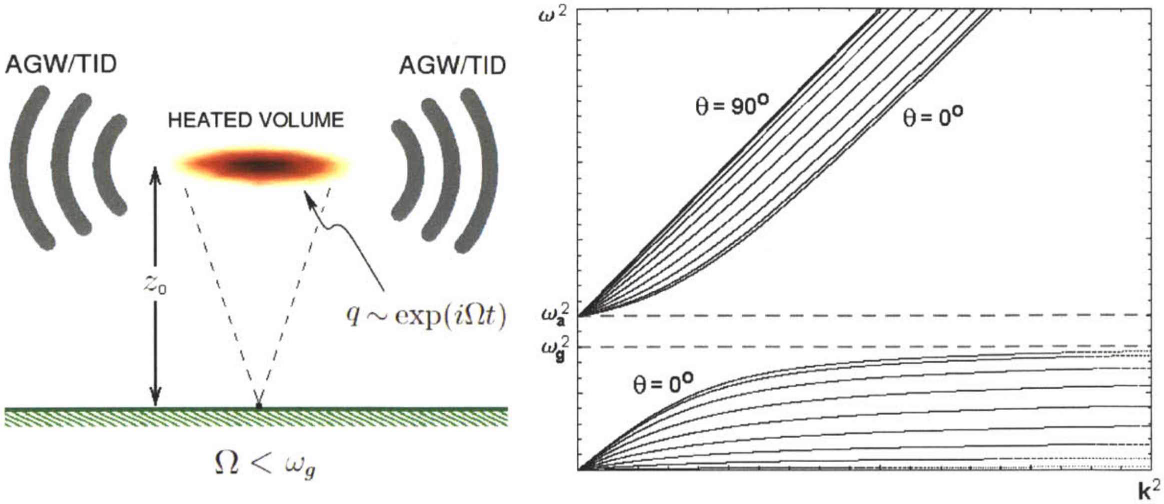

Figure 3-1: Schematic illustration of the field experiment to generate AGW/TID via modulated RF heating (left). Plot of the AGW dispersion curves for various elevation angle θ from horizontal (right). To generate AGWs, the modulation frequency Ω must be below the local Brunt-Vaisala frequency ω_g.

some AGWs being radiated out from the heated plasma volume. This is illustrated schematically on the left panel of Figure 3-1.

The dispersion relation for acoustic-gravity waves in an isothermal atmosphere, i.e. constant and uniform background temperature, is given by [*Hines*, 1960]:

$$\omega^4 - \omega^2 c_s^2 (k_x^2 + k_z^2) + (\gamma - 1) g^2 k_x^2 - \frac{\gamma^2 g^2 \omega^2}{4 c_s^2} = 0 \tag{3.1}$$

where c_s is the sound speed; g is the gravitational acceleration; γ is the ratio of specific heats; ω is the wave angular frequency; and k_x (k_z) denotes the horizontal (vertical) wavenumber, respectively. The corresponding AGW dispersion curves are shown on the right panel of Figure 3-1, for various elevation angle θ between the wavevector $\mathbf{k}$ and the horizontal direction. The high-frequency branch with $\omega > \omega_a \equiv \gamma g / 2 c_s$ is the acoustic waves. Meanwhile, the low-frequency branch with $\omega < \omega_g \equiv \sqrt{\gamma - 1}\, g / c_s$ is the (internal) gravity waves. Note also that for $\omega_g < \omega < \omega_a$ we have an evanescent band in which acoustic-gravity wave propagation is not possible. Given that our goal in this experiment is to generate (internal) gravity waves, we need to have the modulation frequency $\Omega < \omega_g$ in our heating scheme.

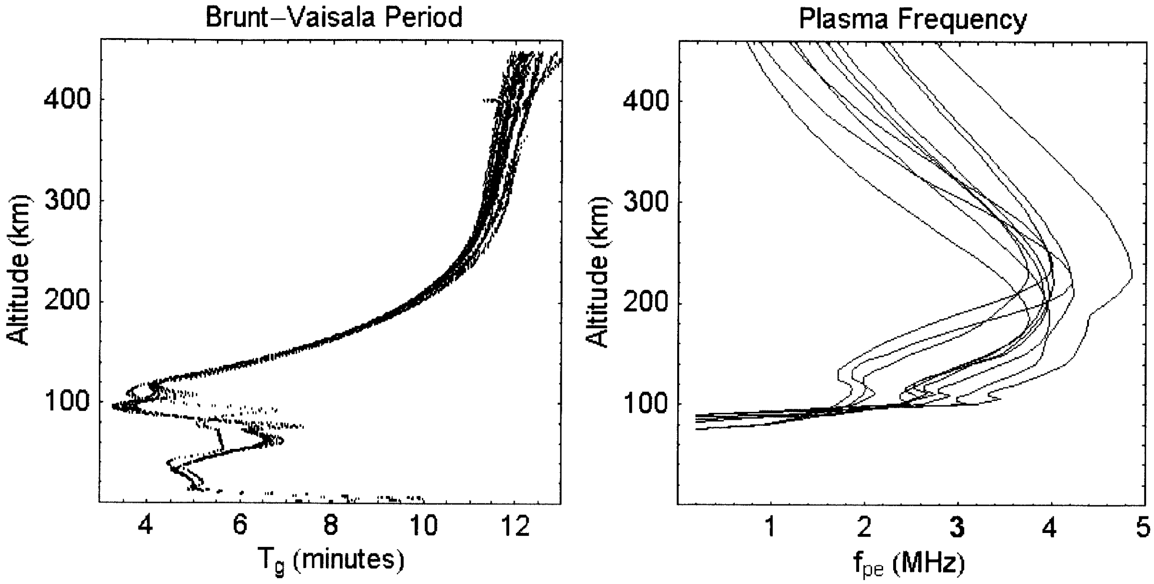

Figure 3-2: Typical altitude profile of Brunt-Vaisala period (left) and ionospheric plasma frequency (right) over Gakona, Alaska, during our experiments. The heating modulation period T needs to be greater than the local Brunt-Vaisala period T_g.

The characteristic frequency ω_g is known as the Brunt-Vaisala frequency, which is the natural frequency for air parcels in the atmosphere to oscillate up and down due to buoyancy [*Kelley*, 1989; *Yeh and Liu*, 1972]. If we allow for an inhomogeneity in the background temperature along the vertical direction, the more general expression for the Brunt-Vaisala frequency is [*Beer*, 1974]:

$$\omega_g = \sqrt{g\left[\frac{1}{T}\frac{\partial T}{\partial z} - \frac{(\gamma-1)}{\gamma}\frac{1}{p}\frac{\partial p}{\partial z}\right]} \tag{3.2}$$

which will be useful for us to estimate the altitude profile of the Brunt-Vaisala period.

By entering the relevant physical parameters from the NRL MSIS-E atmospheric model into Equation 3.2, we can compute the Brunt-Vaisala period $T_g \equiv 2\pi/\omega_g$ as a function of altitude. We are using the geographical coordinate of the HAARP facility (62.4°N, 145°W) for the purpose of this calculation. The result is depicted on the left panel of Figure 3-2. Meanwhile, the right panel of Figure 3-2 shows the typical altitude profile of plasma frequency $f_{\text{pe}}(z)$ based on a series of ionosonde measurements at the same geographical location. Some additional detail on the derivation of the

Brunt-Vaisala frequency as well as the numerical calculation of its altitude profiles can be found in Appendix B of this thesis.

To generate gravity waves, the modulation period $T \equiv 2\pi/\Omega$ needs to be larger than the Brunt-Vaisala period $T_g \equiv 2\pi/\omega_g$ at the altitude of interest. Since typically the maximum plasma frequency is never located higher than 250 km altitude, the heated plasma volume will always be located below this altitude as well. Based on this consideration, we set the modulation period to be $T = 12$ minutes for the HAARP-AGW experiments. For this choice of modulation period, we can verify that $T > T_g$ over most of the altitude range (especially below 250 km) according to our numerical calculation.

3.2 Experimental Setup at the HAARP Facility

The basic setup for the HAARP-AGW experiment is shown in Figure 3-3. Besides the high-power HF transmitter, which creates the time-varying thermal gradients in the ionosphere, the diagram also depicts a number of radio diagnostic instruments that we are using for this experiment. We have ground-based radio diagnostics as well as satellite radio diagnostics, but we have some unfortunate limitation that there will be no optical diagnostics and/or *in situ* diagnostics.

The main reason for us not to have any optical diagnostics is that currently the experiments have to be conducted during the daytime. We had been in the solar minimum for the past few years, and hence the ionospheric plasma density was generally too low for conducting overdense heating experiments at HAARP during the nighttime [see e.g. *Hargreaves*, 1992]. Consequently, during this particular part of the solar cycle we are forced to conduct the HAARP-AGW experiments only during the daytime without any airglow measurements (sensitive optical instruments might be damaged if the sky is too bright). Meanwhile, the option of *in situ* measurements is not feasible for the HAARP-AGW experiments simply because we do not have any suitable probe-carrying satellites that orbit near an altitude of ~250 km and the HAARP facility is just not located in a rocket firing range.

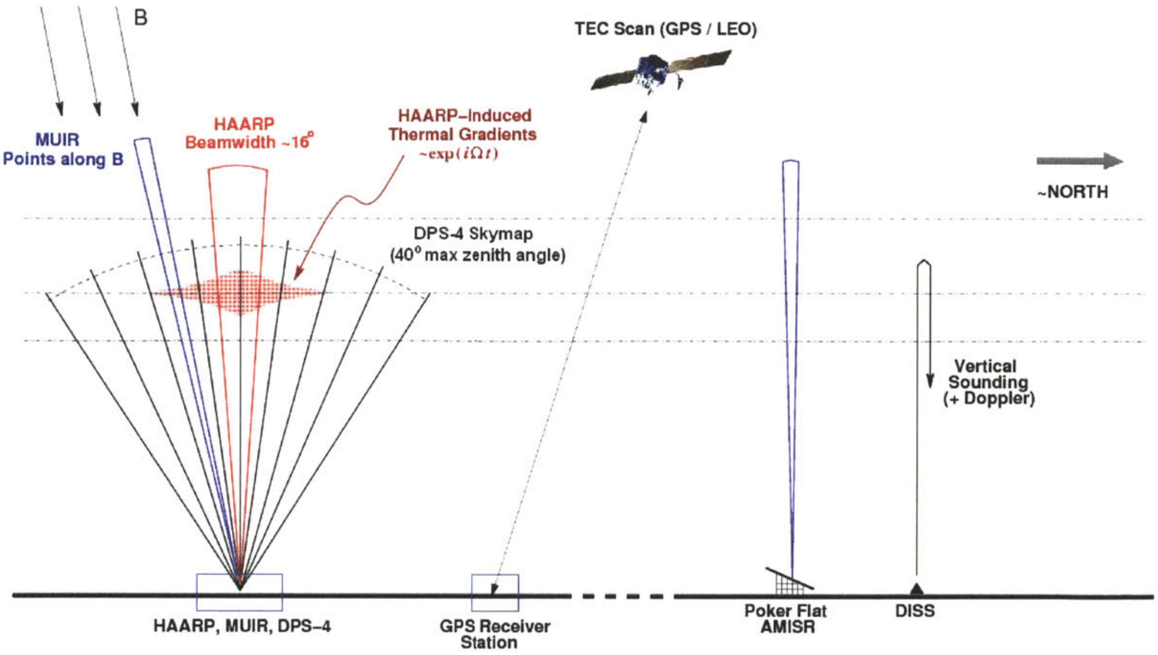

Figure 3-3: The basic experimental configuration of the HAARP-AGW experiment, depicting the most relevant diagnostic instruments.

The radio diagnostic instruments for this experiment are mostly located on-site at the HAARP facility; including the DPS-4 digisonde, MUIR radar, and GPS/LEO receiver units. In addition, we have a few off-site radio diagnostic instruments as well, such as the Poker Flat AMISR (~300 km northwest of the HAARP site) and the Kodiak SuperDARN radar (not shown in the diagram).

The digisonde is a reflectometry diagnostic instrument, which will provide us with both ionogram and skymap measurements (Chapter 4). The MUIR radar will give some information on the line-of-sight Doppler velocity (Chapter 5). Meanwhile, the Poker Flat AMISR and the Kodiak SuperDARN can also be used to detect AGW/TID signatures (Chapter 6). Finally, during the GPS/LEO satellite pass we would be able to obtain some TEC measurements (Chapter 7). If only optical diagnostic instruments can be operated during the experiments, we would also be able to use all-sky imagers and Fabry-Perot interferometers to help diagnose heater-generated AGWs/TIDs through airglow measurements.

The fundamental strategy for an effective use of these diagnostic instruments in HAARP-AGW experiments is to (1) look for pronounced AGW/TID signatures that appear timely during/after the modulated heating scheme is performed, and (2) show that the observed AGWs/TIDs actually originate from the heated region or at least have matching characteristics as the modulation heating cycle. Through this strategy, we ultimately aim to be able to distinguish heater-generated AGWs/TIDs from naturally-occurring ones. By having multi-diagnostic instruments which provide several independent method of measurements, hopefully we will gain a quite significant advantage to confirm the generation of AGWs/TIDs by modulated RF heating.

Chapter 4

Ground-Based Radio Diagnostics Using Digisonde

In this chapter we will discuss the principal use of the digisonde data for HAARP-AGW experiments. We are going to begin by providing a brief overview about the basic operation of a digisonde. Specifically, we will describe how the digisonde routinely performs ionogram and skymap measurements. We will then examine an extensive collection of digisonde ionogram/skymap data recorded for the HAARP-AGW experiments during several campaigns. These ionogram/skymap mesurements revealed that the signatures of heater-generated AGW/TID may appear in several different ways. Our overall findings from the digisonde data indicate that AGWs/TIDs has been succesfully generated by the modulated HF heating during our experiments.

4.1 Basic Functions of a Digisonde

The digisonde (= digital ionosonde) is one of the most basic ground-based diagnostic instrument for studying space plasmas. It is a swept-frequency HF radar that typically operates in the 1-25 MHz frequency range [see e.g. *Rawer*, 1993; *Hunsucker and Hargreaves*, 2002]. The two main types of digisonde data are in the forms of ionograms and skymaps. Ionograms are mainly used for density profile measurements and for diagnosing turbulence. On the other hand, skymaps contain additional information

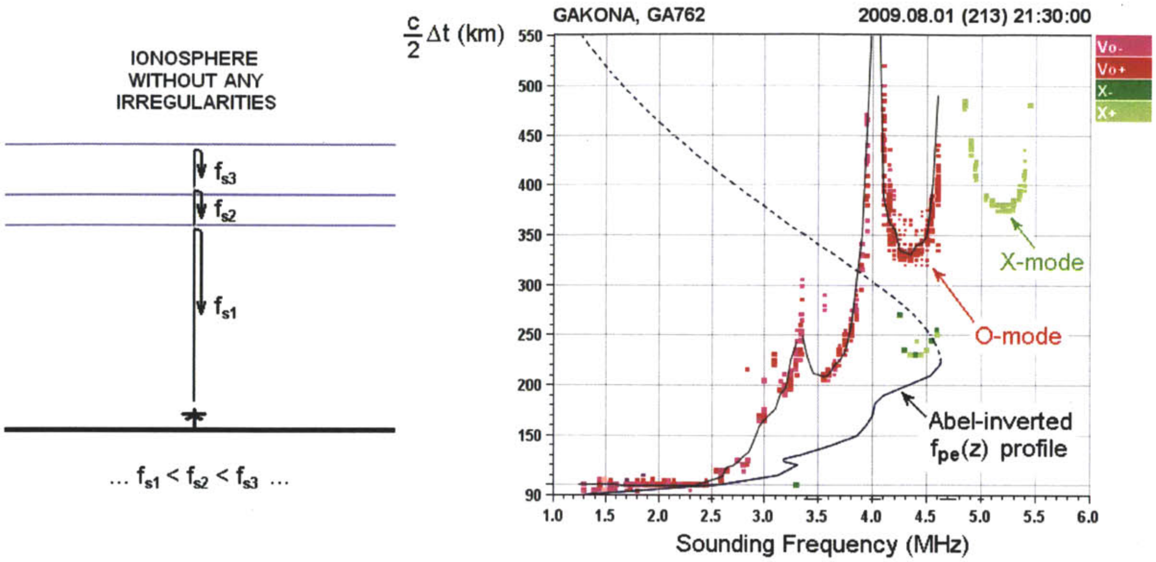

Figure 4-1: Primary usage of the digisonde as a reflectometry diagnostic instrument. The plot of virtual height / virtual range ($\equiv c\,\Delta t/2$) as a function of the sounding frequency is commonly known as an *ionogram*.

on the spatial distribution and Doppler shift of the return echoes. However, skymap measurements are typically constrained to a much smaller set of sounding frequencies than a normal ionogram data acquisition.

As illustrated in Figure 4-1 above, a digisonde is primarily used as a reflectometry diagnostic instrument to determine the ionospheric plasma density profile. The radio diagnostic pulses from the digisonde will propagate upward until reaching the wave cutoff altitude, where they will reflect back. The larger the sounding frequency, generally the higher the reflection altitude would be. The digisonde then records the roundtrip time delay Δt taken by these diagnostic pulses. The scatter plot of virtual height values ($\equiv c\,\Delta t/2$) as a function of the sounding frequency is commonly known as an *ionogram*. There would be two separate traces, which correspond to O-mode and X-mode wave polarizations. One may then perform Abel-inversion on the ionogram traces to obtain the true height profile of the plasma frequency values. The presence of some turbulence usually leads to spread echoes in the ionogram.

A digisonde can also perform skymap measurements, which will also specify the arrival angles (azimuth & zenith) in addition to the time delay. The arrival angles of the return signals are determined through interferometry using a set of receiveing

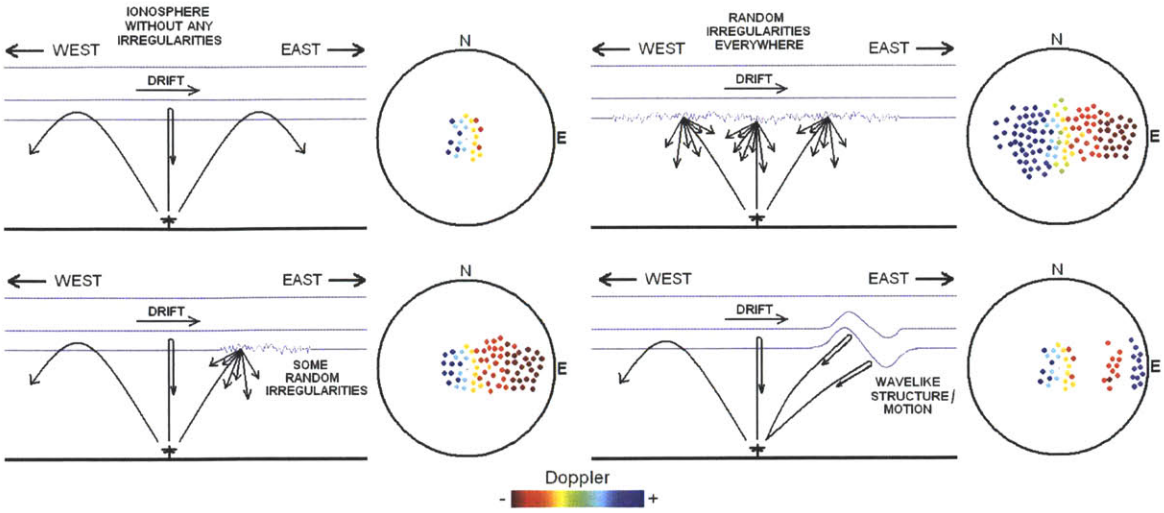

Figure 4-2: Skymap representation of the digisonde data conveys some additional information on the return echoes, such as arrival angles and Doppler shifts. The spatial gradation of Doppler shifts may be used to infer the plasma drift velocity. Meanwhile, AGW/TID have their own characteristic Doppler and spatial signatures.

antennas separated by some distance apart [*Reinisch et al.*, 1998]. In general, the spatial configuration of skymap echoes depends on two things: the overall shape of the plasma density contours (return echoes by total reflection) and the distribution of ionospheric plasma irregularities (return echoes by Bragg scattering). The drift velocity can be inferred from the skymap data based on the Doppler shift pattern. For a uniform drift velocity, typically half of the skymap will be filled with blueshifted echoes while the opposite half will be filled with redshifted echoes. However, the presence of some AGW/TID might alter this typical configuration considerably. This is because AGW can generally propagate in a direction opposite of the plasma drift, and it also inherently carries some wind speed oscillation. A summary of the main concepts regarding skymap measurements is shown in Figure 4-2.

4.2 Digisonde Data from the AGW Experiments

We are now going to examine a number of digisonde measurements taken during the HAARP-AGW experiments. The skymap data are often presented here in terms of

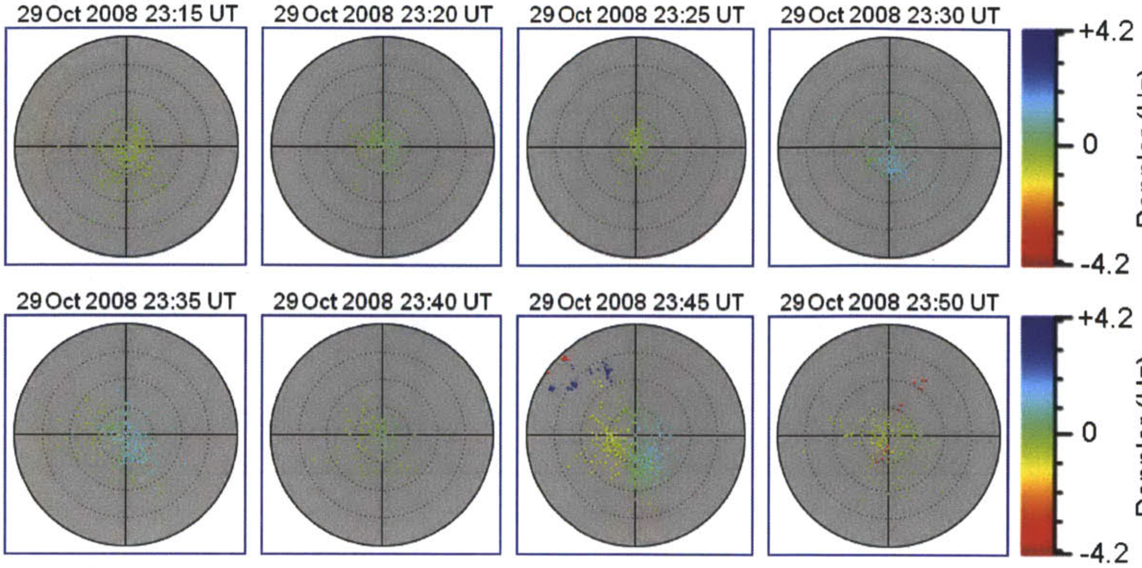

Figure 4-3: A sequence of recorded skymaps during the HAARP-AGW experiment on 29 October 2008. The HF heater was OFF in the time period 23:14–23:26 UT, and the sinusoidal modulation heating was performed in time period 23:26–24:00 UT.

radial-zenith-planar distribution histograms (details can be found in Appendix C).

4.2.1 HAARP-AGW Experiment on 29 October 2008

In Figure 4-3 we have a series of digisonde skymaps that were recorded for the HAARP-AGW experiment on 29 October 2008. The modulated HF heating was performed 23:26–24:00 UT, after being preceded by an OFF period 23:14–23:26 UT. The color for each of the return echoes indicate their respective Doppler shift values, specified according to the colormap.

After two cycles of modulated HF heating had been completed, at 23:45 UT an elongated band of skymap echoes with relatively large Doppler shifts (in both +ve and −ve polarities) appeared on the northwest quadrant. A cluster of skymap echoes containing opposite polarities in the Doppler shift is a sign of some oscillatory wind velocity pattern, which would certainly be the case if some AGW/TID are present in the area. Thus, we have obtained a promising indication that some AGW/TID are generated as a result of the modulated HF heating.

The evidence so far is quite suggestive. However, we have been particularly lucky

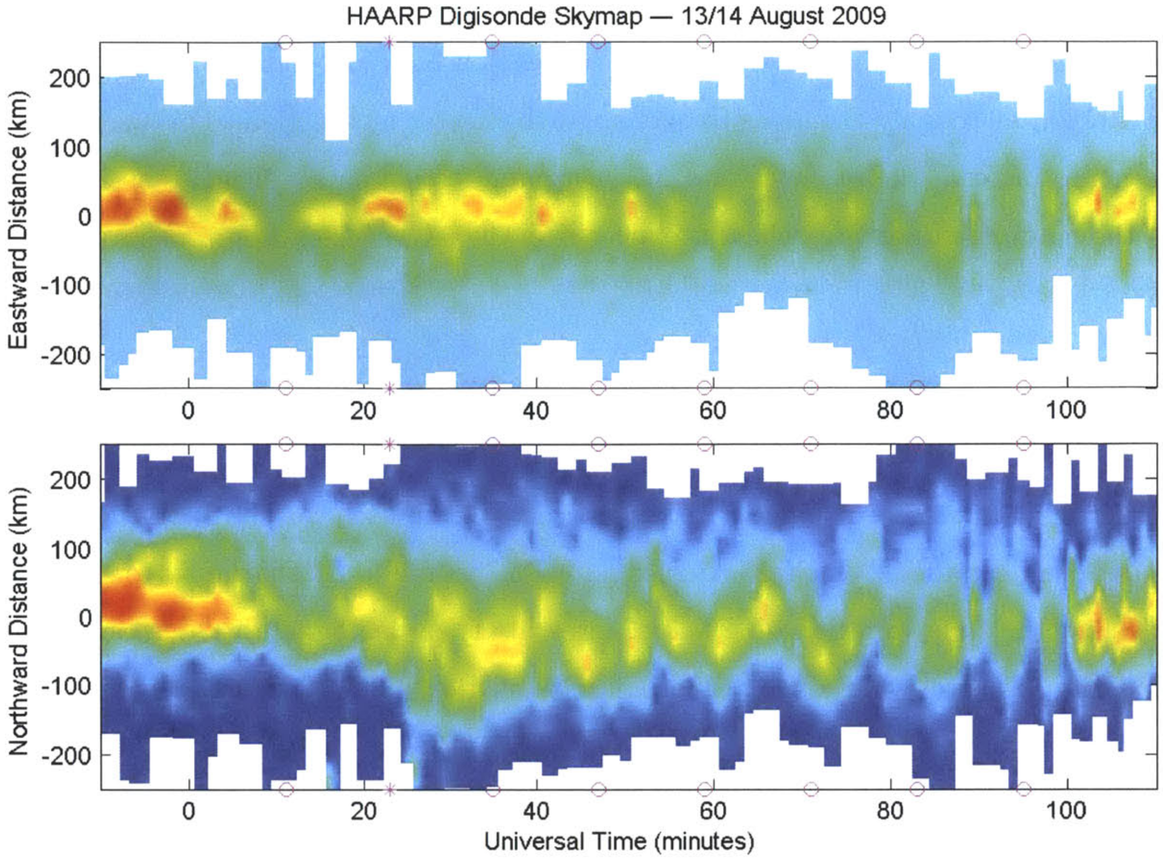

Figure 4-4: The time evolution of planar E/W and N/S distribution of skymap echoes during the HAARP-AGW experiment on 14 August 2009 (00:05–01:39 UT). The markings on the time axis denote the maxima in the power modulation cycle — the asterisk indicates a clipped maxima due to an interruption in the HF heater transmission.

to be able to capture it with only one skymap every five minutes. To improve the odds, for subsequent campaigns we decided to have one skymap every minute instead.

4.2.2 HAARP-AGW Experiment on 13/14 August 2009

In Figure 4-4, we have a plot of the planar E/W and N/S skymap echo distribution for the HAARP-AGW experiment conducted on 14 August 2009 (00:05–01:39 UT). The sinusoidal power modulation cycle was interrupted 00:19–00:25 UT to let an aircraft pass through, thus causing the second power maximum to be clipped (marked by an asterisk on the time axis).

An oscillation that precisely follows the start/stop of the modulated heating can be seen in these distribution plots. The oscillation in the N/S skymap echo distribution is stronger, where the bulk of the skymap echoes shift back-and-forth in position by up to 100 km at roughly the same frequency as the heater modulation. This oscillation seems to indicate the presence of some horizontal forcing on the plasmas as a result of the modulated heating, which is expected in the AGW generation process.

4.2.3 HAARP-AGW Experiment on 14/15 August 2009

In Figure 4-5, we have the radial skymap echo distribution for the HAARP-AGW experiment conducted on 14/15 August 2009 (23:30–01:30 UT). On the bottom panel, we show the time variation of the total integral under this radial distribution. Note that the first two cycles of this sinusoidal modulation (23:30–23:54 UT) had used a pulsed transmission: 0.5 s ON, 4.5 s OFF. The rest (23:54–01:30 UT) was a smooth sinusoidal power variation.

Here, we can see that the bulk of skymap echoes regularly shifted outwards when the transmitted power neared a maximum. At the same time, there is not much reduction in the total integral under the radial distribution during this modulated heating. Furthermore, we can also observe a streak of traveling disturbances emerged radially away from the heated region at approximately 00:30 UT.

Meanwhile, the corresponding planar E/W and N/S skymap echo distribution for this HAARP-AGW experiment is shown on Figure 4-6. We can once more notice the radially propagating disturbance that was generated at around 00:30 UT. From these planar E/W and N/S distributions, it has become clear that this traveling disturbance propagated away from the heated region towards the westward direction.

A zoomed view of this traveling disturbance and a comparison with the plasma drift speed is in Figure 4-7. The plasma drift measurements indicated that the zonal component of the drift velocity had been consistently pointing eastward during this time period. This streak of traveling disturbance was moving in the direction opposite of the plasma drift, clearly indicating a wave propagation aspect.

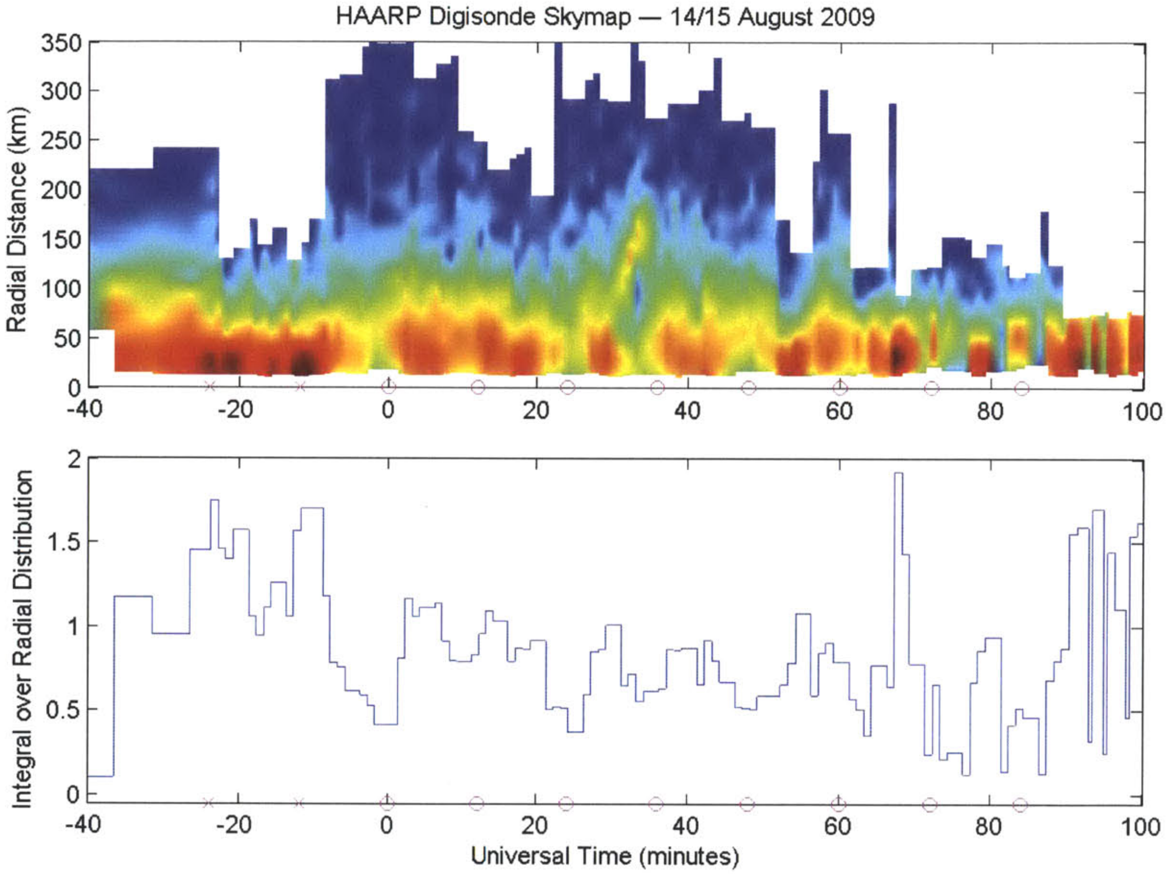

Figure 4-5: The time evolution of the radial distribution of skymap echoes during the HAARP-AGW experiment on 14/15 August 2009 (23:30–01:30 UT). The markings on the time axis denote the maxima in the modulation cycle. The bottom panel shows the integral under this radial distribution as a function of time.

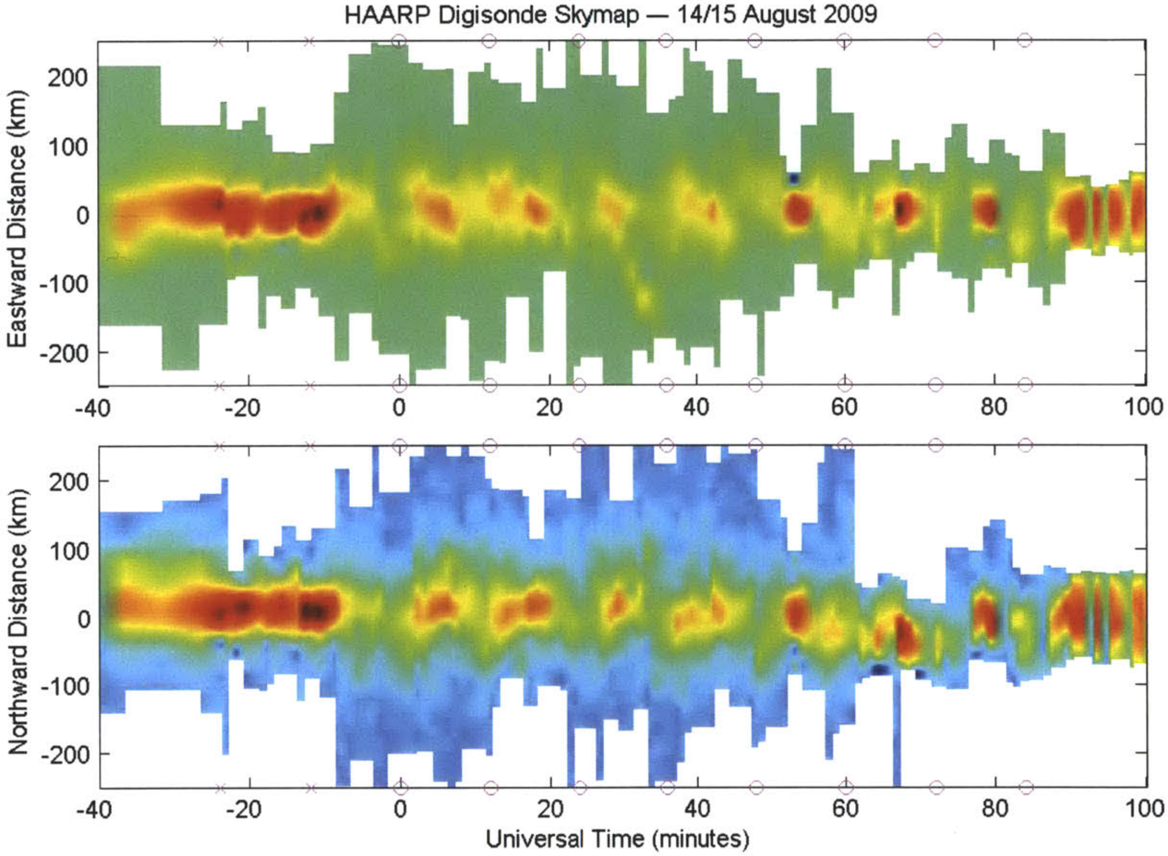

Figure 4-6: The time evolution of planar E/W and N/S distribution of skymap echoes during the HAARP-AGW experiment on 14/15 August 2009 (23:30–01:30 UT). The markings on the time axis denote the maxima in the power modulation cycle.

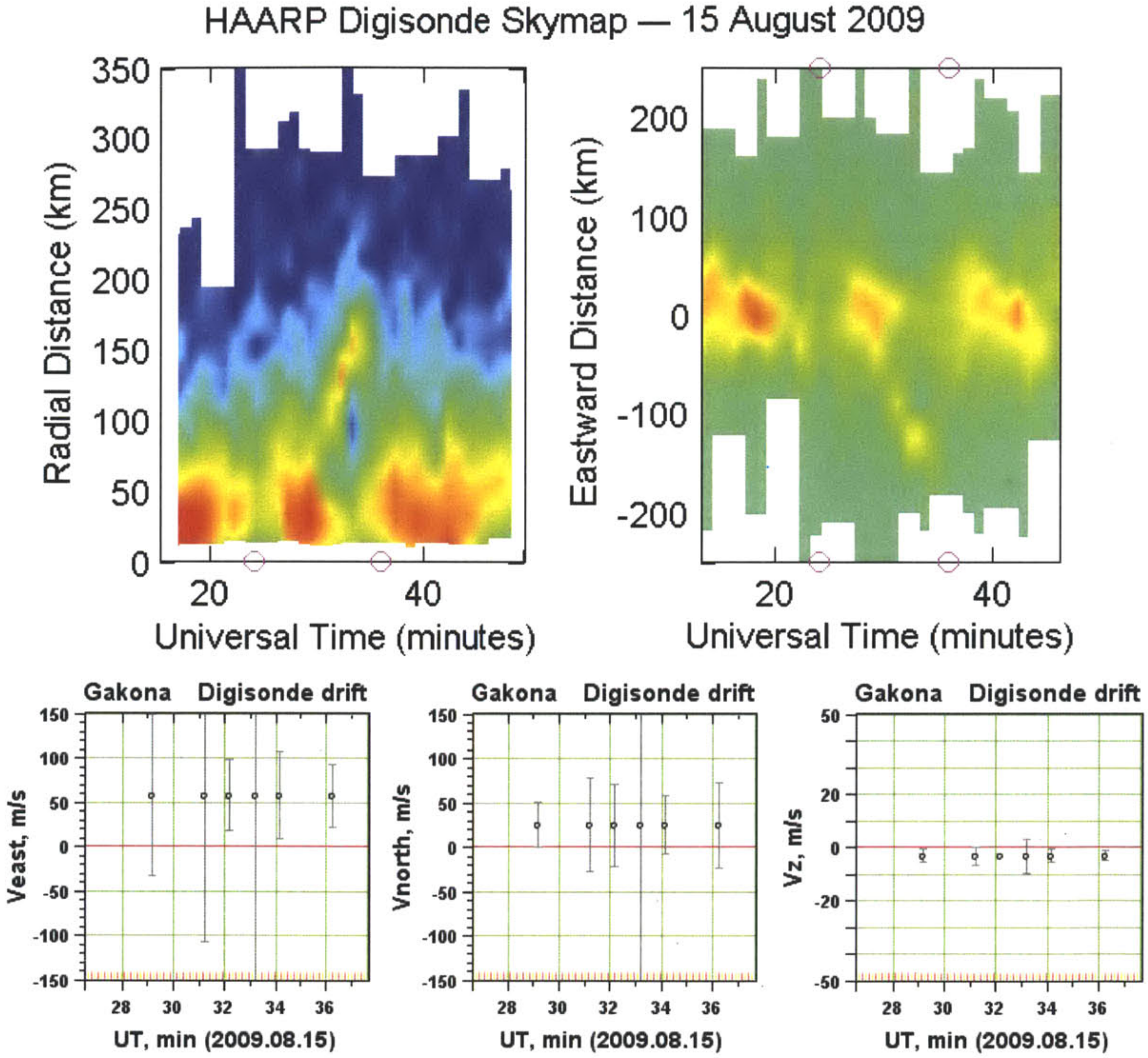

Figure 4-7: Selected portion of the radial and E/W skymap echo distributions from the HAARP-AGW experiment on 14/15 August 2009 (23:30–01:30 UT), showing a streak of ionospheric plasma disturbance that propagated radially outward from the heated region (towards the westward direction). On the other hand, plasma drift measurements during this time period (bottom panels) indicate an approximately consistent northeastward drift velocity.

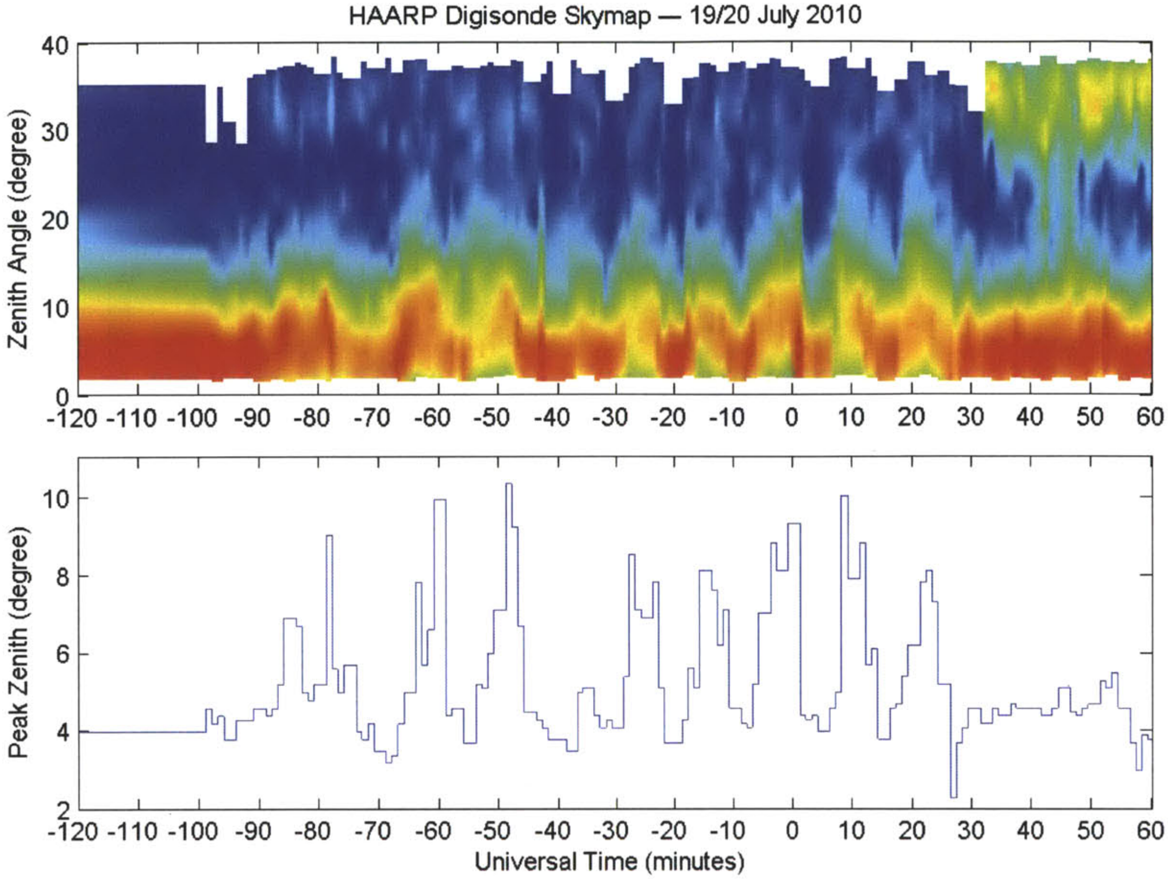

Figure 4-8: The time evolution of the zenith angle distribution of skymap echoes during the HAARP-AGW experiment on 19/20 July 2010 (22:30–00:30 UT). The bottom panel shows the *mode* of this zenith angle distribution as a function of time.

4.2.4 HAARP-AGW Experiment on 19/20 July 2010

In Figure 4-8, we have the zenith skymap echo distribution for the HAARP-AGW experiment on 19/20 July 2010 (22:30–00:30 UT). Also plotted here (bottom panel) is the time variation of the particular zenith angle where the distribution has the largest value — i.e. the *mode* of this zenith angle distribution.

In this skymap data, we can see that the bulk majority of the skymap echoes shifted location back-and-forth during the modulated heating from $t = -90$ min until $t = +30$ min. The echo cluster periodically shifted outwards and then inwards following the 12-minute modulation period of the HF heating cycle. This pattern is even more prominent in the plot of *mode zenith* as a function of time — which is shown on the bottom panel.

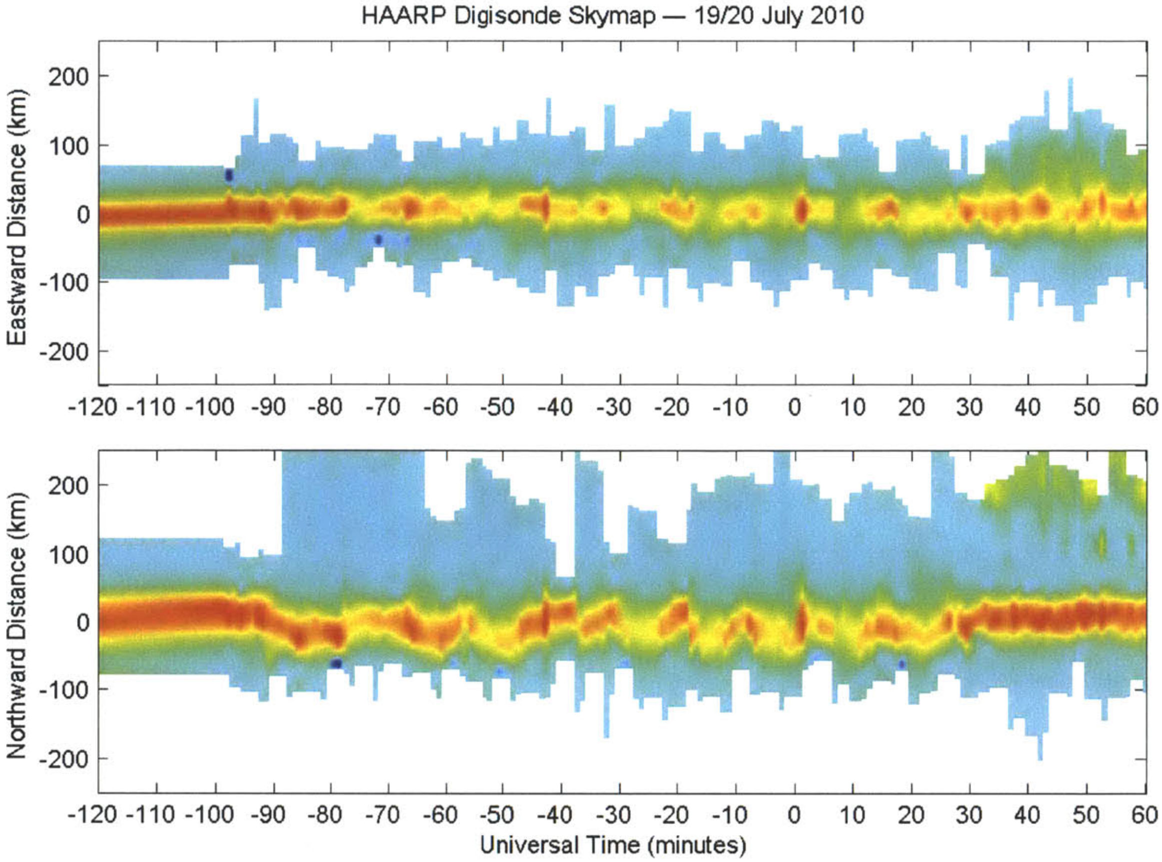

Figure 4-9: The time evolution of planar E/W and N/S distribution of skymap echoes during the HAARP-AGW experiment on 19/20 July 2010. The modulation heating was performed in the time period 22:30–00:30 UT.

Furthermore, the planar E/W and N/S skymap echo distribution for this HAARP-AGW experiment is shown on Figure 4-9. In these planar distributions, the periodic shift in the overall echolocation can be seen as a wavelike oscillation (more prominent in the N/S distribution). This oscillation promptly starts at $t = -90$ min and then stops at $t = +30$ min, thus unmistakably a result of the modulated heating pattern.

This oscillation is similar to what we had found previously (c.f. Subsection 4.2.2), where it indicates the presence of periodic horizontal forces which generate AGW/TID. We can also see that there is not much reduction of total skymap echoes during this wavelike oscillation. The cluster of skymap echoes simply shift position back-and forth. In other words, the total integral under the distribution roughly stays constant over time as in our previous finding (c.f. Subsection 4.2.3).

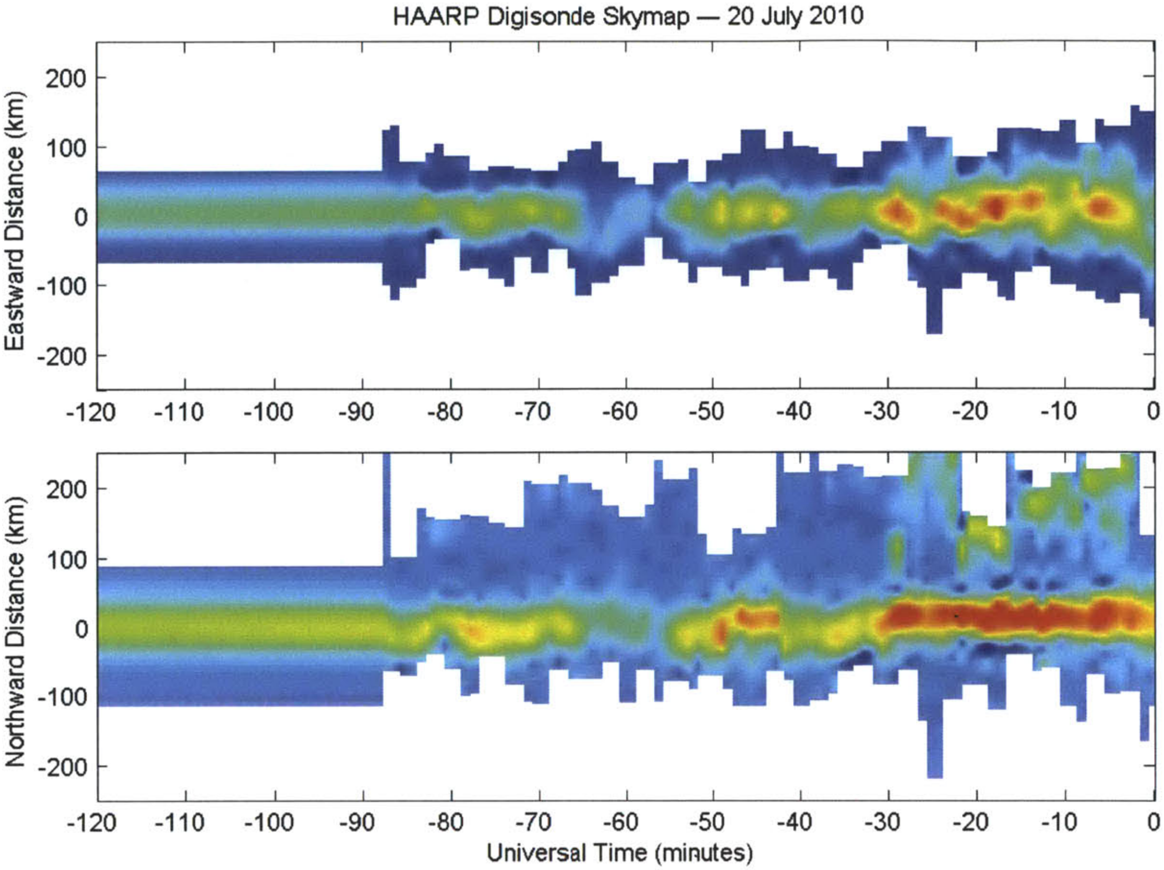

Figure 4-10: The time evolution of planar E/W and N/S distribution of skymap echoes during the HAARP-AGW experiment on 20 July 2010. The sinusoidal modulation heating was performed in the time period 22:30–23:30 UT.

4.2.5 HAARP-AGW Experiment on 20 July 2010

Figure 4-10 shows the planar E/W and N/S skymap echo distribution for the HAARP-AGW experiment conducted on 20 July 2010 (22:30–23:30 UT). In this skymap data, we once more have a wavelike oscillation of the bulk echolocation which matched the AGW modulation cycle. The periodic back-and-forth shift in the echolocation starts immediately after we began the modulated HF heating, and it also promptly ceased once the modulated heating stopped. The oscillation is almost equal in magnitude for both E/W and N/S echo distributions. During the AGW modulation, there is no obvious sign of traveling disturbances emerging out from the heated region. It is quite unclear whether the receding yellow patches (north of the heated region) visible starting at $t \approx -20$ min is caused by the AGW modulation cycle or not.

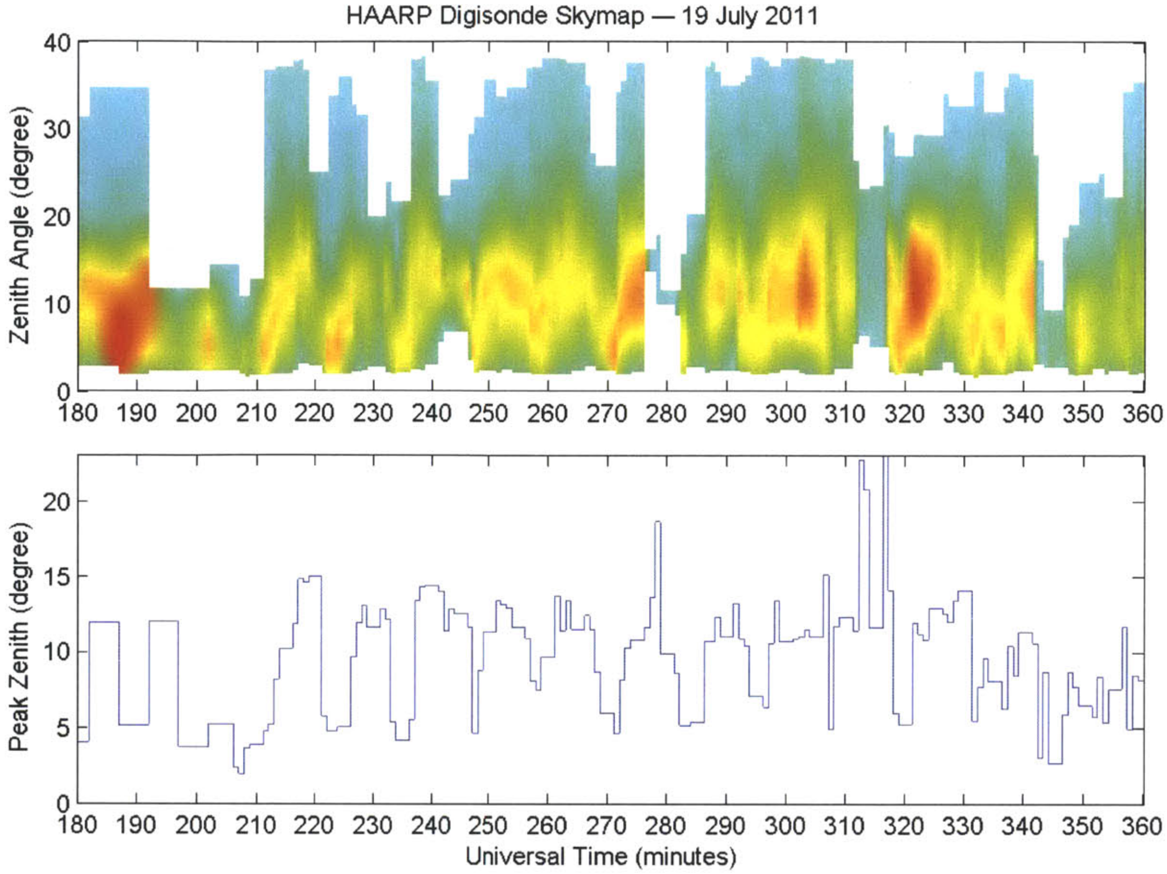

Figure 4-11: The time evolution of the zenith angle distribution of skymap echoes during the HAARP-AGW experiment on 19 July 2011 (03:30–05:30 UT). The bottom panel shows the *mode* of this zenith angle distribution as a function of time.

4.2.6 HAARP-AGW Experiment on 19 July 2011

Figure 4-11 shows the plot of zenith skymap echo distribution for the HAARP-AGW experiment on 19 July 2011 (03:30–05:30 UT). In addition, on the bottom panel we plotted the *mode* of this zenith angle distribution as a function of time. In these plots, the experiment start time is $t = 210$ min and the stop time is $t = 330$ min.

This time, we find that there are a few sequential streaks of traveling disturbances that propagated out from the heated region. The repetitive pattern of inward and outward shift in the time evolution of the *mode zenith* is also consistent with this observation. Namely, we noticed that the outward shift is rather gradual while the inward shift is quite abrupt. These periodic pattern occurred with a periodicity of approximately 12 minutes, matching that of the modulated HF heating cycle.

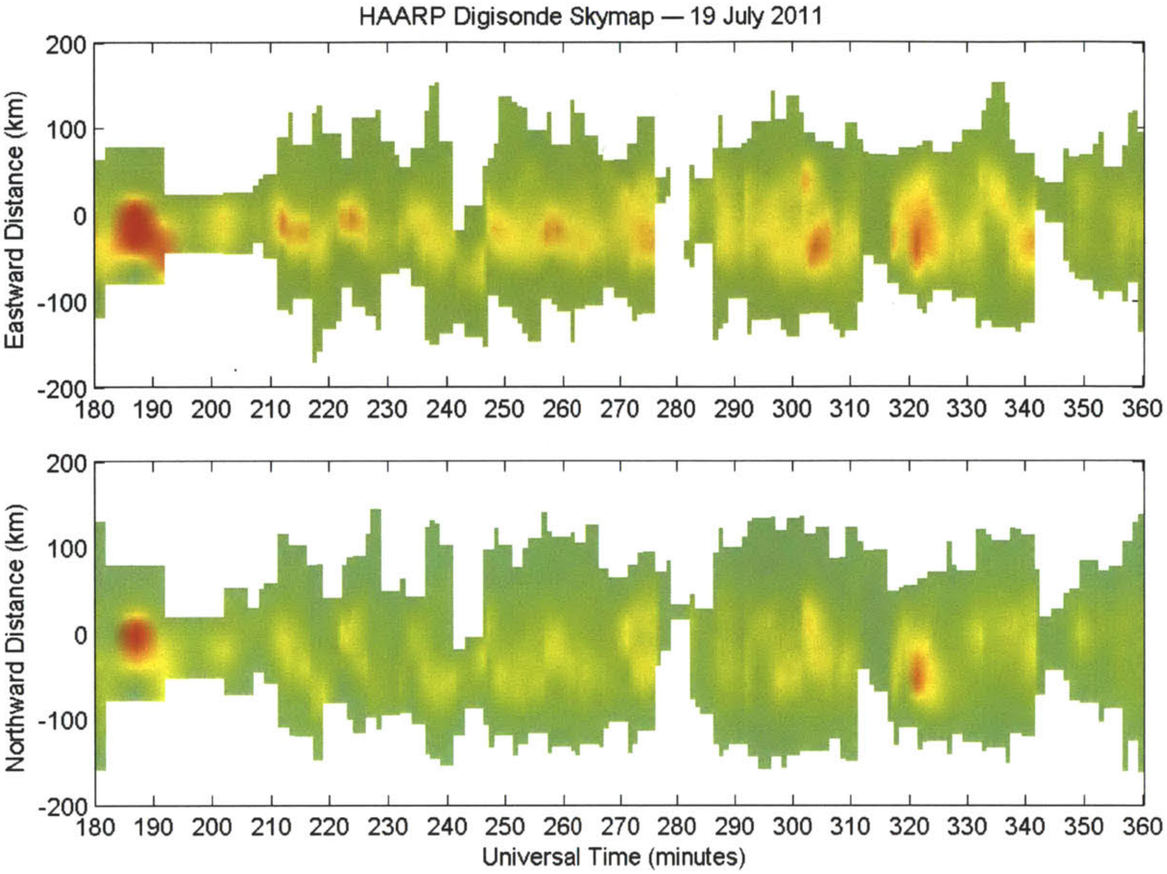

Figure 4-12: The time evolution of planar E/W and N/S distribution of skymap echoes during the HAARP-AGW experiment on 19 July 2011 (03:30–05:30 UT). We can see a number of streaks emerging radially outward from the heated region. These streaks shifted out 100 km in 10 minutes, giving an apparent speed of ~160 m/s.

Meanwhile, the planar E/W and N/S skymap echo distribution for this HAARP-AGW experiment is shown on Figure 4-12. We can now see clearly that the direction of propagation for these traveling disturbances is southward, and this direction is rather persistent. On the other hand, the meridional component of plasma drift velocity during this time period was not steady. Initially (03:20 UT) it was 50 m/s southward but then gradually switch direction, passing zero at around 04:00 UT, until it finally (05:35 UT) became 100 m/s northward. Based on this mismatch, we can be confident that these streaks cannot be heater-produced turbulent eddies that were carried downstream by the plasma drift. These streaks had exhibited some wave propagation aspect by going against the plasma drift, and therefore strongly indicate that AGW/TID had been generated as a result of the modulated HF heating.

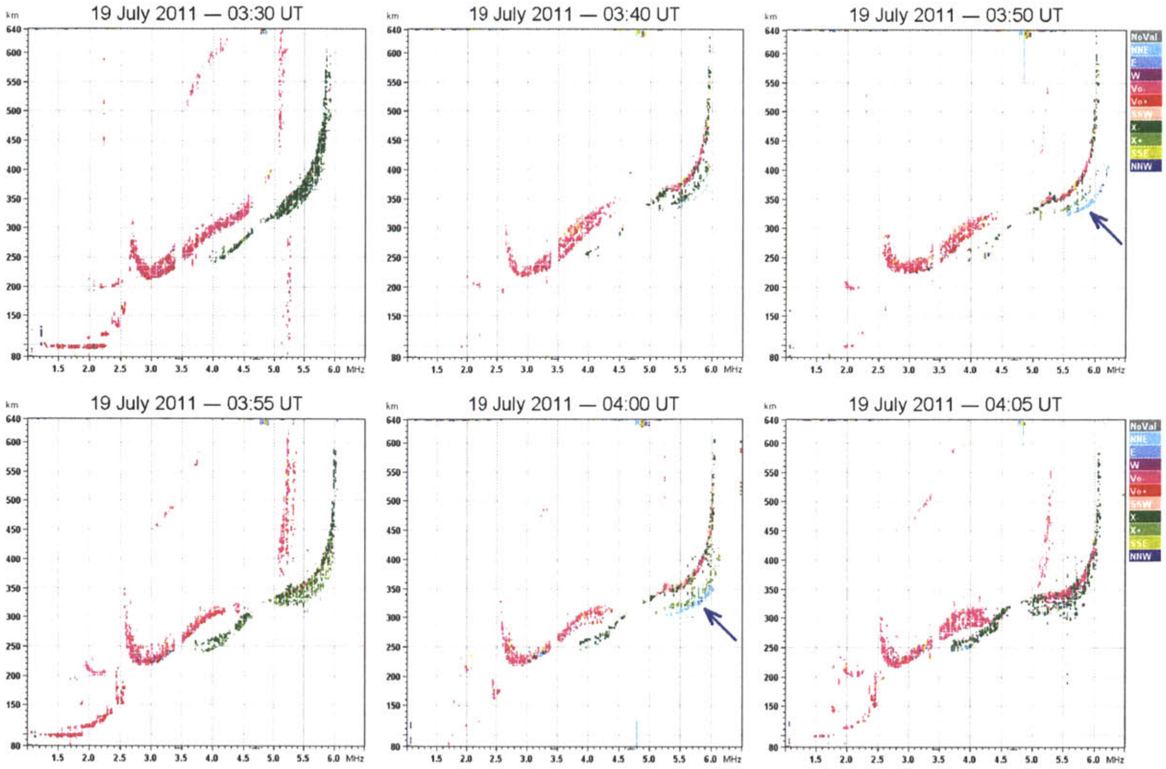

19 July 2011 — 03:30 UT

19 July 2011 — 03:40 UT

19 July 2011 — 03:50 UT

19 July 2011 — 03:55 UT

19 July 2011 — 04:00 UT

19 July 2011 — 04:05 UT

Figure 4-13: A number of recorded ionograms during the HAARP-AGW experiment on 19 July 2011 (03:30–05:30 UT). Note the episodic appearance of additional traces in the ionograms every 10 minutes or so, as indicated by the arrow.

In addition, we also observed some interesting features in the ionogram data during this HAARP-AGW experiment. Once every 10–15 minutes, we would have an additional set of X-mode traces in the ionograms. These additional X-mode traces appeared below the main X-mode traces, with a clear gap between them. A sequence of several sample ionograms delineating this phenomenon are shown in Figure 4-13. This feature has not been observed in any of the previous AGW experiments so far.

Since we are only acquiring one ionogram every 5 minutes, it is difficult to say with certainty whether or not these additional ionogram traces appeared periodically every 12 minutes — the exact same periodicity as the heating modulation. However, these anomalous echoes were not observed prior to the time period allocated for the HAARP-AGW experiment; and they were no longer observed after the experiment had been completed. Hence, it is very likely that these additional ionogram traces have something to do with the AGW heating modulation.

Judging from their curved shape, these additional ionogram traces correspond to a total reflection (wave propagation cutoff) instead of Bragg scattering. Most likely, they had been caused by back-reflections from oblique direction. For this to happen, the ionospheric tilt at some distance away from the heated region must have been changing periodically — allowing for some total back-reflections when the tilt is at a certain suitable angle. In the case where HAARP-generated AGWs/TIDs are indeed propagating away from the heated region, the ionospheric tilt in the surrounding area is surely affected and may thus vary periodically following the AGW oscillation. This scenario might therefore explain the periodic appearance of these additional X-mode traces in the ionograms during the HAARP-AGW experiment.

Finally, although the heater-generated artificial AGWs are expected to be produced isotropically with respect to the heated region, the observed TID signatures in the skymap data seem to show some apparent directionality on the case-by-case basis. Namely, we observed some TID signatures on the northwest sector in the 29 October 2008 data; signatures of westward-propagating TID in the 14/15 August 2009 data; and signatures of southward-propagating TID in the 19 July 2011 data. It should be noted that the favorable condition that gives rise to return echoes in the skymap data actually depends on the precise configuration of the plasma layer and the background magnetic field. This sensitive aspect angle requirement might be further confounded by the possible distortion of the AGW wavefront by the background neutral wind. For these reasons, the isotropy might not be fully visible in the skymap data.

In summary, we have examined a collection of digisonde data recorded during the HAARP-AGW experiments. When the modulated HF heating cycle is running, a number of distinct features can be seen in either skymap or ionogram data. Some of these features are quite intuitive for us to attribute as unambiguous signatures of HAARP-generated AGW/TID, while others are still quite unclear. To some extent, this uncertainty can be resolved because it is possible to simulate the digisonde data for a given ionospheric plasma layer configuration using numerical ray tracing. Later in Chapter 8 of this thesis, we are going to discuss some relevant results from our numerical ray tracing simulations.

Chapter 5

Ground-Based Radio Diagnostics Using MUIR

In this chapter, we are going to discuss our ground-based measurements using the Modular UHF Ionospheric Radar (MUIR) to detect HAARP-generated AGWs/TIDs. First, we will explain the general idea on how the MUIR radar data can be exploited to identify some characteristic signatures of AGW/TID generated by the sinusoidal modulation heating cycle. Finally, we will give a walk-through of the data analysis procedures together with the results. The finding seems to indicate that AGWs are being radiated out from the heated volume during the HAARP-AGW experiments.

5.1 The Basic Diagnostic Strategy

The MUIR radar is essentially an incoherent scatter radar (ISR) except that the receiver aperture is considerably smaller than other major ISR facilities around the globe. The general principle of ISR operations is essentially the same as that of collective Thomson scattering diagnostics. Just like a normal ISR, the MUIR radar measures the ion-acoustic lines and plasma lines [see e.g. *Beynon and Williams*, 1978]. Usually a long integration time is not necessary for measuring HF-enhanced ion-acoustic lines and the plasma lines, but we we will absolutely need to average over many radar pulses to detect the thermal level incoherent scatter spectra in general.

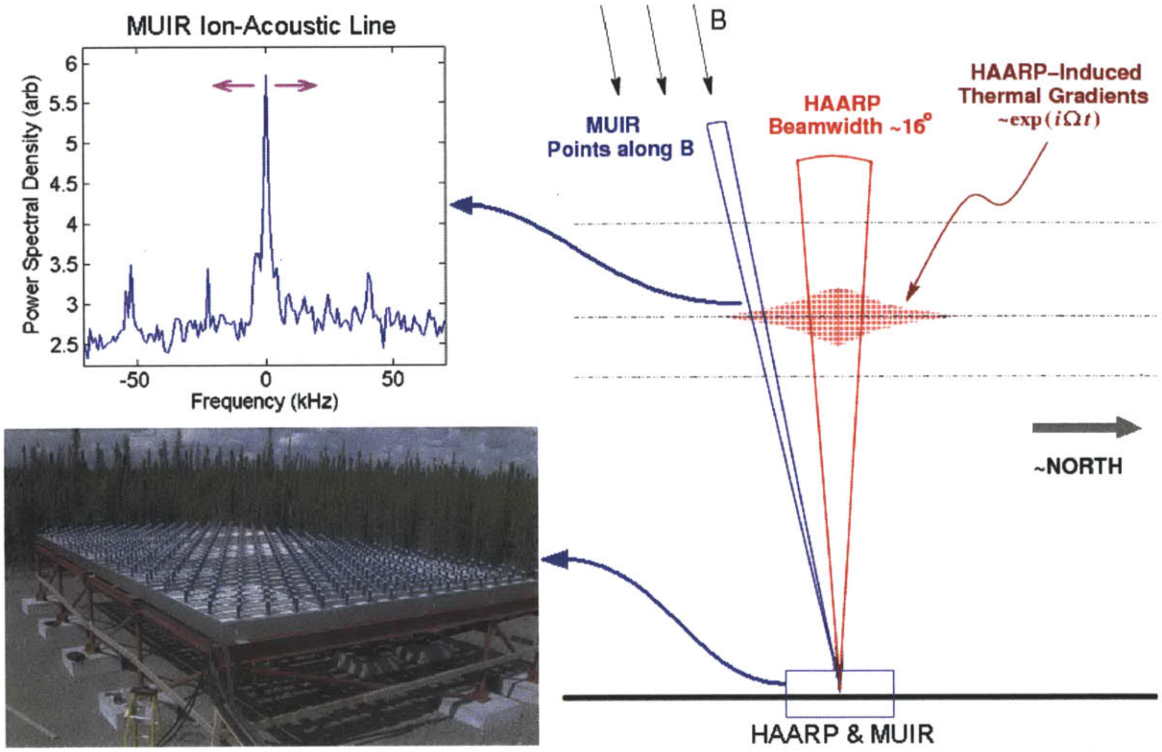

Figure 5-1: A schematic illustration on the strategy for using MUIR in the HAARP-AGW experiment. We point the radar beam just outside the heated plasma volume, and look for the corresponding periodic time variation in the line-of-sight velocity (back-and-forth shift in the backscatter spectra) that would indicate AGW/TID being radiated out from the heated plasma volume.

Besides density and pressure fluctuations, gravity waves in general also carry some oscillation in the wind speed. If we have some gravity waves that propagate radially away from the heated region, then typically there should be some oscillatory wind speed pattern present in the surrounding region. Therefore, we shall point the MUIR radar beam outside the heated volume to measure the line-of-sight (LOS) velocity of the plasma. We will then look for periodic time variation in the LOS velocity with a period that matches the sinusoidal modulation period $T = 12$ minutes of the HF heating cycle. Such wavelike oscillation in the LOS velocity will be manifested in the MUIR radar data as a periodic back-and-forth shift in the centroid of the ion-acoustic line. This idea is illustrated schematically in Figure 5-1.

This scheme for using MUIR radar is particularly appealing for the HAARP-AGW experiments, because it inherently demonstrates the wave propagation aspect.

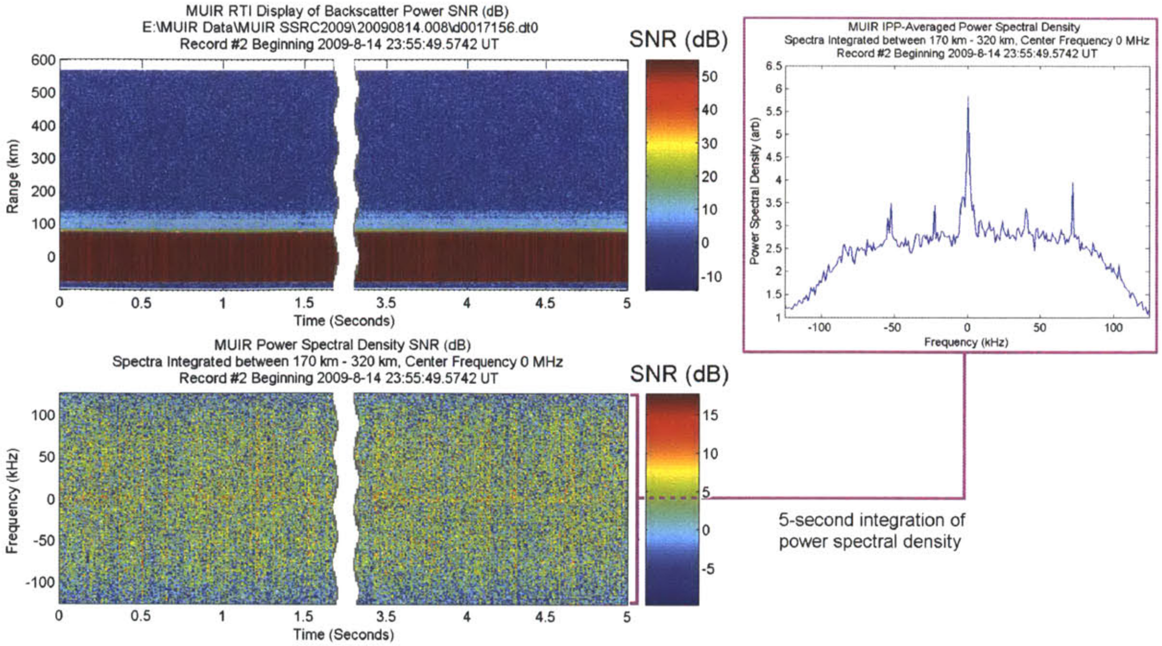

5-second integration of
power spectral density

Figure 5-2: A sample RTI plot of MUIR backscatter radar power (top left). The corresponding MUIR frequency spectra from a selected altitude range around the F-peak (bottom left). The frequency spectra after a 5 second integration (top right).

5.2 Data Analysis Procedures and Results

MUIR radar operates in the UHF band, transmitting at a frequency of 446 MHz with peak power of 512 kW. In addition, the receiver aperture area is 219.8 m^2 and the angular beamwidth is approximately 2.4° [*Oyama and Watkins*, 2007]. For the HAARP-AGW experiments, MUIR radar transmits a long uncoded pulse of 996 μs duration, with an interpulse period of 10 ms. Based on the backscatter radar signal from each pulse, the power spectral density (PSD) can be readily computed using the Fourier transform. A sample RTI plot of MUIR backscatter radar power and the corresponding PSD plot can be found in Figure 5-2. In this case, the PSD was calculated for a selected altitude range — focusing on the ionospheric F-region.

In general, the pulse-by-pulse power spectral density is extremely noisy because the MUIR radar signal is rather weak. However, we can still obtain a sufficiently clean spectra by integrating over many pulses. This procedure is also shown in Figure 5-2, where we eventually have a clear ion-acoustic line in the incoherent scatter spectra

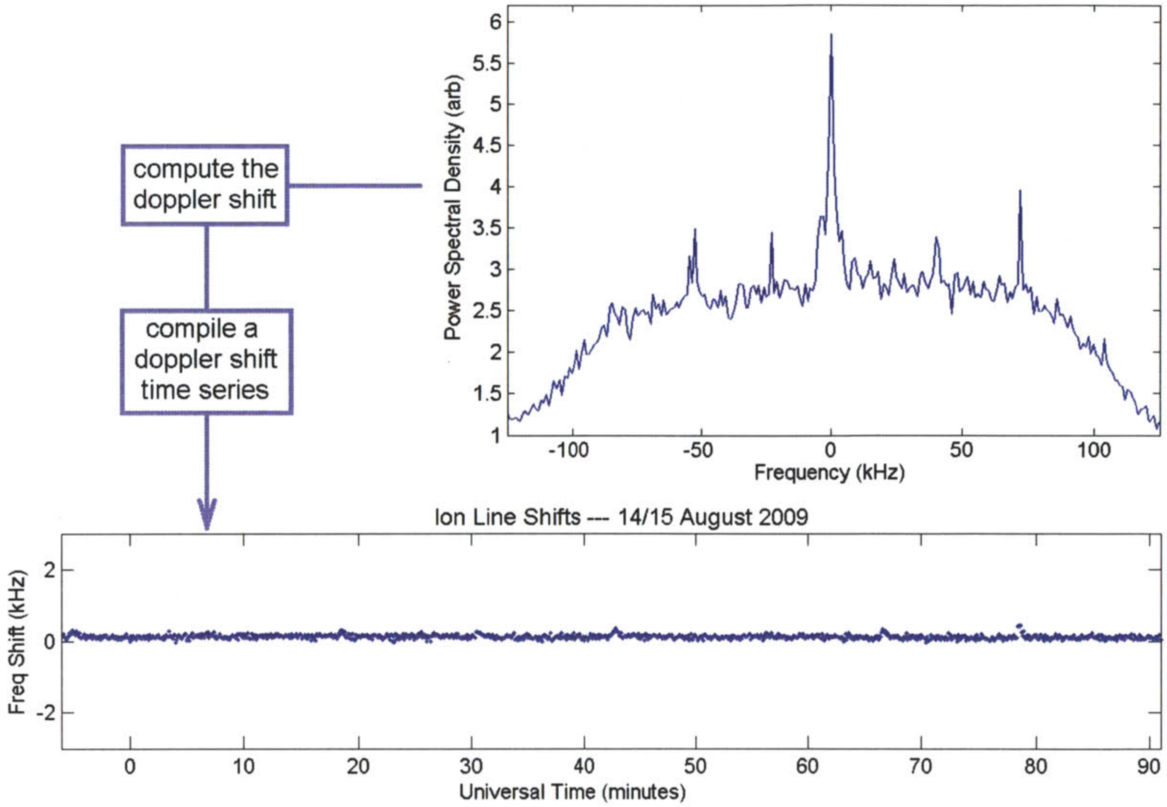

Figure 5-3: From each measurement of ion line spectra (5 second integration), we compute the centroid location and compile the computed Doppler shift values as a time series. By taking the Fourier transform of this Doppler time series, we could reveal the presence of periodic temporal variation in the line-of-sight velocity.

after integrating for a duration of 5 seconds — which corresponds to 500 radar pulses.

For each of the MUIR ion line spectra after the 5 second integration, we compute the centroid position of the ion line peak. We then compile a time series of these Doppler shift values. Now we would like to know if the centroid of the ion-acoustic line is shifting back-and-forth periodically with a period of $T = 12$ minutes. By taking the Fourier transform, we should be able to reveal the presence of any periodic time variation in this Doppler time series. The overall flowchart of this procedure for analyzing MUIR radar data is depicted in Figure 5-3.

There is a correspondence between Doppler shift in the radar data and the LOS plasma velocity. Assuming an oscillatory wind speed of $\delta v \approx 100$ m/s due to some gravity waves, we can expect a resulting Doppler shift of $\Delta f = 2 f_0 \delta v / c \approx 0.3$ kHz. Here $f_0 = 446$ MHz is the MUIR radar frequency and c denotes the speed of light.

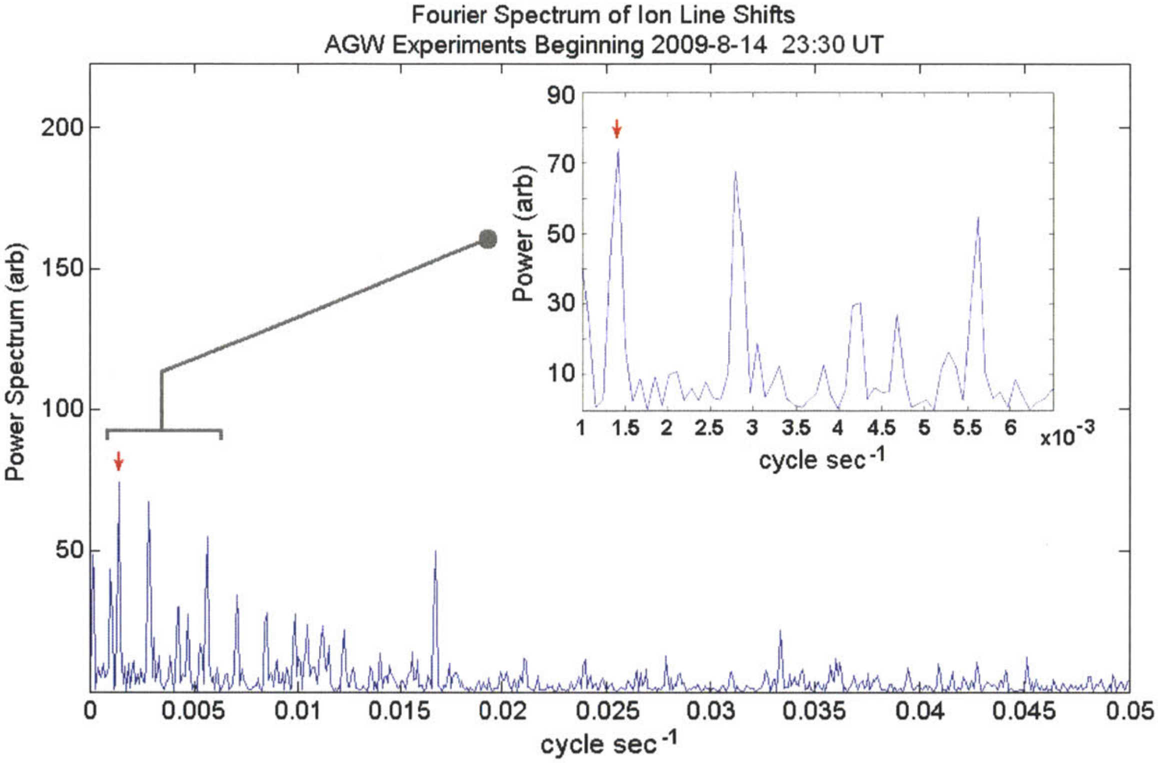

Figure 5-4: Fourier spectrum of the Doppler time series from the HAARP-AGW experiment on 14/15 August 2009 (23:30–01:30 UT). It reveals periodic time variation with a frequency close to 1.39 mHz, which corresponds to the period $T = 12$ minutes of the HF heating modulation.

Figure 5-4 shows the resulting Fourier periodogram of the MUIR Doppler time series obtained from one of the HAARP-AGW experiments. The sinusoidal HF heating modulation had a period of $T = 12$ minutes, which corresponds to a frequency of approximately 1.39×10^{-3} Hz. In this periodogram we can definitely see a clear peak at around 1.4 mHz, which is very close to the modulation frequency selected for the HAARP-AGW experiments. Furthermore, a number of harmonics at the multiples of 1.4 mHz can be seen in the periodogram as well. However, it seems that these harmonics rapidly decayed and never went beyond 15 mHz. In general, the presence of these harmonics means that the 12-minute periodic variation of the LOS Doppler velocity is not a pure sinusoidal time evolution. The possibility of it to be a sign of some nonlinearity is still quite unclear. At this point, our primary focus is simply to demonstrate that AGWs are indeed being radiated out from the heated volume.

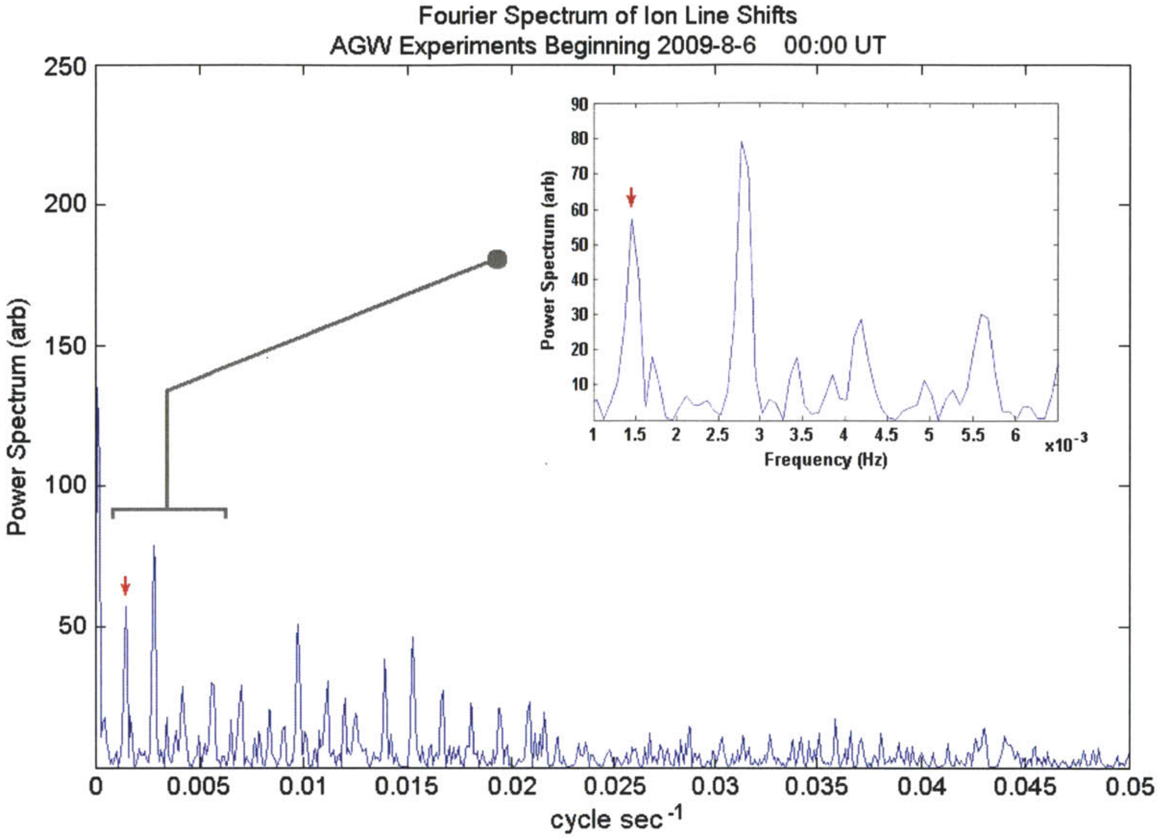

Figure 5-5: Fourier spectrum of the Doppler time series from the HAARP-AGW experiment on 6 August 2009 (00:00–02:10 UT). It reveals periodic time variation with a frequency close to 1.39 mHz, which corresponds to the period $T = 12$ minutes of the HF heating modulation.

The same kind of features had been consistently observed during other runs of the HAARP-AGW experiments as well. Figure 5-5 shows the Fourier spectrum of the MUIR Doppler time series from another run of the HAARP-AGW experiments. Again we find a clear peak around 1.4 mHz, together with its harmonics which seem to persist as far as around 20 mHz or so.

In summary, the MUIR radar data had indicated the presence of a quite significant oscillatory LOS velocity in the area surrounding the heated region during the HAARP-AGW experiments. The period of this LOS velocity oscillation matches that of the HF heating modulation cycle ($T = 12$ minutes). We thus have obtained a quite affirmative evidence that some AGWs/TIDs are indeed being radiated out from the heated region as a result of the modulated HF heating.

Chapter 6

Other Ground-Based Radio Diagnostic Instruments

For the HAARP-AGW experiments, we also have some data obtained from a few off-site radio diagnostics instruments. They include (1) Poker Flat AMISR radar and (2) Kodiak SuperDARN radar. This chapter will provide an overview of what we have learned from the data recorded by both radars during the HAARP-AGW experiments. The results are generally in agreement with other observations obtained from the on-site diagnostic instruments. Although there is a considerable uncertainty in terms of the propagation direction, we did observe some AGW/TID signatures in both AMISR and SuperDARN radar data following the sinusoidal modulation performed by the HAARP heater.

6.1 Poker Flat AMISR Radar

This Advanced Modular Incoherent Scatter Radar (AMISR) is located at 65.13°N and 147.47°W — near the Poker Flat Research Range in Alaska. The Poker Flat AMISR (sometimes also referred to as PFISR) is at a distance of roughly 328 km north of the HAARP facility. It operates at a frequency of 446 MHz, with an aperture area of approximately 900 m^2 (30 m × 30 m). Some additional details on the Poker Flat AMISR can be found at http://isr.sri.com/iono/amisr/.

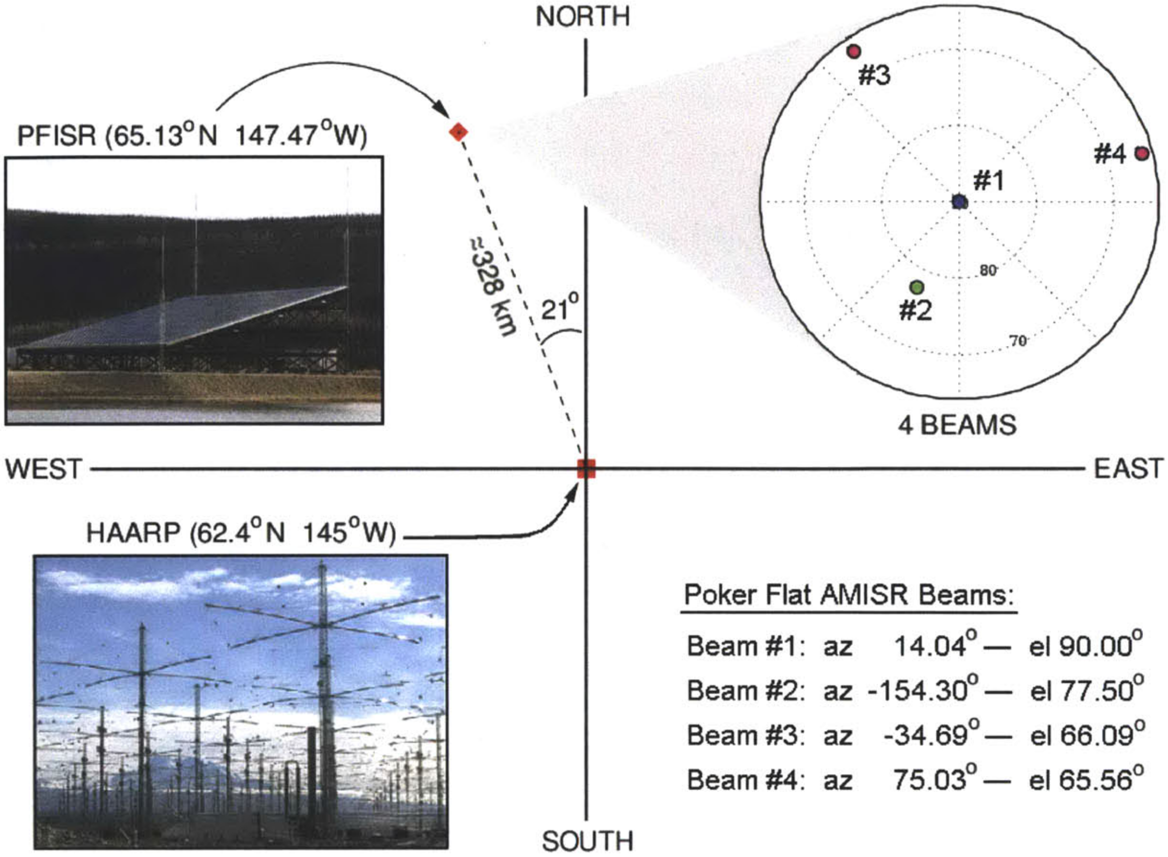

Poker Flat AMISR Beams:

Beam #1:	az	14.04° —	el 90.00°
Beam #2:	az	-154.30° —	el 77.50°
Beam #3:	az	-34.69° —	el 66.09°
Beam #4:	az	75.03° —	el 65.56°

Figure 6-1: A diagram showing the relative location of HAARP facility and Poker Flat AMISR site, together with some basic information on the AMISR beam configuration.

We received the support of Poker Flat AMISR radar during the HAARP-AGW experiment conducted on 29 October 2008 (22:50–24:00 UT). The radar was actually scheduled to run for a separate project unrelated to our experiment, but we were granted access to the relevant data. The AMISR radar was running continuously for approximately 72 hours on 28–30 October 2008, and thus covered our experimental period fully. Some details on the relative geographical configuration and the selected AMISR beam configuration are shown In Figure 6-1. If AGWs are being generated as a result of the modulated HF heating (and they survive the ∼300 km propagation), then we might expect some AGW/TID signatures to appear in the PFISR data after some time delay. It should be noted that this particular beam configuration was not optimized for inferrring the propagation direction, but it should be adequate for basic detection of TID signatures.

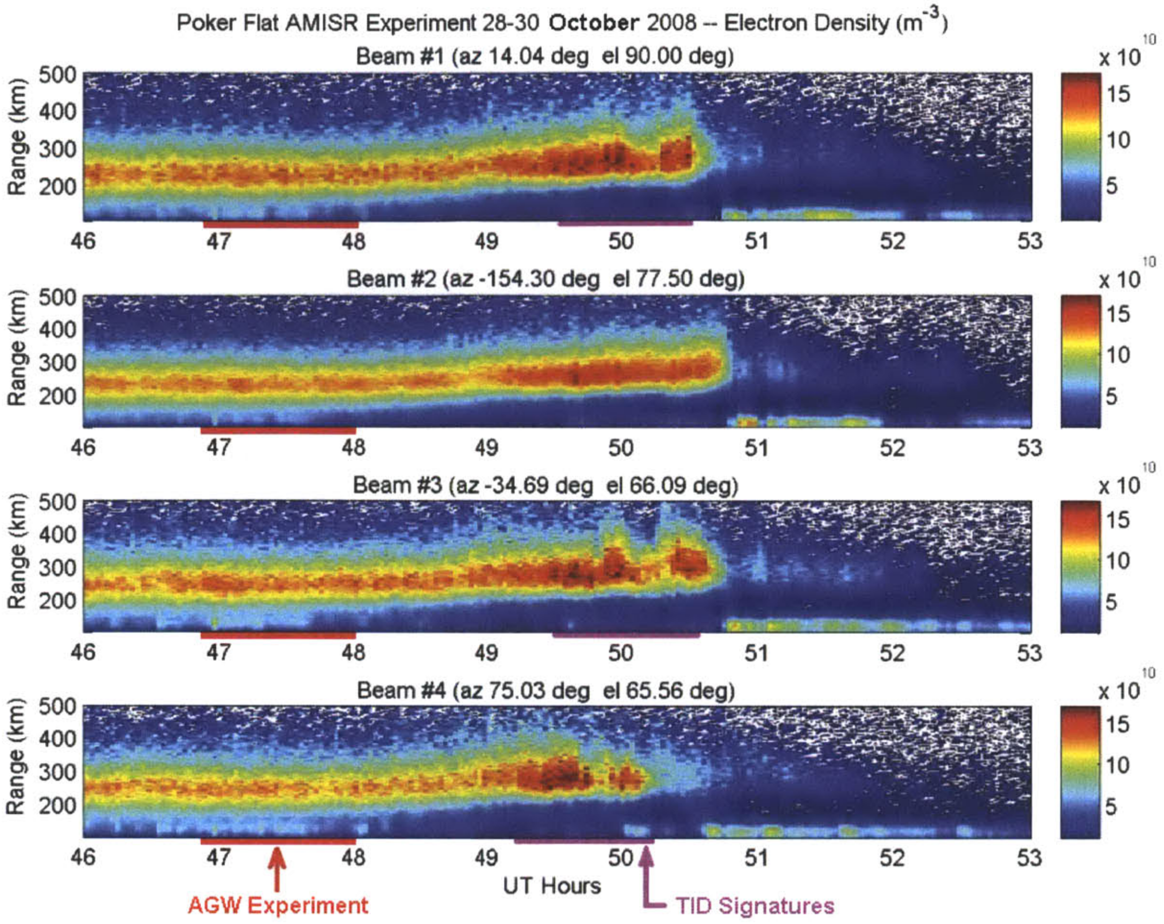

Figure 6-2: RTI plots of electron density profile measurement along each AMISR beams from the HAARP-AGW experiment on 29 October 2008 (22:50–24:00 UT). Roughly an hour after the modulated heating ("AGW Experiment") was completed, some AGW/TID signatures were observed over the Poker Flat AMISR site.

In Figure 6-2 we have the RTI plots of plasma density profile measurements from all 4 radar beams we used in this PFISR operation. These RTI plots span a time period from 22:00 UTC on 29 October 2008 until 05:00 UTC on 30 October 2008. On the time axis of these plots, the start time of the HAARP-AGW experiment is at $t = 46.84$ hour and the stop time is at $t = 48$ hour. The geomagnetic condition was relatively quiet with $K_p = 3.1$ on the average. The data in these RTI plots indicate that roughly 2∼3 hours after the "AGW experiment" was conducted at HAARP site, some TID signatures were seen over Poker Flat. Some of the TID signatures are relatively clear and some (especially in beam #2) are not. We will next look at the RTI plots of the net plasma density fluctuations for some further comparison.

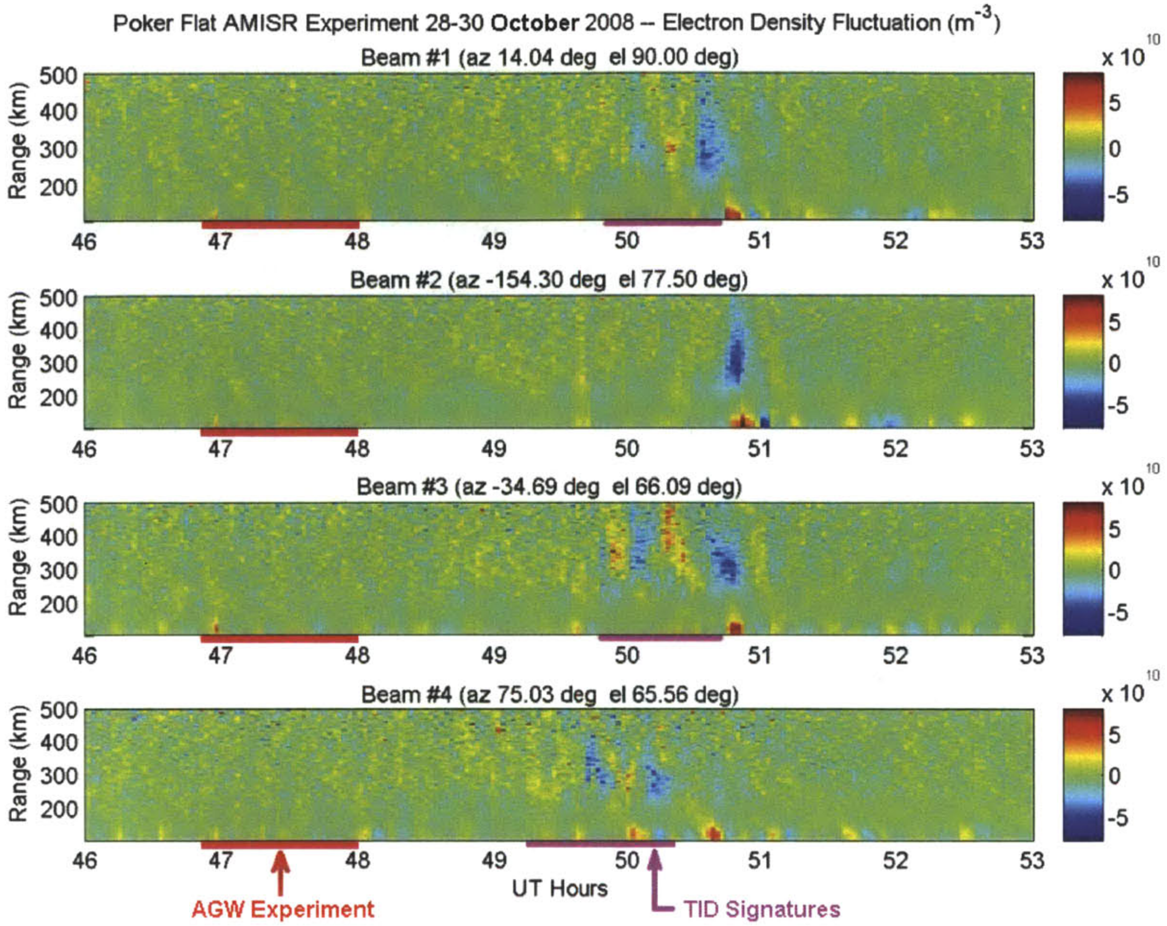

Figure 6-3: Essentially the same as Figure 6-2, except that these are the RTI plots of the *net electron density fluctuations* along the four AMISR beams.

Figure 6-3 shows the RTI plots of the net plasma density fluctuations from the same dataset as before. The overall TID signatures are much clearer in this case, especially for beam #3 where the TID signatures can be most clearly seen. Since the geomagnetic condition was very quiet at the time, it is highly unlikely for us to have unwanted contamination from auroral AGW/TID. This is a quite suggestive evidence that HAARP-generated AGWs can propagate over a relatively long distance. The distance between the HAARP facility and the PFISR site is approximately 328 km, and these TID signatures were eventually observed after 2∼3 hour time delay. If this 328 km distance had been traveled in 2–3 hours, we may then infer a propagation speed of roughly 30–46 m/s. These values are quite consistent with typical propagation speed of MSTIDs, which is in the order of a few tens of m/s.

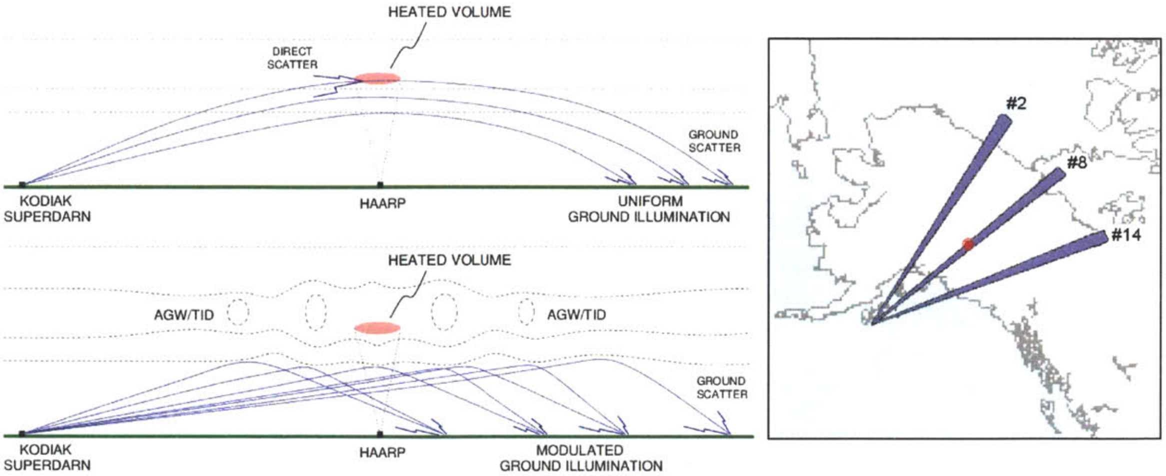

Figure 6-4: A schematic illustration on how AGW/TID signatures can be identified in HF radar data. Instead of giving a direct backscatter, AGW/TID will modulate the intensity of ground-scatter echoes at the skip distance. The radar beams for the experiment are shown in the map. Red circle marks the location of the HAARP facility, which is approximately 670 km away from the Kodiak SuperDARN site.

6.2 Kodiak SuperDARN Radar

Another off-site instrument that we are using is the Kodiak SuperDARN radar. This is an HF radar located on the Kodiak island, approximately 670 km southwest from the HAARP facility. There are 16 possible beam configurations (numbered 0–15) for the Kodiak SuperDARN radar, with beam #8 pointing directly towards the HAARP-heated region. During the HAARP-AGW experiments, we are using 3 SuperDARN radar beams (#2, #8, #14) as illustrated in Figure 6-4. These three selected beams are separated by 19.4° apart, and the horizontal angular beamwidth of each individual beam's main lobe is 4.5°.

Since the heated region itself is generally full of turbulent plasma structures and field-aligned irregularities, there would certainly be some direct Bragg backscatter signals from the heated plasma volume. However, we do not expect that the HAARP-generated AGW/TID would give any significant direct Bragg scatter. This is because the wavelength of heater-generated AGW/TID would typically be in the order of a few tens of kilometers — too large to satisfy Bragg backscatter condition with the incoming HF radio diagnostic wave from the Kodiak SuperDARN radar.

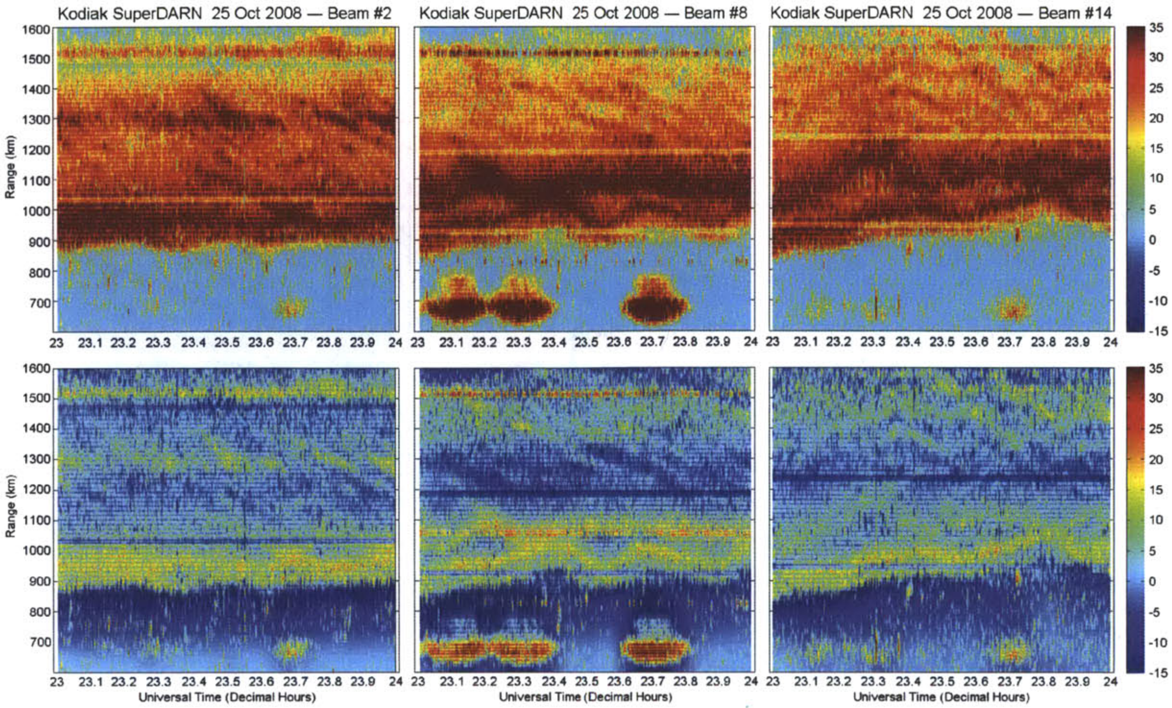

Figure 6-5: RTI plots of Kodiak SuperDARN radar data from the HAARP-AGW experiment conducted on 25 October 2008 (23:00–24:00 UT). Shown are the raw backscatter power (top panels) and their respective net perturbations (bottom panels) for all three beams used in the experiment.

In our analysis, we will look for AGW/TID signatures using the pattern of ground scatter echoes instead. This method for observing AGW/TID using HF radars had been employed previously [see e.g. *Bristow et al.*, 1994; *Bristow and Greenwald*, 1995; *He et al.*, 2004; and *Senior et al.*, 2006]. In the presence of some AGW/TID, the ground illumination pattern would be spatially modulated due to a focusing/defocusing effect. This concept is depicted schematically in Figure 6-4.

Figure 6-5 shows the Kodiak SuperDARN data from one of the HAARP-AGW experiments. The experiment started at 23:00 UT and ran for an hour until 24:00 UT. It began with 2 cycles of 12 min-period power modulation, followed by an OFF period for 12 minutes, 1 cycle of 12 min-period power modulation, and finally we have another OFF period for 12 minutes. During this experiment, the SuperDARN radar collected data using the beam configurations which we had described earlier (beams #2, #8 and #14). Note also that the "range" for all the RTI plots in Figure 6-5 denotes the *slant range* along the ray path — not the altitude above the ground.

When the HF heater was ON (23:00–23:24 UT and also 23:36–23:48 UT) we can see a strong radar signal at a slant range of about 670 km. These are the direct backscatter from the HAARP-heated volume. Some modulation pattern in the ground scatter echoes are quite visible at a slant range of about 1300 km (approximately twice the distance between Kodiak SuperDARN radar and the heated region). This pattern of modulated ground scatter echoes confirmed the presence of AGW/TID around the heated region when we performed the modulated HF heating. The geomagnetic condition was very quiet with $K_p = 0.6$ on the average, thus rendering the occurence of auroral AGW/TID unlikely. Unfortunately, we were unable to record data using the Kodiak SuperDARN prior to 23:00 UT and after 24:00 UT. Otherwise, we would have been able to use those time periods as comparison.

Chapter 7

Satellite TEC Diagnostics

After discussing much about various types of ground-based radio diagnostic methods for the HAARP-AGW experiments, in this chapter we are going to examine some LEO/GPS satellite measurements for detecting the characteristic signatures of heater-generated AGW/TID. When LEO/GPS satellites pass through an area around a receiver unit, we would be able to obtain a scan of total electron content (TEC) values along the satellite's piercing point trajectory. In this case, the ionospheric piercing point (IPP) is chosen along the line connecting the satellite and the receiver at an altitude of ~250 km, near the maxima of ionospheric plasma density. With a proper timing between start/end time of the HF heating period and the scheduled satellite pass, we hope that the satellite's IPP will be able to intercept the heater-generated AGW/TID wavefronts as they spread out from the heated region. The signatures of AGW/TID will typically appear in the form of ripple pattern in the TEC perturbation (TECP) signals.

In this chapter we are going to discuss the low-earth-orbit (LEO) satellite data first. Because of the low orbit and the fast orbiting speed, a LEO satellite pass usually lasted only for ~15 minutes. Therefore, during a LEO satellite pass, we would be able to obtain a rapid TEC scan from one side of the heated region to the opposite side in a short time. Ideally, we would like to arrange for an experiment schedule in which the LEO satellite pass happens immediately after the modulated HF heating cycles had been completed. In the LEO TEC data, we are looking for a particularly

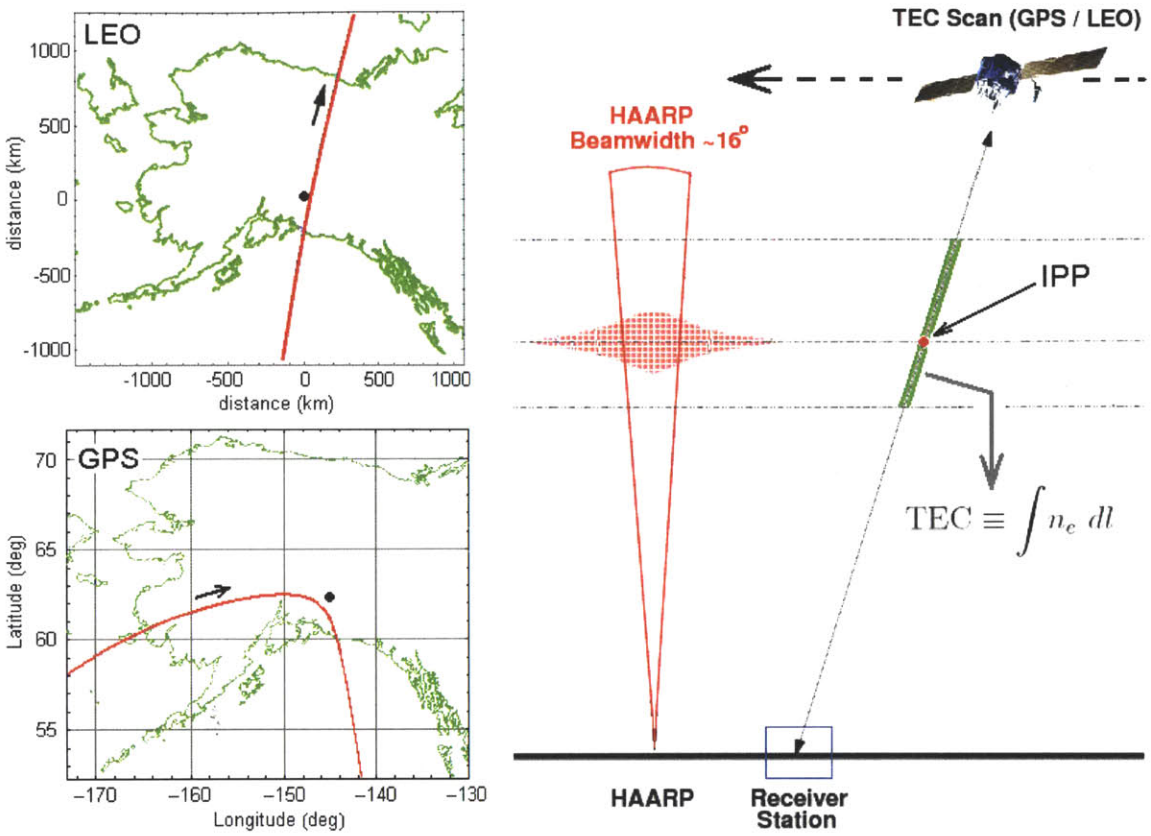

Figure 7-1: A schematic diagram of TEC measurement by a satellite-receiver pair for the HAARP-AGW experiment. During a satellite pass, the IPP trajectory might be able to intercept the AGW/TID ripples that spread radially outwards.

symmetric TECP ripple pattern around the heated region — indicating that we have point-source AGW/TID being radiated out from the heated plasma volume.

After that, we will discuss the TEC measurements from GPS satellite pass. Near the HAARP facility, a typical GPS satellite pass lasts for approximately 3 hours — much longer than a LEO satellite pass duration. We usually arrange for a schedule in which the GPS satellite pass will start well before we begin the modulated HF heating cycle. At the start time of our AGW heating cycles, we anticipate that the GPS satellite's IPP will almost reach the point of closest approach relative to the heated region. In general, during our AGW experiments the GPS satellite's IPP will not directly pass through the heated region. Instead, the GPS IPP will simply slow down while turning around just outside the heated region. In the GPS TEC data, we are going to try to detect the AGW signatures in the Fourier frequency spectra of the recorded TECP signal. The overall settings for both LEO and GPS satellite passes are depicted in Figure 7-1.

7.1 TEC Measurements from LEO Satellite Pass

The type of LEO satellite pass that we consider to be particularly useful for the HAARP-AGW experiment has a typical IPP track similar to the one shown on the upper left panel of Figure 7-1. If AGW/TID are being generated as a result of the modulated HF heating, then we can expect to see some TID signatures in the TECP signal. Furthermore, the characteristic TECP pattern will ideally have some symmetry with respect to the center of the heated region. In other words, we should generally have a set of TEC fluctuation pattern on one side of the heated region, accompanied by the corresponding pair of similar TEC fluctuations on the opposite side of the heated region. Such occurrence of TECP pattern would indicate that we are indeed detecting AGW/TID that originated from the heated region, not naturally-occurring ones that simply happened to pass by the area.

7.1.1 The TECP Scan Signals

We are going to discuss some LEO TECP data recorded during two separate runs of HAARP-AGW experiment. The first one was obtained from OSCAR satellite pass on 29 July 2008, and the other one was from COSMOS satellite pass on 30 July 2008. Both of these LEO satellite passes occurred at the end of the allocated time window for our experiments, after several cycles of AGW modulation had been successfully completed. We are looking for the characteristic TECP ripple pattern on both sides of the heated region, matching the number of AGW cycles that we had performed prior to each satellite pass.

Figure 7-2 shows the TECP data from LEO satellite pass near the end of our experiment on 29 July 2008. The allocated time window for the HAARP-AGW experiment on that day was 03:00–04:12 UT, and the satellite pass happened during 03:49–04:04 UT (15 minute duration). The heating modulation pattern is depicted

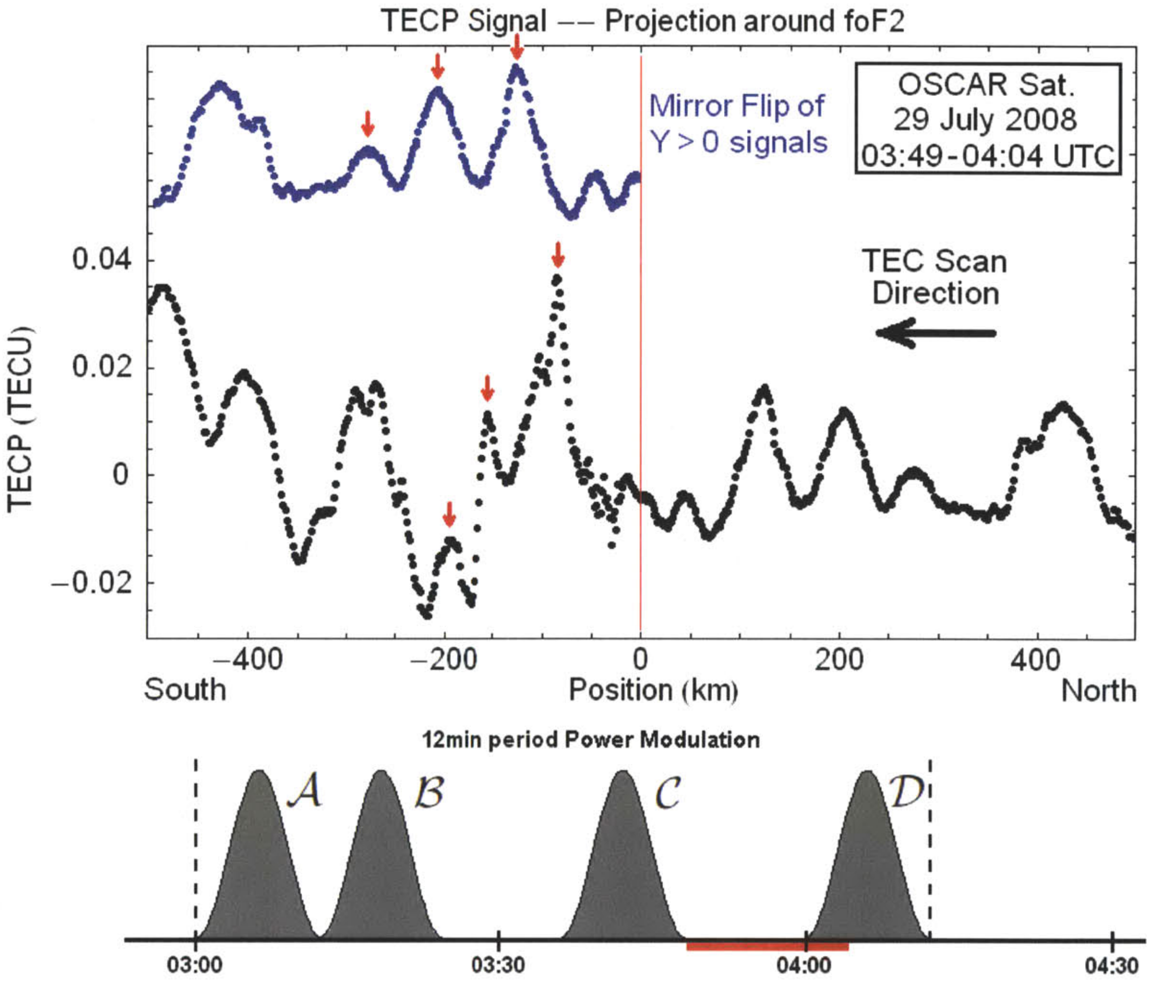

Figure 7-2: The result of a TECP scan from LEO satellite pass on 29 July 2008. The satellite pass happened after 3 (three) cycles of HAARP-AGW heating modulation had been completed.

on the bottom part of the figure, while the satellite pass duration is marked by the red line on the time axis.

This satellite pass gives us a north-to-south scan of TEC values on a relatively straight IPP trajectory. The IPP was nominally chosen to be at 230 km altitude, close to the F2 peak of the ionospheric plasma layer. For comparison purposes, a mirror copy of the TECP signal from the north side is also displayed together with the TECP signal on the south side.

As the LEO satellite pass happened just after we completed 3 cycles of AGW modulation, here we identify 3 corresponding pairs of TECP bumps/peaks on both

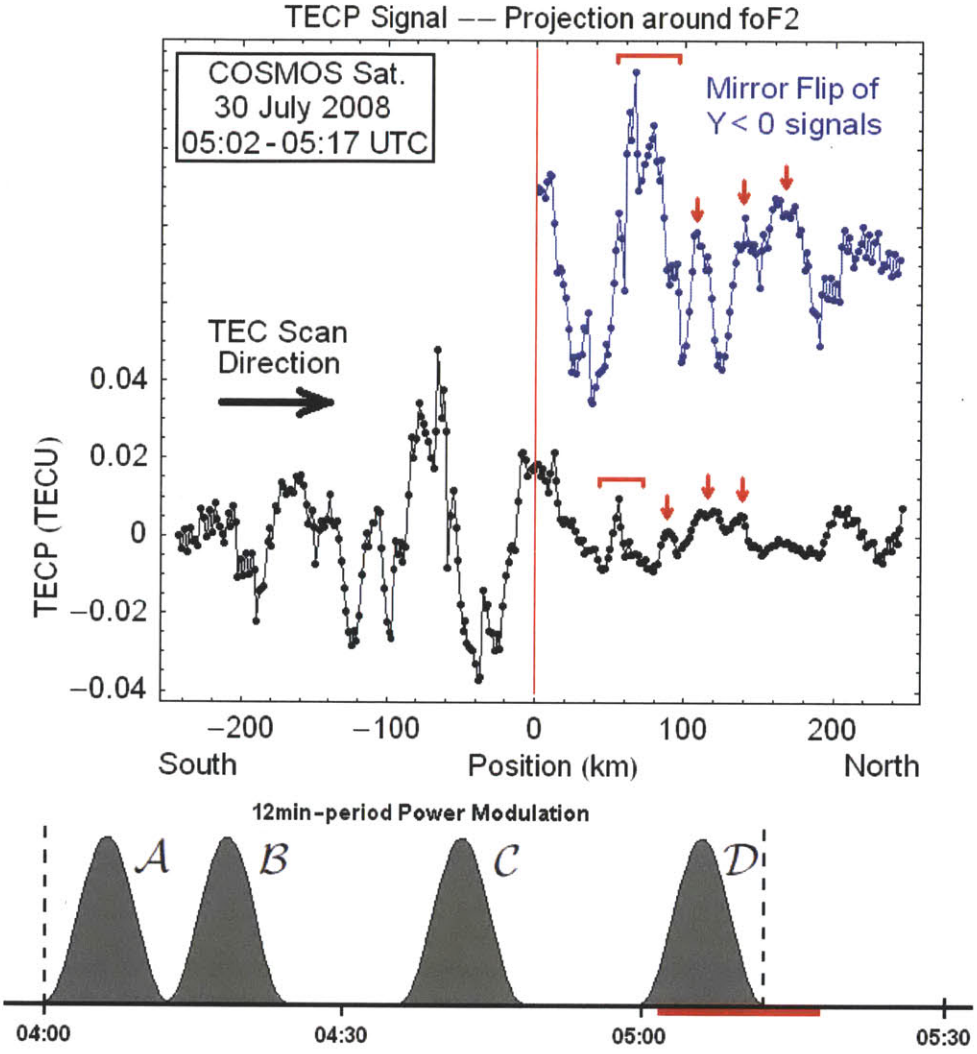

Figure 7-3: The result of a TECP scan from LEO satellite pass on 30 July 2008. The satellite pass happened after 4 (four) cycles of HAARP-AGW heating modulation had been completed.

the north and south sides — the closest ones to the center point. Presumably, these TECP peaks correspond to the heating cycles labeled $\mathcal{A}$, $\mathcal{B}$, and $\mathcal{C}$ in the modulation pattern. The 3 peaks we identified on the north side are relatively clear, possible candidates for some AGW/TID ripple pattern radiating out from the heated region as a result of the modulated heating. The 3 peaks we identified on the south side, on the other hand, are quite badly distorted. The ripple pattern on the north had spread out to a 300 km distance, while the ones on the south had only reached a distance of 250 km away from the center of the heated region.

Similarly, Figure 7-3 shows the TECP data obtained from LEO satellite pass at the end of our experiment on 30 July 2008. The HAARP-AGW modulation was performed within time period 04:00–05:12 UT, and the satellite pass itself happened during 05:02–05:17 UT (15 minute duration). The power modulation pattern is again shown on the bottom part, with the satellite pass duration marked by the red line on the time axis. This time, the satellite pass gives us a south-to-north scan of TECP values along its IPP trajectory (also chosen to be at 230 km altitude).

As the LEO satellite pass this time happened after 4 cycles of AGW modulation had been completed, here we identify 4 pairs of TECP bumps/peaks on both the north and south sides — the closest ones to the center point. In this case, these 4 peaks presumably correspond to the cycles labeled $\mathcal{A}$, $\mathcal{B}$, $\mathcal{C}$, and $\mathcal{D}$ in the power modulation pattern. For comparison purposes, we have put a mirror copy of the TECP signal from the south side together with the TECP signal on the north side. These 4 pairs of TECP peaks have some similarities in shape/configuration, except that the ones on the north side seem to be more compressed than the ones on the south side. In other words, the ripple pattern on the north side looks like a shrunken version of the ones on the south side. The data also shows that the TECP ripples on the south had spread out to a 200 km distance, while the ones on the north had spread out only to a distance of 150 km.

Using the TECP signal recorded during a number of LEO satellite passes right after the HAARP-AGW modulation, we have identified some characteristic ripple pattern on both sides of the heated region. The similarities in shape/configuration and the asymmetries of these discernible TECP ripple patterns indicate that they could be the signatures of heater-generated AGW/TID, with a considerable distortion due to some background neutral wind. This conjecture shall be examined by performing some wave kinematics analysis. Namely, we are going to verify whether or not these ripple patterns actually correspond to a symmetric wave radial propagation that had been shifted/distorted, and whether or not the amount of distortion is consistent with the assumption of a simple background wind.

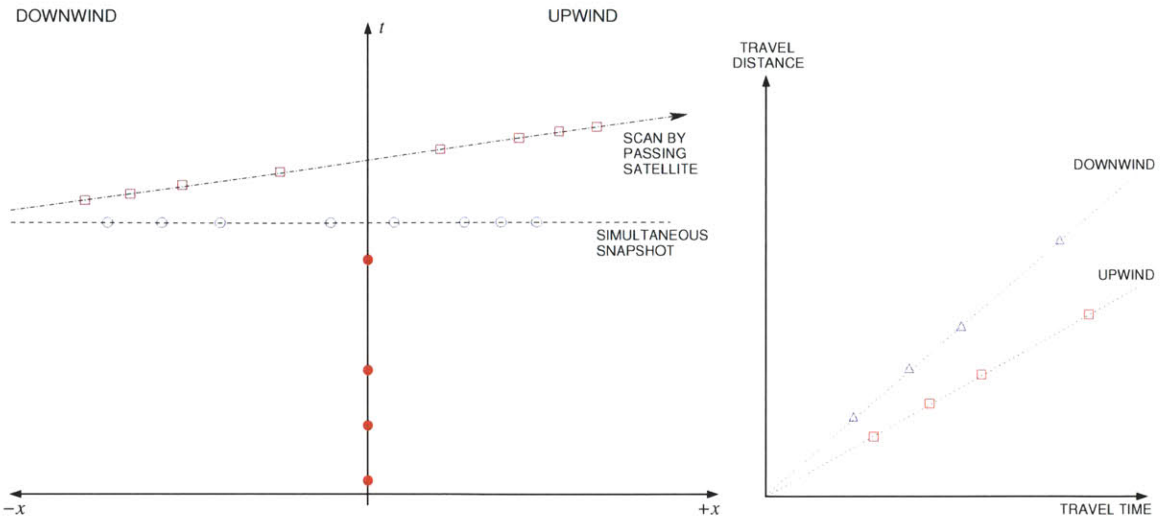

Figure 7-4: Theoretical propagation lines of some wave disturbance originating from a point source, in the presence of a constant uniform background wind (left). Based on the *time-of-birth* of each wavefront and the corresponding *time-of-interception* by a moving observer, one may graph the *travel distance* against the *travel time* (right).

7.1.2 Wave Kinematics Analysis

In order to further investigate our current findings from the LEO satellite pass data, we shall also perform some wave kinematics analysis. The overall goal of this analysis is to obtain some data points for the *travel distance* as a function of the *travel time*. This task can be performed using our knowledge on each of the identified TECP ripple patterns, together with the specific timing of the power modulation cycles in each experiment. In terms of our LEO satellite pass measurements, the *travel distance* is simply the TECP peak position relative to the center of the heated region as it was intercepted by the piercing point of the satellite. Meanwhile, the corresponding *travel time* is the elapsed time interval from the presupposed *time-of-birth* until the *time-of-interception*.

A simple diagram for this wave kinematics analysis is depicted in Figure 7-4, assuming a point-like wave source. In the presence of some background wind, the wave propagation for the upwind and downwind sides would generally be different. In the data plot of *travel distance* vs *travel time* for each of the intercepted wavefronts, we therefore expect two separate linear propagation lines with different slopes for the

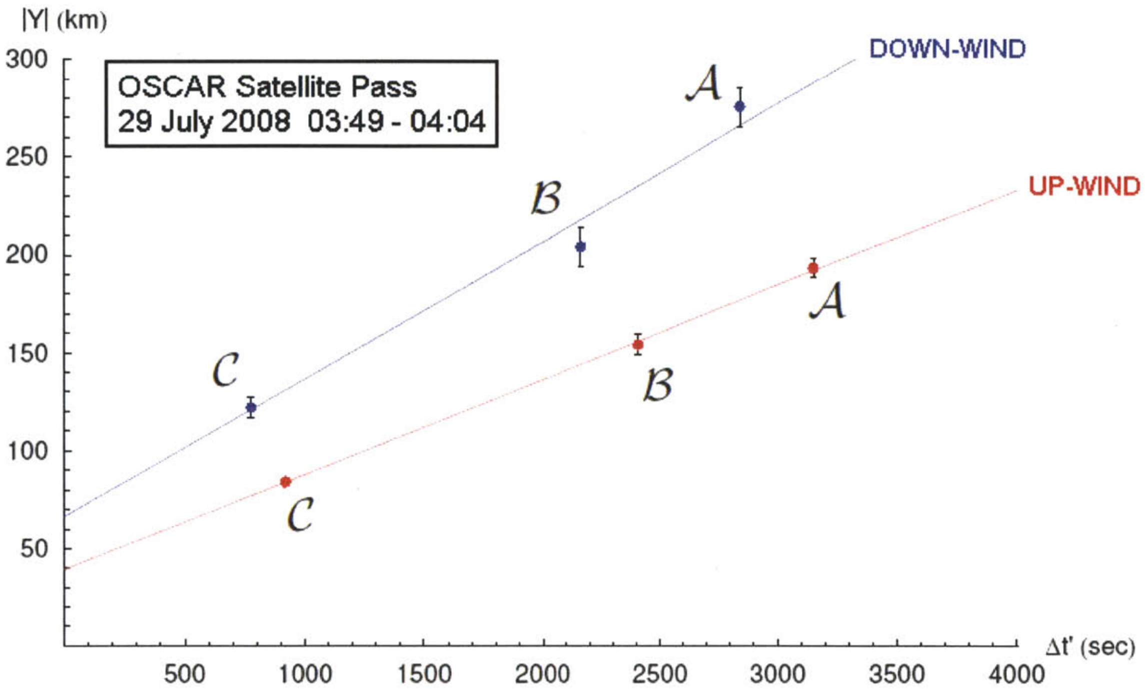

Figure 7-5: The wave kinematics analysis result of the LEO satellite pass data from 29 July 2008. Note the nonzero intercept in the *travel distance* vs *travel time* plot for both upwind and downwind propagation curves.

upwind and downwind sides.

The precise position for each of the identified TECP peaks are determined by fitting a set of parabolic curves on isolated segments of the TECP scan data. The exact *time-of-interception* for all of these TECP peaks are also calculated in the same way (using the TECP–vs–time records). For our analysis, the *time-of-birth* is taken to be the maxima in the power modulation pattern. Hence we have all the necessary elements to compute the *travel distance* and the *travel time*. These procedures are carried out for all the identified TECP peaks from both the OSCAR (29 July 2008) and COSMOS (30 July 2008) satellite pass data.

Figure 7-5 shows the wave kinematics analysis results for the TECP data recorded during the OSCAR satellite pass (29 July 2008). As expected, we have two linear propagation lines with different slopes that correspond to the upwind and downwind sides. We numerically estimate the propagation speed to be $v = 48 \pm 1$ m/s for the upwind side, and $v = 70 \pm 8$ m/s for the downwind side. These two propagation speed

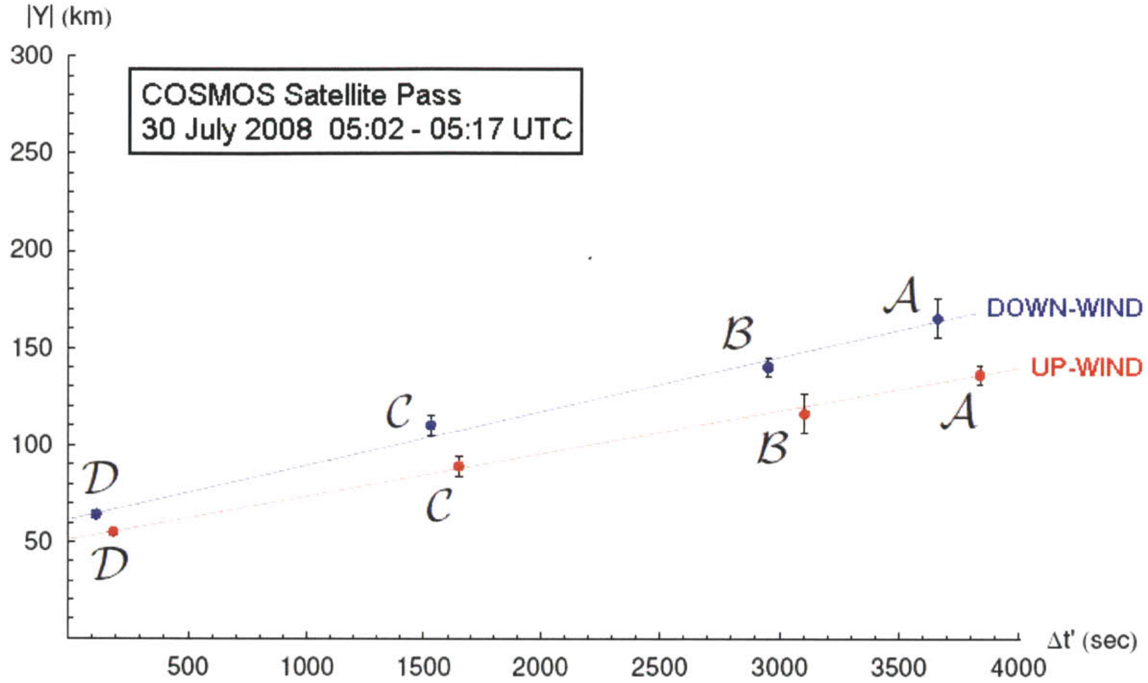

Figure 7-6: The wave kinematics analysis result of the LEO satellite pass data from 30 July 2008. Note the nonzero intercept in the *travel distance* vs *travel time* plot for both upwind and downwind propagation curves.

values average to $v \approx 60$ m/s. Curiously, we find that these two propagation lines do not start out from the center of the heated region. Rather, they seem to emerge from a distance of approximately 50 km away from the center of the heated region.

Meanwhile, Figure 7-6 shows the wave kinematics analysis results for the TECP data recorded during the COSMOS satellite pass (30 July 2008). Like before, we also obtain two linear propagation lines with different slopes that correspond to the upwind and downwind sides. This time we numerically estimate the propagation speed to be $v = 22 \pm 1$ m/s for the upwind side, and $v = 28 \pm 2$ m/s for the downwind side. These two propagation speed values average to $v \approx 25$ m/s. Furthermore, the two propagation lines in this case seem to also emerge from a distance of approximately 50 km away from the center of the heated region — the same as what we found earlier in the 29 July 2008 LEO satellite data.

The wave kinematics analysis confirms that we are indeed intercepting some AGW/TID wavefronts that originate from the heated region, and it also seems to

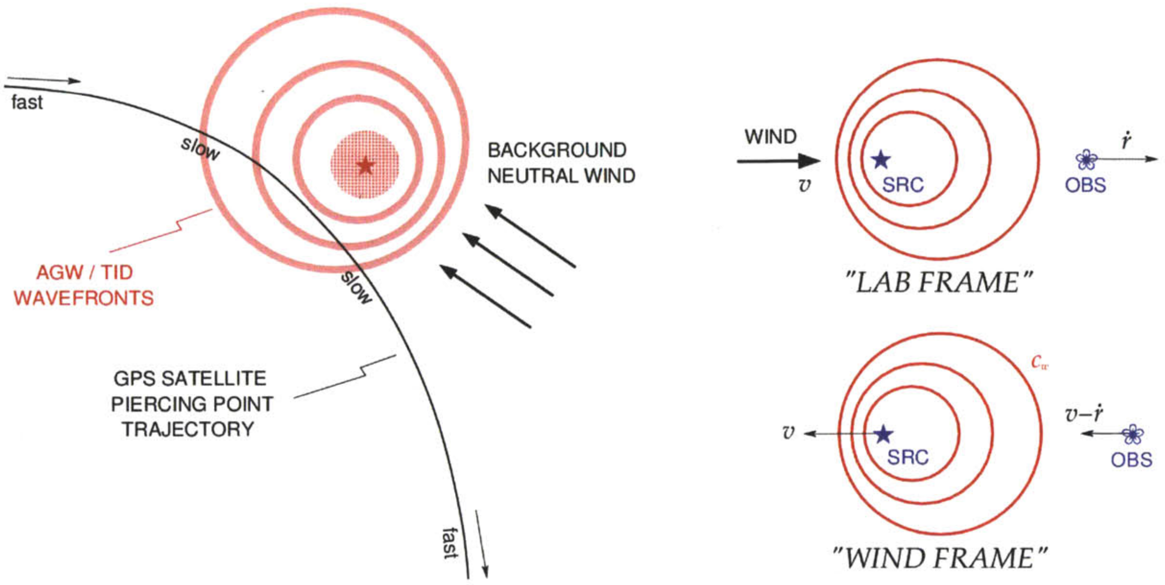

Figure 7-7: A schematic illustration of the typical IPP trajectory during a GPS satellite pass for the HAARP-AGW experiments (left). A diagram describing the Doppler shift in GPS TECP signal due to some background neutral wind (right).

indicate that AGW/TID are actually generated at the *edge* of the heated region. Indeed the temperature gradient would be largest along the edge of the heated region. This fact might explain why we have an extended AGW source in our experiments.

7.2 TEC Measurements from GPS Satellite Pass

The typical IPP trajectory for GPS satellite pass near the HAARP facility has been depicted earlier on the lower left corner of Figure 7-1. Since GPS satellites orbit at an altitude of ~20,000 km, the IPP typically relocates rapidly when it is far away from the receiver location but slows down significantly when it is very close to the receiver location. Figure 7-7 shows a more detailed illustration of the GPS IPP trajectory during the HAARP-AGW experiments.

During HAARP-AGW experiments, the GPS IPP track usually curves and does not directly pass through the heated region. We are going to exploit this particular circumstances to detect heater-generated AGW/TID. When the IPP slows down while turning around near the heated region, we are going to let the AGW/TID ripples pass through. We will then examine the Fourier frequency spectra from the recorded TECP signal. Since the observation point (i.e. the GPS IPP) is moving, we may expect to have some Doppler frequency shift in the detected AGW/TID. In this case, both the IPP speed and the background neutral wind will have some contribution to the resulting Doppler frequency shift.

In order to be able to estimate the amount of this Doppler shift, we will consider the 1-D version of the actual scenario. First, we are going to look at the basic physical configuration of the wave source and the observer in the "lab frame" (upper right corner of Figure 7-7). The wind is blowing in one direction (colinear with the observer's velocity) to distort the radiated wavefronts. Next, we shall switch into the "wind frame" (lower right corner of Figure 7-7) where the source is moving but the medium is now stationary — i.e. no wind in this reference frame. By transforming into a moving reference frame where we no longer have any wind, the Doppler frequency shift $\Delta f \equiv f' - f$ can be straightforwardly determined:

$$f' = \frac{c_w + v - \dot{r}}{c_w + v} f_0 \quad \Rightarrow \quad \frac{\Delta f}{f_0} = -\frac{\dot{r}}{c_w + v} \tag{7.1}$$

where f_0 is the original (unshifted) wave frequency, f' is the measured frequency by the observer, c_w is the wave speed relative to the medium, $\dot{r}$ is the radial component of the observer's radial velocity (+ve if the IPP is moving away from the wave source), and v is the wind velocity (+ve if the IPP is on the downwind side of the wave source).

We will now examine a set of GPS satellite pass measurements for the HAARP-AGW experiment conducted on 25 October 2008 (23:00-24:00 UT). The essential data from this GPS satellite measurements are shown on Figure 7-8. The top panel shows the recorded absolute TEC values, the middle panel shows the TECP signal obtained after detrending the absolute TEC values, and the bottom panel shows the radial velocity component of the GPS IPP during this satellite pass.

We have designated two separate time windows in this dataset. One time window is during 21:05–23:00 UT ($t = -175$ min until $t = -60$ min) and the other one is during 23:00–00:55 UT ($t = -60$ min until $t = +55$ min). The first time window will be used

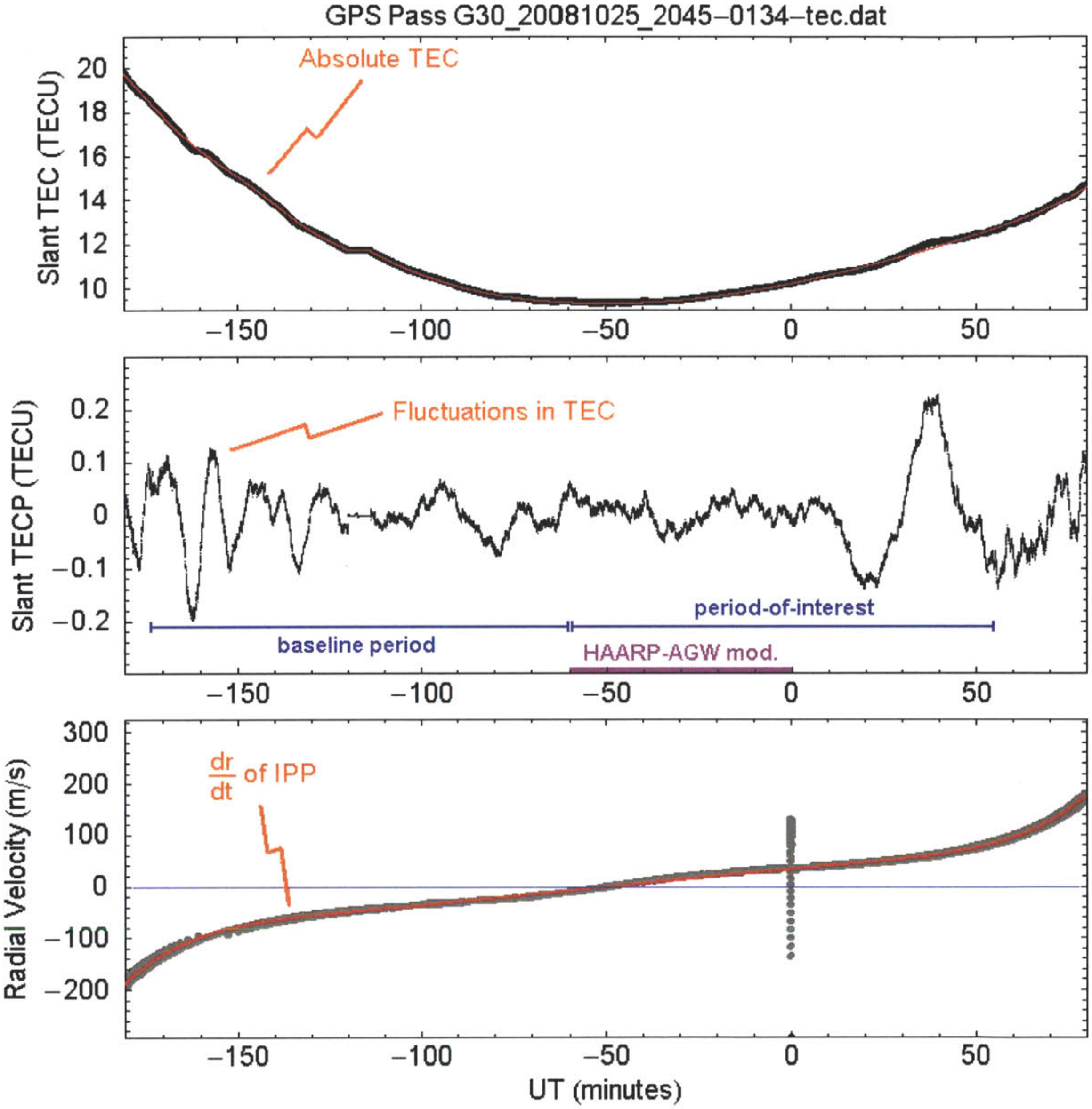

Figure 7-8: Summary of TEC measurement results from a GPS satellite pass for the HAARP-AGW experiment on 25 October 2008 (23:00–24:00 UT). Shown above are the absolute TEC values (top), the net TEC fluctuations after trend removal (middle), and the radial relative velocity between the IPP and the heated region (bottom). The time period for the modulated HF heating is marked by a purple line on the time axis, labeled "HAARP-AGW mod".

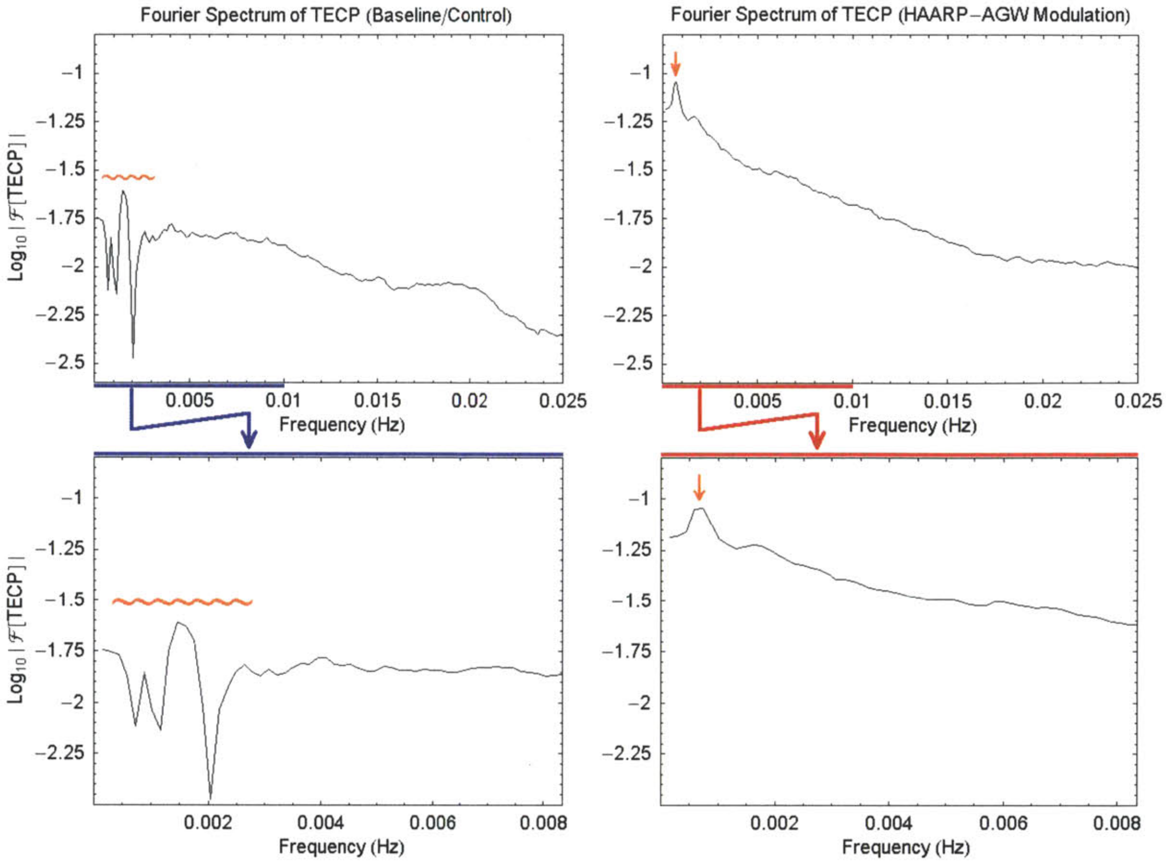

Figure 7-9: Fourier frequency spectra of the GPS TECP signals recorded for the HAARP-AGW experiment on 25 October 2008 (23:00–24:00 UT). We have the spectra from a baseline/control period before the modulated RF heating started (left), as well as the spectra from time period during/after the modulated RF heating (right).

as a baseline/comparison, and the other one is the time period of interest for finding the characteristic signatures of heater-generated AGW/TID. We will then compare the Fourier frequency spectra of the TECP signal from these two time windows. It should also be noted that the geomagnetic condition was very quiet at that time, with $K_p = 0.6$ on the average (c.f. Section 6.2 of this thesis).

The computed Fourier frequency spectra from these two time periods are shown in Figure 7-9. The plots on the left column show the Fourier spectra of the TECP signal from the baseline period, while the plots on the right column show the Fourier spectra of the TECP signal from the main period of interest. On each columns, the one on the top is the TECP frequency spectra in the range of 0–25 mHz and the one on the bottom is the exact same graph zoomed in the frequency range of 0–8 mHz.

Compared to the baseline TECP spectra prior to the AGW modulation, we can see that the TECP frequency spectra during/after the HAARP-AGW modulation had a well-defined peak located at approximately 0.7 mHz. This peak is almost one order of magnitude higher than the baseline level. It markedly indicates the presence of a continuous wavelike oscillation in the TECP signal throughout the second time window, which was not there initially during the first time window. This type of behaviour in the TECP signal is much expected if AGW/TID had been generated by the sinusoidal power modulation pattern while the GPS IPP was coasting slowly just outside the heated region the whole time.

In addition, an overlay of the two TECP frequency spectra from the baseline period and the HAARP-AGW modulation period are depicted in Figure 7-10. This time, the TECP spectra on the top is in the range of 0–30 mHz and the one on the bottom is zoomed in the frequency range of 0–10 mHz.

The power modulation pattern in the HAARP-AGW experiments had a period of $T = 12$ min, which corresponds to a frequency of about 1.4 mHz. The pronounced peak we found in the TECP spectra is centered at approximately 0.7 mHz. During/after the AGW modulation, the GPS IPP was moving away from the heated region with a radial velocity of $\dot{r} \approx 50$ m/s — as evident from the bottom panel of Figure 7-9. It is therefore reasonable that the detected signal experienced a Doppler frequency shift of $\Delta f = -0.7$ mHz (i.e. a redshift from $f_0 = 1.4$ mHz to $f' = 0.7$ mHz). Based on Equation 7.1, a relative Doppler shift of $\Delta f/f_0 = -\frac{1}{2}$ implies $c_w + v = 2\dot{r} \approx 100$ m/s in this case. We did not have the actual measurements of the neutral wind, but if we assume a neutral wind speed in the order of 50 m/s then this estimate would yield an intrinsic wave speed c_w in the order of 50–150 m/s.

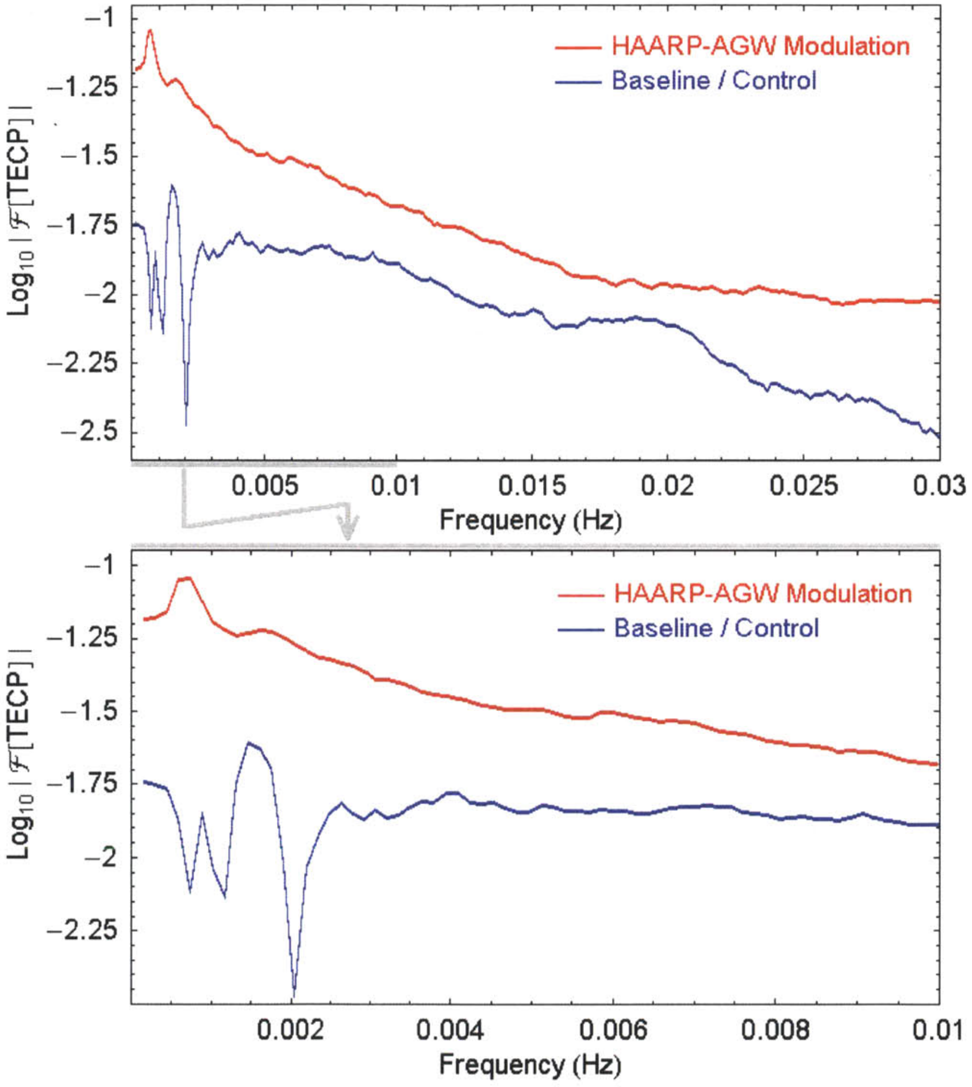

Figure 7-10: Basically the same as in Figure 7-9 except that the two Fourier spectra are now overlaid together for an easier and more direct visual comparison.

Chapter 8

Modeling and Simulation

In this chapter we are going to discuss some modeling and simulation works to complement the experimental data that we have so far. The characteristic signatures of heater-generated AGW/TID in some cases have a few unexpected features that need to be explored. Hopefully these modeling and simulation results can provide some further insight to understanding the experimental data that we have gathered.

First of all, we will discuss a simple fluid model calculations of heater-generated AGWs. The pressure and density fluctuation patterns that we obtained using this fluid model calculation had been particularly useful to cross-check our LEO satellite pass observations. The fluid model precisely predicts that the resulting AGW/TID disturbances in our experiments should originate from the edge of the heated region, matching the empirical wave propagation curves derived from our LEO satellite pass data (c.f. Chapter 7 of this thesis).

Finally we will discuss a set of numerical ray tracing studies to simulate the digisonde data. This simulation thoroughly examines how the characteristic signatures of AGW/TID are expected to appear in the digisonde data under various circumstances. The ray tracing simulation results had confirmed a number of observed features in the experimental data (c.f. Chapter 4 of this thesis) to be the signatures of heater-generated AGW/TID, as opposed to the signatures of naturally-occuring gravity waves in the upper atmosphere.

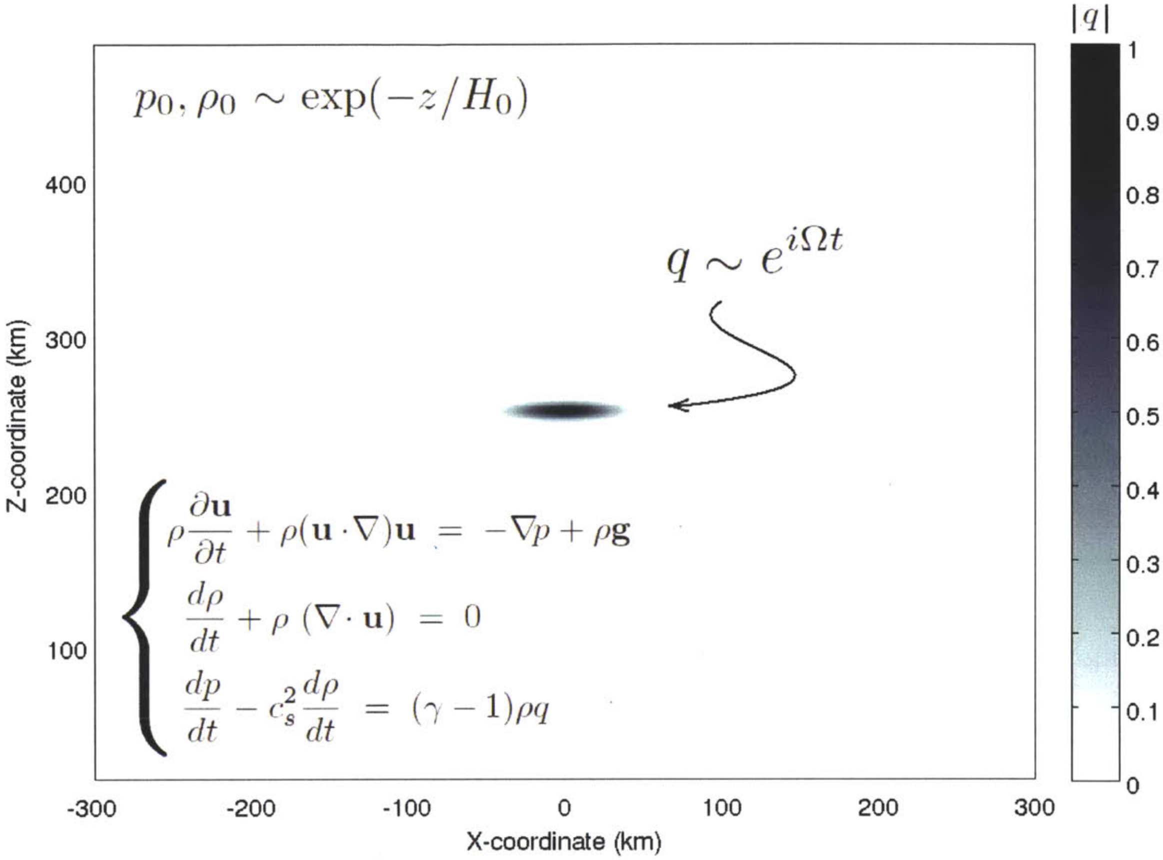

Figure 8-1: The basic setup for the fluid model of heater-generated AGWs. In the modeled heated region, the rate of heat deposition q is sinusoidally varying in time. We seek to obtain the pressure fluctuations δp as a function of position and time.

8.1 Fluid Model of Heater-Generated AGW

In this fairly simple mathematical model for the heater-generated gravity waves, we are going to solve the fluid equations with an oscillatory source term q in the energy balance equation. The basic setup of this model is depicted in Figure 8-1. We are assuming the case of an isothermal atmosphere (i.e. constant and uniform background temperature) so that the background pressure and density decay exponentially with respect to altitude, i.e. $p_0, \rho_0 \sim \exp(-z/H_0)$ where $H_0 \equiv k_B T_0/Mg$ is the atmospheric scale height. The rate of heat deposition will be made to be sinusoidally varying in time as $q \sim e^{i\Omega t}$. Furthermore, the spatial profile of the heat deposition rate itself would model the overall shape of the HAARP-heated region. In this case we have selected a gaussian profile in both r and z coordinates for the heat deposition rate, so that:

$$q(r,z,t) = q_0 \; e^{-r^2/R^2} \; e^{-(z-z_0)^2/\sigma_z^2} \; e^{i\Omega t} \tag{8.1}$$

where z_0, σ_z, and R are a number of adjustable parameters.

Assuming a constant background temperature T_0, the system of coupled partial differential equations that govern the time evolution of density ρ, pressure p, and fluid velocity $\mathbf{u}$ of gases in the upper atmosphere is as follows [see e.g. *Kelley*, 1989; *Schunk and Nagy*, 2000]:

$$\begin{aligned}
\rho\frac{\partial \mathbf{u}}{\partial t} + \rho(\mathbf{u}\cdot\nabla)\mathbf{u} &= -\nabla p + \rho\mathbf{g} && (8.2)\\
\frac{d\rho}{dt} + \rho\,(\nabla\cdot\mathbf{u}) &= 0 && (8.3)\\
\frac{dp}{dt} - c_s^2\frac{d\rho}{dt} &= (\gamma-1)\rho q && (8.4)
\end{aligned}$$

where $\mathbf{g} = -g\hat{z}$ is the gravitational acceleration (vertically downward), γ is the ratio of specific heats (assumed to be constant), and c_s is the adiabatic sound speed (also assumed to be constant). The quantity q in the RHS of Equation 8.4 is the rate of heat deposition (unit of e.g. J kg^{-1} s^{-1}) that we have specified earlier. Note also that $\frac{d}{dt} = \frac{\partial}{\partial t} + \mathbf{u}\cdot\nabla$ is the Lagrangian derivative.

We are going to linearize the fluid equations, and then solve for the resulting pressure fluctuations δp in the steady state. Following similar approach to an earlier work by *Grigor'ev* [1975], we will exploit the cylindrical symmetry in this problem to obtain an analytical expression for the rescaled pressure fluctuation $\psi \equiv \delta p \; e^{z/2H_0}$ in terms of an integral:

$$\psi = iB_{oo}\int_0^\infty dk \int_{-\infty}^\infty d\kappa \; \frac{k \; J_0(kr) \; e^{-k^2R^2/4} \; [\frac{g}{2H_0} - \Omega^2 + i\kappa g] \; e^{-\kappa^2\sigma_z^2/4} \; e^{-i\kappa z}}{\left[\frac{\Omega^2}{c_s^2} - \frac{1}{4H_0^2} + \left(\frac{\omega_g^2}{\Omega^2} - 1\right)k^2 - \kappa^2\right]} \tag{8.5}$$

where $B_{oo} \equiv (\gamma-1)\rho_{oo} \; q_0 R^2 \sigma_z \sqrt{\pi} \; e^{\sigma_z^2/16H_0^2} \; e^{i\Omega t}/4\pi c_s^2 \Omega$. In turn, we will evaluate this integral numerically to obtain ψ in our computational domain. Finally, the actual pressure fluctuation $\delta p = \psi \; e^{-z/2H_0}$ can be recovered easily. The details of this model calculation can be found in Appendix D of this thesis.

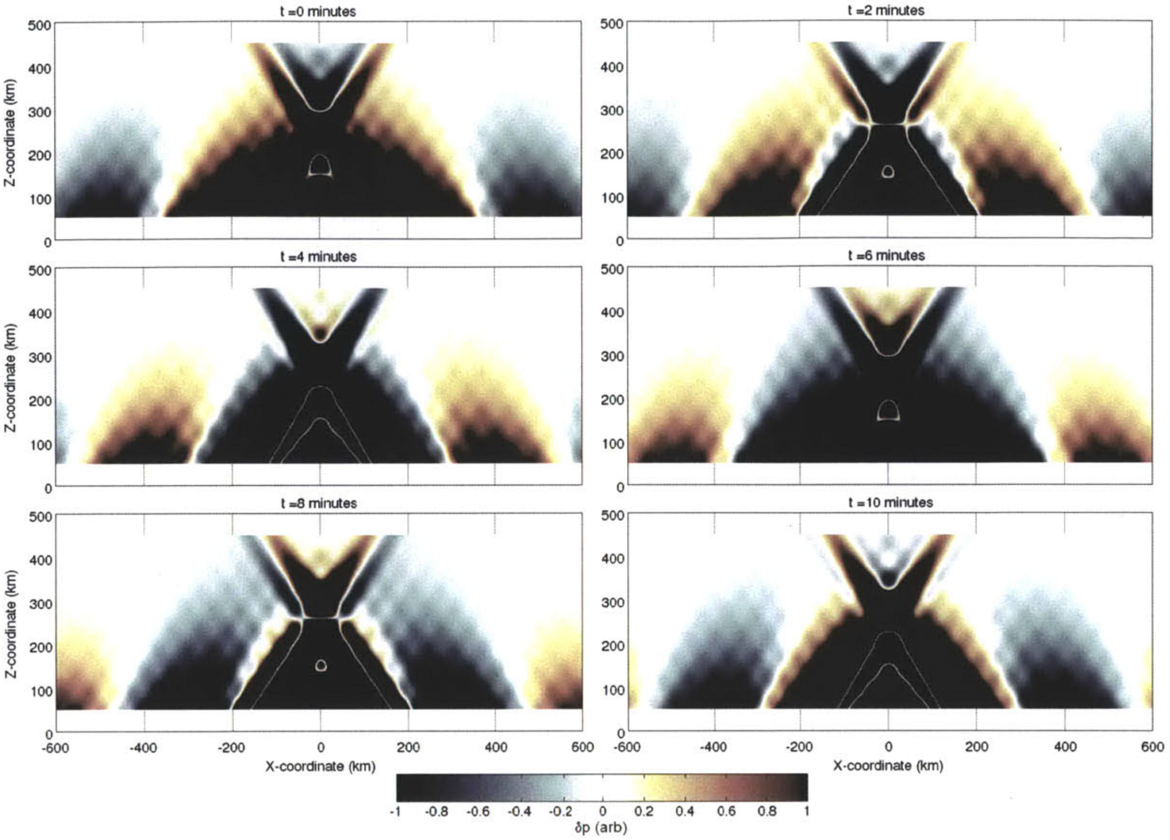

Figure 8-2: A series of snapshots (2 minutes apart) from the fluid model calculations. Each panel shows the spatial pattern of the pressure fluctuations δp at a given time. The modulation period of the heat deposition rate for this fluid model calculation was 12 minutes (same as in the actual field experiment).

In our fluid model calculations, we have set $z_0 = 250$ km, $\sigma_z = 5$ km, $R = 30$ km, and $2\pi/\Omega = 12$ minutes — in order to closely mimic the physical condition in the actual field experiments. Furthermore, we have selected the background temperature to be $T_0 = 1000$ K, and hence giving a scale height of $H_0 = 52.7$ km. A representative sequence of the calculated pressure fluctuation pattern $\delta p\,(x, z, t)$ is depicted in Figure 8-2. From these series of snapshots, we can see some disturbances propagating outwards from the heated region to either direction. This pattern represents the steady state response to the sinusoidal periodic heat deposition, and it would repeat itself once every 12 minutes in this case.

From this fluid model calculation results, we also decide to compute the height-integrated pressure fluctuations to analyze the time evolution of these disturbances

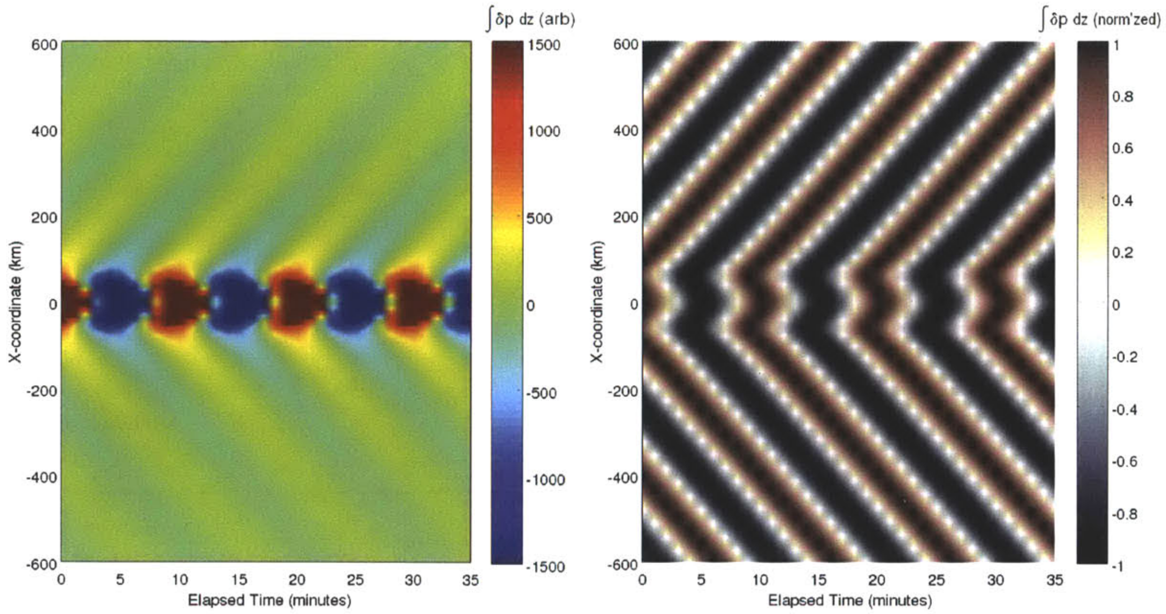

Figure 8-3: The time evolution of height-integrated pressure fluctuations from the fluid model calculation. The left plot is simply $\int \delta p \; dz$ as a function of x and t, while the right plot shows the same quantity after being normalized to its value at $x = 0$.

more closely. In this case, the height-integrated pressure fluctuations will be used as a proxy for the TECP signal — which was measured experimentally using our satellite diagnostics. More specifically, we would like to examine $\int \delta p \, dz$ as a function of both time and the horizontal spatial coordinate. The end results are depicted in Figure 8-3. The left panel simply shows the quantity $\int \delta p \, dz$, and the right panel shows the normalized version of $\int \delta p \, dz$ (normalized to its value at $x = 0$).

In Figure 8-3 above, we can clearly see that the propagation lines are coming out radially on both sides of the heated region. Moreover, the particularly interesting feature of this result is very apparent in the plot of normalized $\int \delta p \, dz$ on the right panel. Here we can easily recognize that the wave propagation lines are W-shaped, and not V-shaped. Such W-shaped propagation lines indicate that the gravity wave disturbance generated by the periodic heat deposition indeed start out from the edge of the heated region, i.e. from $x \approx \pm 50$ km and not $x = 0$ km. In fact, this particular behaviour is what we found in the TECP data from LEO satellite pass during/after the HAARP-AGW experiments. The fluid model calculations therefore precisely predicts what had been experimentally observed using the LEO TEC diagnostics.

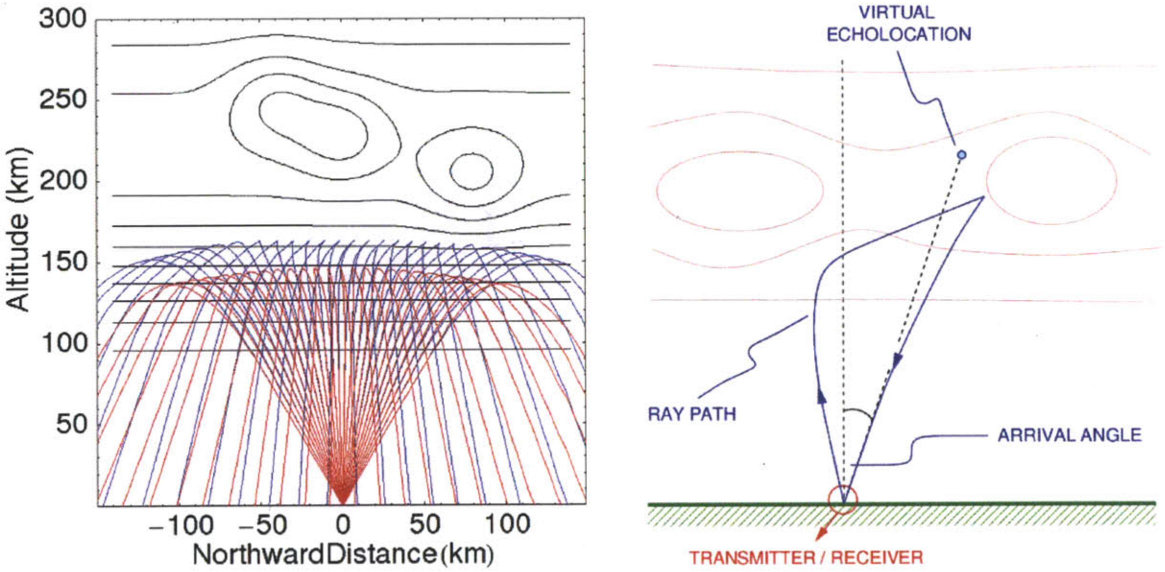

Figure 8-4: The basic setup of the numerical ray tracing study for simulating the skymap data. With a prescribed configuration of the ionospheric plasma layer, we solve for the ray paths of the diagnostics wave launched from the digisonde (left). For rays that do return, we then determine the corresponding *virtual echolocation* (right).

8.2 Ray Tracing Simulation of Digisonde Data

In addition to modeling how AGWs can be generated by periodic heat deposition, we are also interested in figuring out how exactly such AGW/TID might appear in the data from the diagnostic instruments. In this case, we are particularly interested in simulating the digisonde skymap and ionogram data. The refraction of the radio diagnostic pulses as they propagate in the inhomogeneous ionospheric plasma layer makes the digisonde data sometimes especially challenging to interpret. Hopefully this numerical ray tracing study would help clarify some of the features observed in the digisonde data during the HAARP-AGW experiments, and provide us with useful insight for using this diagnostic instrument more effectively in the future.

The basic setup for this numerical ray tracing simulation is depicted schematically in Figure 8-4. First of all, we are going to prescribe a plasma layer configuration that can be adjusted parametrically. For a given configuration of the ionospheric plasma layer and the background geomagnetic field, we will solve the ray tracing equation for the radio wave pulses that are launched upwards at various angles. Both O-mode

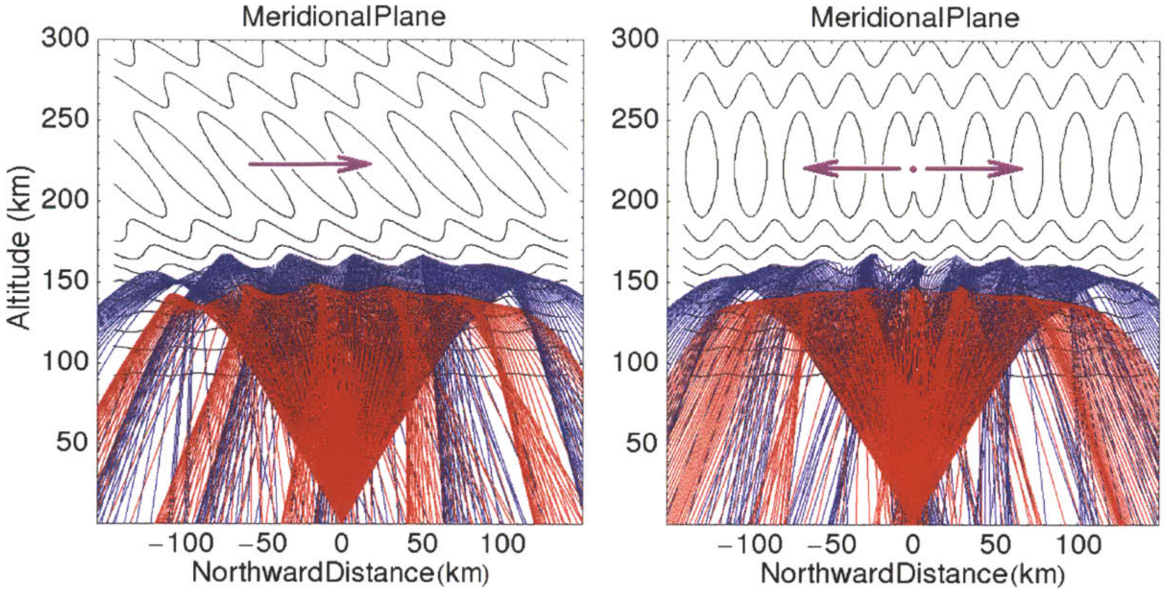

Figure 8-5: The two configurations of ionospheric disturbances to be contrasted in this numerical ray tracing study: passing-by disturbances (left) and point-source disturbances (right). The O-mode/ X-mode raypaths are shown in blue/red colors.

and X-mode wave polarizations are used in this simulation (O-mode ray paths are shown in blue color, and X-mode ray paths are shown in red color). From the solution to the ray tracing equation, we selected the ray paths that land close enough to the transmitter/receiver location on the ground. For such ray paths, we store the time delay information together with the arrival angle. Based on the time delay and the arrival angle, we finally calculate the corresponding *virtual echolocation* to imitate the digisonde data collection procedures in general.

In this ray tracing study, we specifically aim at finding a reliable way to definitively distinguish heater-generated AGW/TID from naturally-occurring AGW/TID in the digisonde skymap data. Thus, we are going to investigate the outcome of two distinct ionospheric plasma layer configurations that contain traveling disturbances:

1. Wavelike disturbances that pass by and propagate in one direction only.
2. Wavelike disturbances from a point source that spread out in both directions.

These two ionospheric plasma layer configurations are depicted in Figure 8-5, together with several sample ray paths (O-mode and X-mode polarizations) of the diagnostic wave pulses launched from the digisonde. As we let the plasma layer configuration evolves step-by-step in each of these two cases, the resulting ray paths will also change accordingly. By gathering sufficient data points at every stage, we hope to be able to see how the time evolution in the spatial distribution of the virtual echolocations would differ between these two contrasted cases.

An overall summary of the results from the first case (passing-by disturbances) is shown in Figure 8-6. Plotted here are the horizontal projection of the O-mode virtual echolocation as a function of time, for 3 different sounding frequencies. The ionospheric plasma layer itself was modeled using Chapman layer with scale height of $H_0 = 60$ km and maximum plasma frequency of $f_{\mathrm{pe,max}} = 4.95$ MHz at $z_0 = 220$ km, superposed with 5% wavelike field-aligned irregularities that propagate northward ($\lambda_\perp = 30$ km). The background geomagnetic field points downward and northward (dip angle of 50° from horizontal), with a field strength corresponding to electron gyrofrequency of $f_{\mathrm{ce}} = 1$ MHz. We can see that for almost all sounding frequencies we have the same qualitative behaviour: the echolocations shift position following the direction of the traveling disturbances, passing through the center point $x = 0$ and continuing up to a certain distance northward.

Meanwhile, an overall summary of the results from the second case (point-source disturbances) is shown in Figure 8-7. Plotted again here are the horizontal projection of the O-mode virtual echolocation as a function of time, for 3 different sounding frequencies. We have the same geomagnetic field configuration as before: field strength corresponding to electron gyrofrequency of $f_{\mathrm{ce}} = 1$ MHz, and a dip angle of 50° from horizontal. The ionospheric plasma layer was again modeled using the Chapman layer formula with scale height of $H_0 = 60$ km and maximum plasma frequency of $f_{\mathrm{pe,max}} = 4.95$ MHz at $z_0 = 220$ km, but this time superposed with 5% upright wavelike irregularities that originate from a point source directly overhead and spread out in both directions ($\lambda = 30$ km). We can see that for sounding frequencies $f = 4.0$ MHz and $f = 4.8$ MHz, we have traces of echolocations emerging outward from the center point $x = 0$ — predominantly towards the southward direction. This southward preference occurs even though the prescribed ionospheric disturbances are going towards

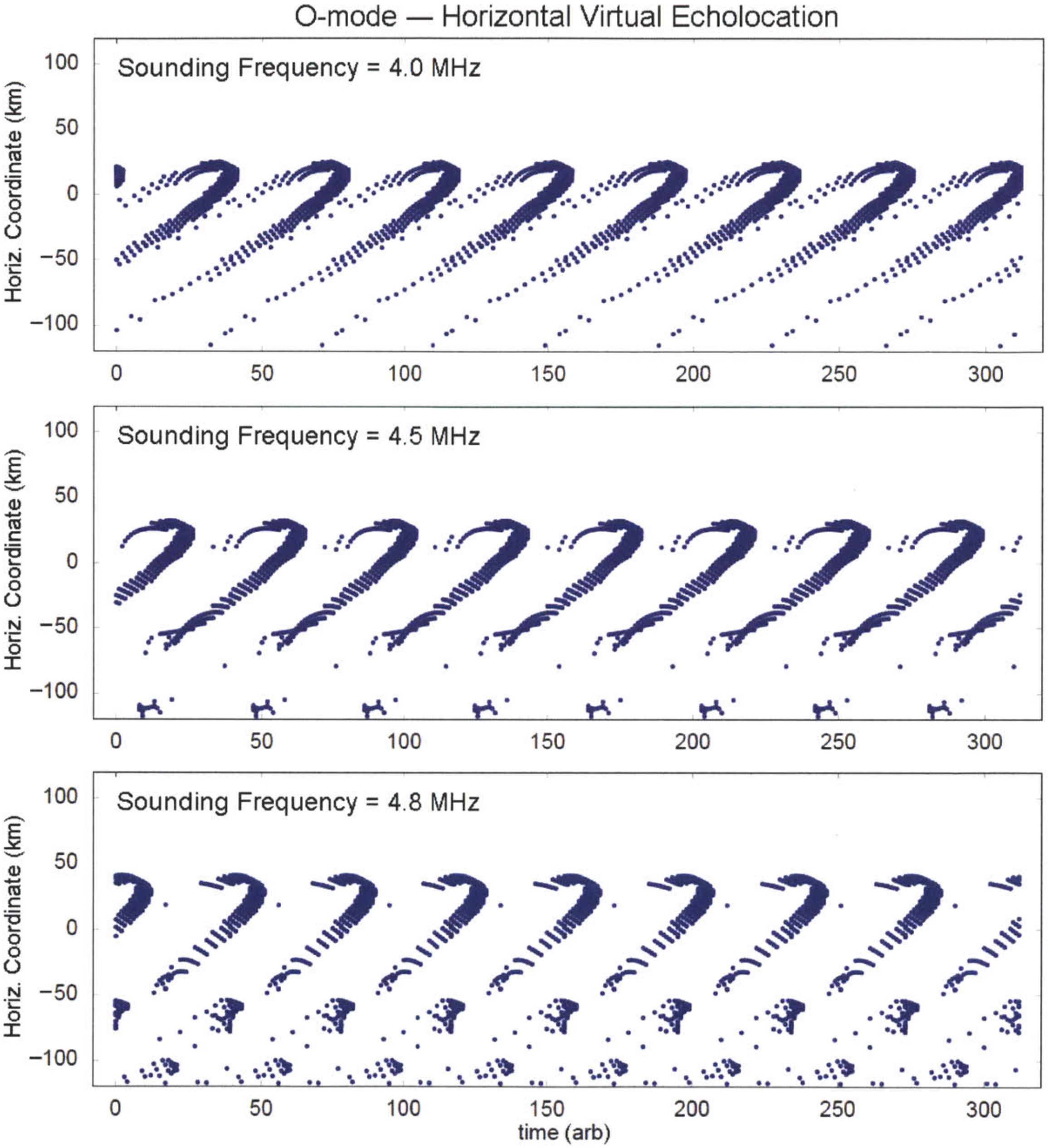

Figure 8-6: Some numerical ray tracing simulation results for passing-by disturbances. Plotted are the horizontal virtual echolocation distribution as a function of time, for three representative sounding frequencies (ordinary wave polarization).

both directions from the source point. On the other hand, for $f = 4.4$ MHz we see that the bulk majority of these echolocations simply shift outward and inward periodically. These findings qualitatively match the actual skymap data recorded during the HAARP-AGW experiments: some datasets show clear streaks that propagated radially away from the origin towards a certain direction, while other datasets only show a periodic back-and-forth shift of the bulk echolocations.

Furthermore, we would like to investigate some of the curious features we observed in the ionogram data from the HAARP-AGW experiment on 19 July 2011. In this case, we found some additional X-mode ionogram traces that appear episodically once every 12 minutes or so, roughly matching the heating modulation cycle. It was suspected that these episodic X-mode ionogram traces had been caused by periodic changes in ionospheric tilt at some distance away from the heated region. Such periodic change in ionospheric tilt is indeed expected if the heated region actually generates AGW/TID as we intended. A suitable amount of tilt would allow for significant amount of oblique return signals through total reflection, but perhaps this configuration only occurs in a narrow window. This speculation is summarized diagrammatically in Figure 8-8.

Using the same methodology as before, we can also simulate how the ionogram data would look like when there are some gravity wave disturbances. This may be achieved by performing the ray tracing calculation for several finely-spaced sounding frequencies at each stage, and finally compiling the result in one ionogram plot.

We prescribed the same ionospheric plasma configuration as the one giving us the result in Figure 8-7 (i.e. point-source disturbances). We then ran the ray tracing simulations using finely-spaced sounding frequencies between 5.1 and 5.5 MHz in order to synthesize a sequence of X-mode ionograms in this frequency range. We shifted the embedded wavelike pattern by 1 km step at a time, and then synthesized one simulated ionogram after each shift. The wavelength of these periodic disturbances is $\lambda = 30$ km, hence everything will be back to its original configuration after 30 km shift. In these calculations, we retained the same type of information as in the original skymap simulation (including arrival angle), so that the vertical and oblique echoes

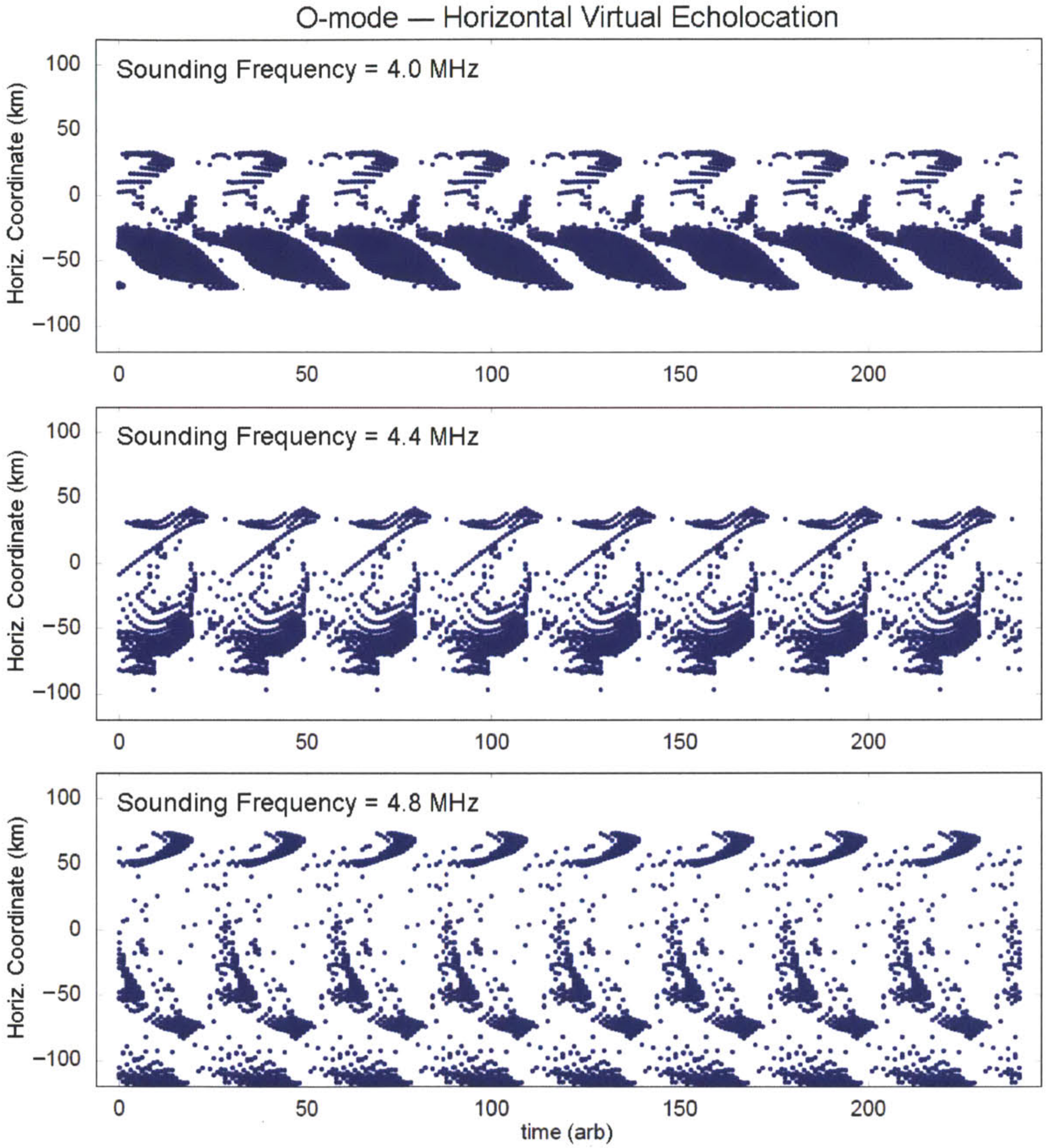

Figure 8-7: Some numerical ray tracing simulation results in the case of point-source disturbances. Plotted are the horizontal virtual echolocation distribution as a function of time, for three representative sounding frequencies (ordinary wave polarization).

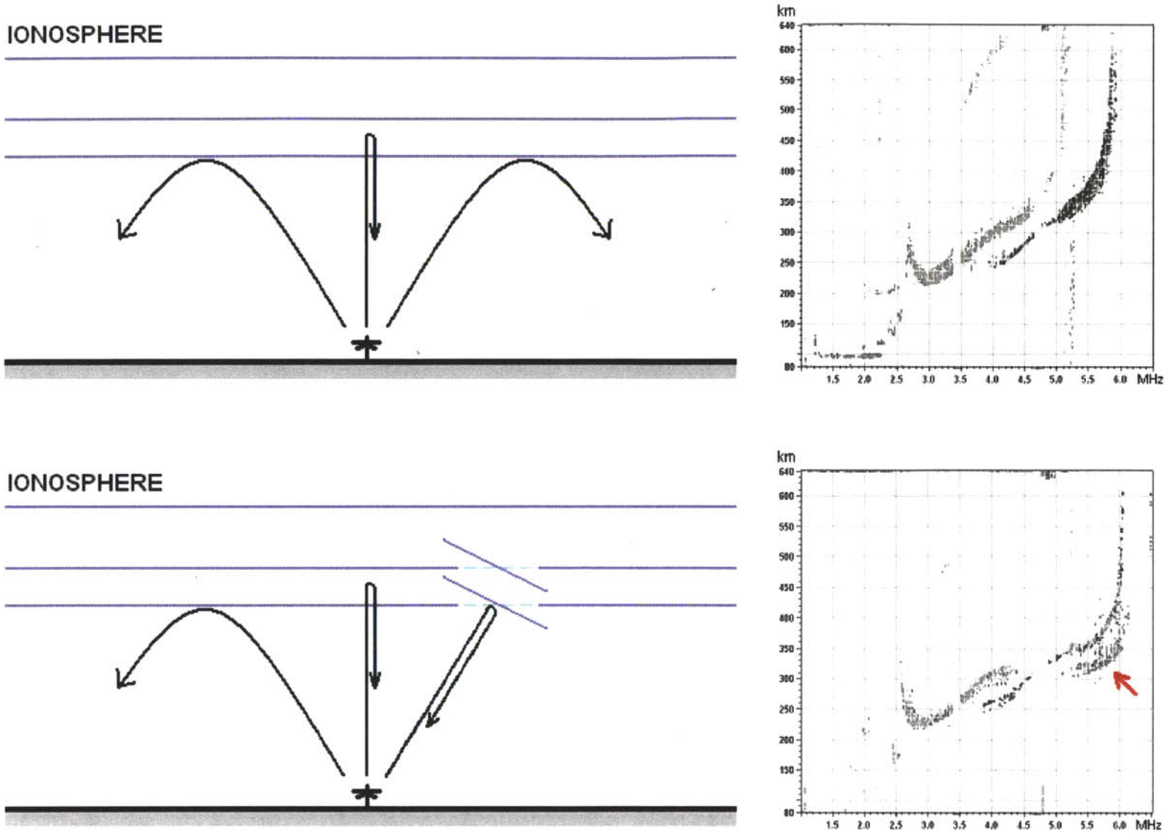

Figure 8-8: The hypothesized scenario behind the additional X-mode traces in the ionograms during HAARP-AGW experiment (c.f. Subsection 4.2.6 of this thesis). These additional traces are suspected to be return echoes from oblique directions due to periodic changes in ionospheric tilt at some distance away.

can still be identified in the synthesized ionograms. In this ionogram simulation, we will separate the vertical and oblique echoes at the median value of the zenith arrival angle distribution.

The main highlight of this ionogram simulation is depicted in Figure 8-9. In these sinthesized ionograms, the vertical (oblique) echoes are those with the zenith arrival angle less (larger) than 7°. For the most part, the vertical and oblique traces in these simulated ionograms are mixed together in a large cluster. However, at shift values of 20 and 21 km, a group of oblique echoes can be seen separating downward to form a distinct trace with a clear gap from the main trace. This pattern qualitatively mimics the appearance of additional X-mode traces in the actual ionograms recorded during the 19 July 2011 HAARP-AGW experiment, as shown earlier in Figure 4-13

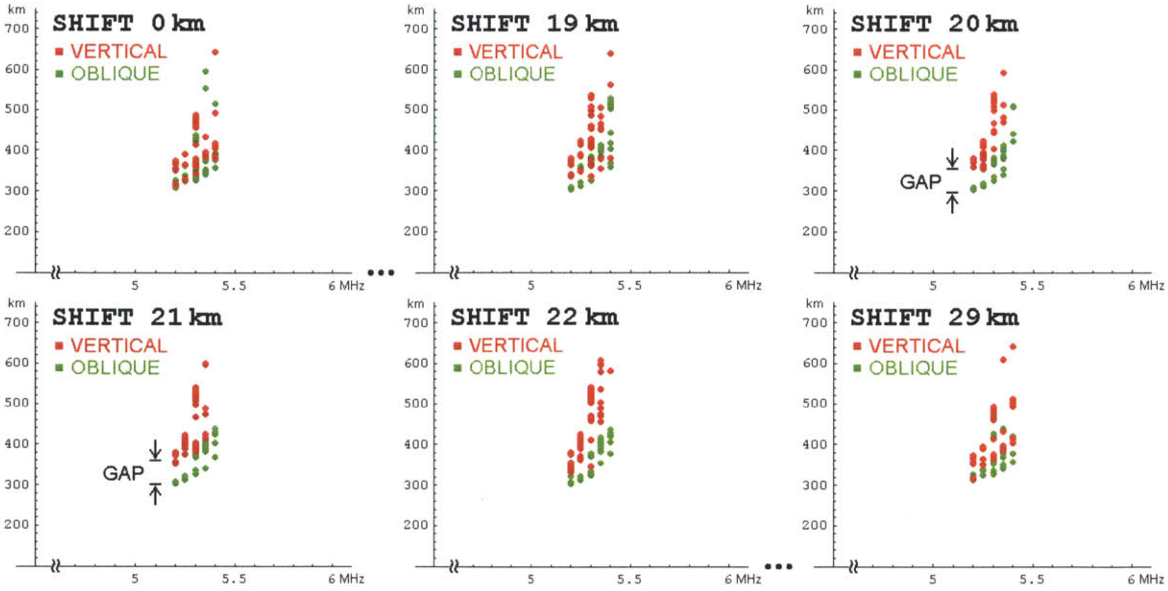

Figure 8-9: A set of X-mode polarization ionograms from the ray tracing simulation, when some point-source disturbances are embedded in the ionospheric plasma layer. The listed *shift* values indicate how far the periodic spatial pattern had spread out.

and then Figure 8-8. Moreover, out of the 30 evaluated shift values, this "separation" only happens at 2 consecutive shift values. It might therefore explain the episodic nature in the appearance of these additional ionogram traces during the actual field experiment. Had the timing been off, we could have easily missed those additional X-mode traces in the ionogram data. This situation is very much like the pattern of elongated band observed in the skymap data shown several chapters ago in Figure 4-3.

More intuitively, the "downward separation" of the oblique ionogram echoes can be explained as follows. The oblique rays generally do not penetrate the plasma layer as deep as the vertical rays do. Therefore, the oblique rays mostly stay outside of the dense plasma region during their propagation. In contrast, the vertical rays penetrate deeper into region of a denser plasma, causing the group velocity to slow down significantly during this part of their propagation path. As a consequence, although the physical trajectory of the oblique rays might be longer than that of the vertical rays, the virtual/apparent trajectory (based solely on the travel time) of the oblique rays could actually be shorter than that of the vertical rays in this case.

Chapter 9

Data Discussions

In Chapters 4–7, we have closely examined several characteristic signatures of the artificial AGW/TID as recorded by various ground-based and satellite diagnostic instruments during our heating experiments. Some of the curious features in the diagnostic data had been quite successfully verified and explained through numerical model/simulations, which were presented in detail in Chapter 8. A number of key findings from our experiments and modeling/simulations include:

- **Digisonde Skymap Data**. During the HAARP-AGW experiments, we had observed that the horizontal echolocation of return echoes in the skymap data responds periodically following the modulated HF heating cycle. However, the overall pattern is not always qualitatively the same. In some cases, we do see a cluster of skymap echoes repeatedly shifting radially away from the heated region — indicating that some traveling disturbances had been generated. In some other cases, we could only see the echolocation shifting back-and-forth (outward and then inward) periodically. We had performed a numerical ray tracing study to simulate the digisonde skymap data, and it had provided some verification that these two different patterns are actually consistent with some TIDs that spread radially away from the heated region (distinguishable from passing-by natural TIDs). It was found that the choice of sounding frequency affects the qualitative echolocation pattern quite heavily.

- **Ionogram Data**. During our HAARP-AGW experiment on 19 July 2011, we observed some additional traces in the recorded ionograms. These additional traces appeared episodically below the main ionogram trace, roughly once every 12 minutes (which equals to the heating modulation period). We then suspected that these additional ionogram traces had come from some oblique return echoes as the ionospheric tilt at a certain distance away from the heated region is being affected by the heater-generated AGW/TID. We also try to simulate the ionogram data in our numerical ray tracing study, and the results generally corroborate our proposed scenario involving the oblique return echoes.

- **LEO Satellite Data**. Based on the results of our wave kinematics analysis using the TECP data recorded during LEO satellite passes immediately after the HAARP-AGW experiment, we found that the heater-generated artificial AGW/TID seem to originate from the *edge* of the heated region (approximately at a distance of 50 km from the center point). By setting up a fluid model to numerically simulate the generation of AGW/TID in our heating experiments, we found that the propagation lines of these heater-generated AGW/TID indeed start out at a certain distance away from the center of the heated region — consistent with the experimental finding from LEO satellite measurements.

At this point, we have gathered a number of suggestive evidence indicating that AGW/TID are indeed being radiated out from the heated plasma volume as a direct result of the modulated HF heating. We shall now take a few steps further in analyzing the physical properties of such artificial AGW/TID.

In this chapter, we are going to have a thorough discussion on two specific areas: (1) the typical propagation speed of heater-generated AGW/TID, and (2) the overall efficiency in the generation of artificial AGW/TID via modulated HF heating. Based on the digisonde and MUIR data, the propagation speed of artificial AGW/TID in our heating experiments typically lies in the range of 77 m/s to 140 m/s. Meanwhile, it is also estimated that approximately 23%–34% of the total transmitted HF power goes into generating AGW/TID in this case.

9.1 Propagation Speed of HAARP-AGW

From the available literature on the observation of naturally-occurring medium-scale traveling ionospheric disturbances (MSTIDs) with wavelengths in the order of several tens of km, a propagation speed in the range of a few tens of m/s or perhaps around 100–200 m/s is quite common [see e.g. *He et al.*, 2004; *Tsugawa et al.*, 2007]. For large-scale TIDs with wavelengths in the order of several hundreds of km, faster propagation speed up to ∼500 m/s might even be possible [see e.g. *Williams*, 1996]. The artificial AGW/TID generated during the HAARP-AGW experiments have a wavelength of several tens of km, and therefore could generally be classified into the MSTID category.

Using the data from TECP measurements during selected LEO satellite passes (c.f. section 7.1 in Chapter 7), we have already obtained a preliminary estimate for the propagation speed of heater-generated artificial AGW/TID. The wave kinematics analysis of the LEO satellite data gives a wave propagation speed in the range of 25–60 m/s, which fit the typical propagation speed of MSTIDs. Meanwhile, our GPS TEC measurements (c.f. section 7.2 in Chapter 7) produce an estimated propagation speed in the range of 50–150 m/s for the heater-generated AGW/TID. In this chapter, we are going to discuss a set of alternative ways to calculate the propagation speed using ground-based radio diagnostic instrument data. Hopefully, this complementary approach will contribute to a more complete perspective on the propagation speed of the artificial AGW/TID generated in our heating experiments.

We are going to start our discussion with the digisonde skymap data recorded during the HAARP-AGW experiment on 14/15 August 2009 (23:30–01:30 UTC). On the top panel of Figure 9-1 we reproduce the two plots we have shown previously in Chapter 4 (c.f. subsection 4.2.3). In these skymap echo distribution-evolution plots, a streak of traveling disturbances can be seen to come out from the center point (where the heated region is located) and propagate in the westward direction. On the middle panel, we have a sequence of individual skymaps from this time period. In the northwest sector of these skymaps, we may notice a cluster of return echoes that moves

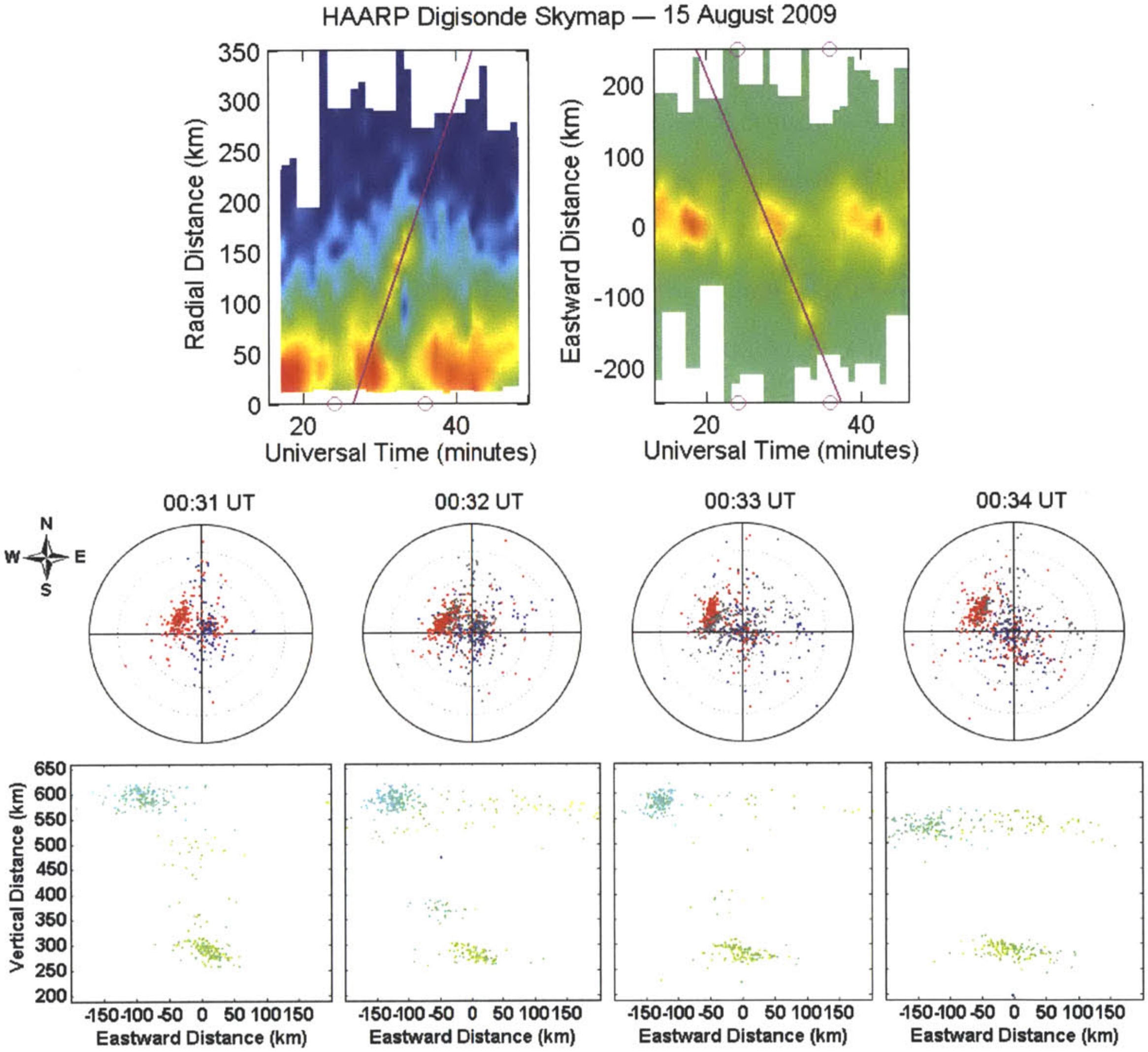

Figure 9-1: Streak of traveling disturbances that were observed in the skymap echo distribution-evolution plots from the HAARP-AGW experiment, 23:30–01:30 UTC on 14/15 August 2009 (top panels). The diagonal purple lines are the straight-line fit to this streak. Also shown are the conventional skymaps (middle panels) and the virtual echolocation plots along the east-vertical plane (bottom panels) from the time period when the streak was observed.

steadily westward in one frame to another. Meanwhile, on the bottom panel we have the corresponding side-view virtual echolocation plots — from the same time period as the skymaps depicted on the middle panel. In these virtual echolocation plots, the westward-propagating disturbances can be recognized as a cluster of skymap echoes at an apparent vertical distance of $\sim$600 km above the ground.

From the radial distribution plot, a straight-line fit to the observed outward streak had revealed an apparent horizontal propagation speed of $\frac{dr}{dt} = 370 \pm 30$ m/s. On the other hand, the straight-line fit from the planar E/W distribution plot gives us an apparent horizontal propagation velocity of $\frac{dx}{dt} = -440 \pm 50$ m/s. Hence, the apparent propagation speed of this artificial traveling disturbances is $v = 390 \pm 26$ m/s on the average. This value is evidently too large for the typical MSTID propagation speed. This gross overestimation likely stems from the fact that virtual range recorded in the skymap data is generally larger than the real/actual range of the reflecting region(s) in the ionosphere. In order to obtain a more realistic value for the propagation speed, we will therefore have to correct for the stretching factor between real and virtual range of the return echoes in the skymap data.

In practice, we can empirically determine the stretching factor between real and virtual echolocation in the skymaps by looking at the relation between real and virtual height in the ionograms during this time period. In an ionogram, we have the virtual height ($\equiv c\,\Delta t/2$ for all return signals from the vertical direction) as a function of the sounding frequency. The virtual height profile can be Abel-inverted to yield the real height profile, taking into account that the radio diagnostic pulse slows down considerably below the speed of light in vacuum c while traversing through the plasma. The stretching factor would generally be largest for sounding frequencies near the peak/maximum plasma frequency in the ionospheric layer. Based on the comparison between the virtual height profile and the Abel-inverted real height profile, we may compute the stretching factor and then apply the same factor for the return signals from the oblique directions in the skymap data as well.

In Figure 9-2, we have a composite ionogram from time period 00:25–00:40 UTC on 15 August 2009. The virtual height profile in this ionogram (pink data points with

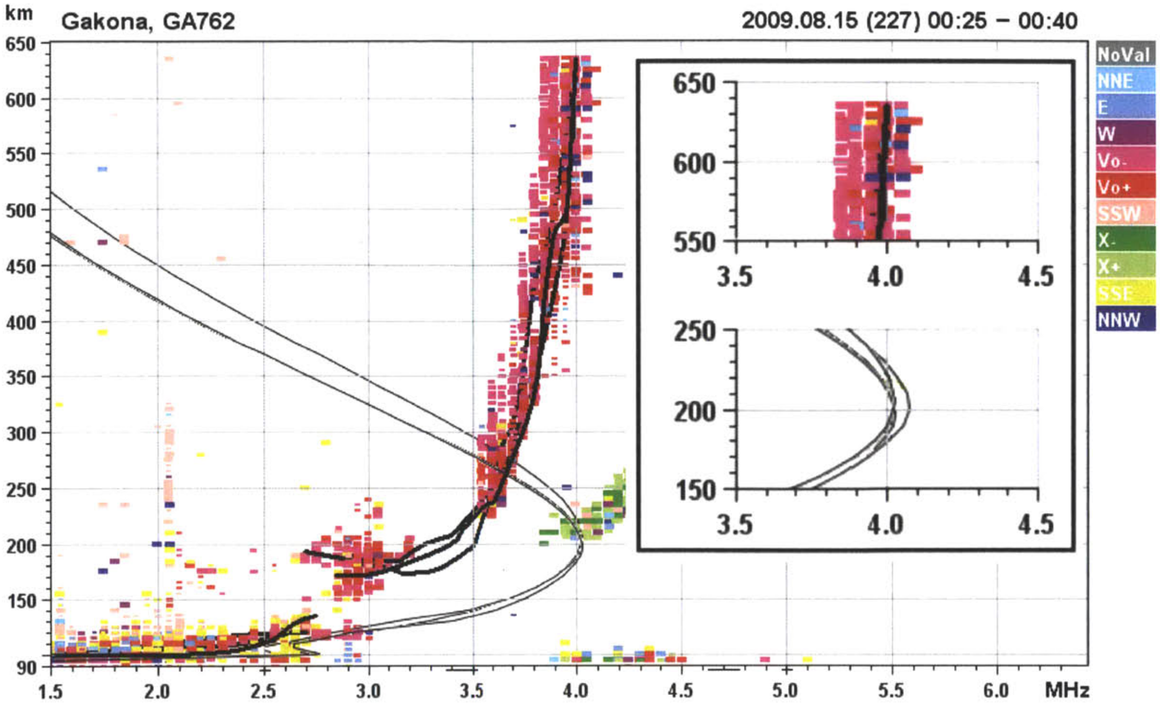

Figure 9-2: A set of composite ionograms from the same time period as in Figure 9-1. Based on the original ionogram traces and the Abel-inverted f_{pe} profile, we see that return echoes at a virtual range of ~600 km have an actual range of 150–200 km (conversion down by a factor of 3–4).

thick black trace) had been Abel-inverted to yield the real height profile (smooth thin black curve). As we had remarked earlier, the cluster of skymap echoes associated with the traveling disturbances under consideration is located at an apparent altitude of ~600 km. Referring to the composite ionogram shown in Figure 9-2, return echoes with a virtual height of ~600 km would have a real height of 150–200 km. Hence, we have a stretching factor of 3–4 between real and virtual height.

Applying this stretching factor to both vertical and horizontal components of the virtual echolocations in the skymap data, one may see that the apparent horizontal propagation speed must be scaled down by the same numerical factor. Adjusted by this stretching factor, the apparent $\frac{dr}{dt}$ will be scaled down to 98 ± 6 m/s, while the apparent $\frac{dx}{dt}$ will be scaled down to 130 ± 9 m/s. In summary, this correction finally yields an estimated propagation speed in the range of 92–139 m/s, which is more reasonable in relation with the known typical propagation speed of MSTIDs.

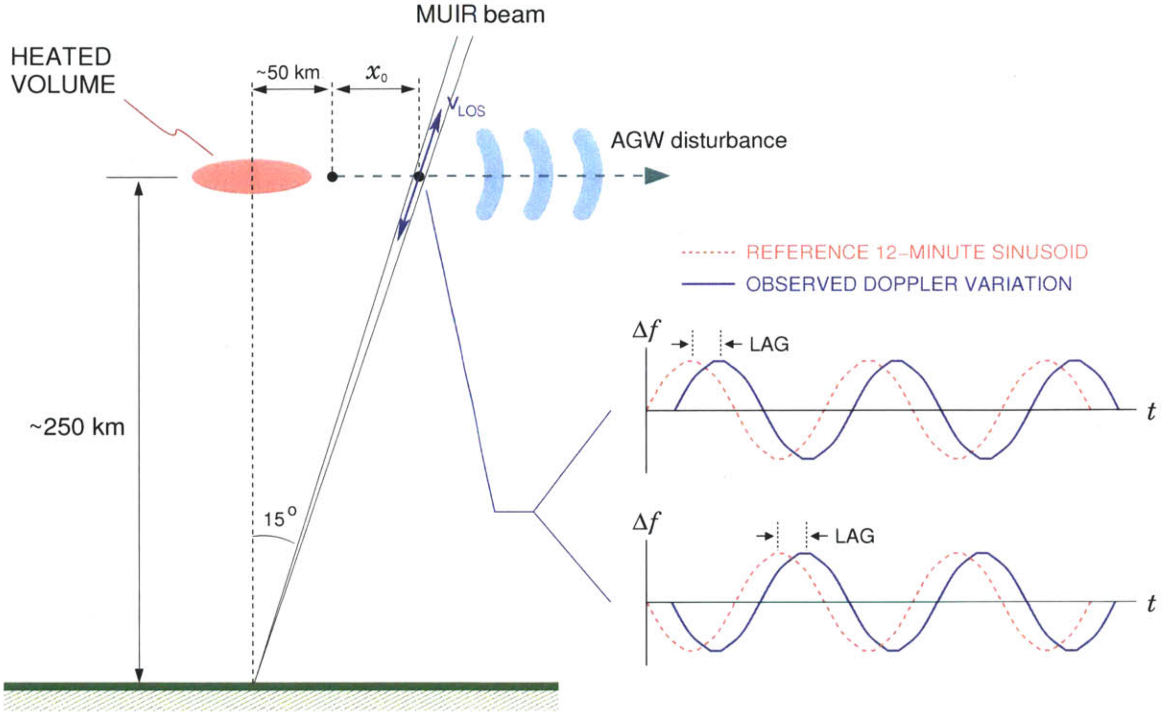

Figure 9-3: A diagram illustrating the diagnostics of heater-generated AGWs/TIDs at HAARP using MUIR radar, through the detection of periodic time variation of the LOS velocity. Since the radar beam points outside the heated plasma volume, we may expect a slight time lag in the observed oscillatory LOS Doppler velocity.

We will now discuss the use of MUIR radar data to estimate the propagation speed of heater-generated AGW/TID at HAARP. As elaborated previously in Chapter 5, the characteristic signatures of HAARP-AGW appear in the MUIR radar data as a periodic time variation of the ion line Doppler shift. This pattern arises because there are some periodic fluid velocity fluctuations associated with the AGW. During our experiments, the MUIR radar beam points well outside the heated region; and thus there could be a significant time delay between the AGW/TID generation by the heated plasma volume and the subsequent detection at the MUIR diagnostic beam. The overall concept is illustrated schematically in Figure 9-3.

As depicted in the diagram, the heated plasma volume is located at an altitude of approximately 250 km and the MUIR radar beam points at 15° from the vertical. Hence, at ~250 km the MUIR beam is approximately $250\,\text{km} \times \tan 15^\circ = 67$ km from the center of the heated region. Furthermore, from the wave kinematics analysis of LEO satellite data (c.f. section 7.1 in Chapter 7) we know that AGW/TID are generated at the *edge* of the heated region — roughly 50 km from the center point. Hence, in this case the heater-generated AGW disturbances must cover a distance of approximately $x_0 = 67 - 50 = 17$ km from being produced by the pulsating heated region until finally being detected by the MUIR diagnostic beam. If we can determine the time lag τ_0 of the observed LOS Doppler variation in the MUIR radar data (relative to a reference sinusoid based on the heating cycle), then we should be able to estimate the propagation speed of the artificial AGW/TID generated from the heated plasma volume. However, as indicated by the diagram in Figure 9-3, there is no clear up/down preference for the starting direction of the oscillatory LOS Doppler velocity fluctuations. We must therefore consider both possibilities in each individual experiment, and then uphold the one case that yields a causal time lag.

By setting the time offset in a way that the sinusoidal heater power modulation cycle starts precisely at $t = 0$, then the oscillatory Doppler variation recorded in the MUIR radar data would be given by $\Delta f \sim \pm \sin\left[\Omega(t - \tau_0)\right]$ while the reference sinusoid is simply $s_{\text{ref}}(t) \sim \pm \sin \Omega t$. In order to determine the time lag τ_0, we are going to examine the complex phase angle in the Fourier spectra. Specifically, we will compare the complex phase angle of the Doppler shift time series relative to the complex phase angle of the reference sinusoid. Furthermore, since the Doppler shift time series is lagging behind the heating cycle, it is also expected that the Doppler shift time series would have a smaller complex phase angle than that of the reference sinusoid. In other words, the oscillatory Doppler variation in MUIR data can be expressed as $\Delta f \sim \pm \sin(\Omega t + \Delta\varphi)$ with a relative phase difference $\Delta\varphi < 0$ for a causal time lag. With the relative phase angle $\Delta\varphi$ known, the propagation speed can then be written simply as follows:

$$c_w = \frac{x_0}{\frac{|\Delta\varphi|}{360^\circ} \cdot T}$$

where $T \equiv 2\pi/\Omega = 12$ minutes is the period of the heater power modulation cycle in our experiments. In the above expression, note that the relative phase angle $\Delta\varphi$ is given in unit of degrees.

Figure 9-4 shows a set of Doppler time series derived from the MUIR radar data during one of the HAARP-AGW experiments, together with its Fourier spectrum. The top panel shows the Doppler time series, the middle panel shows the Fourier power spectrum, and the bottom panel shows the Fourier phase angle spectrum (relative to the reference sinusoid). The heater modulation cycle during the experiment has a period of $T = 12$ minutes, which corresponds to a frequency of $f \approx 1.39$ mHz. We can see a sharp peak at ~1.4 mHz in the Fourier power spectrum plot, indicating a periodic time variation in the Doppler shift with a period close to 12 minutes. Moreover, the negative-valued relative phase angle ($\Delta\varphi \approx -116.9°$) at this frequency indicates a lag of $\tau_0 \approx 233.9$ sec between the observed Doppler variation and the power modulation cycle. This much time lag to cover a distance of $x_0 \approx 17$ km corresponds to an AGW propagation speed of $c_w \approx 72.7$ m/s.

Furthermore, below is a short list summarizing the successful cases of our Fourier spectrum analysis from the experimental measurements using MUIR radar:

Experiment Date/Time		$\Delta\varphi$ (deg)	c_w (m/s)
29 Jul 2008	03:00–04:12 UTC	−112.05°	75.86 m/s
30 Jul 2008	04:00–05:12 UTC	−103.15°	82.40 m/s
6 Aug 2009	00:00–02:10 UTC	−108.66°	78.22 m/s
14 Aug 2009	00:05–01:39 UTC	−107°	79.44 m/s
14/15 Aug 2009	23:30–01:30 UTC	−116.94°	72.69 m/s

From the above list, the mean propagation speed is 77.72 m/s with a standard deviation of 3.67 m/s. Meanwhile, the median of the inferred propagation speed is 78.22 m/s with an interquartile range of 3.58 m/s. Hence, we can conclude that the MUIR radar data gives an overall estimate of 78 ± 4 m/s for the propagation speed of the heater-generated artificial AGW/TID.

In summary, the estimated propagation speed of the heater-generated artificial AGW/TID seems to match the typical value of the propagation speed of MSTIDs in general. Based on the analysis of our TEC data (using GPS and LEO satellites) and ground-based measurements (using digisonde and MUIR), the calculated propagation speed ranges from a few tens of m/s up to around 150 m/s.

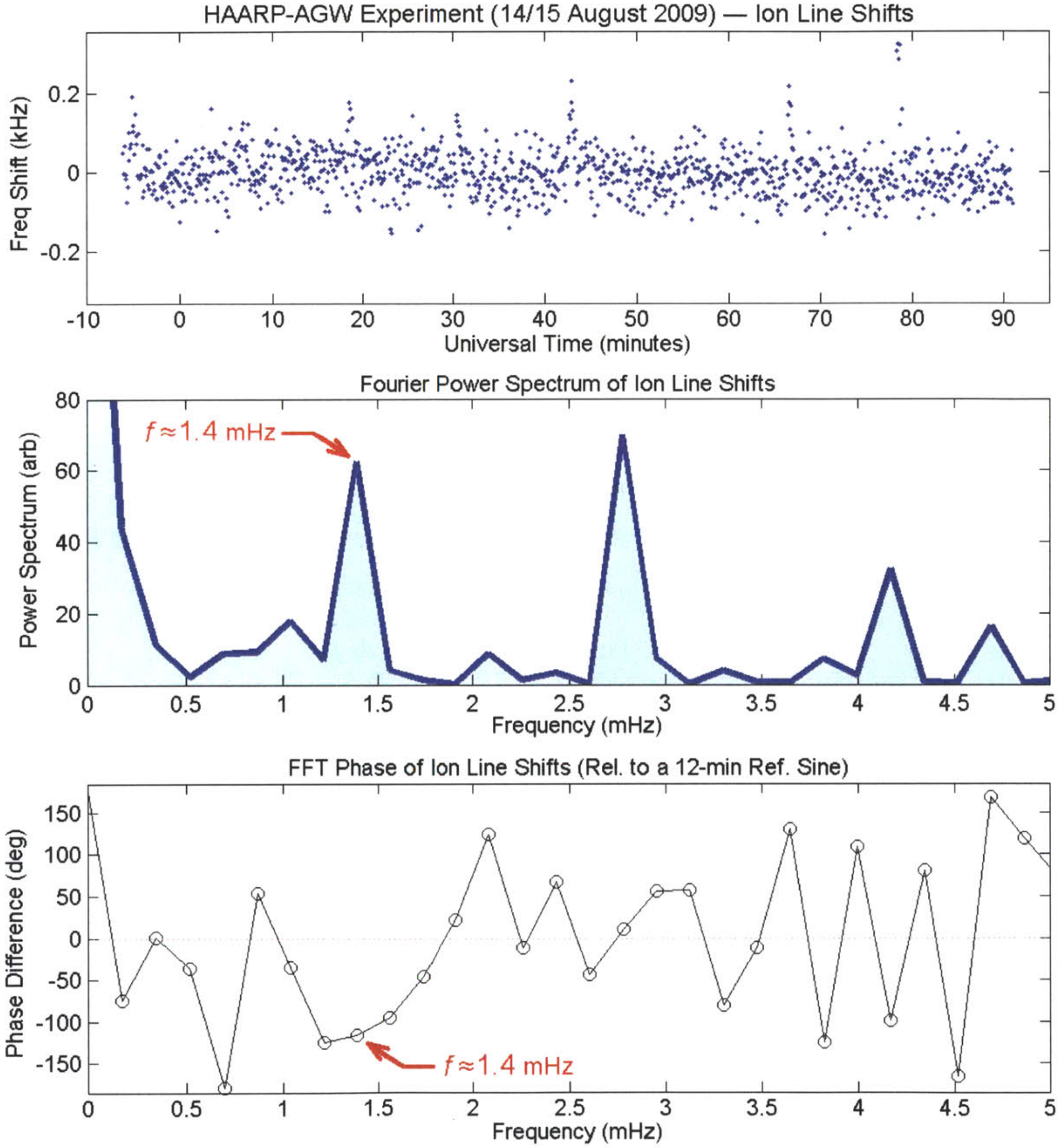

Figure 9-4: A set of MUIR LOS Doppler data from the HAARP-AGW experiment, 23:30–01:30 UTC on 14/15 August 2009. Shown are the Doppler time series (top), the power spectrum of its Fourier components (middle), and the corresponding relative phase angle spectrum (bottom).

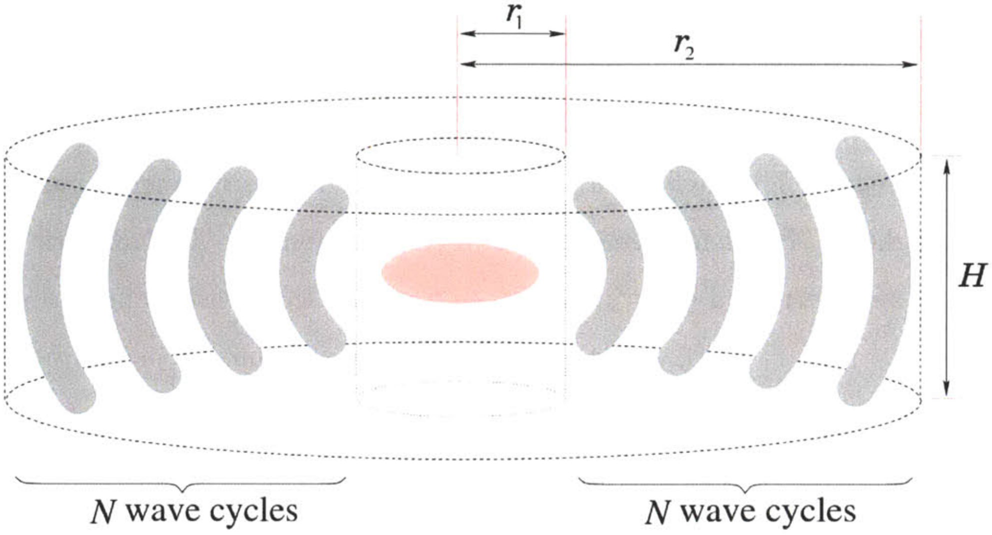

Figure 9-5: A schematic illustration of the specified integration volume for the HAARP-AGW empirical energy budget calculation.

9.2 Efficiency of HAARP-AGW Generation

The final topic for our discussion is the overall energy efficiency of the physical process responsible for generating the artificial AGW/TID in our HF heating experiments. In order to compute this efficiency, we would have to calculate the mechanical energy associated with the AGW disturbances that are being radiated out from the heated region, and then compare it to the total transmitted energy from the HF heater. In this energy budget calculation, we are going to make use of the following expression for the AGW energy density [*Watada*, 2009]:

$$E(\omega, k) = \left[\frac{\omega_g^2 k^2}{\omega^2} - \frac{\omega^2}{c_s^2}\right] \frac{P\,P^*}{(\omega_g^2 - \omega^2)} \tag{9.1}$$

where $P \equiv \delta p/\sqrt{\rho_0}$ is the scaled pressure fluctuations associated with the AGW (with ρ_0 being the background mass density of the neutrals), ω_g is the Brunt-Vaisala frequency, c_s is the adiabatic sound speed, whereas ω and k denote the frequency and the wavenumber of the AGW, respectively. The dimension of $E(\omega, k)$ itself is energy per unit volume (unit is e.g. $\mathrm{J/m^3}$). The total mechanical AGW energy can be readily obtained by integrating $E(\omega, k)$ over the volume occupied by the heater-generated AGW/TID. This integration volume is illustrated schematically in Figure 9-5.

The torus-shaped integration volume for this energy budget calculation has an inner radius r_1, outer radius r_2, and height H. The inner radius $r_1 \approx 50$ km signifies the location at the edge of the heated region where AGW/TID are being generated initially (c.f. section 7.1 in Chapter 7), and the outer radius r_2 corresponds to how far away the AGW/TID had spread out at a certain moment. The numerical value for r_2 has to be determined experimentally on a case-by-case basis. Furthermore, for the propagation from r_1 to r_2, we assume that wave dissipation is generally negligible. Meanwhile, we had selected the height H to be the vertical scale height of the atmosphere (also in the same order of magnitude as the thickness of ionospheric F-layer). Numerically, $H \equiv k_B T_0/Mg \approx 40$ km.

Although we have an analytical expression for the AGW energy density $E(\omega, k)$, there is a problem because we actually do not have any direct measurement of the pressure fluctuations. Instead, what we have are the TECP measurements from LEO satellite passes during/after the HAARP-AGW experiments. Thus, for practical reasons, we would like to be able to express the AGW energy density $E(\omega, k)$ in terms of the TECP. It turns out that we can achieve this objective by assuming that the fractional density fluctuation in the neutral is approximately equal to the fractional fluctuation in both plasma density as well as the TEC. In other words, we are assuming:

$$\frac{\delta n}{n_0} \approx \frac{\delta n_e}{n_e} \approx \frac{\text{TECP}}{\text{TEC}}$$

which implicitly also means that the actual value of these fractional fluctuations is approximately constant with altitude. Within our integration volume, which is only about 40 km thick, this assumption certainly seems to be a quite reasonable one. Using the ideal gas law together with the above assumptions, the scaled pressure fluctuations P can then be re-expressed as follows:

$$P \equiv \frac{\delta p}{\sqrt{\rho_0}} = \gamma k_B T_0 \sqrt{\frac{n_0}{M}} \cdot \frac{\delta n}{n_0} \approx \gamma k_B T_0 \sqrt{\frac{n_0}{M}} \cdot \frac{\delta n_e}{n_e} \approx \gamma k_B T_0 \sqrt{\frac{n_0}{M}} \cdot \frac{\text{TECP}}{\text{TEC}}$$

which will enable us to have an expression for the AGW energy density $E(\omega, k)$ in terms of relative fluctuations in the TEC. The background neutral density n_0

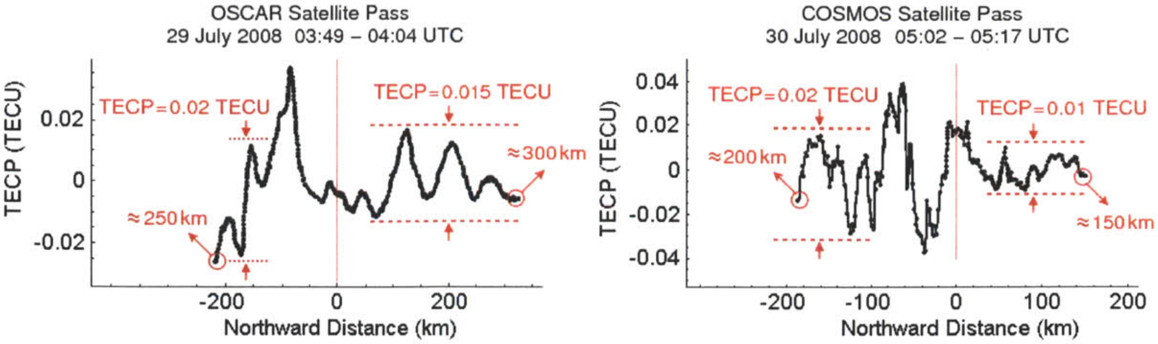

Figure 9-6: A summary of TECP measurements during HAARP-AGW experiments, from OSCAR satellite pass (29 July 2008) and COSMOS satellite pass (30 July 2008).

and temperature T_0 will be estimated using the NRL MSIS-E atmospheric model. Furthermore, we will only consider atomic oxygen molecules at this altitude.

Figure 9-6 shows the two sets of TECP data from LEO satellite measurements that we are going to use for this energy budget calculation. We can see here that the observed TECP signal typically has an amplitude of 0.01–0.02 TECU. In the meantime, the background TEC value must be computed directly using the plasma density profile obtained from ionogram (i.e. reflectometry) measurements.

Furthermore, we are still going to need the wavenumber k, the sound speed c_s, and the Brunt-Vaisala frequency ω_g for computing the AGW energy density $E(\omega, k)$. To obtain the wavenumber $k \equiv \frac{2\pi}{\lambda}$, we will first have to estimate the AGW wavelength based on the total distance covered by all of the completed wave cycles. To be specific, it is going to be computed as $\lambda = \frac{1}{N}(r_2 - r_1)$ where N denotes the total number of wave cycles that fit within the experimental time window. Meanwhile, the adiabatic sound speed c_s ($\equiv \sqrt{\frac{\gamma k_B T_0}{M}}$) and the Brunt-Vaisala frequency ω_g will be calculated at an appropriately selected altitude z_0 using the NRL MSIS-E atmospheric model. For a more detailed description on our numerical calculation of the Brunt-Vaisala frequency in the ionosphere, please see Appendix B of this thesis.

As a final step in calculating the overall efficiency of HAARP-AGW generation, we have to normalize the total mechanical AGW energy with respect to the total transmitted energy from the HF heater. Even though the maximum/peak power of HAARP heater is 3600 kW, the net transmitted heater power in our experiment is actually $\frac{1}{2} \times 3600$ kW $= 1800$ kW because we are modulating the transmitted heater power sinusoidally between zero and maximum power. Multiplying the net transmitted power by the duration of the experiment Δt will thus give us the total transmitted energy needed for this efficiency calculation.

Table 9.1: Energy conversion efficiency calculation for the AGW generation process, based on the LEO satellite pass data depicted in Figure 9-6.

	OSCAR Sat. (29 July 2008)		COSMOS Sat. (30 July 2008)	
	SOUTH SIDE	NORTH SIDE	SOUTH SIDE	NORTH SIDE
TECP	≈ 0.02 TECU	≈ 0.015 TECU	≈ 0.02 TECU	≈ 0.01 TECU
TEC	≈ 4.1 TECU†	≈ 4.1 TECU†	≈ 3.8 TECU†	≈ 3.8 TECU†
r_1	≈ 50 km†	≈ 50 km†	≈ 50 km†	≈ 50 km†
r_2	≈ 250 km	≈ 300 km	≈ 200 km	≈ 150 km
N	$= 5$ cycles†	$= 5$ cycles†	$= 6$ cycles†	$= 6$ cycles†
λ	≈ 40 km	≈ 50 km	≈ 25 km	≈ 16 km
z_0	≈ 190 km†	≈ 190 km†	≈ 210 km†	≈ 210 km†
T_0	≈ 750 K†	≈ 750 K†	≈ 775 K†	≈ 775 K†
Δt	≈ 60 min†	≈ 60 min†	≈ 72 min†	≈ 72 min†
η	$\approx 29.9\%$	$\approx 15.6\%$	$\approx 51.3\%$	$\approx 16.7\%$
η_{avg}	$= 22.8\%$ (average value)		$= 34\%$ (average value)	

†The same value is applicable for both the South and North sides in a given satellite pass. TEC and z_0 are calculated numerically using the ionogram data; the nominal value for r_1 comes from our wave kinematics analysis; the duration of the experiment determines the values of N and Δt; background temperature T_0 is taken from the MSIS-E model.

Our calculations for the efficiency of HAARP-AGW generation are summarized in Table 9.1. As also hinted by the data plots shown in Figure 9-6 earlier, we are using the TECP data from two LEO satellite passes (OSCAR and COSMOS satellites) during the HAARP-AGW experiments conducted on 29 & 30 July 2008. In each respective LEO satellite pass, we have the TECP ripple pattern on both sides of the heated region. Since there is a possible distortion arising from the background neutral wind, we had decided to carry out the energy budget calculation for each side separately. After averaging the individual results obtained from each side of the heated region, we finally found an overall efficiency in the range of $\eta = 23\%$–34%.

We have just worked out the overall efficiency of the HAARP-AGW generation. The numerical estimate that we obtained for this efficiency is:

$$\eta \equiv \frac{[\text{MECHANICAL AGW ENERGY}]}{[\text{TOTAL TRANSMITTED ENERGY}]} \approx 23\% - 34\%$$

based on the observed amplitude of the resulting TEC fluctuations recorded during LEO satellite pass over HAARP. Now, we would also like to find out if this efficiency estimate can be used to infer some additional information about the heated region itself. By considering the heated region as a form of heat engine that performs some mechanical work (i.e. generating AGW/TID) from the input heat (i.e. RF energy deposited into the plasma), it turns out that we can actually infer the temperature of the heated region. Below, we shall elaborate on this idea and carry out the calculation.

Viewing the HAARP-heated region as a heat engine that operates with a hot reservoir at temperature T_H and a cold reservoir at temperature T_C, then we know that the actual efficiency cannot exceed the Carnot limit:

$$\eta_{\text{EXPT}} \leq 1 - \frac{T_C}{T_H}$$

The hot reservoir of this heat engine would be the interior of the heated region, while the cold reservoir would be the surrouding area where "waste heat" diffuses away. Experimentally, we have determined that $\eta_{\text{EXPT}} \approx 23\%$–$34\%$ and thus we can put a bound on the value of T_H/T_C:

$$\frac{T_H}{T_C} \geq \frac{1}{(1 - \eta_{\text{EXPT}})}$$

The estimate $\eta_{\text{EXPT}} = 23\%$ gives a bound of $T_H \geq 1.3\,T_C$, and $\eta_{\text{EXPT}} = 34\%$ gives $T_H \geq 1.5\,T_C$. Assuming that the HAARP-heated region was originally at an initial equilibirum temperature roughly equal to the ambient temperature, then the cold reservoir temperature T_C may be taken as equal to this initial temperature as well.

We can therefore infer that the temperature of the HAARP-heated region during our experiments is at least 1.3–1.5 times its initial unheated temperature.

Our estimate of $\delta T \gtrsim 0.3\,T_0 \sim 0.5\,T_0$ at HAARP is quite reasonable compared to several direct ion/neutral temperature measurements at other HF heating facilities. From EISCAT facility in Tromso, Norway, *Rietveld et al.* [2003] had reported an ion temperature increase of $\delta T_i \approx 0.6\,T_{i0}$ during the HF heating experiments there. Meanwhile, *Gonzalez et al.* [2005] had reported ion/neutral temperature increase of $\delta T \approx 0.5\,T_0$ during HF heating experiments at Arecibo Observatory, Puerto Rico. Both of these temperature measurements were made through incoherent scatter radar (ISR) observations. It should be noted that these HF heating facilities are similar to HAARP in terms of their operating frequencies, but their total transmitter power (still in the ~MW range) is slightly less than that of the HAARP heater [see e.g. *Stubbe et al.*, 1982; *Lunnen et al.*, 1984].

Although there has not been any ISR measurements of ion/neutral temperature inside the HAARP-heated region, *Milikh et al.* [2008] had reported ion temperature measurements using DEMETER satellite (orbiting at an altitude of ~670 km) over the HAARP facility. When the HAARP heater is operating at full power, their observations suggest an ion temperature increase in the range of $\delta T_i \approx 0.3\,T_{i0}$ up to $\delta T_i \approx 2\,T_{i0}$ in some cases. Once again, these reported values generally agree with our simple temperature estimate based on the thermodynamic Carnot efficiency of HAARP-AGW generation.

Chapter 10

Conclusions

In this thesis, we have investigated the potential role of large-scale anomalous heat sources (e.g. heat wave events) in influencing our space plasma environment through the generation of acoustic-gravity waves (AGW) which might subsequently induce some traveling ionospheric disturbances (TID) over an extensive region. As part of our investigation, we conducted a case study on the summer 2006 North American heat wave event and carried out a series of field experiments at the High-frequency Active Auroral Research Program (HAARP) facility. It is suspected that, as the summer 2006 North American heat wave swept south-eastward across the continent, the dynamical changes / temporal evolution of the associated thermal fronts caused some AGWs to be generated and then triggered intense TIDs over the region. Our field experiments at the HAARP facility is aimed at physically simulating this AGW/TID generation process by creating a sinusoidally time-varying artificial thermal gradient at ionospheric height using HAARP's high-power HF transmitter array. It should be noted that a purely static thermal front probably would not be as effective in generating AGWs.

Through this investigation, we have been able to obtain a number of positive indications that large-scale thermal fronts associated with intense and prolonged heat wave events could potentially generate some AGWs capable of triggering ionospheric plasma disturbances over extended areas. Our Madrigal GPS TEC data analysis over the North American sector during the summer 2006 heat waves had shown a quite affirmative correlation between the heat wave event and the increasing TID activity. Meanwhile, our field experiments at the HAARP facility had also demonstrated that sinusoidally time-varying thermal gradients are indeed capable of generating some artificial AGW/TID in the ionosphere.

Although so far we have achieved quite satisfactory results in the HAARP-AGW experiments, there is certainly some room for improvements. The rather obvious targets for future improvement are on the optimal use of radio diagnostic instruments, and the inclusion of optical airglow measurements. The details about some of the specific points to be improved in future experiments can be found below:

- **Digisonde Skymap Data.** For the skymap data acquisition, so far the HAARP digisonde had only been configured to record return echoes in O-mode polarization. According to our ray tracing studies (see Appendix E), skymap echoes in X-mode polarization may be able to reveal certain characteristics of the ionospheric layer not discernible otherwise. With the prospect of a better characterization of the heater-generated AGW/TID, it would be advantageous to record skymap data in both O-mode and X-mode polarizations.

- **Airglow Measurements.** So far, we have not been able to perform airglow measurements during the HAARP-AGW experiments. The main reason is that, optical instruments for airglow measurements can only be operated during the nighttime (to avoid damage to the photomultipliers) while we had to perform the HAARP-AGW experiment during the daytime only (to ensure a sufficiently high plasma density during the solar minimum). Hence, if conditions allow (possibly during solar maximum or at other heating facilities), it is preferable to perform this experiment at night along with some airglow diagnostics.

In general, we are looking for improvements that would allow for a better diagnostics of the heater-generated artificial AGW/TID. Because the data from certain radio diagnostic instruments (e.g. digisonde skymaps or ionograms) might be intrinsically non-intuitive to interpret due to strong refraction of the rays, the availability of some optical diagnostic instruments would be extremely helpful. Hopefully, we are going to be able to further verify the results of HAARP-AGW experiments in physically simulating the role of large-scale thermal fronts in generating AGW/TID.

To a certain extent, these experimental findings might bring forward a number of new realizations on what could be affecting our space environment. In most cases, dramatic occurrences of extremely intense AGW/TID had been associated with many types of catastrophic and impulsive events such as: earthquakes, tsunamis, volcano eruptions, thermonuclear device detonations, or strong geomagnetic storms due to massive coronal mass ejections (CMEs), etc. Such events would generally produce severe ionospheric disturbances that last only for a relatively short period of time (1–2 days at most). On the other hand, large-scale thermal gradients associated with prolonged heat wave events would only generate ionospheric disturbances with a relatively moderate intensity, but might last for a significantly longer time period (∼several weeks). Because of its moderate intensity, AGW/TID from large-scale thermal fronts might not be a cause for immediate concern and there is no real need for us to be wary at this point. However, we still have to keep an eye on this phenomenon because some climate models have in fact predicted that a warmer earth climate could potentially lead to a more frequent, more intense, and longer-lasting heat waves in the future [*Meehl et al.*, 2004]. Therefore, in the face of global climate change, anomalous large-scale natural heat source might be steadily gaining quite an important role in influencing our space environment.

Appendix A

Madrigal GPS-TEC Data Analysis

We have been using the Madrigal GPS TEC data extensively in our investigation of the possible connection between prolonged severe heat wave events and the potential increase in the level of ionospheric plasma disturbances (discussed in Chapter 2). The GPS-derived TEC data from the worldwide GPS receiver network is especially useful for monitoring the ionospheric plasma condition over an area for a long period of time. In our particular case, we are interested in measuring the level of ionospheric disturbances over the North American sector. In order to measure the level of ionospheric plasma disturbances, we will needfully have to compute the TEC perturbation (TECP) signal using the absolute TEC data.

Here, first of all, we are going to describe a relatively simple and reliable method for calculating the TECP signal from the absolute TEC data. We will then discuss a practical use of the TECP data analysis in our case study of the summer 2006 North American heat wave event. In this case study, we will present some additional details which were not mentioned previously in Chapter 2.

A.1 TECP Calculation

The Madrigal database provides us with measurements of absolute TEC values at various geographical coordinate as a function of time. In the dataset, a 24-hour period is divided into 288 5-minute blocks, and the spatial coordinate is discretized into 1° × 1° latitude and longitude grid. For every 5-minute block, we are given a snapshot of the recorded TEC values in each of these latitude/longitude bins. Note also that some latitude and longitude bins might not have data coverage (i.e. blind spot). For our study of ionospheric disturbances, we need to compute the TECP as a function of both space and time — using the given absolute TEC measurements.

In general, TECP may be defined as the deviation of the actual TEC value from the equilibrium/background value. Using the given absolute TEC data, there are several possible ways to estimate what the "background TEC" value should be. We are going to discuss some of these methods, including the one that we had finally employed in our data analysis.

One way to determine the "background TEC" is by taking a climatic average. This method could potentially be very thorough and rigorous, but unfortunately it requires large amount of data that span over many years in order to yield an accurate estimate. In addition to the regular diurnal variation, there could be some seasonal variation in the TEC value as well. Thus, we cannot simply average over a one-year data to obtain one single representative "background TEC" value. Instead, we will have to build up a "quiet day curve" of absolute TEC values over several-year period. For efficiency reason, we decide not to employ this climatic average method.

Another approach is to infer the spatial distribution of "background TEC" using individual snapshot of absolute TEC values over certain region, one instant at a time. In this particular approach, we will (1) take a snapshot of the TEC values as a function of the geographical coordinate at a given instant, (2) infer the spatial distribution of "background TEC" as a function of latitude/longitude via smoothing or fitting, (3) subtract the estimated spatial distribution of "background TEC" from the original absolute TEC snapshot, and (4) repeat for all other instants. This method might involve fitting a surface (absolute TEC as a function of latitude and longitude), which might be quite cumbersome in general. It is desirable to keep things simple, and thus we decide not to employ this method for calculating TECP.

Finally, we can also try to infer the "background TEC" by estimating its diurnal variation at a given geographical coordinate (latitude and longitude), one location

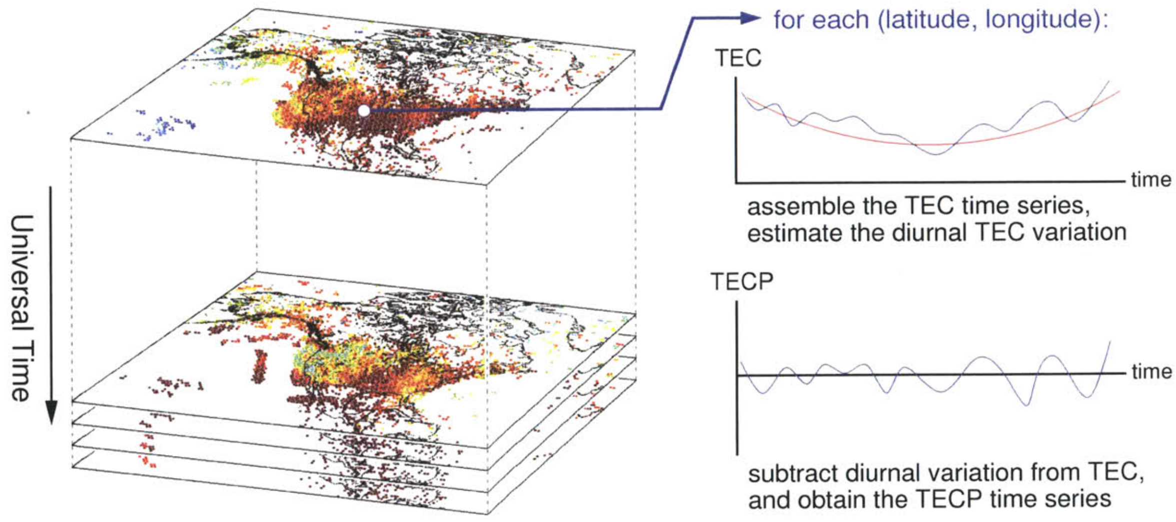

Figure A-1: A schematic illustration of the TECP calculation procedures for our analysis of the Madrigal GPS TEC data.

at a time. In this last-ditch approach, we will (1) select a relevant geographical coordinate, (2) assemble the time series of absolute TEC values at this given location, (3) estimate the diurnal TEC variation from this time series via a polynomial fit, (4) subtract the estimated diurnal variation curve from the absolute TEC time series to obtain TECP, and (5) repeat for all other coordinate locations. This method is relatively straightforward to implement because it only involves 1-D curve fitting. For practical reasons, we finally decide to employ this method for calculating the TECP signal from the absolute TEC data.

A schematic illustration of the favorably selected TECP calculation procedure is depicted in Figure A-1. As mentioned before, the diurnal TEC variation is inferred using a polynomial fit. The polynomial degree for the curve fitting is adjustable, but so far we have obtained satisfactory results with a 10th order polynomial function. For all of our analysis, we have used the same polynomial order to estimate the diurnal TEC variation in our TECP calculation procedure.

To further ensure an accurate estimate of the diurnal variation, we decide to pad the daily TEC time series at the beginning (00:00 UT) and the end (24:00 UT) using 3-hour segment of previous day's data and next day's data, respectively. In addition, we also try to prevent some occasional outliers from affecting our diurnal variation

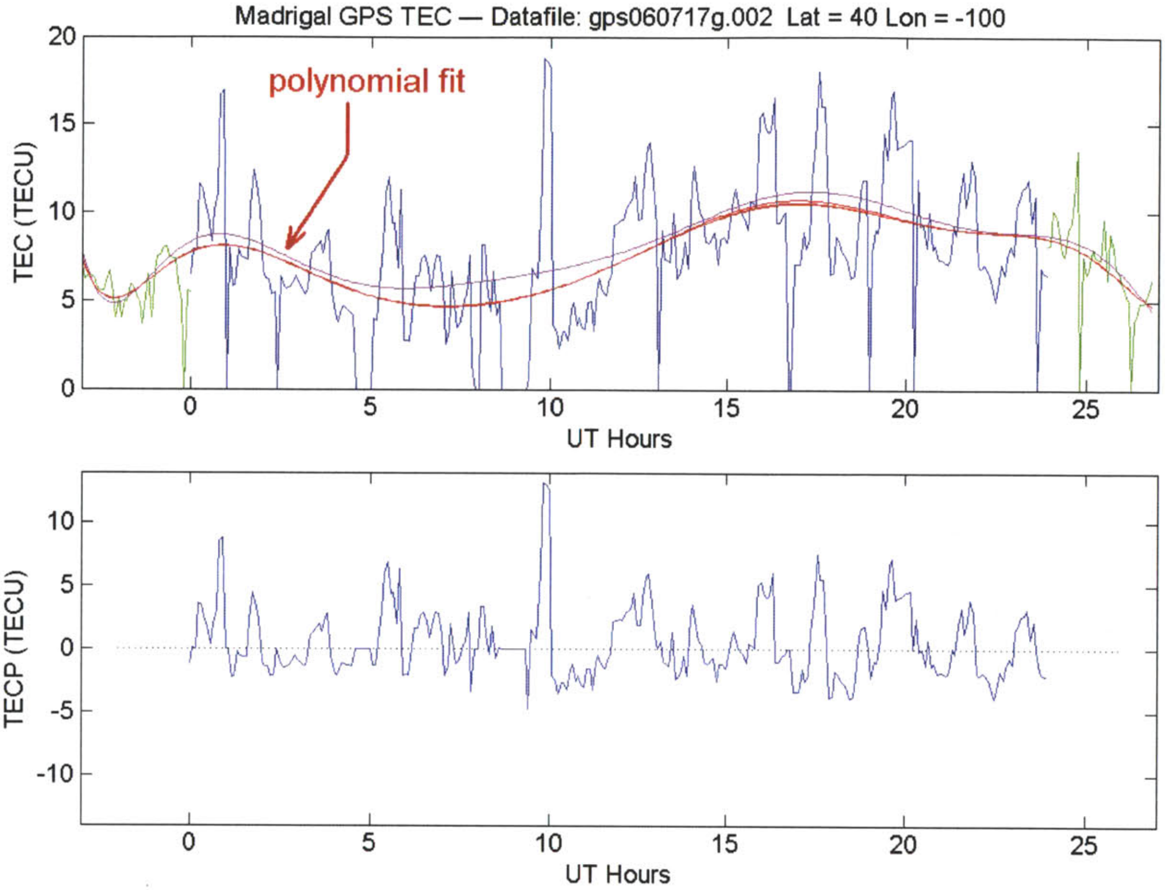

Figure A-2: A sample TEC time series along with the polynomial fit as an estimate of the diurnal TEC variation at a given geographic coordinate (top), and the resulting TECP time series signal (bottom). The TEC signal is padded at both the front and the back (green traces), and the polynomial fitting process is iterated to systematically exclude outliers/spikes (the initial guess is purple, converging into the red curve).

estimates. We implement this objective by iterating the polynomial fit a few times after systematically excluding the suspected outlier data points (the ones that result in |TECP| > 5 TECU). This strategy generally works well because outliers in the TEC data often appear in the form of sharp spikes.

A representative example of the working procedure for estimating the diurnal TEC variation and calculating the TECP signal can be found in Figure A-2. The top panel shows the absolute TEC time series, together with the estimated diurnal TEC variation. The initial estimate is shown as a purple polynomial curve. The iterated polynomial fit eventually converges into the red curves after the outlier points had been excluded. The resulting 24-hour TECP signal is depicted on the bottom panel.

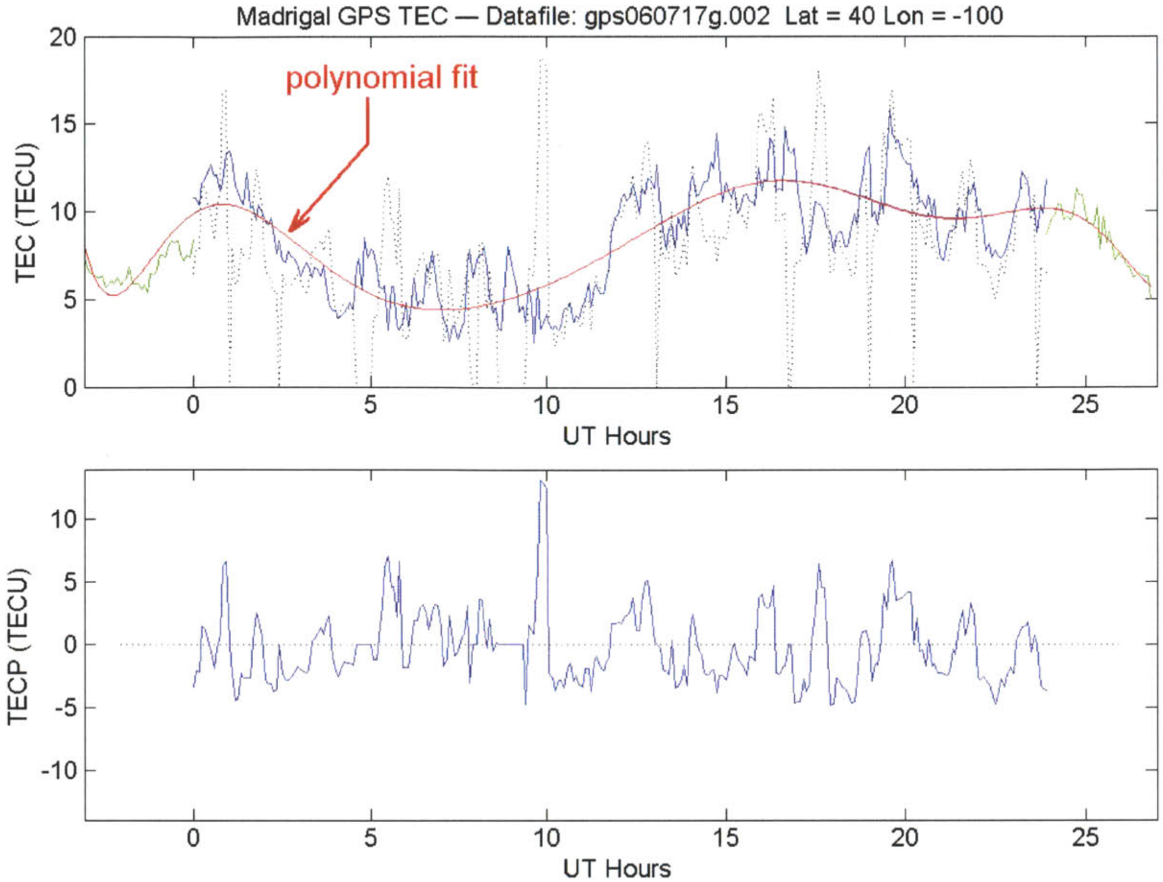

Figure A-3: Essentially the same as in Figure B-2, but this time we perform the polynomial fit to a smoothed version (via spatial averaging) of the TEC time series. On the top panel, dotted black trace is the original TEC signal and solid blue trace is the smoothed TEC signal. The bottom panel shows the resulting TECP time series.

As an alternative approach, we also try to mitigate the adverse effects of outlier data points via some spatial averaging. In this case, we perform a running median (using 3° × 3° lat/lon window) on the original absolute TEC data to try to eliminate sharp spikes. We then perform the polynomial fit on the TEC time series from the spatially-smoothed data. Like previously, the estimated diurnal TEC variation will then be subtracted from the original TEC time series to calculate the TECP.

Figure A-3 shows an example of this refined procedure for estimating the diurnal TEC variation and calculating the TECP. In this case, evidently there is no need to iterate the polynomial fit anymore. Note that the estimated diurnal variation is then subtracted from the original TEC time series (not the spatially-smoothed one).

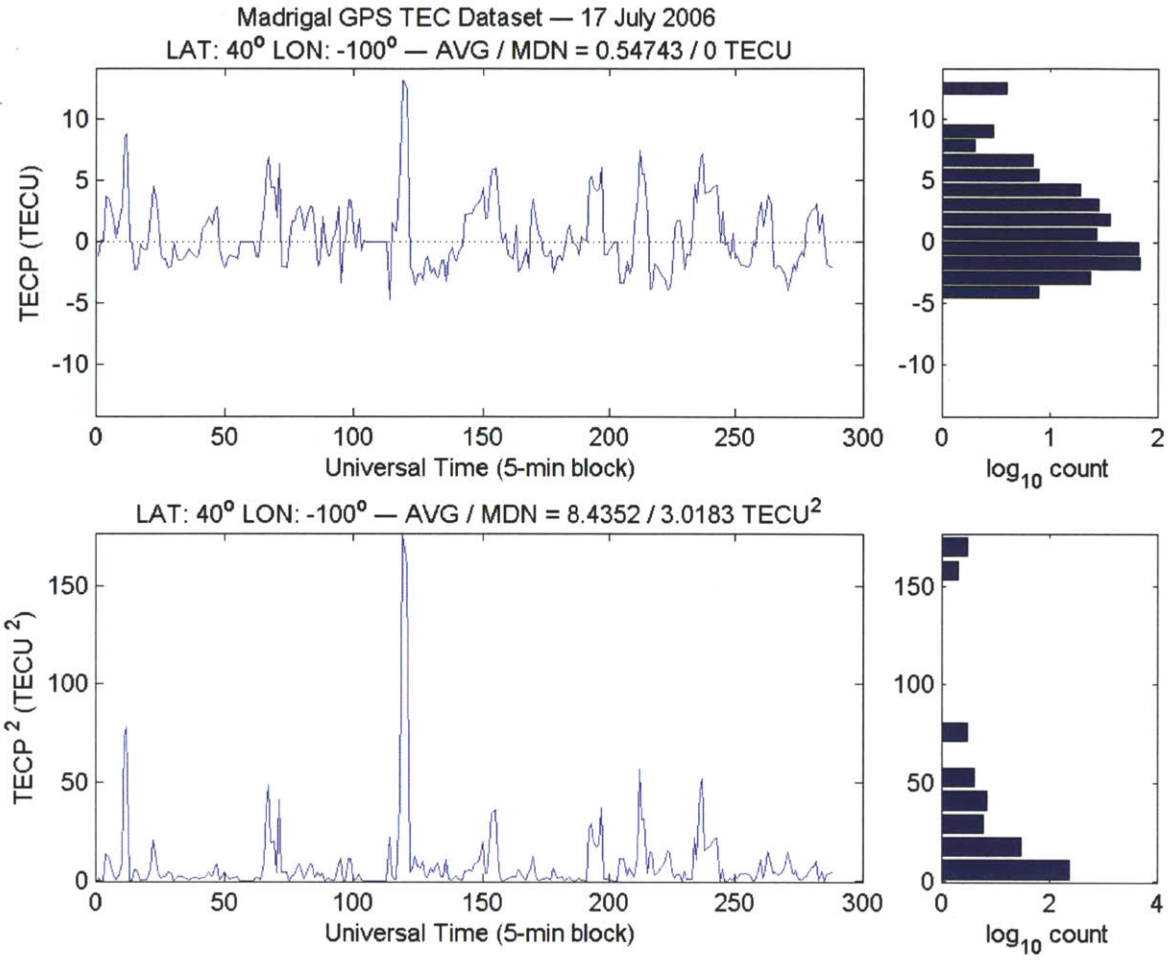

Figure A-4: A sample set of TECP and squared-TECP time series signal from a given geographic coordinate, along with the distribution histogram of their values.

Now that we have a 24-hour TECP signal for all latitudes/longitudes from each day's data, we would like to have a quantitative measure for the average level of fluctuations that exist in the TECP signal. This is going to be useful for our goal to monitor TID activity over a long period of time. Figure A-4 shows the statistical properties of both the TECP signal and the squared-TECP signal for a given 24-hour period. We see that the histogram for the TECP signal values is slightly skewed towards the positive side, and the histogram for the squared-TECP signal values seems to have a very long tail. Therefore, rather than using the root-mean-square value, it is probably better to use the root-median-square value of the TECP signal as a measure for the daily average of TECP fluctuations. In our discussions, "RMS" shall mean "root-median-square" onless otherwise noted.

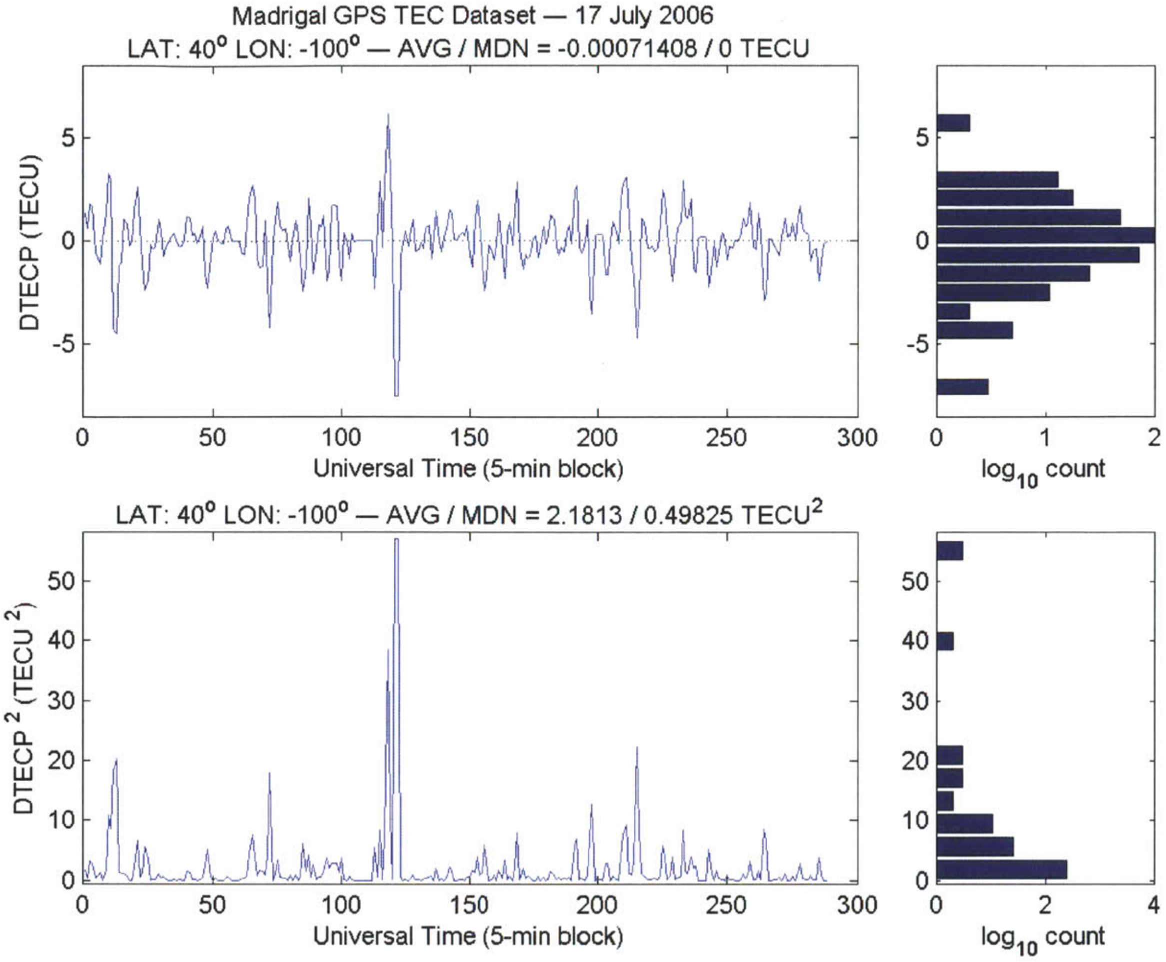

Figure A-5: A sample set of DTECP and squared-DTECP time series signal from a given geographic coordinate, along with the distribution histogram of their values.

In addition to the TECP signal, we also decide to compute the time-differenced TECP signal — i.e. the differential TECP (DTECP) signal. The DTECP signal is proportional to the time rate of change in TECP — the proportionality constant being the time step Δt (= 5 min, in our case). Figure A-5 shows the statistical properties of both the DTECP signal and the squared-DTECP signal for a given 24-hour period. We see that the histogram for the DTECP signal values is generally less skewed compared to that for the TECP signal. Nonetheless, the histogram for the squared-DTECP signal values also has a quite long tail — just like the squared-TECP signal values. Although not an entirely independent quantity, we hope that the DTECP signal would be able to complement the TECP signal in some ways.

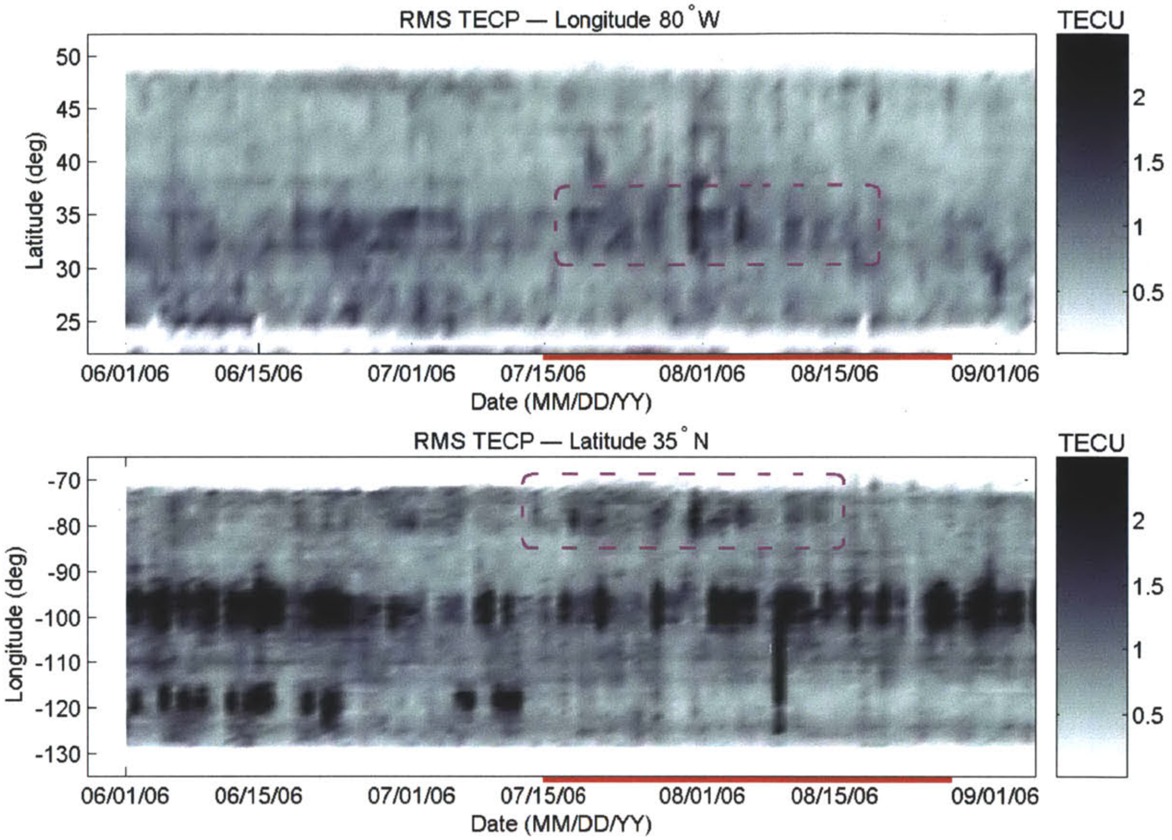

Figure A-6: Time evolution of the latitudinal/longitudinal slice of RMS DTECP values over a selected region over North America in the summer 2006. The heat wave period is highlighted in red on the time axis.

A.2 Case Study of Summer 2006 Heat Wave

As an application of this TECP calculation procedure, we will present a case study on the summer 2006 North American heat wave event. In particular, we will present some additional details which were not mentioned previously in Chapter 2.

For the purpose of surveying the data, we realized that it would be useful to plot the time evolution of certain longitudinal/latitudinal slice of the RMS TECP and RMS DTECP data. This approach is very similar to the use of *keogram* plots for surveying all-sky airglow measurements [see e.g. *Eather et al.*, 1976]. Figure A-6 shows the time evolution of selected latitudinal/longitudinal slice of the summer 2006 RMS TECP data over North America. Here, some increase in the RMS TECP values during the heat wave period can be identified around lat 35°N and lon 80°W.

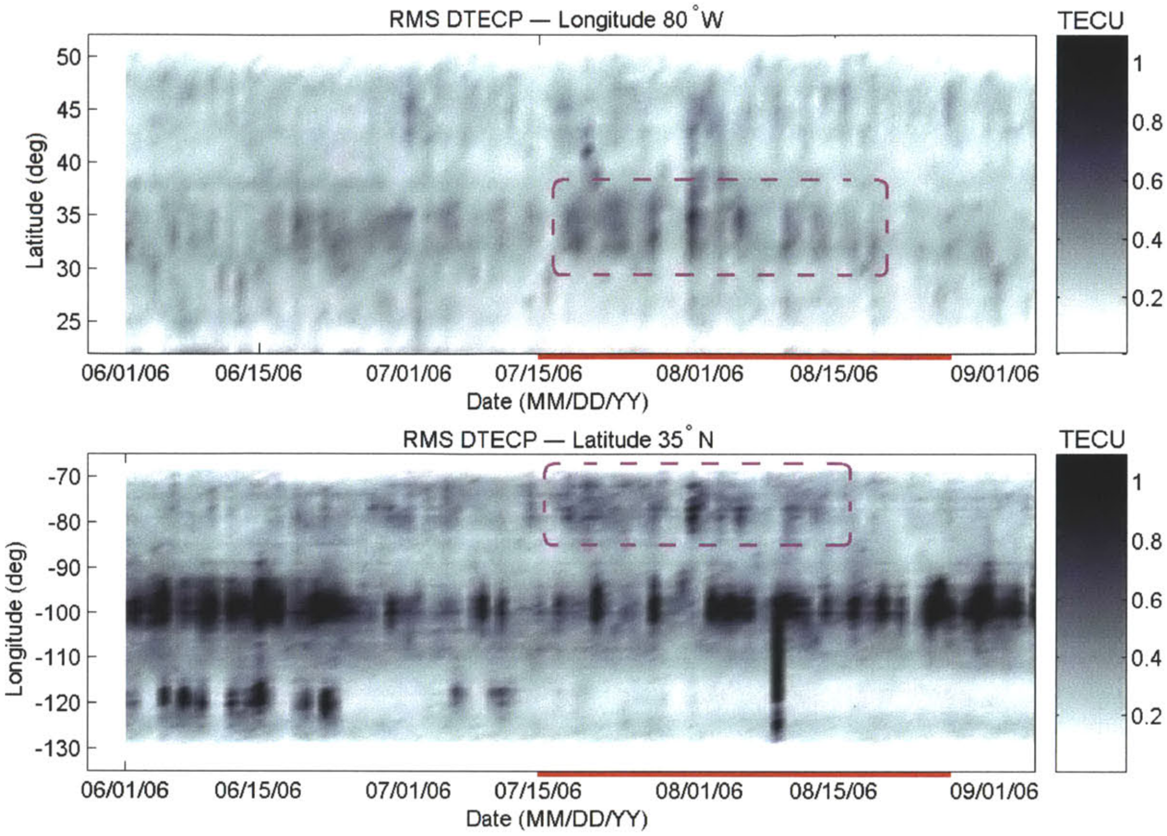

Figure A-7: Time evolution of the latitudinal/longitudinal slice of RMS DTECP values over a selected region over North America in the summer 2006. The heat wave period is highlighted in red on the time axis.

In order to obtain a separate verification of this evidence, we will also repeat the same surveying procedure for the RMS DTECP data. Figure A-7 shows the time evolution of the RMS DTECP values along the same latitudinal and longitudinal slice as before. This time, the color plots looks significantly cleaner — indicating that there is generally less noise in the DTECP signal than in the TECP signal. Once again, we can identify a prompt increase in the RMS DTECP values during the heat wave period around latitude 35°N and longitude 80°W.

Based on its timing, this particular increase in the RMS TECP and RMS DTECP values does seem to be related to the occurrence of the heat wave event. We now need to focus our attention at this discerned location (i.e. lat 35°N and lon 80°W). The next step is to spatially average the RMS TECP and RMS DTECP values around this geographical coordinate to obtain a clearer picture on their time evolution.

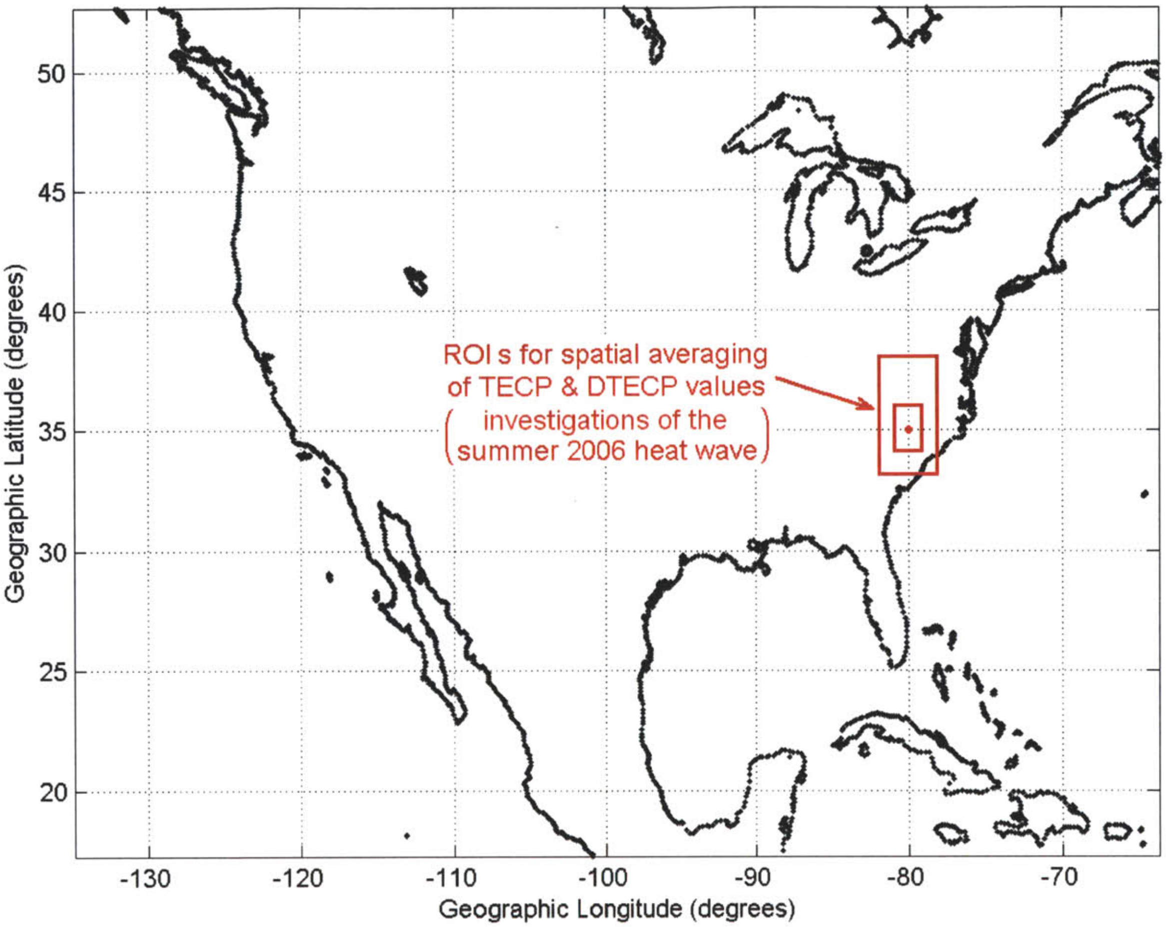

Figure A-8: Several ROIs around an area over North America where the RMS TECP and RMS DTECP values seem to exhibit a prompt increase during the summer 2006 heat wave period, based on some indications observed in Figures A-6 and A-7.

In the analysis that follows, the RMS TECP and RMS DTECP values will be spatially averaged within certain region-of-interest (ROI) around latitude 35°N and longitude 80°W. After the spatial averaging, we can generally expect that systematic effects will hold out while random occurrences will tend to cancel/smooth out. For this purpose, we had selected 3 different ROIs of various sizes as illustrated in Figure A-8. By observing the gradual amount of noise reduction as we slowly enlarge the size of the ROI, hopefully we would be able to sort out any systematic trend more easily. As systematic effects in the time evolution become more evident after the spatial averaging, we should be able to make some assessment on the overall increase in the RMS TECP and RMS DTECP values related to this heat wave event.

The exact specifications of the ROIs to be used for the spatial averaging are as follows. First, we will examine the time evolution of RMS TECP and RMS DTECP at the point location 35°N and 80°W. Next, we will enlarge the ROI for spatial averaging to span $34° - 36°$N and $79° - 81°$W (i.e. 3° lat × 3° lon). Finally, we will use a larger ROI that spans $33° - 38°$N and $78° - 82°$W (i.e. 6° lat × 5° lon).

Figure A-9 shows the time evolution of the spatially-averaged RMS TECP values around 35°N and 80°W, calculated using the 3 different ROIs we specified above. During the heat wave period (highlighted in red on the time axis) we can see a systematic increase in the RMS TECP values, marked by a quite sudden rise shortly after the heat wave event started. This notable trend (including the sudden rise) did not diminish as we incrementally expand the ROI size. On the other hand, some of the RMS TECP variations observed between 15 June 2006 and 10 July 2006 tend to subside as we use larger ROI for the spatial averaging. Hence, the apparent activity that happened a month before the heat wave event is probably only a set of random sporadic occurrences. This disposition considerably heightens the significance of the sudden rise in the RMS TECP observed at the beginning of the heat wave period. Taking the initial jump as a measure, we estimated that the overall RMS TECP had increased by $\sim$0.5 TECU above the baseline during the heat wave event.

Meanwhile, Figure A-10 shows the general time evolution of the spatially-averaged RMS DTECP values around 35°N and 80°W using the 3 different ROIs that we had selected. We expect to see more-or-less the same qualitative features that corroborate the trend we had discovered using the RMS TECP data. Indeed, here we have also found a noticeable systematic increase in the RMS DTECP values during the heat wave period, starting shortly after the heat wave event began. The initial rise in the RMS DTECP value at the beginning of the heat wave period is not as sharp as what we had found in the RMS TECP data, but the general trend remains approximately the same. In this case, we estimated that the overall RMS DTECP values during the heat wave period had increased by $\sim$0.2 TECU above the baseline.

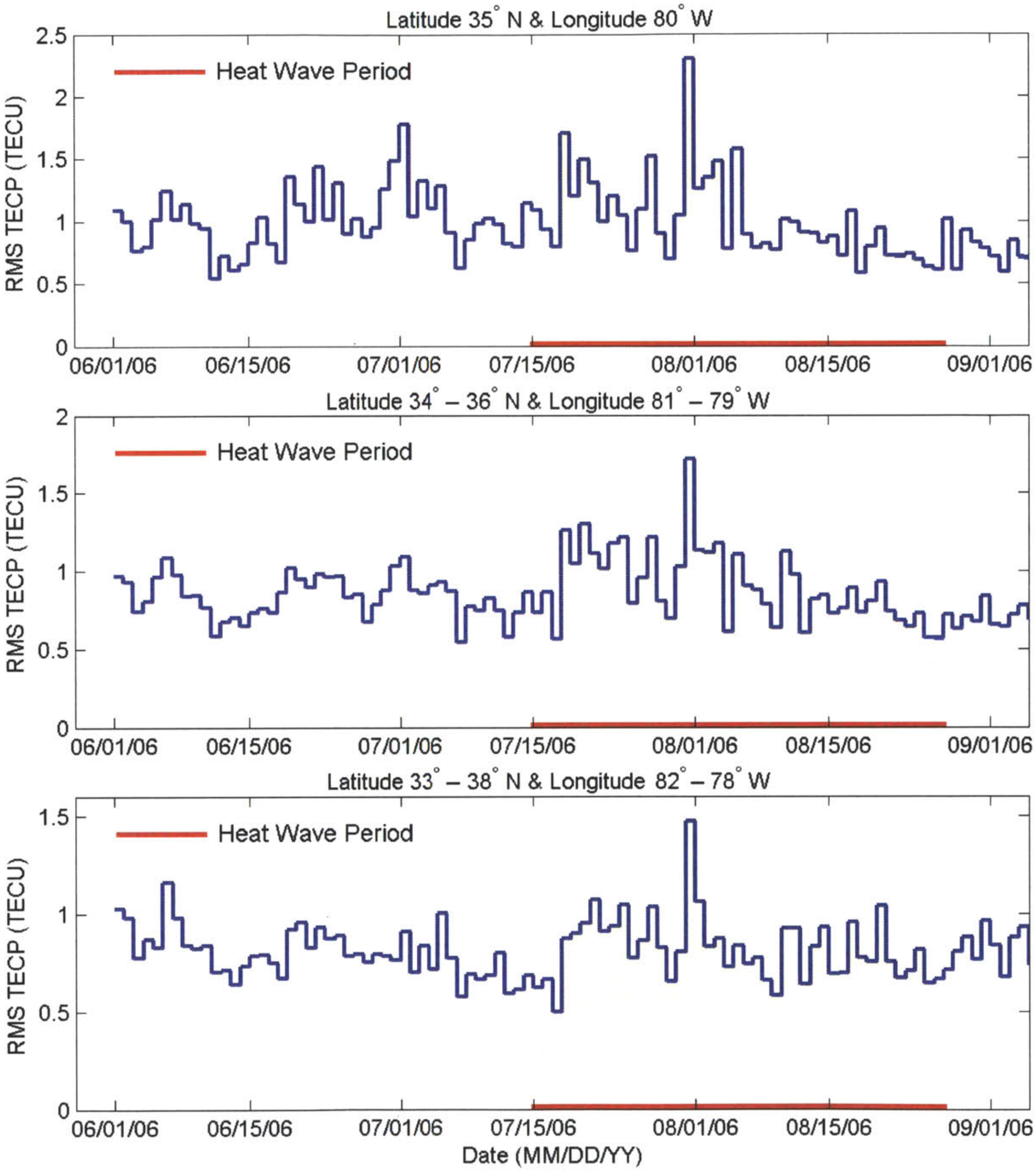

Figure A-9: The RMS TECP time series around a selected geographic coordinate over North America in summer 2006 (computed using three different choices of ROI). The heat wave period is highlighted red on the time axis.

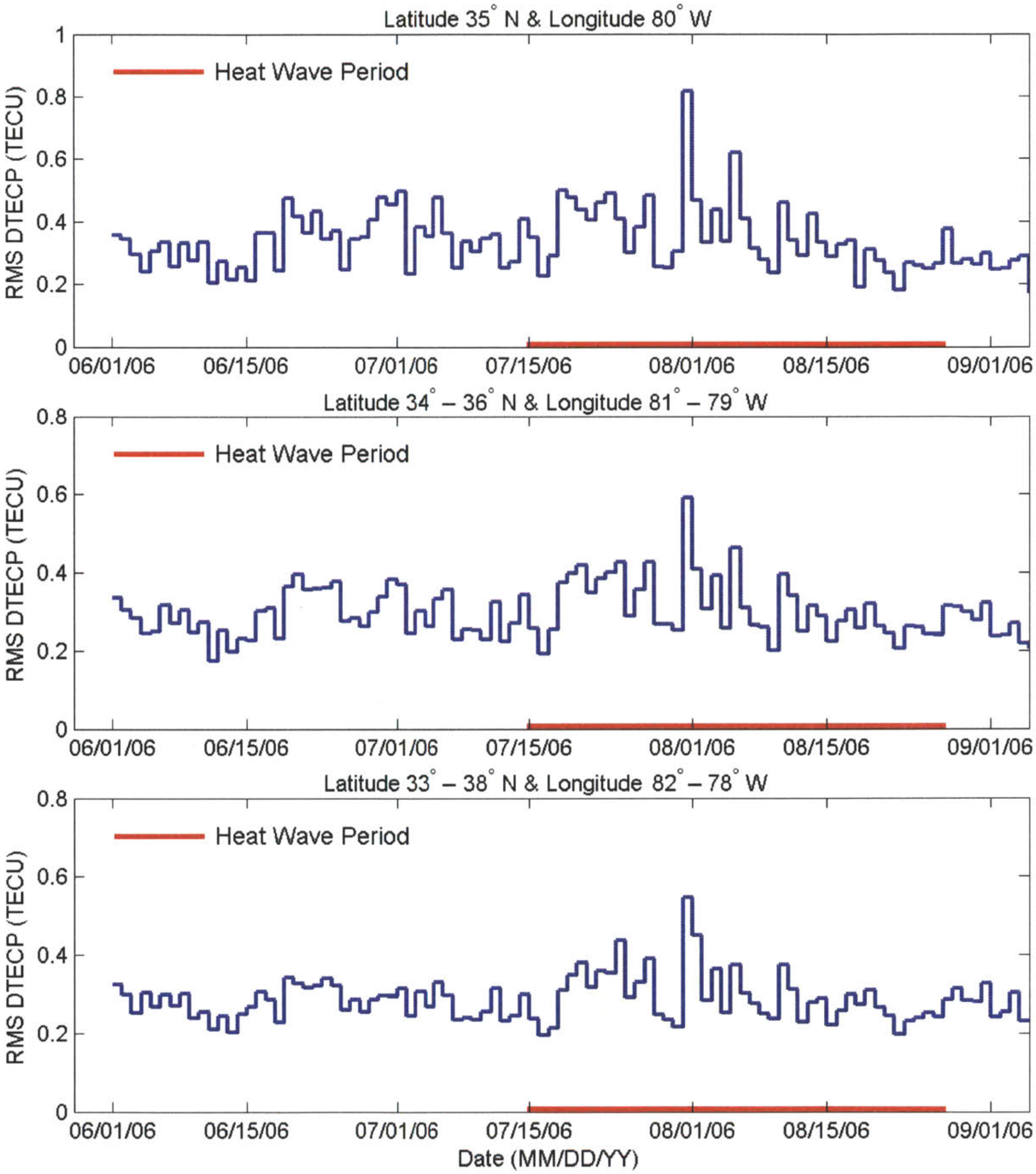

Figure A-10: The RMS DTECP time series around a selected geographic coordinate over North America in summer 2006 (computed using three different choices of ROI). The heat wave period is highlighted red on the time axis.

Appendix B

The Brunt-Vaisala Frequency

The Brunt-Vaisala frequency is a characteristic frequency related to the physical property of acoustic-gravity waves. It is the natural frequency for the up-and-down oscillation of air parcels in the atmosphere, which is governed by the balance between gravity and buoyancy. The low-frequency branch of acoustic-gravity waves exists only below this resonant frequency. This low-frequency branch is usually known as the (internal) gravity waves and this wave branch is the one that we are trying to generate in the HAARP-AGW experiments so far. Here we will provide a simple analytical derivation of the Brunt-Vaisala frequency as well as a numerical calculation on the altitude dependence of the Brunt-Vaisala frequency.

B.1 Simple Derivation

The Brunt-Vaisala frequency (or sometimes *buoyancy frequency*) is a characteristic oscillation frequency of air parcels in the atmosphere. Our atmosphere is a fluid in an overall hydrostatic equilibrium where gravity is properly balanced by buoyancy — with background pressure and density that decrease with height. At the equilibrium state, the downward gravitational force F_g on an air parcel is exactly compensated by the upward buoyant force F_b. However, when this air parcel is displaced upward, the surrounding air at this new altitude is lighter and consequently the air parcel will tend to sink back down. Similarly, when this air parcel is displaced downward,

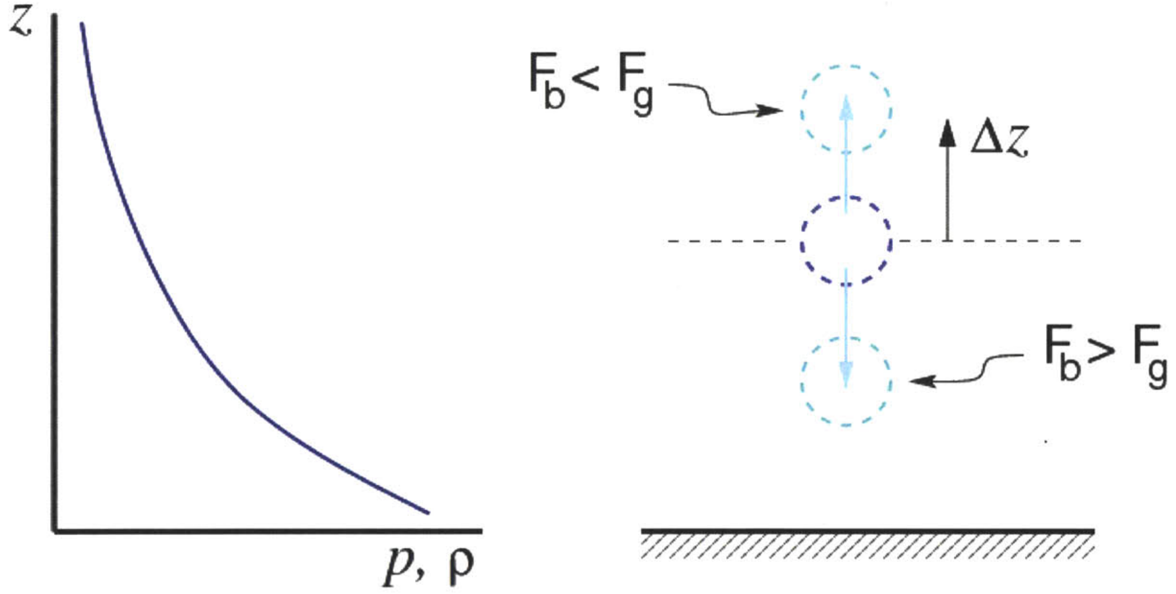

Figure B-1: A diagram illustrating the natural oscillation of atmospheric air parcels at the Brunt-Vaisala frequency, in a convectively stable atmosphere.

the denser surrounding air will cause this air parcel to float back up towards the initial equilibrium altitude. Thus, in a convectively stable atmosphere, we will have a characteristic up-and-down oscillation of air parcels which is the main underlying physical mechanism behind acoustic-gravity waves (especially at low frequencies). This mechanism is shown schematically in Figure B-1.

Suppose that at an altitude z the ambient pressure and density are p and ρ, respectively. An air parcel in hydrostatic equilibrium at this altitude will also have the same pressure and density (i.e. p and ρ). Now let us displace this particular air parcel to a new altitude $z+\Delta z$ where the local ambient pressure and density there are p' and ρ', respectively. After all the adiabatic changes, the new pressure and density inside our air parcel are now p^* and ρ^* at this new altitude. The thermodynamic process inside individual air parcels can be assumed to be adiabatic because the time scale for thermal equilibration is definitely much longer than that for pressure equilibration. This also tells us that $p^* = p'$, because pressure equilibration happens almost instantaneously and there should be absolutely no jump in pressure across the air parcel boundary.

Using the adiabaticity condition p/ρ^γ = constant, we can obtain the following relation for the pressure and density inside the air parcel before and after the vertical displacement:

$$\frac{p}{\rho^\gamma} = \frac{p'}{\rho^{*\gamma}} \quad \Rightarrow \quad \rho^* = \rho \left(\frac{p'}{p}\right)^{1/\gamma} \tag{B.1}$$

Now, note that $p' \approx p + \frac{\partial p}{\partial z}\Delta z$. Therefore,

$$\rho^* \approx \rho \left(1 + \frac{1}{p}\frac{\partial p}{\partial z}\Delta z\right)^{1/\gamma} \approx \rho + \frac{\rho}{\gamma p}\frac{\partial p}{\partial z}\Delta z \tag{B.2}$$

Similarly, note also that $\rho' \approx \rho + \frac{\partial \rho}{\partial z}\Delta z$. Based on the chain rule we can write $\frac{\partial \rho}{\partial z} = \frac{\partial \rho}{\partial p}\frac{\partial p}{\partial z} + \frac{\partial \rho}{\partial T}\frac{\partial T}{\partial z}$, and using the ideal gas law $p = \rho\, k_B T/m_0$ we may obtain:

$$\rho' \approx \rho + \left[\frac{m_0}{k_B T}\frac{\partial p}{\partial z} + \frac{(-m_0)\,p}{k_B T^2}\frac{\partial T}{\partial z}\right]\Delta z = \rho + \frac{\rho}{p}\frac{\partial p}{\partial z}\Delta z - \frac{\rho}{T}\frac{\partial T}{\partial z}\Delta z \tag{B.3}$$

Combining the result from Equations B.2 and B.3, we have:

$$\rho^* - \rho' = \; \ldots \; = \left[\frac{\rho}{T}\frac{\partial T}{\partial z} - \frac{(\gamma-1)\rho}{\gamma p}\frac{\partial p}{\partial z}\right]\Delta z \tag{B.4}$$

The Newton's second law of motion for the displaced air parcel is therefore:

$$\rho^* \frac{d^2 \Delta z}{dt^2} = -(\rho^* - \rho')g = -\left[\frac{\rho}{T}\frac{\partial T}{\partial z} - \frac{(\gamma-1)\rho}{\gamma p}\frac{\partial p}{\partial z}\right] g\,\Delta z \tag{B.5}$$

and since $\rho \approx \rho^*$, we finally obtain the following:

$$\frac{d^2 \Delta z}{dt^2} + \left[\frac{1}{T}\frac{\partial T}{\partial z} - \frac{(\gamma-1)}{\gamma p}\frac{\partial p}{\partial z}\right] g\;\Delta z = 0 \tag{B.6}$$

which represents a simple harmonic oscillatory motion for the variable Δz with an angular frequency ω_g, defined as:

$$\omega_g = \sqrt{g\left[\frac{1}{T}\frac{\partial T}{\partial z} - \frac{(\gamma-1)}{\gamma p}\frac{\partial p}{\partial z}\right]} \tag{B.7}$$

This characteristic oscillation frequency is what becomes known as the Brunt-Vaisala frequency. Note also that $\partial p/\partial z$ is generally negative for all altitudes.

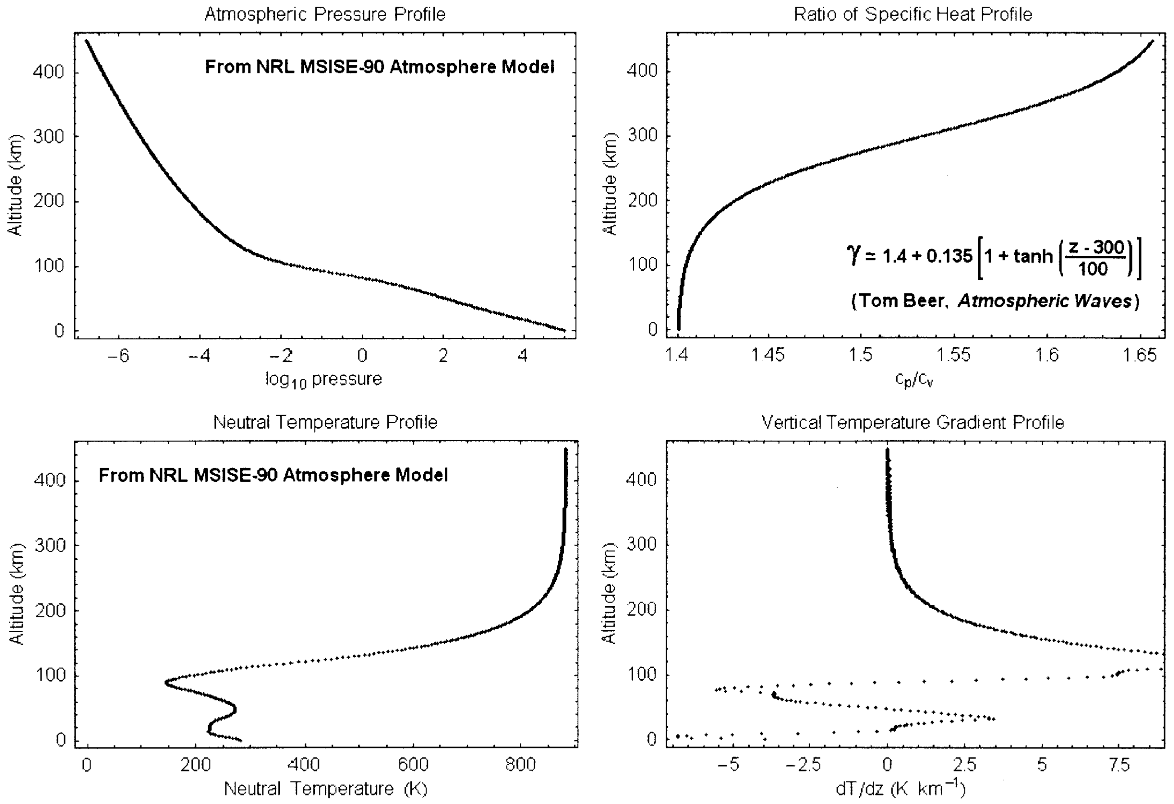

Figure B-2: A number of physical parameters (from the MSIS atmospheric model or other empirical formulas) that are necessary for determining the Brunt-Vaisala oscillation frequency.

B.2 Survey Using the MSIS Atmospheric Model

For the purpose of planning the HAARP-AGW experiments, it is quite important for us to estimate the altitude dependence of the Brunt-Vaisala frequency. Using the formula given in Equation B.7 and the MSIS-E atmospheric model from the Naval Research Laboatory (NRL), we are going to numerically compute the Brunt-Vaisala period $T_g \equiv 2\pi/\omega_g$ as a function of altitude. Most of the physical parameters that we need for this calculation can be obtained directly (or derived) from the NRL MSIS-E atmospheric model. The only exception is the altitude profile of specific heat ratio $\gamma \equiv c_p/c_v$, for which we are going to use the empirical formula given in *Beer* [1974]. All the main ingredients necessary for this calculation are depicted in Figure B-2.

In carrying out this numerical calculation, we had used the web-based interface of the NRL MSIS-E-90 atmospheric model that can be accessed online at the URL http://omniweb.gsfc.nasa.gov/vitmo/msis_vitmo.html. The pressure and temperature profiles shown in Figure B-2 had been obtained using this atmospheric model. Although not directly listed as an output of the model, the altitude profile of the vertical temperature gradient can still be computed numerically using the MSIS temperature profile. Meanwhile, the empirical formula that we had used for the specific heat ratio $\gamma \equiv c_p/c_v$ as a function of altitude is [*Beer*, 1974]:

$$\gamma = 1.4 \; + \; 0.135 \left[1 + \tanh \left(\frac{z[\mathrm{km}] - 300}{100} \right) \right] \tag{B.8}$$

A sample result of this numerical calculation can be found in Figure B-3 — using the geographical coordinate of the HAARP facility (62.4°N and 145°W). This graph shows the estimated altitude profile of the Brunt-Vaisala period $T_g \equiv 2\pi/\omega_g$ in the altitude range between 10 km to 450 km. For altitudes below 100 km or so, the Brunt-Vaisala period seems to be varying wildly with altitude. On the other hand, we seem to have a purely monotonic increase in the Brunt-Vaisala period for all altitudes higher than 100 km. After many trials, we found that this altitude profile is generally different for various time-of-year but had been quite consistent (in terms of both absolute value and trend) for altitudes between 100 km and 300 km. In other words, the result of this numerical model calculation is sufficiently reliable for altitudes between 100 km and 300 km — which is the most relevant altitude range for the HAARP-AGW experiments.

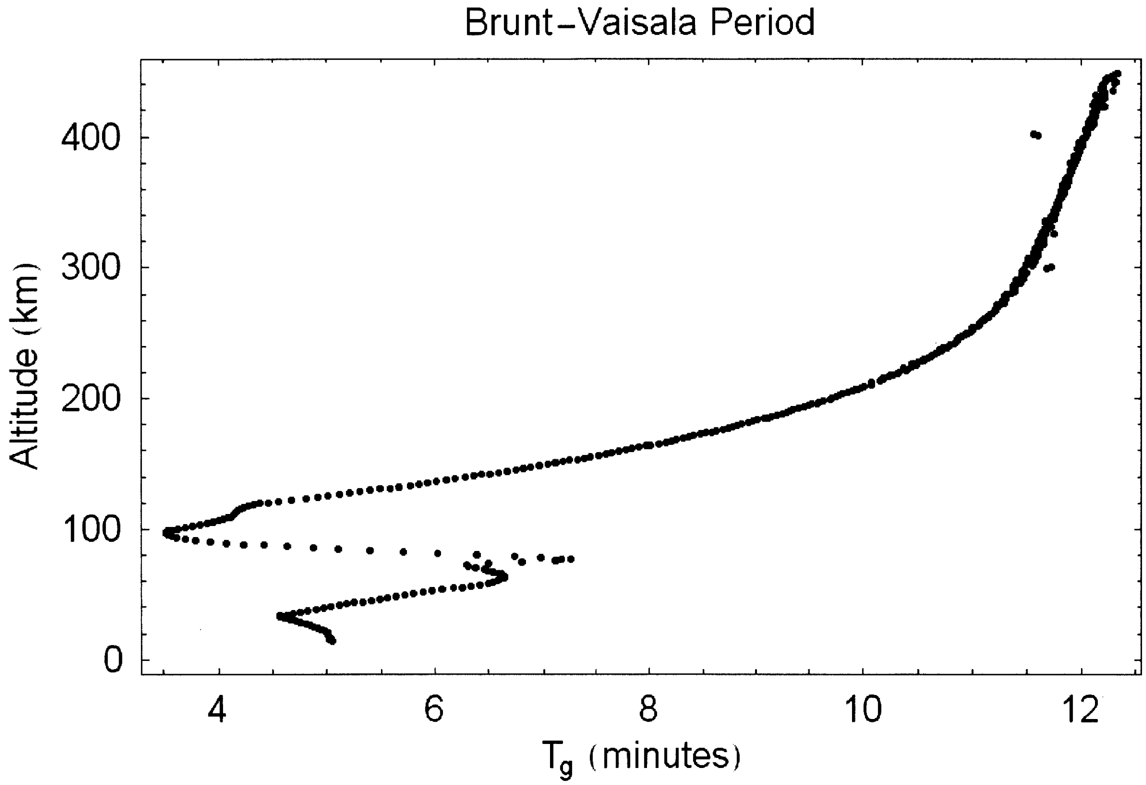

Figure B-3: An altitude profile of the Brunt-Vaisala period ($T_g \equiv 2\pi/\omega_g$) calculated using the physical parameters shown in Figure B-2.

Appendix C

Skymap Data Analysis Procedure

Here, we are going to give a brief overview on the methodology that we had adopted to examine, analyze, and interpret the digisonde skymap data. The development of this skymap data analysis procedure was motivated by our need to carefully monitor various dynamical changes that happen in the ionospheric plasma layer during our experiments. Although this skymap data display format was specifically devised for the HAARP-AGW experiments, it might actually be useful for other types of ionospheric heating experiment as well. In addition, it could even be implemented for routine observation of natural ionospheric phenomena all year round.

As part of its diagnostic instrument suite, HAARP research station operates a DPS-4D digisonde manufactured by Lowell Digisonde International, LLC. The skymap data recorded by the digisonde is primarily used for ionospheric plasma drift measurements. The plasma drift calculation can be carried out using a skymap data analysis and visualization software, called DriftExplorer. The DriftExplorer software is provided by the UMass Lowell Center for Atmospheric Research (UMLCAR), with detailed information available online at http://ulcar.uml.edu/Drift-X.html.

However, we certainly need to look beyond simple plasma drift velocity calculation in the HAARP-AGW experiments. We are therefore interested in coming up with special ways to display and analyze skymap data more effectively, so that we can infer as much information from the data as possible. We shall first consider all types of information contained in the skymap data and then weigh our options.

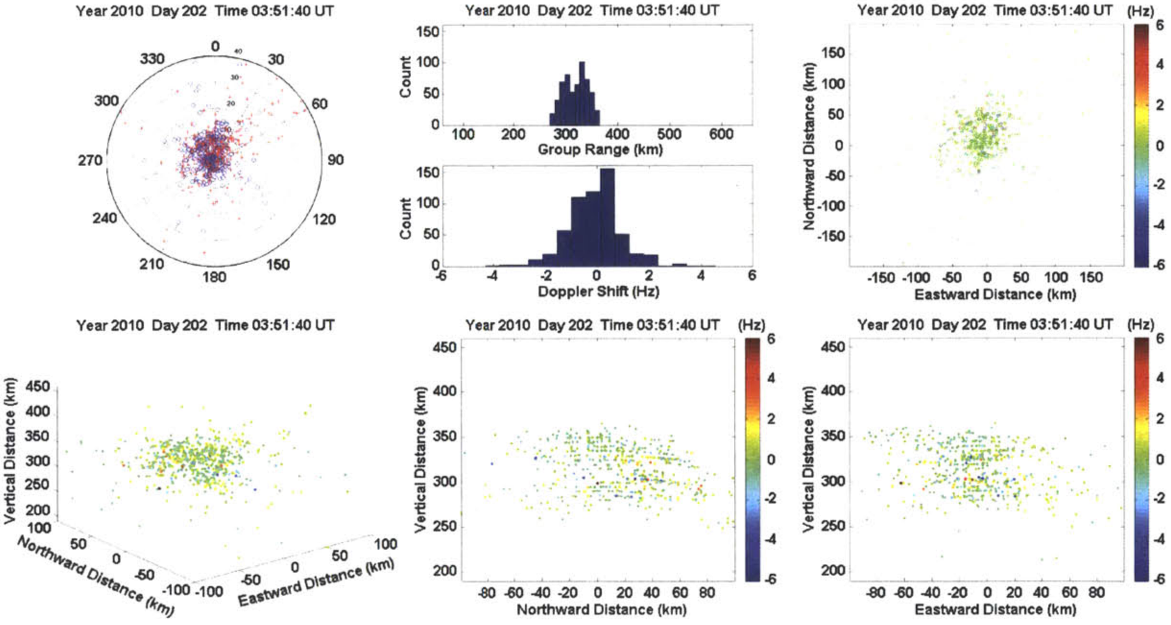

Figure C-1: An overview of several different ways to display the basic information contained in each individual skymap data.

The return echoes in a skymap generally contain information on the Doppler shift, virtual range, and arrival angles. Figure C-1 shows several possible ways to display all of these informations. First of all, we have the option to plot the return echoes in a polar plot based on their zenith and azimuth arrival angles — i.e. a standard skymap display. Simple histogram summary can then reveal how the virtual range and the Doppler shift are collectively distributed in this skymap data. Alternatively, we can also combine both range and zenith/azimuth information to calculate the *virtual echolocations* in terms of linear distance coordinate. The virtual echolocations can be displayed using various types of scatter plot (bird's eye view, 3-D perspective, or sideways view) with the Doppler shift information embedded using a colormap.

In general, scatter plots of the virtual echolocation tend to be more informative than the standard skymap display of zenith/azimuth polar plot. Using the virtual echolocation plots, it is relatively easy to make a quick assessment on the overall echo distribution pattern along the horizontal and vertical directions. Although the virtual echolocation might not represent the exact physical location of the reflection/ scattering region, this data visualization option had been very helpful nonetheless.

If we denote R as the virtual range, θ_{arr} the zenith arrival angle, ϕ_{arr} the azimuth arrival angle starting clockwise from the north; then the coordinate transformation formulas for calculating the virtual echolocation (X, Y, Z) are as follows:

$$\begin{aligned} X &= R \sin\theta_{\text{arr}} \sin\phi_{\text{arr}} \qquad \text{(C.1)} \\ Y &= R \sin\theta_{\text{arr}} \cos\phi_{\text{arr}} \qquad \text{(C.2)} \\ Z &= R \cos\theta_{\text{arr}} \qquad \text{(C.3)} \end{aligned}$$

where X is +ve eastward, Y is +ve northward, and Z is +ve vertical upward. Once the virtual echolocations (X, Y, Z) have been calculated for all return echoes, we can then display them in various types of scatter plot as we described earlier.

During the HAARP-AGW experiment, we record one skymap every minute and we have to study how the overall configuration of the skymap echoes evolves as a function of time. By looking at the time evolution of the skymap echo configuration, we hope to be able to infer the dynamical changes that occur in the ionospheric plasma layer. However, there had been a major difficulty which arises from the fact that we would have to examine a large number of skymaps frame-by-frame in order to clearly perceive the apparent dynamical changes. The situation is more-or-less the same for the standard skymap display in terms of zenith/azimuth angle, and for the scatter plots of virtual echolocations.

In order to allow for a more convenient way to examine large number of skymap data, we are going to reduce each individual skymap into a number of univariate distribution histograms. For each specific histogram type, we can easily stack a number of them in a chronological sequence as a surface plot to study how it evolves as a function of time. By doing so, we will have a particularly compact way to summarize a large number of skymap measurements. Moreover, we can use this visualization method to reveal notable temporal trends in the skymap data effectively without having to compile any animations or large array of individual snapshots.

After a number of trials, we have finally determined that a single skymap shall be reduced into 4 univariate histograms. More specifically, the 4 parameters/variables

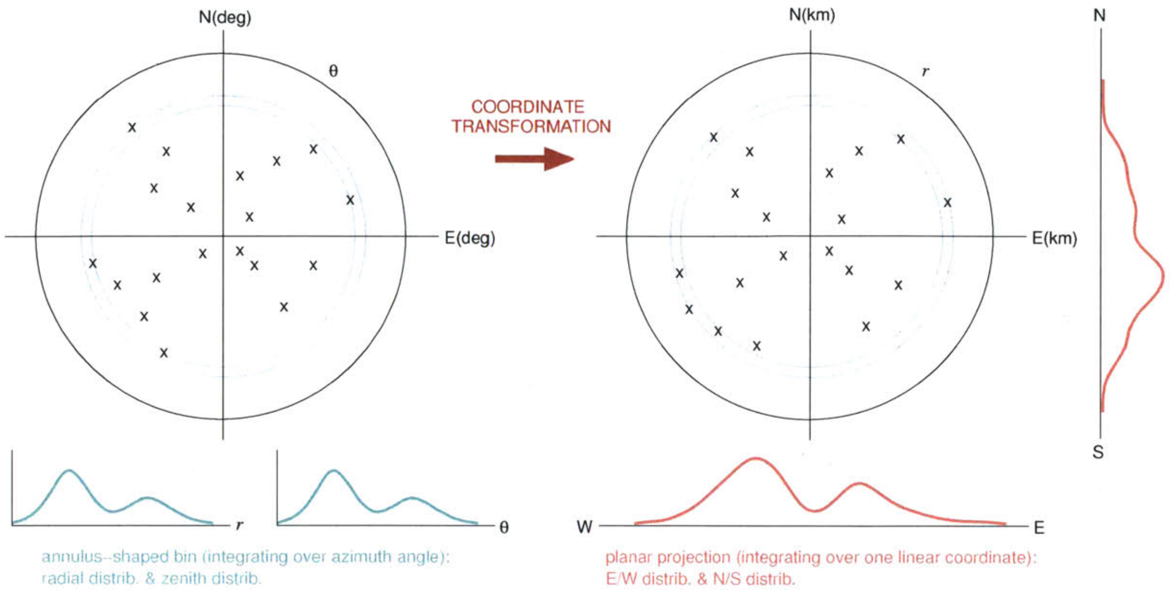

Figure C-2: A schematic illustration of the skymap data analysis procedure where a set of radial-zenith-planar (RZP) echo distribution histograms are calculated from each individual digisonde skymap.

to be used for constructing those distribution histograms are: (1) horizontal radial distance, (2) zenith angle, and (3-4) projected linear distances along the E/W and N/S planes. The general procedure for constructing these skymap echo distribution histograms is depicted diagrammatically in Figure C-2. For the radial and zenith distribution histograms, we are essentially integrating using annulus-shaped bins. On the other hand, we are basically integrating along one of the linear coordinate in order to obtain the E/W and N/S planar projection histograms.

Finally, we have some real examples where we use the radial-zenith-planar (RZP) echo distribution histograms to reveal notable temporal trends in the skymap data. Figure C-3 shows the RZP echo distribution histograms as a function of time, from our skymap measurements during one of the HAARP-AGW experiments. Meanwhile, Figure C-4 shows the same type of graphs, but this time from a different type of heating experiment. From these examples, we can compare and see clearly that the skymap echo distribution evolves in a unique way during the HAARP-AGW experiments — as compared to other settings. Hopefully, this case comparison can significantly add to our data discussion presented earlier in Chapter 4.

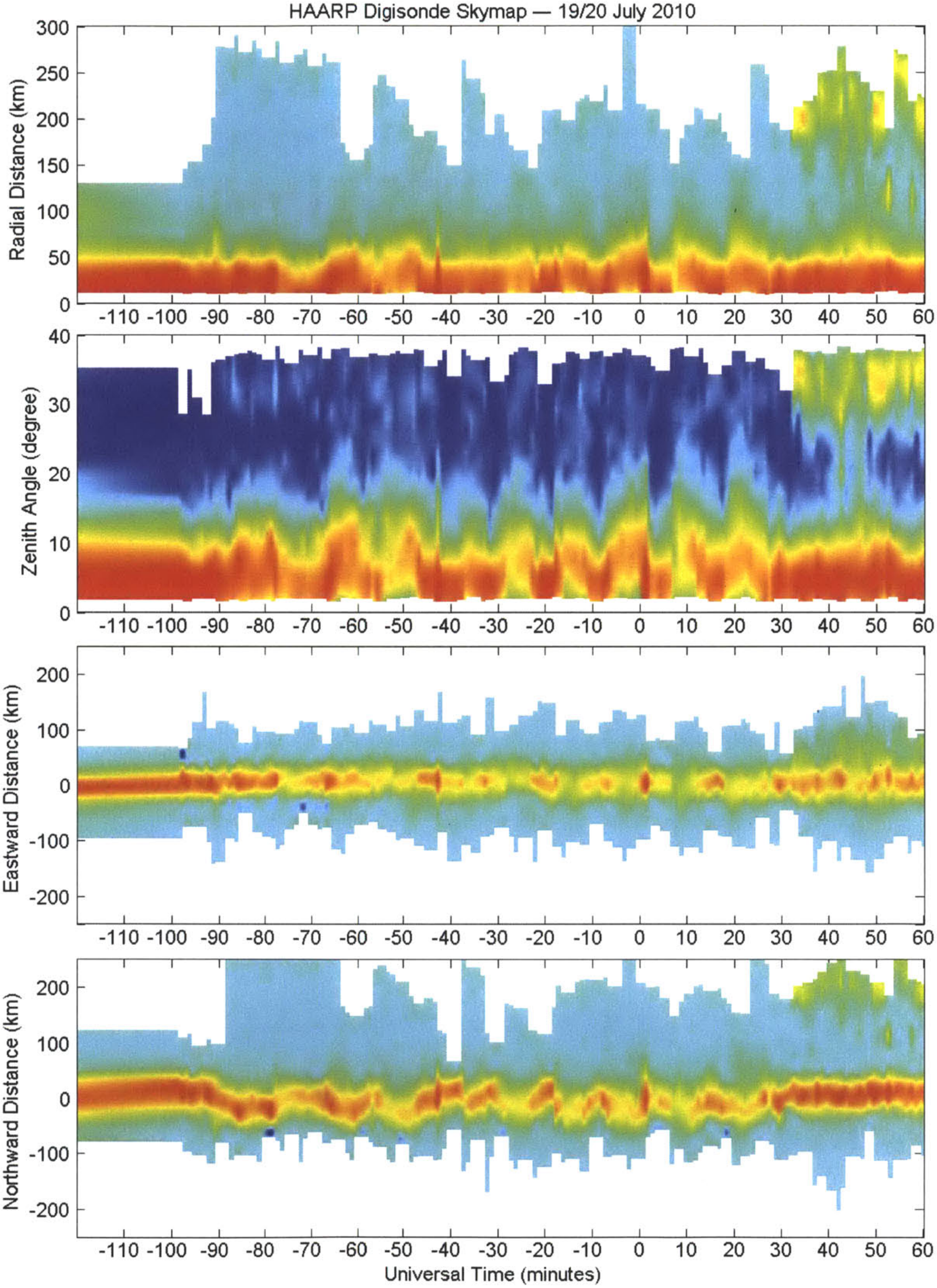

Figure C-3: A sample time evolution of the skymap echo distribution histograms during a HAARP-AGW experiment (running from $t = -90$ min to $t = +30$ min).

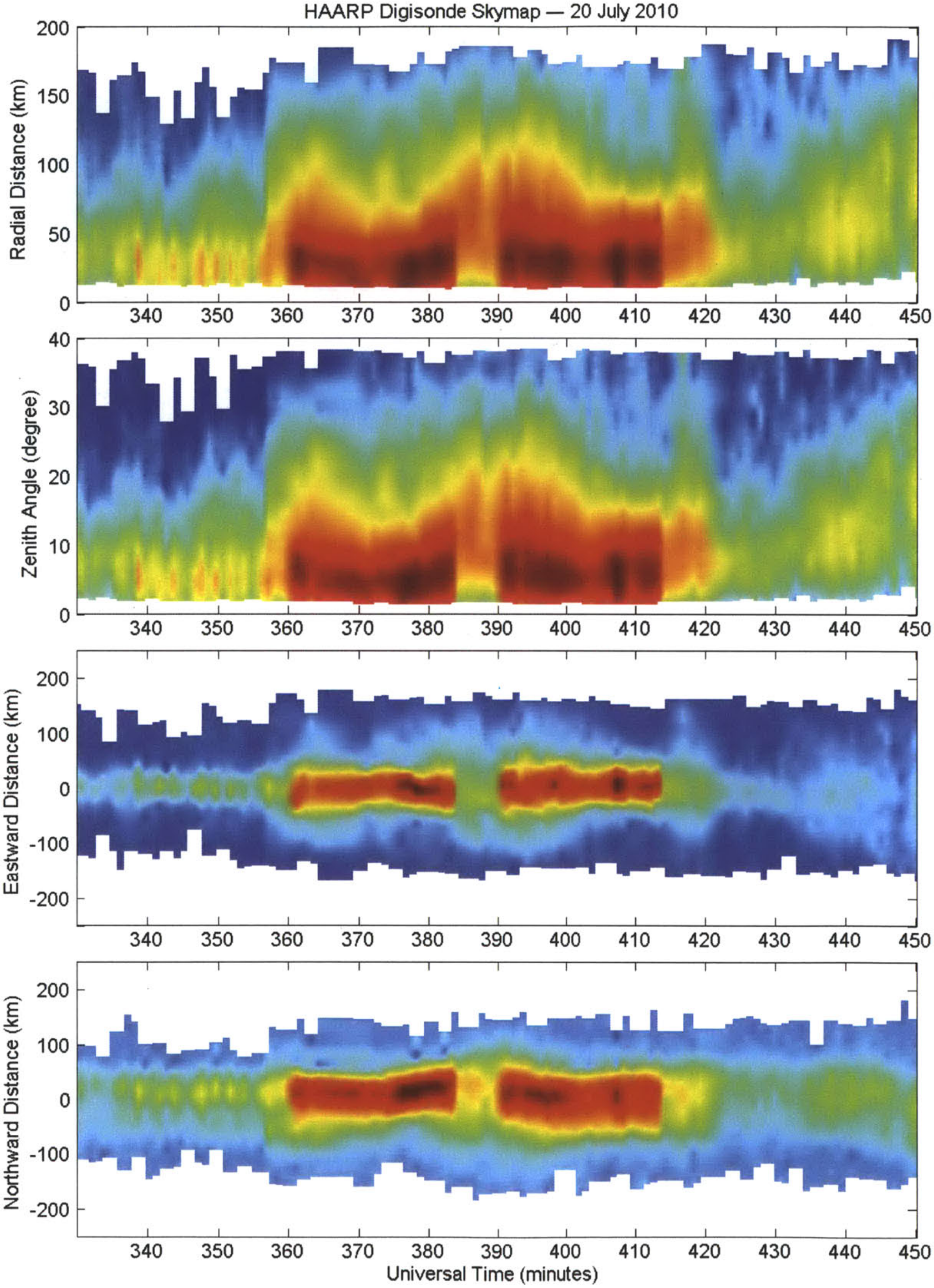

Figure C-4: A sample time evolution of the skymap echo distribution histograms during another type of HF heating experiment performed at the HAARP facility.

Appendix D

Semi-Analytical Fluid Model

Here we are going to discuss a detailed formulation of our fluid model simulation of heater-generated AGW/TID, which had been the basis for some of the results presented earlier in Chapter 8. We will start with a general formulation and basic setup of the fluid model, followed by an analysis to obtain the solution to the system of coupled partial differential equations (PDEs) that we had laid out.

In our formulation, we are going to include a sinusoidally time-varying source term in the energy balance equation. The specific region where heat is being periodically deposited will be modeled to closely resemble the heated plasma volume in the actual field experiments. Furthermore, we are assuming an isothermal atmosphere in our model calculation, thus giving a constant Brunt-Vaisala frequency for all altitudes. We will restrict ourselves to a linear model (assuming low-amplitude fluctuations), and our goal here is to obtain the resulting steady-state pressure fluctuations that arise due to the periodic heat deposition.

We attempt to work towards the solution (i.e. pressure fluctuations as a function of position and time) analytically as much as possible, but must resort to numerical computation at the end. We will first combine the linearized system of PDEs into a single higher-order PDE in terms of the pressure fluctuations, and then try to obtain a solution for it. In particular, we are going to employ the Fourier-Bessel (Hankel) integral transformation to work out the solution in terms of an integral. Finally, the integral will be evaluated numerically after some simplifications.

D.1 The Basic Formulation and Setup

Assuming a constant background temperature T_0; the density ρ, pressure p, and fluid velocity $\mathbf{u}$ of gases in the upper atmosphere obey the following system of partial differential equations [see e.g. *Kelley*, 1989; *Schunk and Nagy*, 2000]:

$$\begin{aligned} \rho\frac{\partial \mathbf{u}}{\partial t} + \rho(\mathbf{u}\cdot\nabla)\mathbf{u} &= -\nabla p + \rho\mathbf{g} && \text{(D.1)} \\ \frac{d\rho}{dt} + \rho\,(\nabla\cdot\mathbf{u}) &= 0 && \text{(D.2)} \\ \frac{dp}{dt} - c_s^2\frac{d\rho}{dt} &= (\gamma-1)\rho q && \text{(D.3)} \end{aligned}$$

where $\mathbf{g} = -g\hat{z}$ is the gravitational acceleration (downward), γ is the ratio of specific heats (assumed to be constant), and c_s is the adiabatic sound speed (also assumed to be constant). The quantity q in the RHS of Equation D.3 is the rate of heat deposition (prescribed, with a unit of e.g. J kg^{-1} s^{-1}). Note also that $\frac{d}{dt} = \frac{\partial}{\partial t} + \mathbf{u}\cdot\nabla$ is the Lagrangian derivative.

In an earlier analysis of this problem by *Grigor'ev* [1975], the spatial profile of the heat deposition q was modeled as a thin horizontal disk with a 2D gaussian profile along the horizontal direction, i.e.

$$q = q(x,y,z,t) = q_0\; e^{-r^2/R^2}\;\delta(z)\;e^{i\Omega t}$$

where $r^2 \equiv x^2 + y^2$, and $\delta(z)$ denotes the Dirac delta (distribution) function.

We are going to adopt the same analytical solution method as *Grigor'ev* [1975], but with a slightly more general profile for the heat deposition rate. Instead of an infinitesimally thin disk, the heat deposition region will be modeled as a spheroid with gaussian profiles in both vertical and horizontal directions, i.e.

$$q = q(x,y,z,t) = q_0\; e^{-r^2/R^2}\;e^{-z^2/\sigma_z^2}\;e^{i\Omega t}$$

A graphical representation of this particular model for the heat deposition profile is depicted schematically in Figure D-1.

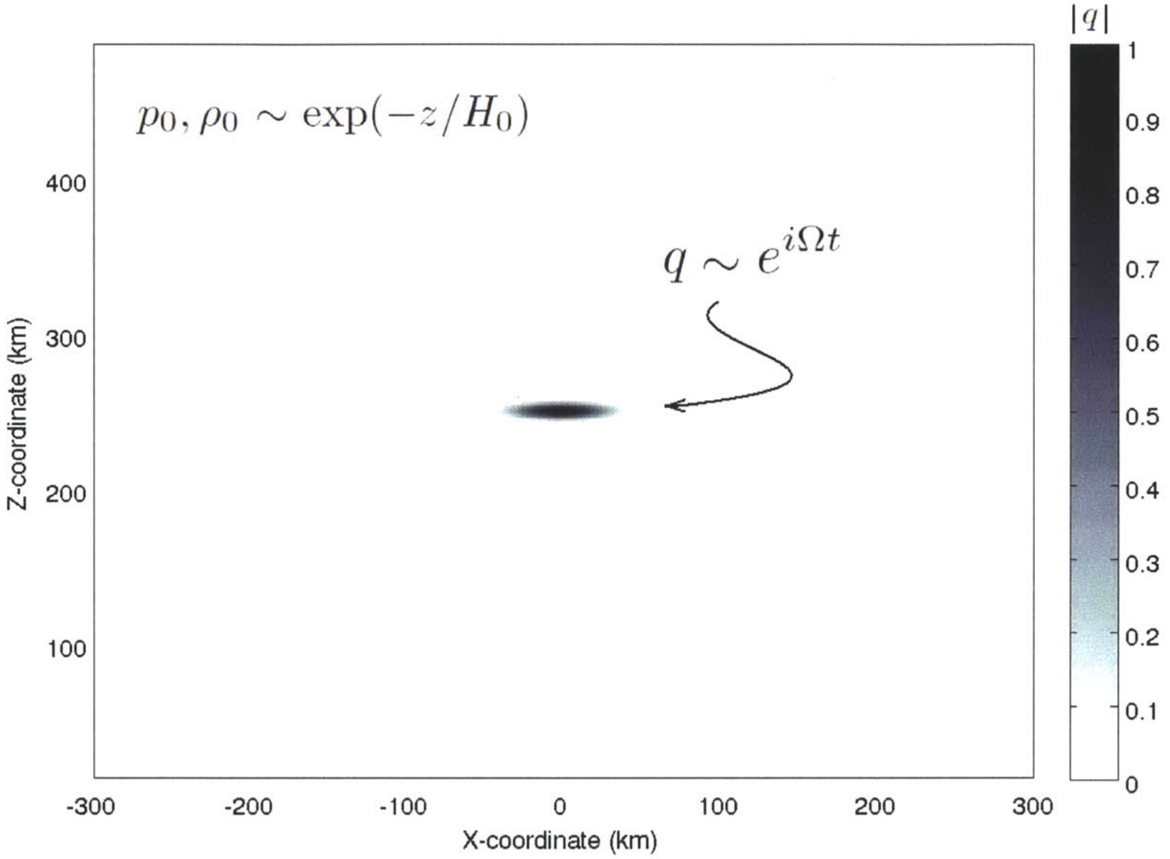

Figure D-1: The basic setup for the fluid model of heater-generated AGWs. In the modeled heated region, the rate of heat deposition q is sinusoidally varying in time. We also assume a constant and uniform background temperature T_0.

In our analysis, we will adopt an atmospheric model where the background temperature is assumed to be constant and uniform. Under such circumstances, the background pressure and density are exponentially decreasing with altitude, i.e., $p_0, \rho_0 \sim \exp(-z/H_0)$. We are particularly interested in obtaining a solution in the steady-state condition, as a response to the source term in Equation D.3 which is varying sinusoidally with time, i.e. $q \sim \exp(i\Omega t)$.

For simplicity, we will leave out any boundaries and look only for approximate solutions by employing small sinusoidal perturbations to each variables ρ, p, and $\mathbf{u}$. We will begin with the linearization of our non-linear coupled PDE system D.1–D.3, followed by a reduction from a system of (linearized) coupled PDEs into a single PDE, and finally we will be working towards a solution using an integral transform.

Applying perturbative expansions, we set the total density, pressure, and fluid velocity to be $\rho = \rho_0 + \rho_1$, $p = p_0 + p_1$, and $\mathbf{u} = \mathcal{O} + \mathbf{u}_1$ (where $|\rho_1| \ll \rho_0$ and $|p_1| \ll p_0$). Note that the equilibrium pressure and density do not have any time dependence, i.e. $\frac{\partial \rho_0}{\partial t} = 0$ and $\frac{\partial p_0}{\partial t} = 0$, which implies $-\nabla p_0 + \rho_0 \mathbf{g} = 0$. This is the very familiar hydrostatic equilibrium condition; and indeed, it tells us that $p_0, \rho_0 \sim \exp(-z/H_0)$ with $H_0 = p_0/\rho_0 g = c_s^2/\gamma g$ if the background temperature is assumed to be constant.

Keeping only the leading first-order terms and neglecting all higher-order terms, from Equations D.1–D.3 we will obtain a linearized system of PDEs:

$$\begin{aligned} \rho_0 \frac{\partial \mathbf{u}_1}{\partial t} &= -\nabla p_1 + \rho_1 \mathbf{g} && \text{(D.4)} \\ \frac{\partial \rho_1}{\partial t} + \rho_0 \nabla \cdot \mathbf{u}_1 + \mathbf{u}_1 \cdot \nabla \rho_0 &= 0 && \text{(D.5)} \\ \frac{\partial p_1}{\partial t} + \mathbf{u}_1 \cdot \nabla p_0 - c_s^2 \frac{\partial \rho_1}{\partial t} - c_s^2 \, \mathbf{u}_1 \cdot \nabla \rho_0 &= (\gamma - 1) \rho_0 \, q && \text{(D.6)} \end{aligned}$$

This simplifies the problem greatly since we now have a system of linear PDEs instead of non-linear ones, provided that the perturbation terms remain small so that the linearizations are fully justified.

Albeit linear, we still have a system of coupled PDEs to solve (one of them is inhomogeneous). The next stage in our analysis is to reduce the linearized system of coupled PDEs (Equations D.4–D.6) into a single (higher-order) PDE in one of the variables only. Specifically, we want to obtain a single PDE for the pressure p_1.

Before we begin, note that Equation D.6 can be further simplified using a few substitutions. Because $p_0, \rho_0 \sim \exp(-z/H_0)$ and $c_s^2 \equiv \gamma p_0/\rho_0$, one can see that $\nabla p_0 = (c_s^2/\gamma) \nabla \rho_0$. Therefore, we have

$$\frac{\partial p_1}{\partial t} - c_s^2 \frac{\partial \rho_1}{\partial t} - c_s^2 \frac{(\gamma - 1)}{\gamma} \, \mathbf{u}_1 \cdot \nabla \rho_0 = (\gamma - 1) \rho_0 \, q \qquad \text{(D.6}'\text{)}$$

which looks considerably simpler. We are now ready to start reducing our system of PDEs into a single PDE.

First, by taking $\nabla\cdot$ [Equation D.4], we have

$$\frac{\partial}{\partial t}\left[\nabla\cdot(\rho_0\mathbf{u}_1)\right] = -\nabla^2 p_1 + \mathbf{g}\cdot\nabla\rho_1$$

and by taking $\frac{\partial}{\partial t}$[Equation D.5], we have

$$\frac{\partial^2\rho_1}{\partial t^2} + \frac{\partial}{\partial t}[\nabla\cdot(\rho_0\mathbf{u}_1)] = 0$$

If we combine the above two relations to eliminate terms containing $\nabla\cdot(\rho_0\mathbf{u}_1)$, noting that $\mathbf{g}\cdot\nabla\rho_1 = -g\frac{\partial\rho_1}{\partial z}$, then we obtain

$$\frac{\partial^2\rho_1}{\partial t^2} - \nabla^2 p_1 - g\frac{\partial\rho_1}{\partial z} = 0 \tag{D.7}$$

Next, by taking $(1/g)$ $\mathbf{g}\cdot$ [Equation D.4], we have

$$\frac{\partial}{\partial t}\left[\frac{\mathbf{g}\cdot\mathbf{u}_1}{g}\right] = \frac{\rho_1 g}{\rho_0} - \frac{\mathbf{g}\cdot\nabla p_1}{\rho_0 g}$$

and by taking $\frac{\partial}{\partial t}$[Equation D.6$'$], with an aid of the explicit formula $\nabla\rho_0 = (\rho_0/gH_0)\mathbf{g}$, we are going to have

$$\frac{\partial^2 p_1}{\partial t^2} - c_s^2\frac{\partial^2\rho_1}{\partial t^2} - \frac{(\gamma-1)}{\gamma}\,\frac{\rho_0 c_s^2}{H_0}\,\frac{\partial}{\partial t}\left[\frac{\mathbf{g}\cdot\mathbf{u}_1}{g}\right] = (\gamma-1)\rho_0\,\frac{\partial q}{\partial t}$$

And thus we can combine the latest two relations above, eliminating the terms that contain $[\mathbf{g}\cdot\mathbf{u}_1]$, to give

$$\frac{\partial^2 p_1}{\partial t^2} - c_s^2\frac{\partial^2\rho_1}{\partial t^2} - \frac{(\gamma-1)c_s^2}{\gamma H_0}\left[g\rho_1 - \frac{\mathbf{g}\cdot\nabla p_1}{g}\right] = (\gamma-1)\rho_0\,\frac{\partial q}{\partial t} \tag{D.8}$$

Now, we can substitute $\frac{\partial^2\rho_1}{\partial t^2}$ from Equation D.7 into Equation D.8. By also noting that $\mathbf{g}\cdot\nabla\rho_1 = -g\frac{\partial\rho_1}{\partial z}$ and $\mathbf{g}\cdot\nabla p_1 = -g\frac{\partial p_1}{\partial z}$, we will obtain

$$\frac{\partial^2 p_1}{\partial t^2} - c_s^2\left[\nabla^2 p_1 + g\frac{\partial\rho_1}{\partial z}\right] - \frac{(\gamma-1)c_s^2}{\gamma H_0}\left[g\rho_1 + \frac{\partial p_1}{\partial z}\right] = (\gamma-1)\rho_0\,\frac{\partial q}{\partial t} \tag{D.9}$$

Next, by taking $\frac{\partial^2}{\partial t^2}$[Equation D.9 (9)], we have

$$\frac{\partial^4 p_1}{\partial t^4} - c_s^2 \frac{\partial^2}{\partial t^2} \nabla^2 p_1 - \frac{(\gamma - 1)c_s^2}{\gamma H_0} \frac{\partial^2}{\partial t^2} \frac{\partial p_1}{\partial z} - g c_s^2 \left[\frac{\partial}{\partial z} \frac{\partial^2 \rho_1}{\partial t^2} + \frac{(\gamma - 1)}{\gamma H_0} \frac{\partial^2 \rho_1}{\partial t^2} \right] = (\gamma - 1)\rho_0 \frac{\partial^3 q}{\partial t^3}$$

We can use Equation D.7 to substitute for $\frac{\partial^2 \rho_1}{\partial t^2}$ in the above expression, and obtain

$$\begin{aligned} \frac{\partial^4 p_1}{\partial t^4} - c_s^2 \frac{\partial^2}{\partial t^2} \left[\nabla^2 + \frac{(\gamma - 1)}{\gamma H_0} \frac{\partial}{\partial z} \right] p_1 - g c_s^2 \left[\frac{\partial}{\partial z} + \frac{(\gamma - 1)}{\gamma H_0} \right] \nabla^2 p_1 & \\ - g^2 c_s^2 \left[\frac{\partial^2 \rho_1}{\partial z^2} + \frac{(\gamma - 1)}{\gamma H_0} \frac{\partial \rho_1}{\partial z} \right] &= (\gamma - 1)\rho_0 \frac{\partial^3 q}{\partial t^3} \end{aligned}$$

Meanwhile, by taking $\frac{\partial}{\partial z}$[Equation D.9], we have

$$\begin{aligned} \frac{\partial}{\partial z} \frac{\partial^2 p_1}{\partial t^2} - c_s^2 \frac{\partial}{\partial z} \left[\nabla^2 + \frac{(\gamma - 1)}{\gamma H_0} \frac{\partial}{\partial z} \right] p_1 - g c_s^2 \left[\frac{\partial^2 \rho_1}{\partial z^2} + \frac{(\gamma - 1)}{\gamma H_0} \frac{\partial \rho_1}{\partial z} \right] & \\ = (\gamma - 1)\rho_0 \frac{\partial^2 q}{\partial z\, \partial t} + (\gamma - 1) \frac{\partial \rho_0}{\partial z} \frac{\partial q}{\partial t} & \end{aligned}$$

Therefore, if we combine the latest two relations to eliminate the terms containing z-derivatives of ρ_1 (and use the fact that $\frac{\partial \rho_0}{\partial z} = -\frac{\rho_0}{H_0}$), we will then obtain

$$\begin{aligned} \frac{\partial^4 p_1}{\partial t^4} - \left[c_s^2 \nabla^2 + \left(g + \frac{(\gamma - 1)c_s^2}{\gamma H_0} \right) \frac{\partial}{\partial z} \right] \frac{\partial^2 p_1}{\partial t^2} - \frac{(\gamma - 1) g c_s^2}{\gamma H_0} \left[\nabla^2 - \frac{\partial^2}{\partial z^2} \right] p_1 & \\ = (\gamma - 1)\rho_0 \left[\frac{\partial^2}{\partial t^2} + \frac{g}{H_0} - g \frac{\partial}{\partial z} \right] \frac{\partial q}{\partial t} & \quad \text{(D.10)} \end{aligned}$$

which only contains pressure fluctuations p_1 as the unknown. Thus, we now have successfully reduced the system of coupled PDEs into one single (higher-order) PDE in terms of just one of the unknown.

At this point, we want to introduce a new variable $\psi = p_1 \; e^{z/2H_0}$. In other words, we need to substitute $p_1 = \psi \; e^{-z/2H_0}$ into Equation D.10. We will start by first computing various derivatives of p_1 in terms of ψ:

$$\begin{aligned}
\frac{\partial p_1}{\partial t} &= \ldots = e^{-z/2H_0}\frac{\partial \psi}{\partial t} \\
\frac{\partial^2 p_1}{\partial t^2} &= \ldots = e^{-z/2H_0}\frac{\partial^2 \psi}{\partial t^2} \\
\frac{\partial p_1}{\partial z} &= \ldots = e^{-z/2H_0}\left[\frac{\partial}{\partial z} - \frac{1}{2H_0}\right]\psi \\
\frac{\partial^2 p_1}{\partial z^2} &= \ldots = e^{-z/2H_0}\left[\frac{\partial^2}{\partial z^2} - \frac{1}{H_0}\frac{\partial}{\partial z} + \frac{1}{4H_0^2}\right]\psi \\
\nabla^2 p_1 &= \ldots = e^{-z/2H_0}\left[\nabla^2 - \frac{1}{H_0}\frac{\partial}{\partial z} + \frac{1}{4H_0^2}\right]\psi
\end{aligned}$$

Note that we are going to use the Laplacian operator in cylindrical coordinate system: $\nabla^2 = \frac{1}{r}\frac{\partial}{\partial r}\left(r\frac{\partial}{\partial r}\right) + \frac{1}{r^2}\frac{\partial^2}{\partial \phi^2} + \frac{\partial^2}{\partial z^2}$ and in this particular coordinate system we may denote $\nabla^2 \equiv \nabla_\perp^2 + \frac{\partial^2}{\partial z^2}$. Throughout the remainder of our discussions, we shall refer to the operator $\nabla_\perp^2$ as the "perpendicular-direction" Laplacian.

Hence, in terms of the new variable ψ and after some algebra, we will obtain

$$\begin{aligned}
\frac{\partial^4 \psi}{\partial t^4} - \frac{\partial^2}{\partial t^2}\left[c_s^2\nabla^2 + \left(g - \frac{c_s^2}{\gamma H_0}\right)\frac{\partial}{\partial z} + \left(\frac{(2-\gamma)c_s^2}{4\gamma H_0^2} - \frac{g}{2H_0}\right)\right]\psi - \frac{(\gamma-1)gc_s^2}{\gamma H_0}\nabla_\perp^2\psi \\
= (\gamma - 1)\rho_0 \; e^{z/2H_0}\left[\frac{\partial^2}{\partial t^2} + \frac{g}{H_0} - g\frac{\partial}{\partial z}\right]\frac{\partial q}{\partial t} \quad \text{(D.11)}
\end{aligned}$$

Recalling that $H_0 = c_s^2/\gamma g$ and defining $\omega_g^2 \equiv (\gamma-1)g^2/c_s^2$ and $\omega_A^2 \equiv \gamma^2 g^2/4c_s^2$, one can readily verify that:

$$g - \frac{c_s^2}{\gamma H_0} = 0\,; \qquad \frac{(2-\gamma)c_s^2}{4\gamma H_0^2} - \frac{g}{2H_0} = -\omega_A^2\,; \qquad \frac{(\gamma-1)gc_s^2}{\gamma H_0} = \omega_g^2 c_s^2\,;$$

Thus, Equation D.11 can be further simplified into:

$$\frac{\partial^4 \psi}{\partial t^4} - \frac{\partial^2}{\partial t^2}\left[c_s^2\nabla^2 - \omega_A^2\right]\psi - \omega_g^2 c_s^2 \; \nabla_\perp^2\psi = (\gamma - 1)\;\rho_{oo}\; e^{-z/2H_0}\left[\frac{\partial^2}{\partial t^2} + \frac{g}{H_0} - g\frac{\partial}{\partial z}\right]\frac{\partial q}{\partial t} \quad \text{(D.11}')$$

where we have also substituted $\rho_0 = \rho_{oo} \; e^{-z/H_0}$ into the RHS of Equation D.11.

D.2 Solution via Fourier-Bessel Transformation

We are now left with the task of solving the PDE (Equation D.11$'$) for ψ, from which we can calculate the pressure perturbations $p_1 = \psi\ e^{-z/2H_0}$. In doing so, we decide to restrict ourselves to axially symmetric solutions (i.e. no azimuthal dependence) and we will also consider steady-state condition. These simplifying conjectures shall be exploited as follows: (i) in steady-state we may expect that $\psi \sim \exp(i\Omega t)$ since this is exactly the form of time dependence possesed by the driving/source term, and we are not expecting unstable solutions; (ii) through axial symmetry we reduce the "perpendicular-direction" Laplacian to be $\nabla_\perp^2 = \frac{1}{r}\frac{\partial}{\partial r}\left(r\frac{\partial}{\partial r}\right)$. Moreover, in order to further exploit the axial symmetry, Fourier-Bessel transformation (also known as Hankel transformation) will be employed as part of our analytical solution method. One can refer to e.g. *Zauderer* [1989] for some background on the use of Hankel transform for solving PDEs in a cylindrically symmetric geometry.

We shall begin this task by first imposing the steady-state solution of the form $\psi \sim \exp(i\Omega t)$. This is going to be equivalent to replacing each partial time derivatives $\frac{\partial}{\partial t} \rightarrow i\Omega$ whenever they are acting on either ψ or q (recall that $q \sim \exp(i\Omega t)$ as well). Therefore, from Equation D.11$'$ we will obtain

$$\Omega^4\psi + \Omega^2\left[c_s^2\nabla^2 - \omega_A^2\right]\psi - \omega_g^2 c_s^2\ \nabla_\perp^2\psi$$
$$= (\gamma - 1)\ \rho_{oo}\ e^{-z/2H_0}\left[-\Omega^2 + \frac{g}{H_0} - g\frac{\partial}{\partial z}\right] i\Omega q \quad \text{(D.12)}$$

The next step is to apply the Fourier-Bessel transformation to the above Equation. More precisely, we will apply Fourier transformation for the z-direction and zero-order Fourier-Bessel (Hankel) transformation for the radial direction. In other words, the integral transformation that we will be using is:

$$\tilde{\psi}(k,\kappa) \equiv \mathcal{FB}\left[\psi\right] = \frac{1}{2\pi}\int_{-\infty}^{\infty} dz \int_0^{\infty} dr\ \psi(r,z)\ r\ J_0(kr)\ e^{i\kappa z} \quad \text{(D.13)}$$

The use of this integral transformation will yield an algebraic equation for $\tilde{\psi}$, which should be easier to solve than the differential equation for ψ.

Assuming that the function ψ has a compact support, we can work out and summarize a few essential rules-of-thumb for this type of integral transfomation as follows:

$$\begin{array}{lcl}
\psi & \rightarrow & \tilde{\psi} = \dfrac{1}{2\pi} \displaystyle\int_{-\infty}^{\infty} dz \int_{0}^{\infty} dr \; \psi(r,z) \; r \, J_0(kr) \; e^{i\kappa z} \\
\dfrac{\partial \psi}{\partial z} & \rightarrow & -i\kappa \; \tilde{\psi} \\
\dfrac{\partial^2 \psi}{\partial z^2} & \rightarrow & -\kappa^2 \tilde{\psi} \\
\nabla_{\perp}^2 \psi & \rightarrow & -k^2 \tilde{\psi} \\
\nabla^2 \psi & \rightarrow & -(k^2 + \kappa^2) \; \tilde{\psi}
\end{array}$$

where Bessel Function identities $J_n'(u) = \frac{1}{2}[J_{n-1}(u) - J_{n+1}(u)]$ and $J_{-1}(u) = -J_1(u)$ had been used in deriving the last two items in the above list.

So far we have been closely following the analytical solution method employed by *Grigor'ev* [1975]. However, we have now arrived at a crossroad that will take us onto a different path — because of our own particular choice for the functional form of the heat deposition profile.

With the aid of our short list above, we can apply this integral transformation to Equation D.12 and obtain

$$\begin{aligned}
\Omega c_s^2 \left[\frac{\Omega^2}{c_s^2} - (k^2 + \kappa^2) - \frac{\omega_A^2}{c_s^2} + \frac{\omega_g^2 k^2}{\Omega^2} \right] \tilde{\psi} &= i\,(\gamma - 1)\rho_{oo} \left(\frac{g}{H_0} - \Omega^2 \right) \mathcal{FB} \left[q \; e^{-z/2H_0} \right] \\
&\quad - i\,(\gamma - 1)\rho_{oo}\, g \; \mathcal{FB} \left[\frac{\partial}{\partial z} \left(q \; e^{-z/2H_0} \right) + \frac{q \; e^{-z/2H_0}}{2H_0} \right] \quad \text{(D.14)}
\end{aligned}$$

Note also that in obtaining Equation D.14, we have expressed the last term in the Equation D.12 as

$$\frac{\partial q}{\partial z} \; e^{-z/2H_0} = \frac{\partial}{\partial z} \left(q \; e^{-z/2H_0} \right) + \frac{q \; e^{-z/2H_0}}{2H_0}$$

which is advantageous since now we will only need to explicitly compute $\mathcal{FB} \left[q \; e^{-z/2H_0} \right]$ and we can rely on the rules-of-thumb for the rest of the transformation.

We shall proceed to carry out the necessary computation:

$$
\begin{aligned}
\mathcal{FB}\left[q\ e^{-z/2H_0}\right] &= \mathcal{FB}\left[q_0\ e^{i\Omega t} e^{-r^2/R^2} e^{-z^2/\sigma_z^2}\ e^{-z/2H_0}\right] \\
&= \frac{q_0\ e^{i\Omega t}}{2\pi} \int_{-\infty}^{\infty} dz \int_0^{\infty} dr\ e^{-r^2/R^2} e^{-z^2/\sigma_z^2}\ e^{-z/2H_0} r J_0(kr)\ e^{i\kappa z} \\
&= \frac{q_0\ e^{i\Omega t}}{2\pi} \int_{-\infty}^{\infty} dz\ e^{-z^2/\sigma_z^2}\ e^{-z/2H_0} e^{i\kappa z} \int_0^{\infty} dr\ e^{-r^2/R^2}\ r J_0(kr) \\
&= \frac{q_0\ e^{i\Omega t}}{2\pi} \cdot \sqrt{\pi\sigma_z^2}\ e^{\sigma_z^2/16H_0^2} e^{-\kappa^2\sigma_z^2/4} \cdot \frac{R^2 e^{-k^2R^2/4}}{2}
\end{aligned} \tag{D.15}
$$

where we have used the practical knowledge that the zero-order Hankel transform of $e^{-a^2r^2/2}$ is $\frac{1}{a^2}e^{-k^2/2a^2}$, and the fact that the Fourier transform of $e^{-\alpha z^2}$ is $\sqrt{\frac{\pi}{\alpha}}\ e^{-\kappa^2/4\alpha}$ [see e.g. *Sneddon*, 1951; *Bracewell*, 1978].

Consequently, we also obtain the following:

$$
\mathcal{FB}\left[\frac{\partial}{\partial z}\left(q\ e^{-z/2H_0}\right)\right] = -i\kappa\ \frac{q_0\ e^{i\Omega t}}{2\pi} \cdot \sqrt{\pi\sigma_z^2}\ e^{\sigma_z^2/16H_0^2} e^{-\kappa^2\sigma_z^2/4} \cdot \frac{R^2 e^{-k^2R^2/4}}{2} \tag{D.16}
$$

which follows quite straightforwardly from the second item in our short list of essential rules-of-thumb earlier.

Hence, using Equation D.15 and D.16, we will find from Equation D.14 that

$$
\left[\frac{\Omega^2}{c_s^2} - \frac{1}{4H_0^2} + \left(\frac{\omega_g^2}{\Omega^2} - 1\right)k^2 - \kappa^2\right]\tilde{\psi} = iB_{oo}\left[\frac{g}{2H_0} - \Omega^2 + i\kappa g\right] e^{-\kappa^2\sigma_z^2/4}\ e^{-k^2R^2/4} \tag{D.17}
$$

where we have used the fact that $\frac{\omega_A^2}{c_s^2} = \frac{1}{4H_0^2}$ and also defined

$$
B_{oo} \equiv \frac{(\gamma-1)\rho_{oo}\ q_0 R^2 \sigma_z \sqrt{\pi}\ e^{\sigma_z^2/16H_0^2}\ e^{i\Omega t}}{4\pi c_s^2 \Omega}
$$

From Equation D.17, it is fairly easy to solve for $\tilde{\psi}$. We now have

$$
\tilde{\psi} = \frac{iB_{oo}\left[\frac{g}{2H_0} - \Omega^2 + i\kappa g\right] e^{-\kappa^2\sigma_z^2/4}\ e^{-k^2R^2/4}}{\left[\frac{\Omega^2}{c_s^2} - \frac{1}{4H_0^2} + \left(\frac{\omega_g^2}{\Omega^2} - 1\right)k^2 - \kappa^2\right]}
$$

and we can finally apply the inverse transform to obtain ψ back:

$$\begin{aligned} \psi &= \int_0^\infty dk \int_{-\infty}^\infty d\kappa\; \tilde{\psi}\; k\; J_0(kr)\; e^{-i\kappa z} \\ &= iB_{oo} \int_0^\infty dk \int_{-\infty}^\infty d\kappa\; \frac{k\; J_0(kr)\; e^{-k^2R^2/4}\; [\frac{g}{2H_0} - \Omega^2 + i\kappa g]\; e^{-\kappa^2\sigma_z^2/4}\; e^{-i\kappa z}}{\left[\frac{\Omega^2}{c_s^2} - \frac{1}{4H_0^2} + \left(\frac{\omega_g^2}{\Omega^2} - 1\right) k^2 - \kappa^2\right]} \end{aligned} \tag{D.18}$$

Although we are left with some integrals to evaluate, but as far as solving the PDE we have essentially accomplished our goal. Once we have obtained ψ, we can compute the actual pressure perturbations p_1 via

$$p_1 = \psi\; e^{-z/2H_0}$$

Subsequently, if we know p_1, we can compute the density fluctuations ρ_1 as well. Using Equation D.8, we will obtain the desired expression

$$\rho_1 = \left[\Omega^2 p_1 - \frac{(\gamma-1)c_s^2}{\gamma H_0}\,\frac{\mathbf{g}\cdot\nabla p_1}{g} + i\Omega(\gamma-1)\rho_0 q\right] \Big/ \left[\Omega^2 c_s^2 - \frac{(\gamma-1)gc_s^2}{\gamma H_0}\right]$$

where we have made the replacement $\frac{\partial}{\partial t} \to i\Omega$ since it is assumed that we are already in the steady-state.

Finally, if we know both p_1 and ρ_1, we can compute the fluid velocity $\mathbf{u}_1$ using Equation D.4. At last, we found that

$$\mathbf{u}_1 = \frac{-\nabla p_1 + \rho_1 \mathbf{g}}{i\Omega\rho_0}$$

where, again, we have replaced $\frac{\partial}{\partial t} \to i\Omega$.

All of these realizations will depend largely on evaluating the inverse transform (Equation D.18) to obtain ψ. In the following section, we are going to assess the results that we have so far, and then make some practical simplifications to evaluate the integral in Equation D.18 in order to complete the analysis.

D.3 Further Simplifications for Practical Purposes

The analytical solution method that we employed seems to work quite effectively. The use of Fourier-Bessel (Hankel) transform had successfully produced an analytical expression for the scaled pressure fluctuations ψ in terms of an integral. The actual pressure fluctuations can be obtained via $p_1 = \psi\, e^{-z/2H_0}$ after we are done evaluating the integral. However, evaluating the integral associated with the inverse Hankel transform seems to be a barrier to actually completing the analysis.

Before trying to evaluate the integral numerically, we would like to make some further analytical simplifications. Let us now rewrite Equation D.18 as

$$\psi = -iB_{oo} \int_0^\infty dk\; k\; J_0(kr)\; e^{-k^2R^2/4} \int_{-\infty}^{\infty} d\kappa\; \frac{\left(\frac{g}{2H_0} - \Omega^2 + i\kappa g\right) e^{-\kappa^2\sigma_z^2/4}\; e^{-i\kappa z}}{[\kappa + \eta(k)] \cdot [\kappa - \eta(k)]} \tag{D.18$'$}$$

where $\eta(k) \equiv \left[\frac{\Omega^2}{c_s^2} - \frac{1}{4H_0^2} + \left(\frac{\omega_g^2}{\Omega^2} - 1\right) k^2\right]^{1/2}$.

In this way, we will have to carry out the $d\kappa$-integration before the dk-integration. The $d\kappa$-integral, which is given by

$$I_\kappa(k) \equiv \int_{-\infty}^{\infty} d\kappa\; \frac{\left(\frac{g}{2H_0} - \Omega^2 + i\kappa g\right) e^{-\kappa^2\sigma_z^2/4}\; e^{-i\kappa z}}{[\kappa + \eta(k)] \cdot [\kappa - \eta(k)]}$$

could probably be evaluated via contour integration in the complex κ-plane. Note that, depending on the value of k and other parameters, the quantity $\eta(k)$ may either be purely real or purely imaginary. By re-expressing $\eta(k)$, we can easily work out what critical value of k separates these two cases: (note that $\Omega < \omega_g < \omega_A$ here)

$$\eta(k) \equiv \left[\left(\frac{\omega_g^2}{\Omega^2} - 1\right) k^2 - \frac{\Omega^2}{c_s^2}\left(\frac{\omega_A^2}{\Omega^2} - 1\right)\right]^{1/2} \quad \Rightarrow \quad k_{\text{crit}} \equiv \frac{\Omega}{c_s}\sqrt{\frac{\omega_A^2/\Omega^2 - 1}{\omega_g^2/\Omega^2 - 1}}$$

It is now clear that the value of $\eta(k)$ is purely imaginary for $k < k_{\text{crit}}$ and purely real for $k \geq k_{\text{crit}}$. When $\eta(k)$ is purely real, we will have a little problem because of the poles/singularities that obstruct our integration path. In general, there is no problem for the case $k < k_{\text{crit}}$ but we certainly need to do something for the case $k \geq k_{\text{crit}}$.

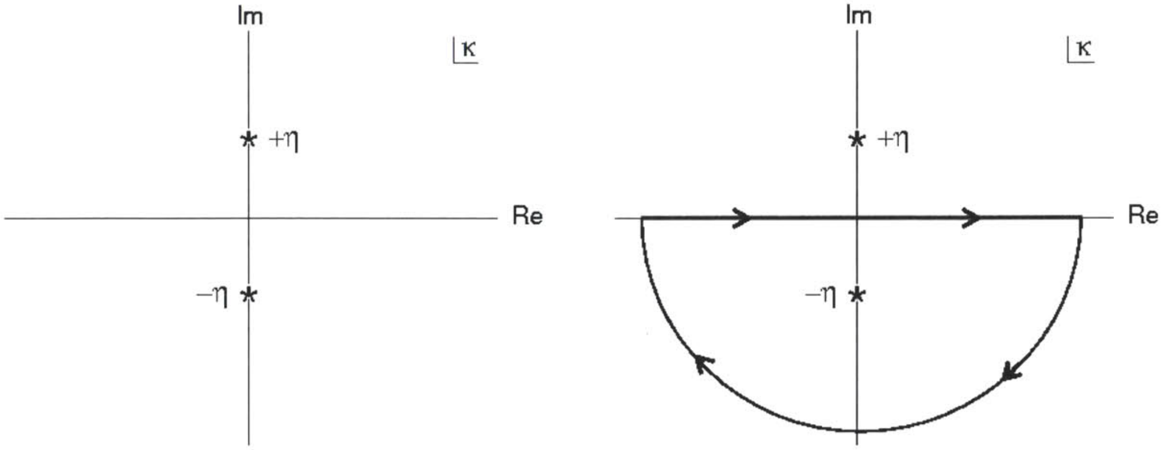

CASE I: $k \in \mathbb{R}$, $k < k_{crit}$

integration contour for CASE I
(no modifications; $k \in \mathbb{R}$, $k < k_{crit}$)

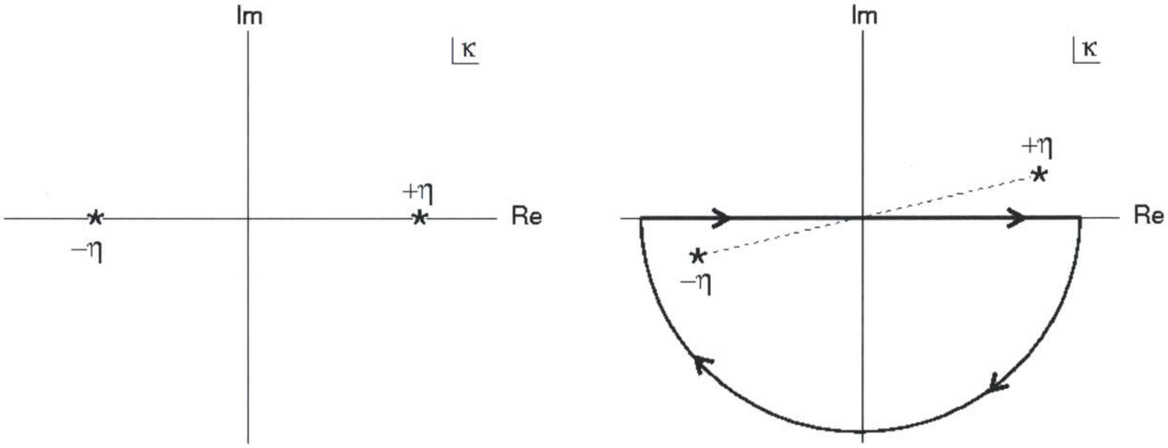

CASE II: $k \in \mathbb{R}$, $k \geqslant k_{crit}$

integration contour for CASE II
(modifications: $k \in \mathbb{C}$, $\mathrm{Re}[k] \geqslant k_{crit}$)

Figure D-2: The selected integration contours in the complex κ-plane for evaluating the scaled pressure perturbation ψ. Also shown are the qualitative location of the poles in the integrand (at $\kappa = \pm\eta$), depending on the values of the wavenumber k.

The poles in the integrand of I_κ are located at $\kappa = \pm\eta(k)$. We will try to handle the case where $\eta(k)$ is purely real by letting the radial wavenumber k to have a small positive imaginary part. In other words, we consider a slight damping in the wave propagation aspect by letting $k \in \mathbb{C}$. Now that $k = k_{\text{Re}} + ik_{\text{Im}}$ ($|k_{\text{Im}}| \ll |k_{\text{Re}}|$), the location of the poles will shift slightly away from the real axis when $k \geq k_{\text{crit}}$ — clearing the integration path. In the case where $k < k_{\text{crit}}$, the poles will shift slightly away from the imaginary axis — without any substantial effect in this case.

Figure D-2 shows the selected integration contours for these two cases together with the corresponding modifications. Note that the integrand of I_κ vanishes at infinity on the lower half of the complex κ-plane, so we shall close the integration contour through the lower half plane to calculate I_κ. Hence, by using the Cauchy's integral theorem we will have

$$I_\kappa = \int_C \frac{f(\kappa)\, d\kappa}{(\kappa + \eta)} = -2\pi i\, f(-\eta) = \pi i \left[\frac{g}{2H_0} - \Omega^2 - ig\,\eta(k)\right] \frac{e^{-\eta^2\sigma_z^2/4}\; e^{+i\eta z}}{\eta(k)} \tag{D.19}$$

Finished with the $d\kappa$-integration, we are now left with the dk-integral to obtain the scaled pressure fluctuations ψ:

$$\psi = -iB_{oo} \int_0^\infty dk\; k\; J_0(kr)\; I_\kappa(k)\; e^{-k^2R^2/4}$$

At this point, note also that we can write $\frac{g}{2H_0} = \frac{\gamma\,\omega_g^2}{2(\gamma-1)}$. Hence, the expression for the scaled pressure fluctuations ψ would be as follows:

$$\psi = \pi B_{oo} \int_0^\infty dk\; k \left[\frac{\gamma\,\omega_g^2}{2(\gamma-1)} - \Omega^2\right] \frac{J_0(kr)}{\eta(k)}\; e^{-k^2R^2/4} e^{-\eta^2\sigma_z^2/4} e^{+i\eta z}$$
$$-\pi i B_{oo} \int_0^\infty dk\; k\, g\; J_0(kr)\; e^{-k^2R^2/4} e^{-\eta^2\sigma_z^2/4} e^{+i\eta z}$$

We can see that the first integral has a singularity when $\eta(k) = 0$, i.e. when $k = k_{\text{crit}}$. Therefore, the first integral should really be carried out over two separate intervals: $k \in [0, k_{\text{crit}})$ and $k \in (k_{\text{crit}}, \infty)$. This procedure should give us the principal value of the first integral. Meanwhile, the second integral is quite straightforward.

In order to facilitate the final prospect of evaluating the integrals numerically, we would like to reduce our current expression for the scaled pressure fluctuations ψ in terms of dimensionless integrals. By defining $\mathfrak{K} \equiv k/k_{\text{crit}}$, then $dk = k_{\text{crit}}\, d\mathfrak{K}$ and we would be able to express η as follows:

$$\eta \equiv \left[\left(\frac{\omega_g^2}{\Omega^2} - 1\right) k^2 - \frac{\Omega^2}{c_s^2}\left(\frac{\omega_A^2}{\Omega^2} - 1\right)\right]^{1/2} \;=\; k_{\text{crit}} \sqrt{(\omega_g^2/\Omega^2 - 1)}\;\sqrt{\mathfrak{K}^2 - 1}$$

Furthermore, since $\omega_A^2 \equiv \frac{\gamma^2 g^2}{4c_s^2} = \frac{\gamma^2 \omega_g^2}{4(\gamma-1)}$ we can also write $\frac{\gamma\,\omega_g^2}{2(\gamma-1)} = \frac{2\,\omega_A^2}{\gamma}$ for the first integral. Thus, in terms of an integral over the dimensionless radial wavenumber $\mathfrak{K}$, the expression for the scaled pressure fluctuations ψ becomes

$$\begin{aligned}\psi = C_1 &\int_0^\infty d\mathfrak{K}\; \mathfrak{K}\, \frac{J_0(\mathfrak{K}\, k_{\text{crit}} r)}{\sqrt{\mathfrak{K}^2 - 1}}\; e^{-\mathfrak{K}^2 k_{\text{crit}}^2 R^2/4}\; e^{-k_{\text{crit}}^2 \sigma_z^2 (\omega_g^2/\Omega^2 - 1)\,(\mathfrak{K}^2 - 1)/4}\; e^{+i k_{\text{crit}} z \sqrt{\omega_g^2/\Omega^2 - 1}\sqrt{\mathfrak{K}^2 - 1}} \\ -C_2 &\int_0^\infty d\mathfrak{K}\; \mathfrak{K}\; J_0(\mathfrak{K}\, k_{\text{crit}} r)\; e^{-\mathfrak{K}^2 k_{\text{crit}}^2 R^2/4}\; e^{-k_{\text{crit}}^2 \sigma_z^2 (\omega_g^2/\Omega^2 - 1)\,(\mathfrak{K}^2 - 1)/4}\; i\, e^{+i k_{\text{crit}} z \sqrt{\omega_g^2/\Omega^2 - 1}\sqrt{\mathfrak{K}^2 - 1}}\end{aligned} \tag{D.20}$$

where the coefficients C_1 and C_2 have been defined as follows:

$$C_1 \equiv \pi B_{oo}\, k_{\text{crit}}\, \Omega^2\, \frac{(2\,\omega_A^2/\gamma\,\Omega^2 - 1)}{\sqrt{\omega_g^2/\Omega^2 - 1}} \qquad \text{and} \qquad C_2 \equiv \pi B_{oo}\, k_{\text{crit}}^2\, g$$

By denoting the first and second integral in Equation D.20 as I_1 and I_2, respectively, we may write $\psi = C_1\, I_1 + C_2\, I_2 = C_2\, (\frac{C_1}{C_2}\, I_1 + I_2)$. The ratio C_1/C_2 conveys the relative importance of the two integrals. If we assume a pure atomic oxygen species and put $g = 9.8$ m/s^2, $\gamma = 5/3$, $2\pi/\Omega = 12$ min, $2\pi/\omega_g = 10$ min, $T = 1000$ K, $R = 30$ km, and $\sigma_z = 5$ km; then $2\pi/\omega_A \approx 9.8$ min, $c_s \approx 928$ m/s, $k_{\text{crit}} \approx 0.01$ rad/km, and therefore $C_1/C_2 \approx 0.93$ is quite typical in this fluid model simulation.

The final formula for ψ (Equation D.20) concludes our discussion on the fluid model. After the integral transforms and some additional simplifications, it is now a relatively simple matter of numerically evaluating the dimensionless integrals with a given set of parameters (repeated at various values of r, z, and t) to obtain $\psi(r, z, t)$ and then $p_1(r, z, t) = \psi\, e^{-z/2H_0}$ in the steady-state.

Appendix E

Numerical Ray Tracing Study

Here we are going to discuss some additional details of our numerical ray tracing study to simulate the digisonde skymap data. We will begin by providing a general description of the ray tracing simulation procedures. In particular, we will elaborate on the suitable form of ray tracing equation and the model for the ionospheric plasma layer. We will then discuss a number of test scenarios that could further illustrate the distinct characteristic signatures (in terms of the skymap echolocations) between point-source ionospheric disturbances and passing-by ionospheric disturbances.

Based on the results of this numerical ray tracing study, we have found that the use of *both* O-mode and X-mode polarizations for the skymap data could potentially give much better diagnostic capabilities. For future endeavors, we therefore recommend that both O-mode and X-mode echoes be recorded when acquiring skymap data.

In ray tracing calculations, one of the main goal is to obtain a parametrized curve $\mathbf{r}(t) \equiv [x(t), y(t), z(t)]$ that represents the propagation path of the wave energy. The *ray path* $\mathbf{r}(t)$ can be calculated by solving the *ray tracing equation* which usually comes in the form of coupled system of ordinary differential equations (ODEs). Basically, it is an initial value problem (IVP) for the ray position $\mathbf{r}$ and the refractive index vector $\mathbf{n} \equiv \frac{c\mathbf{k}}{\omega}$ (where $\mathbf{k}$ is the wavevector). The exact form of the ray tracing equation that needs to be solved in a ray tracing calculation will depend on the wave dispersion relation. In the particular case of electromagnetic wave propagation in magnetized plasmas, we are going to use the Appleton-Hartree dispersion relation.

Recall the familiar Appleton-Hartree dispersion relation for the propagation of electromagnetic waves in magnetized plasmas [see e.g. *Budden*, 1985; *Stix*, 1992]:

$$\frac{c^2k^2}{\omega^2} = 1 - \frac{2X(1-X)}{2(1-X) - Y_T^2 \pm \sqrt{Y_T^4 + 4(1-X)^2 Y_L^2}} \tag{E.1}$$

with the dimensionless parameters X, Y_T, and Y_L defined as follows:

$$X \equiv \frac{\omega_{pe}^2}{\omega^2}; \quad Y_T \equiv \frac{\omega_{ce}}{\omega}\sin\theta\,; \quad Y_L \equiv \frac{\omega_{ce}}{\omega}\cos\theta\,;$$

where θ is the angle between the wavevector $\mathbf{k}$ and background magnetic field $\mathbf{B}_0$. The +ve (−ve) sign in the above dispersion relation corresponds to the ordinary (extraordinary) wave polarization.

In general, phase velocity $\mathbf{v}_\phi$ and group velocity $\mathbf{v}_g$ differ in both magnitude and direction (with an angle α between them). The phase velocity (magnitude $= \omega/k$) points along the direction of the wavevector $\mathbf{k}$, whereas the group velocity (magnitude $= \partial\omega/\partial k$) points along the direction of energy propagation. With regards to the phase velocity, we have the *wave refractive index* which is defined as $n \equiv \frac{c}{v_\phi} = \frac{ck}{\omega}$. Meanwhile, with regards to the group velocity, we have the *group refractive index* which is defined as $n' \equiv \frac{c}{u_z}$ where $u_z \equiv \mathbf{v}_g \cdot \hat{k} = v_g \cos\alpha$. The two are related by $n' = n + \omega\frac{\partial n}{\partial \omega}$. Based on the Appletion-Hartree dispersion relation, the corresponding expression for the group refractive index is [*Davies*, 1965]:

$$n' = n + (1-n^2)^2 \left[\frac{1}{nX} + \frac{Y_T^2}{2n(1-X)^2} \pm \frac{2(1-X)^3 Y_L^2 - XY_T^4}{2nX(1-X)^2\sqrt{Y_T^4 + 4Y_L^2(1-X)^2}} \right] \tag{E.2}$$

Note that the dispersion relation (Equation E.1) is in the form of $\mathbf{n} \cdot \mathbf{n} = \mathcal{N}^2(\mathbf{r}, \mathbf{n})$, where $\mathbf{r} \equiv [x, y, z]$ and $\mathbf{n} \equiv [n_x, n_y, n_z]$. Thus, the wave refractive index n as a function of spatial location and wavevector orientation would simply be $\mathcal{N}(\mathbf{r}, \mathbf{n})$. Similarly, the group refractive index n' as a function of spatial location and wavevector orientation can be obtained by substituting $\mathcal{N}(\mathbf{r}, \mathbf{n})$ for n in Equation E.2.

Next, we shall discuss how a practical set of ray tracing equations can be formulated using the wave dispersion relation, and how one can make the appropriate adjustment to arrive at a form of ray tracing equations suitable for simulating the digisonde data. From the dispersion relation $\mathbf{n} \cdot \mathbf{n} = \mathcal{N}^2(\mathbf{r}, \mathbf{n})$, we can define the following quantity:

$$\mathcal{D}(\mathbf{r}, \mathbf{n}) \equiv \frac{\sqrt{\mathbf{n} \cdot \mathbf{n}}}{\mathcal{N}(\mathbf{r}, \mathbf{n})}$$

While the propagating wave indeed satisfies $\mathcal{D}(\mathbf{r}, \mathbf{n}) = 1$ at all times, the partial derivatives of $\mathcal{D}(\mathbf{r}, \mathbf{n})$ is generally nonzero. It can be proven [see e.g. *Budden*, 1985] that the partial derivatives of $\mathcal{D}(\mathbf{r}, \mathbf{n})$ tell us about the direction of energy propagation and the time rate of change of the refractive index vector $\mathbf{n}$. More precisely, $\nabla_n \mathcal{D}(\mathbf{r}, \mathbf{n})$ points in the direction of energy propagation (i.e. the time-averaged Poynting vector); and $\nabla_r \mathcal{D}(\mathbf{r}, \mathbf{n})$ is colinear with $\frac{d\mathbf{n}}{dt}$. Based on this principle, one has the following set of simple ray tracing equations [*Budden*, 1985]:

$$\frac{d\mathbf{r}}{dt} = \frac{d}{dt}\begin{bmatrix} x \\ y \\ z \end{bmatrix} = c \begin{bmatrix} \partial\mathcal{D}/\partial n_x \\ \partial\mathcal{D}/\partial n_y \\ \partial\mathcal{D}/\partial n_z \end{bmatrix} \tag{E.3}$$

$$\frac{d\mathbf{n}}{dt} = \frac{d}{dt}\begin{bmatrix} n_x \\ n_y \\ n_z \end{bmatrix} = -c \begin{bmatrix} \partial\mathcal{D}/\partial x \\ \partial\mathcal{D}/\partial y \\ \partial\mathcal{D}/\partial z \end{bmatrix} \tag{E.4}$$

which had been implemented numerically by *Dalrymple* [PhD Thesis, MIT, 2001] and *Dorfman* [BS Thesis, MIT, 2005] for their respective ionospheric ray tracing studies. Solving the ray tracing equations will yield the ray path $\mathbf{r}(t)$, which forms a parametrized curve describing the propagation path of the wave energy.

However, the above ray tracing equation (E.3 and E.4) is actually not suitable for simulating the digisonde data. In the digisonde data simulation, we need to determine the exact time-of-flight of diagnostic radio pulses, but unfortunately $\frac{d\mathbf{r}}{dt}$ in Equation E.3 is not equal to the group velocity $\mathbf{v}_g$. Rather, $\frac{d\mathbf{r}}{dt}$ in Equation E.3 is equal to the so-called *ray velocity* $\mathbf{v}_R$, which points in the same direction as the group velocity $\mathbf{v}_g$ but has an entirely different magnitude. In fact, $|\mathbf{v}_R| = |\mathbf{v}_\phi| \sec\alpha$ which could yield an unreasonably large value exceeding the speed of light in vacuum.

For the digisonde data simulation, we require a set of ray tracing equations in which the ray position $\mathbf{r}(t)$ moves along the ray path with a velocity equal to the group velocity $\mathbf{v}_g$. The earlier ray tracing equations (E.3 and E.4) had been shown to be unsuitable for this specific purpose, so we should make some appropriate adjustment. Fortunately, we will only need a rather straightforward modification because the ray velocity $\mathbf{v}_R$ is already pointing in the same direction as the group velocity $\mathbf{v}_g$. Essentially, the earlier ray tracing equations (E.3 and E.4) should be rescaled in such a way that $\frac{d\mathbf{r}}{dt} = \mathbf{v}_g$. First of all, using the group refractive index $n' = n + \omega \frac{\partial n}{\partial \omega}$ we can rescale the ray velocity $\mathbf{v}_R$ into the group velocity $\mathbf{v}_g$ as follows:

$$\mathbf{v}_g = \frac{c}{n' \cos\alpha} \cdot \frac{\mathbf{v}_R}{|\mathbf{v}_R|} = \frac{c \sec\alpha}{\left(n + \omega \frac{\partial n}{\partial \omega}\right)} \cdot \frac{1}{\sqrt{\left(\frac{\partial \mathcal{D}}{\partial n_x}\right)^2 + \left(\frac{\partial \mathcal{D}}{\partial n_y}\right)^2 + \left(\frac{\partial \mathcal{D}}{\partial n_z}\right)^2}} \begin{bmatrix} \partial\mathcal{D}/\partial n_x \\ \partial\mathcal{D}/\partial n_y \\ \partial\mathcal{D}/\partial n_z \end{bmatrix}$$

because $n' \equiv \frac{c}{u_z}$ where $u_z \equiv \mathbf{v}_g \cdot \hat{k} = v_g \cos\alpha$. Furthermore, some basic vector algebra relations also tell us that

$$\cos\alpha = \frac{\mathbf{n} \cdot \mathbf{v}_R}{|\mathbf{n}|\,|\mathbf{v}_R|} \quad \Rightarrow \quad \sec\alpha = \frac{|\mathbf{n}|\,|\mathbf{v}_R|}{(\mathbf{n} \cdot \mathbf{v}_R)} = \frac{n\sqrt{\left(\frac{\partial \mathcal{D}}{\partial n_x}\right)^2 + \left(\frac{\partial \mathcal{D}}{\partial n_y}\right)^2 + \left(\frac{\partial \mathcal{D}}{\partial n_z}\right)^2}}{\left[n_x \frac{\partial \mathcal{D}}{\partial n_x} + n_y \frac{\partial \mathcal{D}}{\partial n_y} + n_z \frac{\partial \mathcal{D}}{\partial n_z}\right]}$$

Therefore, we can finally rescale both Equations E.3 and E.4 to arrive at the following set of ray tracing equations:

$$\frac{d\mathbf{r}}{dt} = \frac{c\,.\,n}{\left(n + \omega \frac{\partial n}{\partial \omega}\right)\left[n_x \frac{\partial \mathcal{D}}{\partial n_x} + n_y \frac{\partial \mathcal{D}}{\partial n_y} + n_z \frac{\partial \mathcal{D}}{\partial n_z}\right]} \begin{bmatrix} \partial\mathcal{D}/\partial n_x \\ \partial\mathcal{D}/\partial n_y \\ \partial\mathcal{D}/\partial n_z \end{bmatrix} \tag{E.5}$$

$$\frac{d\mathbf{n}}{dt} = \frac{-c\,.\,n}{\left(n + \omega \frac{\partial n}{\partial \omega}\right)\left[n_x \frac{\partial \mathcal{D}}{\partial n_x} + n_y \frac{\partial \mathcal{D}}{\partial n_y} + n_z \frac{\partial \mathcal{D}}{\partial n_z}\right]} \begin{bmatrix} \partial\mathcal{D}/\partial x \\ \partial\mathcal{D}/\partial y \\ \partial\mathcal{D}/\partial z \end{bmatrix} \tag{E.6}$$

which would be suitable for our numerical simulation of the digisonde skymap data.

We shall now describe how the ionospheric plasma layer is modeled for this numerical ray tracing study. First, we set up the background ionospheric profile using a simple Chapman function [see e.g. *Whitten and Poppoff*, 1965]:

$$N_{e0} = N_0 \exp\left[\frac{1}{2}\left(1 - \frac{z - z_0}{H_0} - \sec\chi \, . \, e^{-(z-z_0)/H_0}\right)\right] \tag{E.7}$$

where z_0 is the altitude of maximum plasma density, H_0 is the scale height, and χ is the solar zenith angle. We typically set $z_0 = 220$ km, $H_0 = 60$ km, and $\chi = 0°$ in this study. Next, we are going to add some additional wavelike irregularities to the background profile, e.g. $\delta N_e = 3\% \cdot N_{e0} \sin(\mathbf{k}_{\text{IRR}} \cdot \mathbf{r})$. Hence the total plasma density in the modeled ionospheric layer would be given by $N_e = N_{e0} + \delta N_e$. Furthermore, we will also equip δN_e with an adjustable parameter so that the periodic pattern of plasma disturbances can be made to evolve and propagate.

With all the necessary ingredients covered, we are finally ready to discuss our numerical ray tracing study. In brief, the simulation procedure is as follows:

1. Set up the equilibirum ionospheric plasma layer model (use Chapman function), embed a model of traveling ionospheric disturbances (use periodic pattern), and set the background magnetic field strength and orientation (uniform B-field).
2. Select a value of sounding frequency to be used in the numerical simulation.
3. Let the spatial configuration of the prescribed periodic pattern to evolve gradually in small steps until it completes a full cycle. For each spatial configuration:
    (a) solve the ray tracing equation (repeat for various launch angles)
    (b) mark the rays that land "close enough" to the receiver position
    (c) for such qualified rays, record the time delay Δt and the arrival angle θ_{arr}
4. Graph the echolocations based on the tabulated data of Δt and θ_{arr} to see how they change as the pattern of traveling disturbances evolve as a function of time.

In our simulations, the term "close enough" practically means ≤ 5 km. This criteria can be made more stringent if the launch angle is sampled with a finer increment.

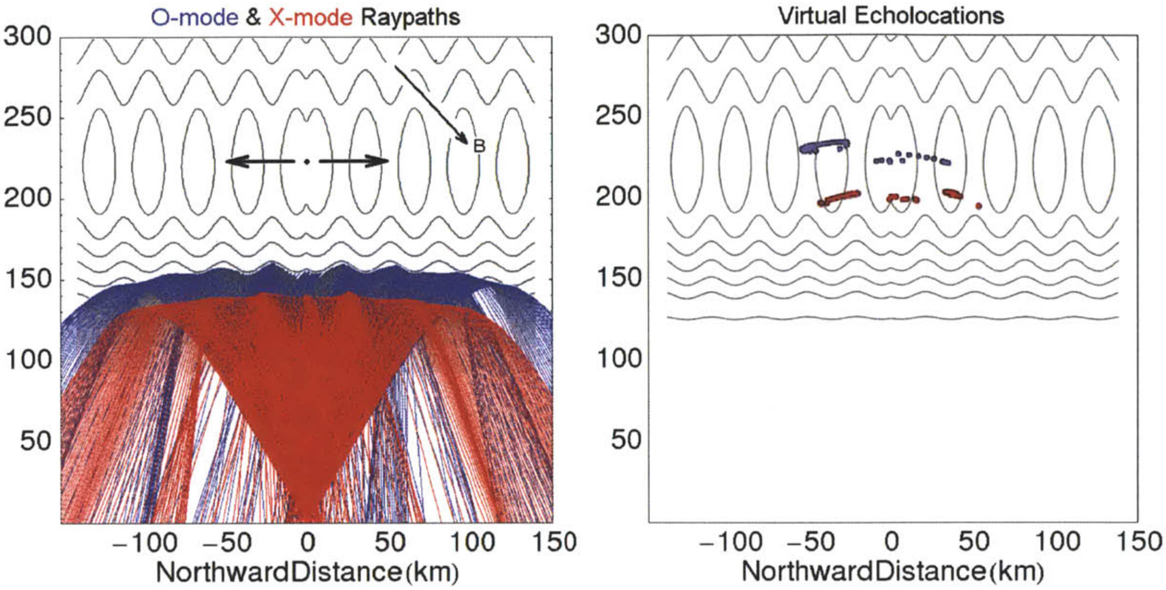

Figure E-1: The configuration of ionospheric plasma disturbance to be investigated in Part 1. The wavelength of these traveling disturbances is $\lambda = 30$ km. The background magnetic field points at 50° from horizontal direction. The peak plasma frequency we used in the ionospheric model is 4.9 MHz, and electron gyrofrequency is 1.0 MHz.

E.1 Ray Tracing Study: Part 1

In this part, we will set up a pattern of periodic disturbances that originate from a single point overhead. These disturbances will be generated continuously and spread out horizontally in both directions. The "digisonde" will launch both O-mode and X-mode radio diagnostic waves into the plasma layer, and then we will record their corresponding echolocations. We are going to vary the sounding frequency using the following values: 4.0, 4.4, 4.8, 5.2, 5.25, 5.3, 5.35, and 5.4 MHz. When the selected sounding frequency becomes larger than the peak plasma frequency, we will no longer have any O-mode echoes. However, we would still have the X-mode echoes since all the sounding frequencies are below the right-hand cutoff frequency.

In this scenario (i.e. point-source ionospheric disturbance), the simulated skymap echolocations can indeed be seen shifting radially outward from the center point. For O-mode echoes, the signatures of radial outward propagation are more dominant on the south side. For X-mode echoes, the signatures appear ~equally on both sides.

Point-source disturbance ($\lambda = 30$ km), sounding frequency 4.0 MHz:

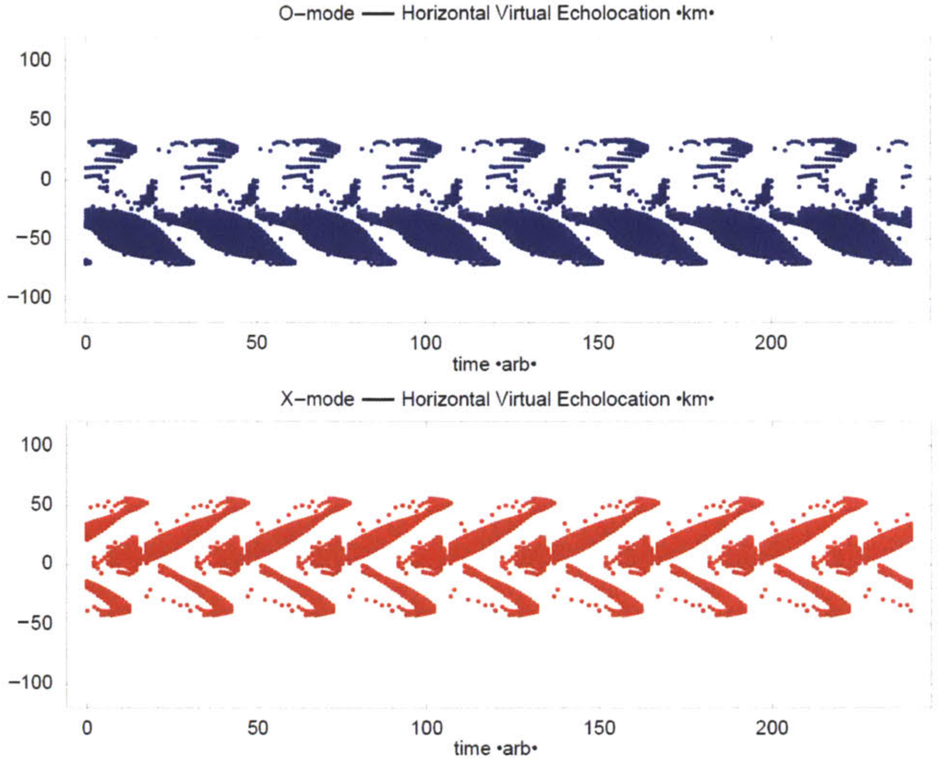

Point-source disturbance ($\lambda = 30$ km), sounding frequency 4.4 MHz:

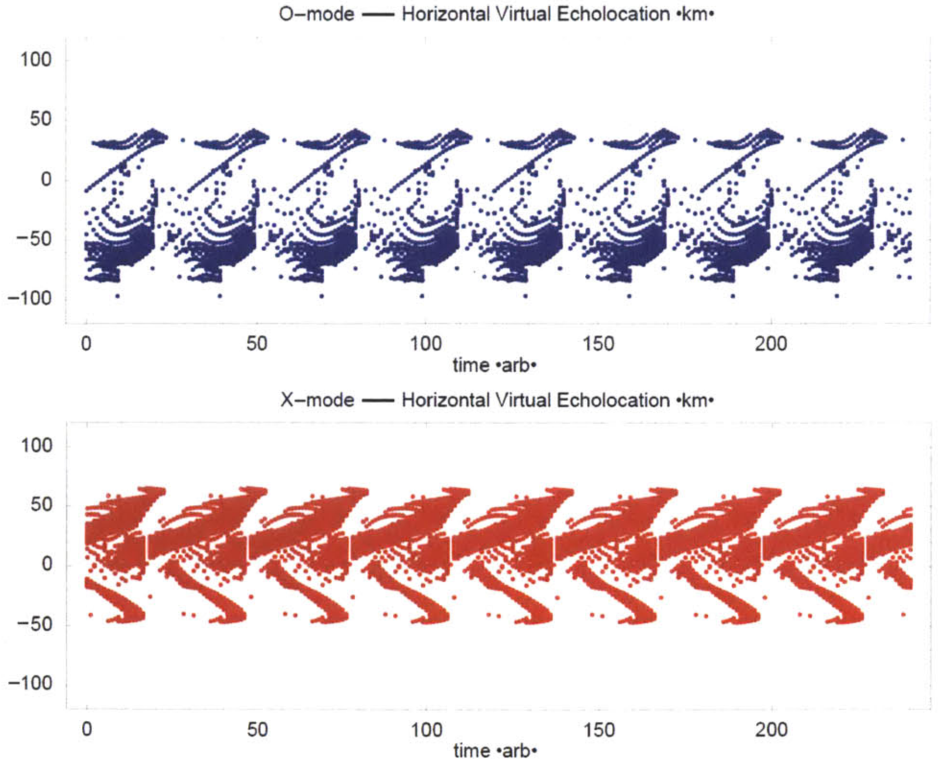

Point-source disturbance ($\lambda = 30$ km), sounding frequency 4.8 MHz:

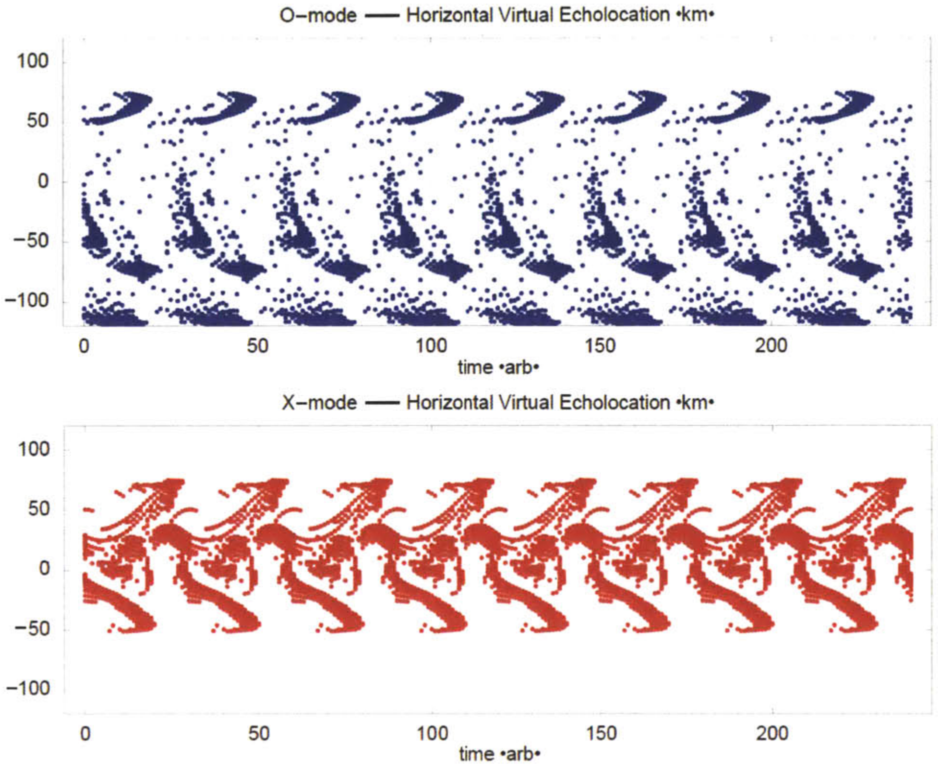

Point-source disturbance ($\lambda = 30$ km), sounding frequency 5.2 MHz:

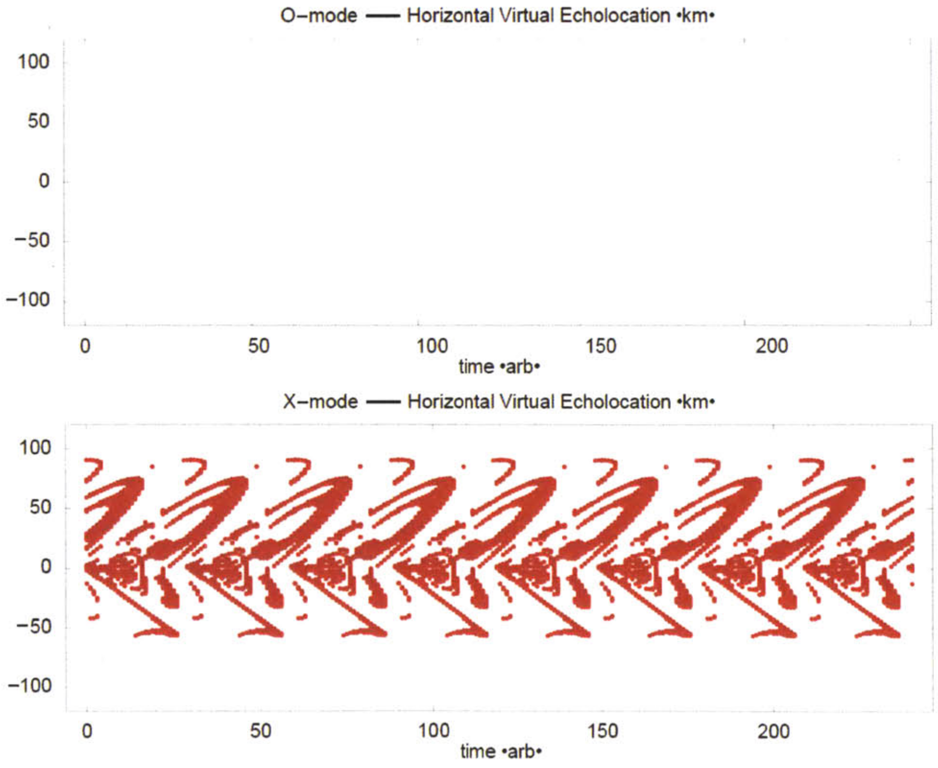

Point-source disturbance ($\lambda = 30$ km), sounding frequency 5.25 MHz:

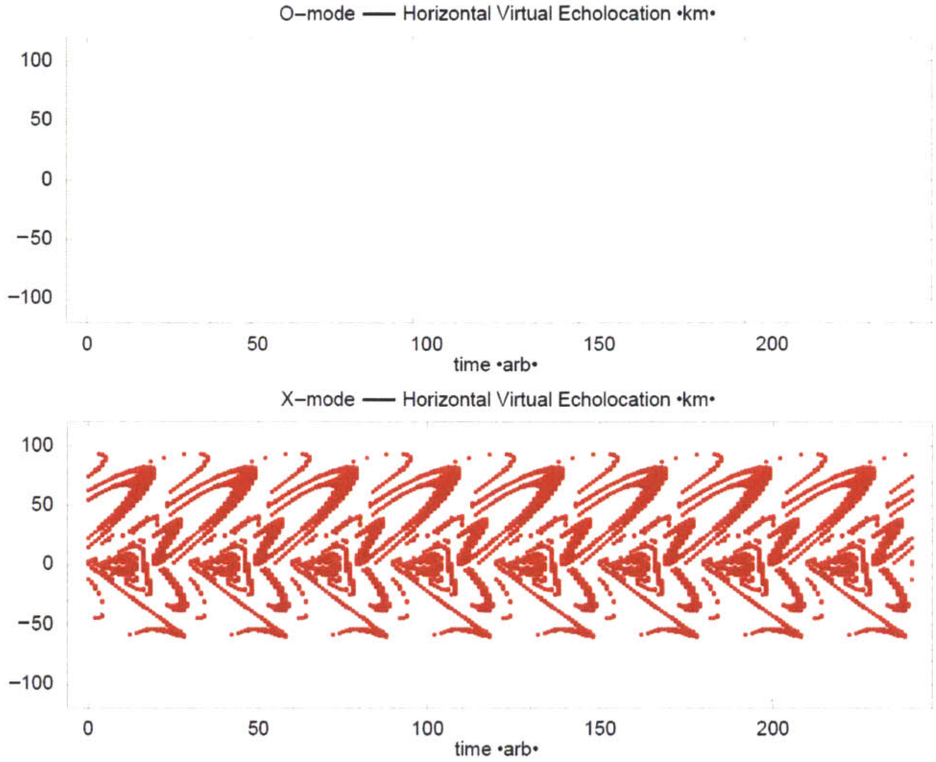

Point-source disturbance ($\lambda = 30$ km), sounding frequency 5.3 MHz:

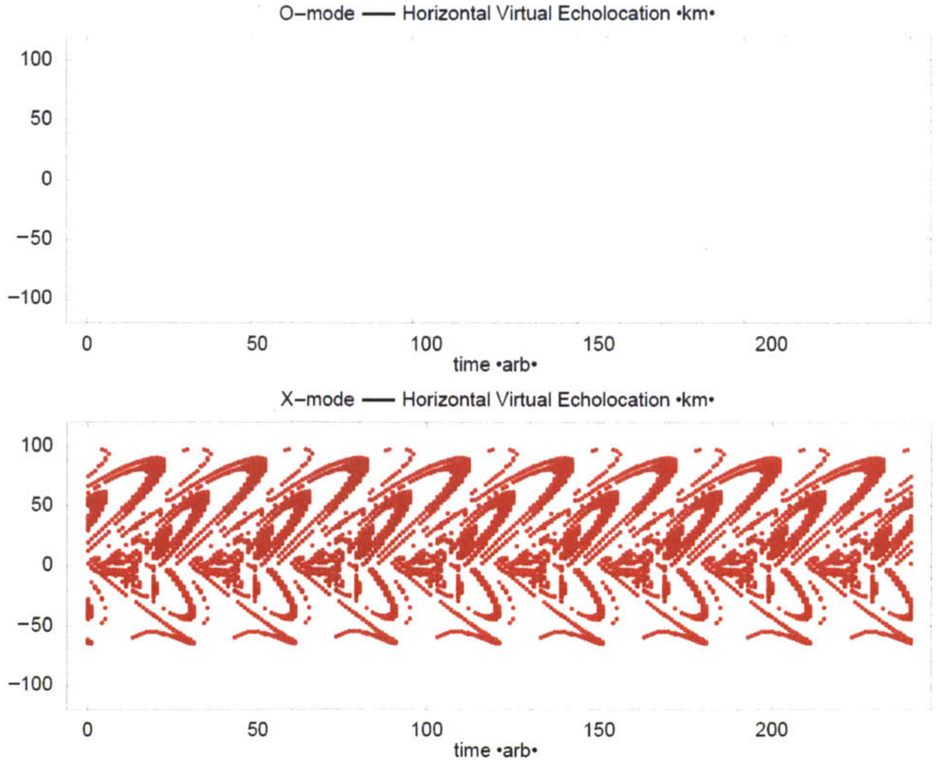

Point-source disturbance ($\lambda = 30$ km), sounding frequency 5.35 MHz:

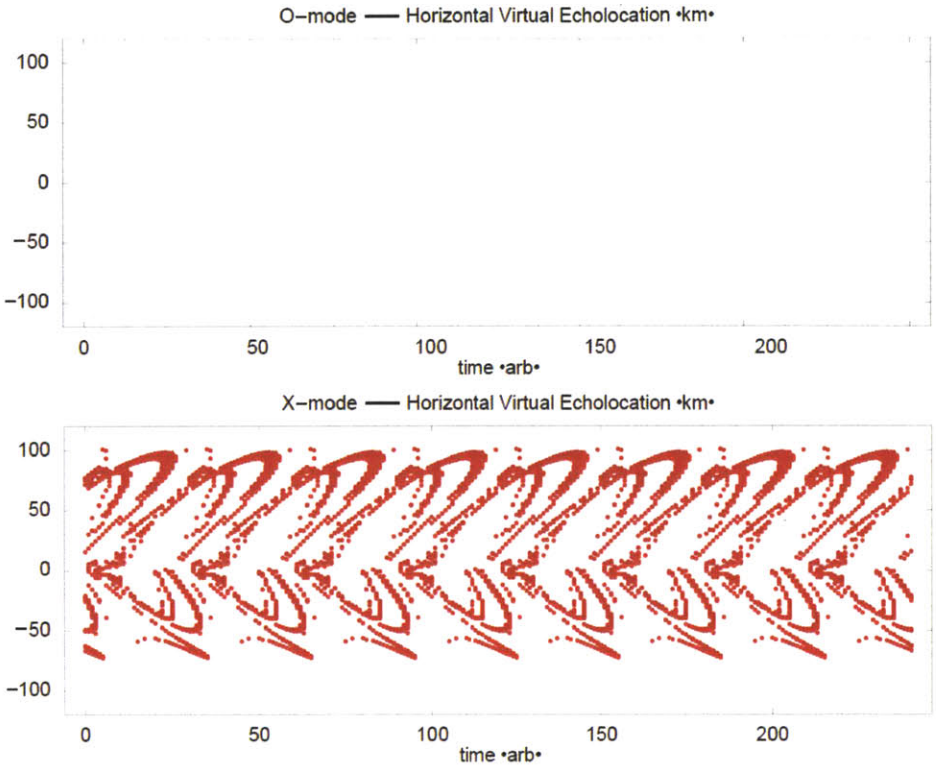

Point-source disturbance ($\lambda = 30$ km), sounding frequency 5.4 MHz:

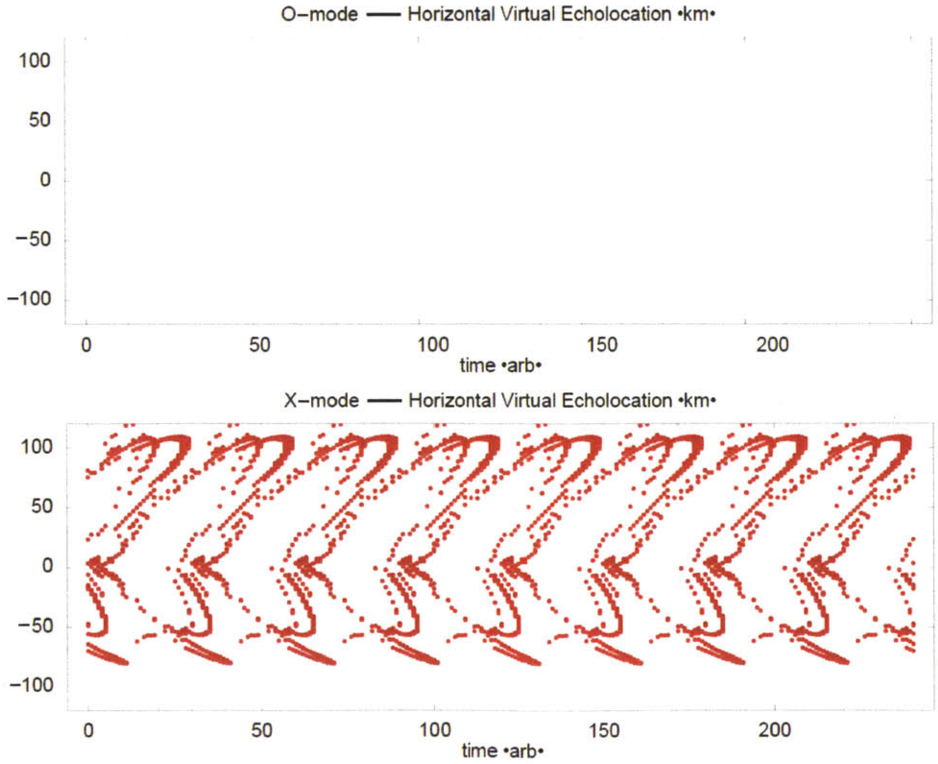

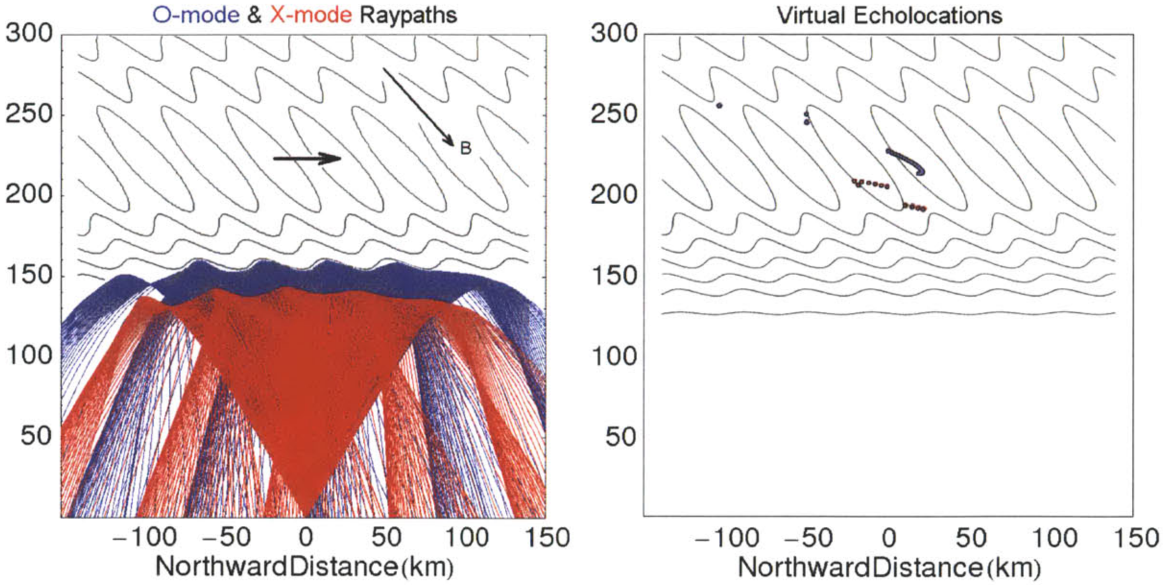

Figure E-2: The configuration of ionospheric plasma disturbance to be investigated in Part 2. Along the horizontal axis, the periodic pattern repeats every ~39 km (the sheet separation is $\lambda_{\perp} = 30$ km). The background magnetic field points at 50° from horizontal direction. Peak plasma frequency in this ionospheric model is 4.9 MHz, and electron gyrofrequency is 1.0 MHz.

E.2 Ray Tracing Study: Part 2

In this part, we are going to set up a pattern of periodic disturbances that will simply pass by overhead and propagate horizontally in one direction only. The "digisonde" will launch both O-mode and X-mode radio diagnostic waves into the plasma layer, and then we will record their corresponding echolocations. In this case we are going to vary the sounding frequency using the following values: 4.0, 4.5, 4.8, and 5.3 MHz. For sounding frequencies larger than the peak plasma frequency, we will no longer have any O-mode echoes. However, we would still have the X-mode echoes as long as the sounding frequency is below the right-hand cutoff frequency.

In this scenario (i.e. passing-by ionospheric disturbance), the simulated skymap echolocations can be clearly seen approaching the center point from one side and then passing through into the opposite side. Qualitatively speaking, there is no significant difference between O-mode and X-mode in this case. At various sounding frequencies, the qualitative features for both wave polarizations had been remarkably similar.

Passing-by disturbance ($\lambda_{\perp} = 30$ km), sounding frequency 4.0 MHz:

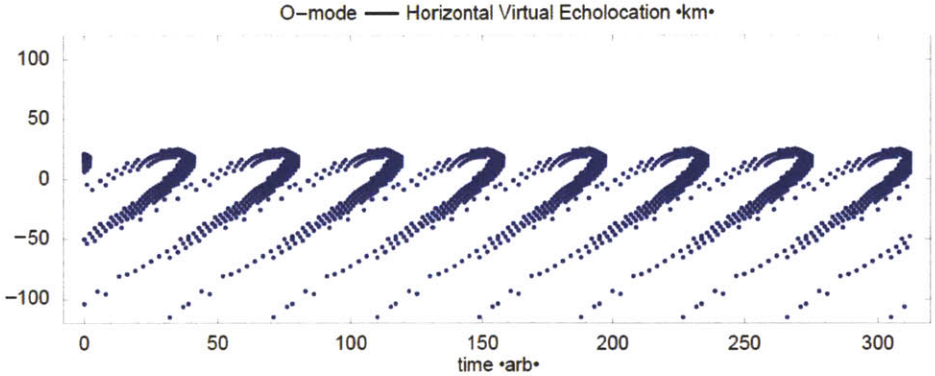

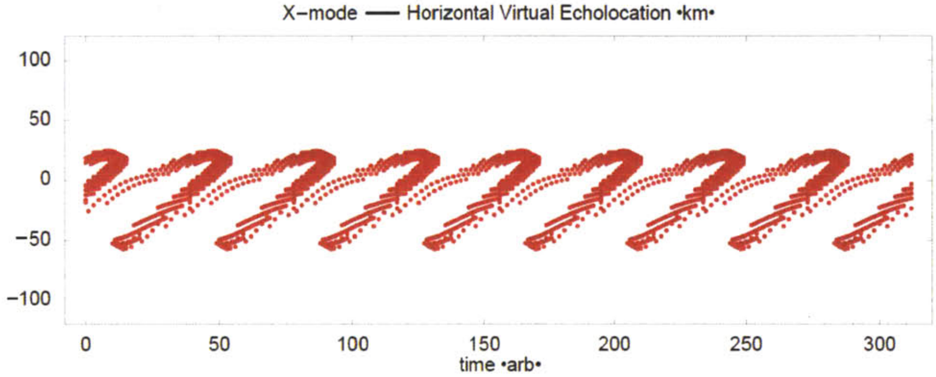

Passing-by disturbance ($\lambda_{\perp} = 30$ km), sounding frequency 4.5 MHz:

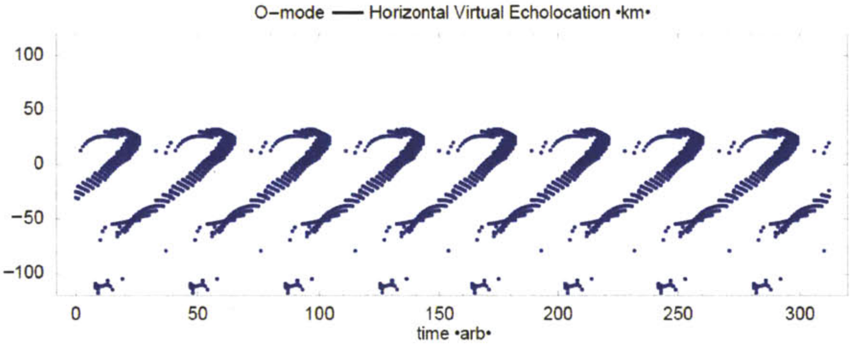

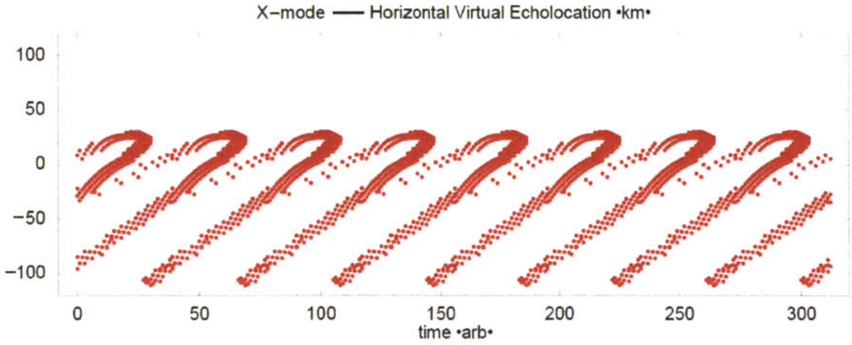

Passing-by disturbance ($\lambda_\perp = 30$ km), sounding frequency 4.8 MHz:

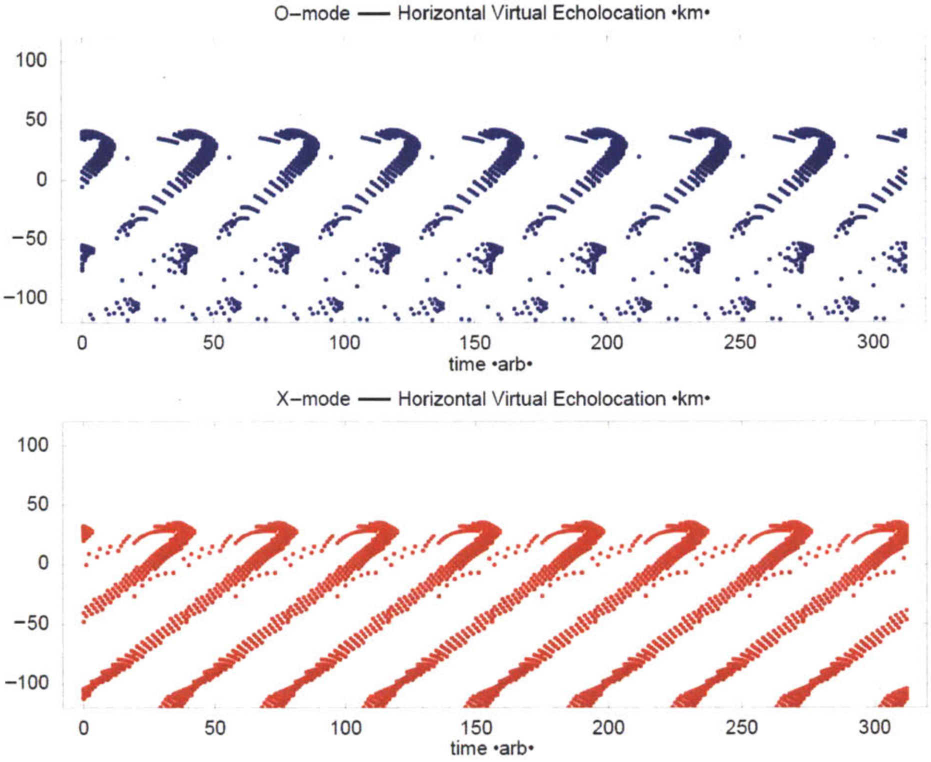

Passing-by disturbance ($\lambda_\perp = 30$ km), sounding frequency 5.3 MHz:

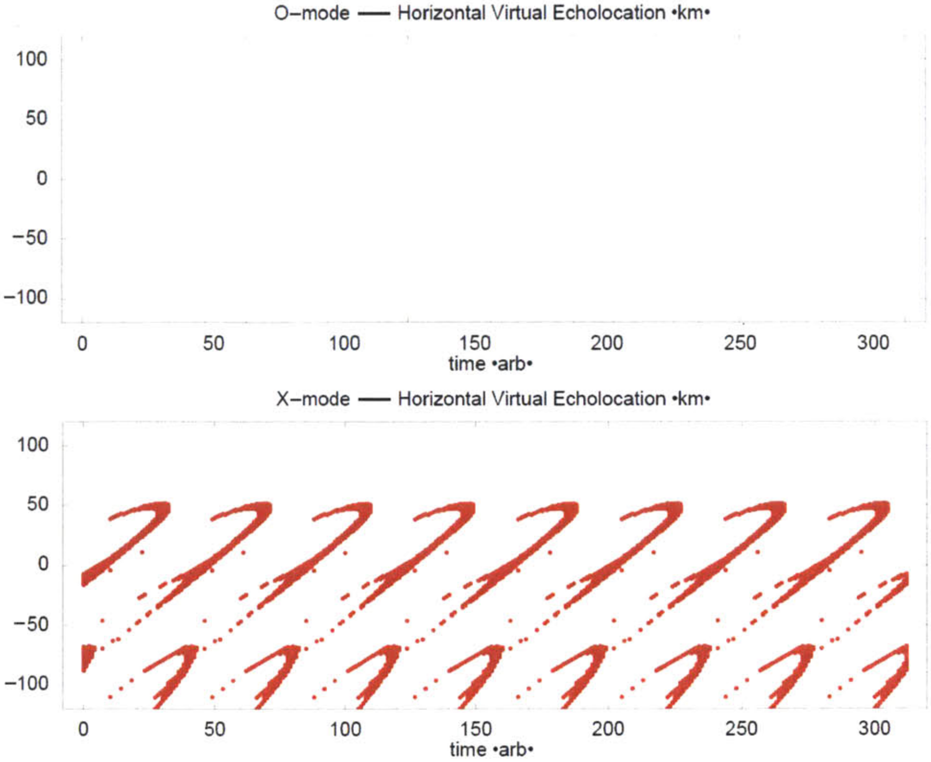

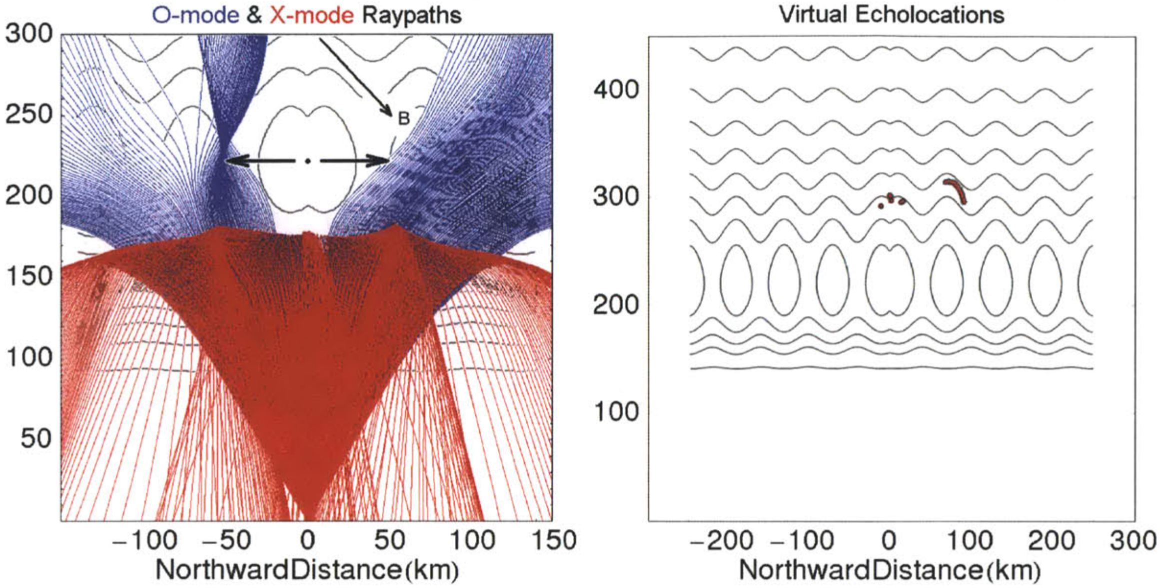

Figure E-3: The configuration of ionospheric plasma disturbance to be investigated in Part 3. The wavelength of these traveling disturbances is $\lambda = 60$ km. The background magnetic field points at 50° from horizontal direction. The peak plasma frequency we used in the ionospheric model is 4.9 MHz, and electron gyrofrequency is 1.0 MHz.

E.3 Ray Tracing Study: Part 3

In this part, we will set up a pattern of periodic disturbances that originate from a single point overhead. The disturbances will be generated continuously and spread out horizontally in both directions. The "digisonde" will launch both O-mode and X-mode radio diagnostic waves into the plasma layer, and then we will record their corresponding echolocations. We vary the sounding frequency using the following values: 5.15, 5.2, 5.25, 5.3, 5.35, 5.4, and 5.45 MHz. All of the selected sounding frequencies are larger than the peak plasma frequency, so there would be no O-mode echoes in this case. Nonetheless, we would certainly have X-mode echoes because those sounding frequencies are below the right-hand cutoff frequency.

This setup is basically a redo of part 1, except that we use a larger wavelength (2×30 km $= 60$ km) for the ionospheric plasma disturbances and we only concentrate on X-mode echoes. Our earlier result from part 1 seems to be quite robust: here we also see the clear pattern of radial outward propagation away from the center point.

Point-source disturbance ($\lambda = 60$ km), sounding frequency 5.15 MHz:

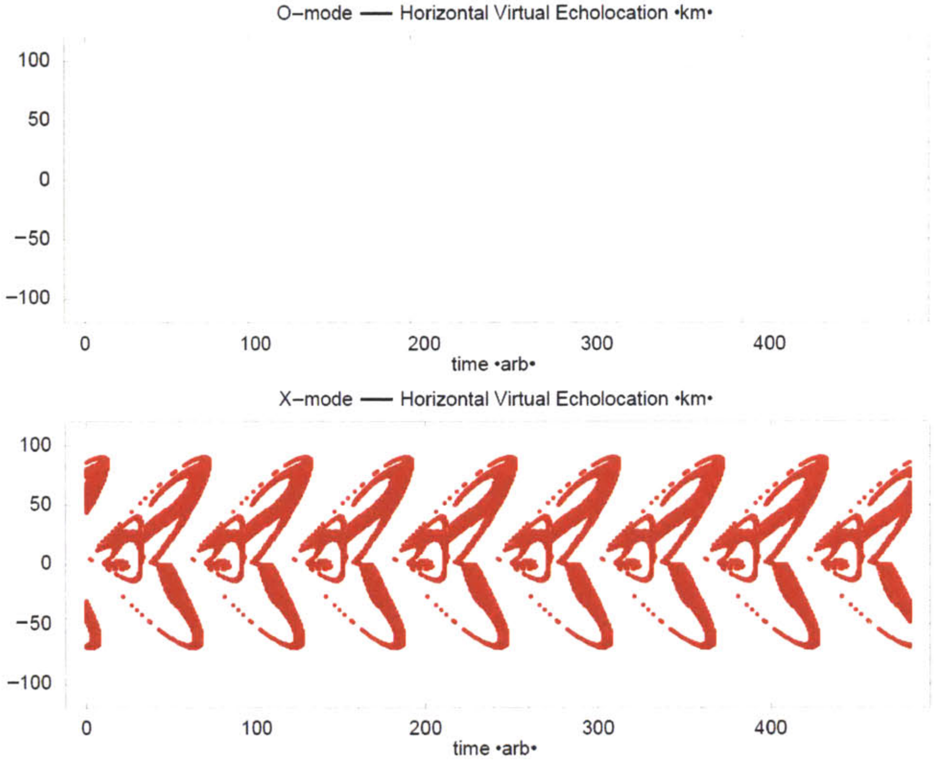

Point-source disturbance ($\lambda = 60$ km), sounding frequency 5.2 MHz:

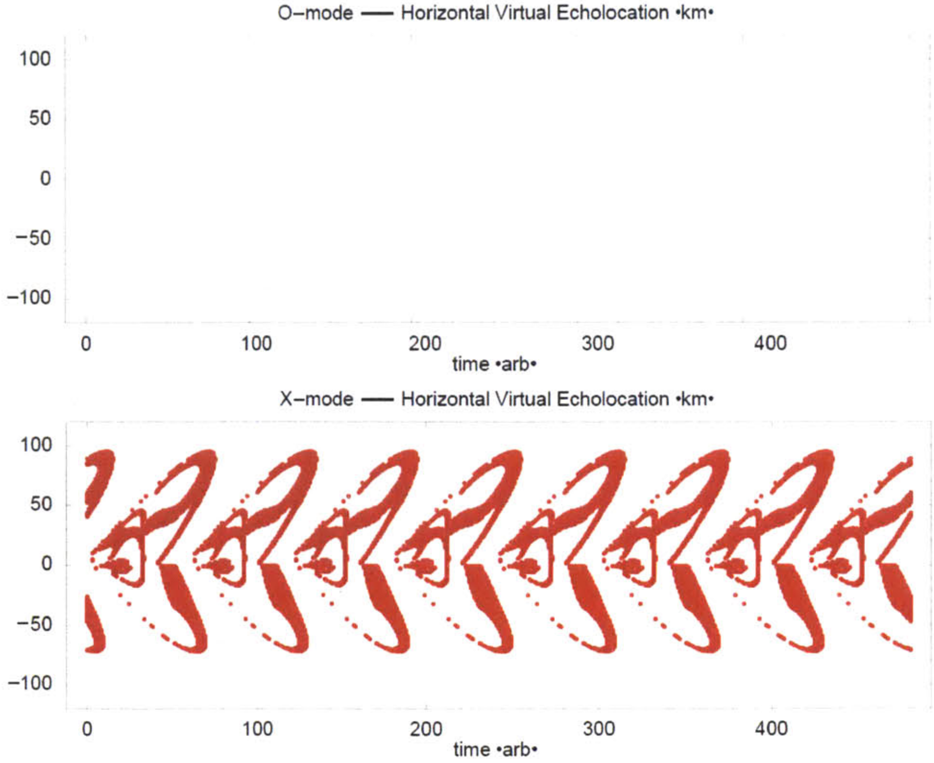

Point-source disturbance ($\lambda = 60$ km), sounding frequency 5.25 MHz:

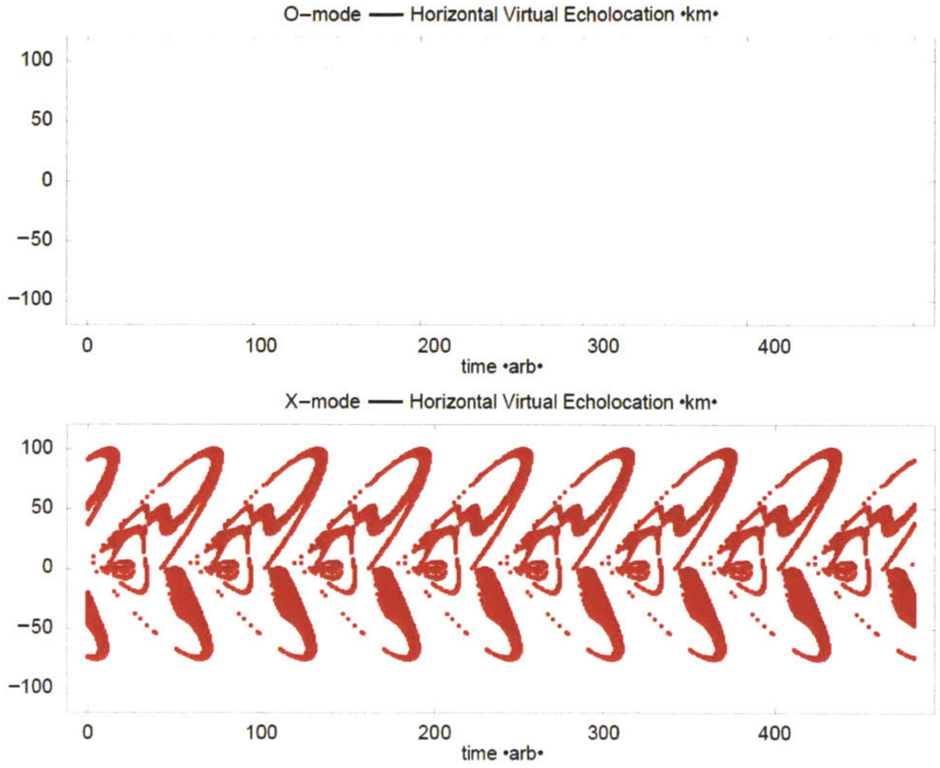

Point-source disturbance ($\lambda = 60$ km), sounding frequency 5.3 MHz:

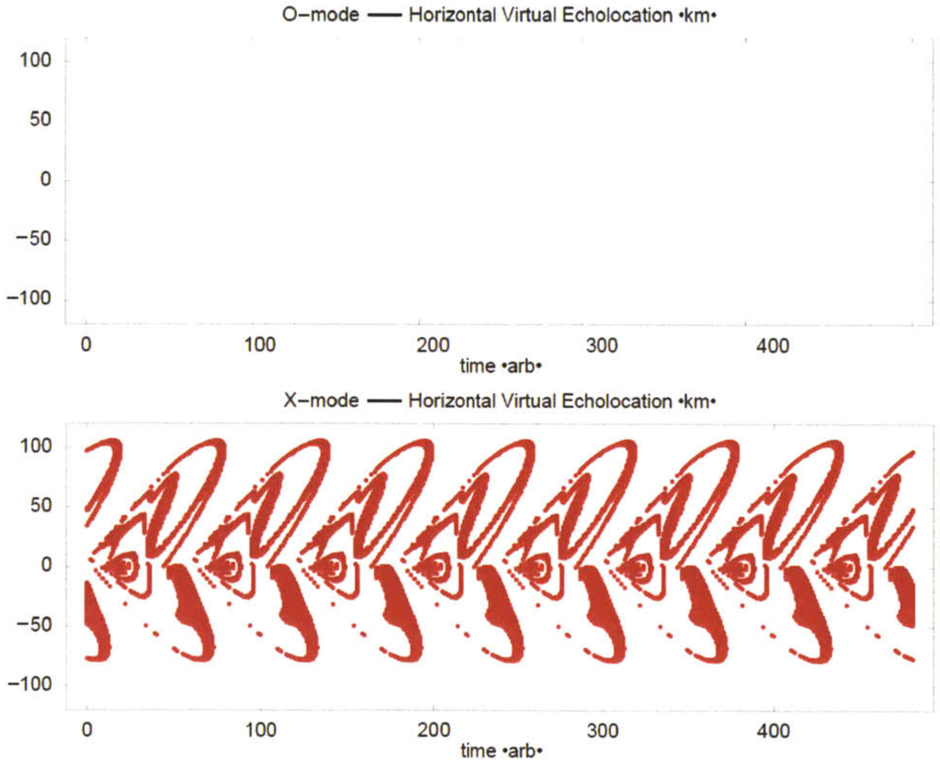

Point-source disturbance ($\lambda = 60$ km), sounding frequency 5.35 MHz:

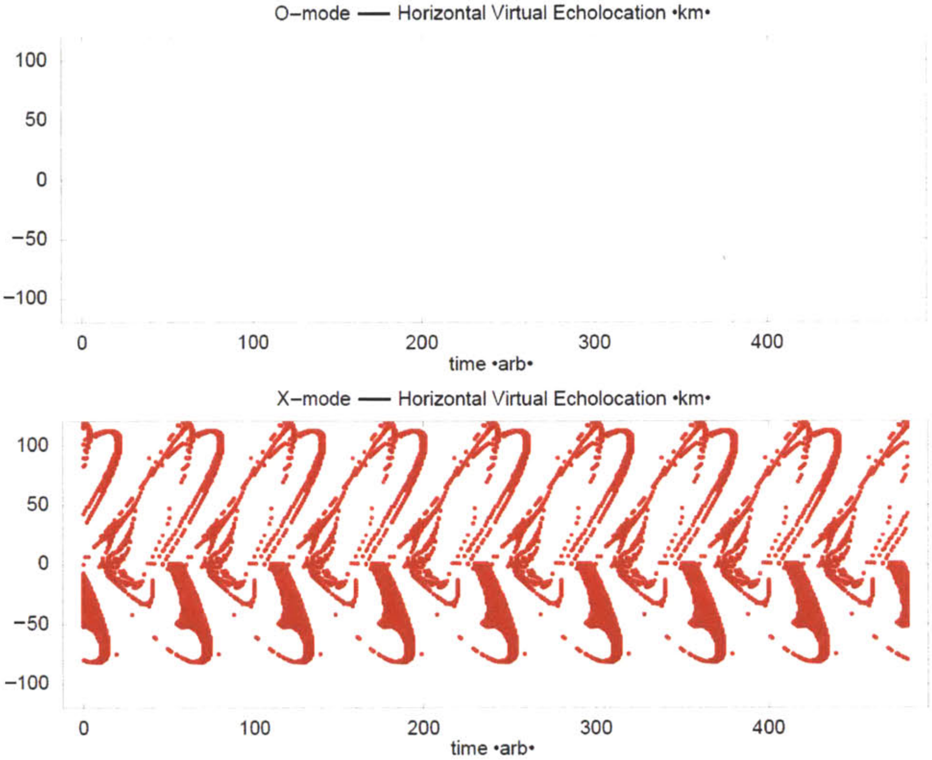

Point-source disturbance ($\lambda = 60$ km), sounding frequency 5.4 MHz:

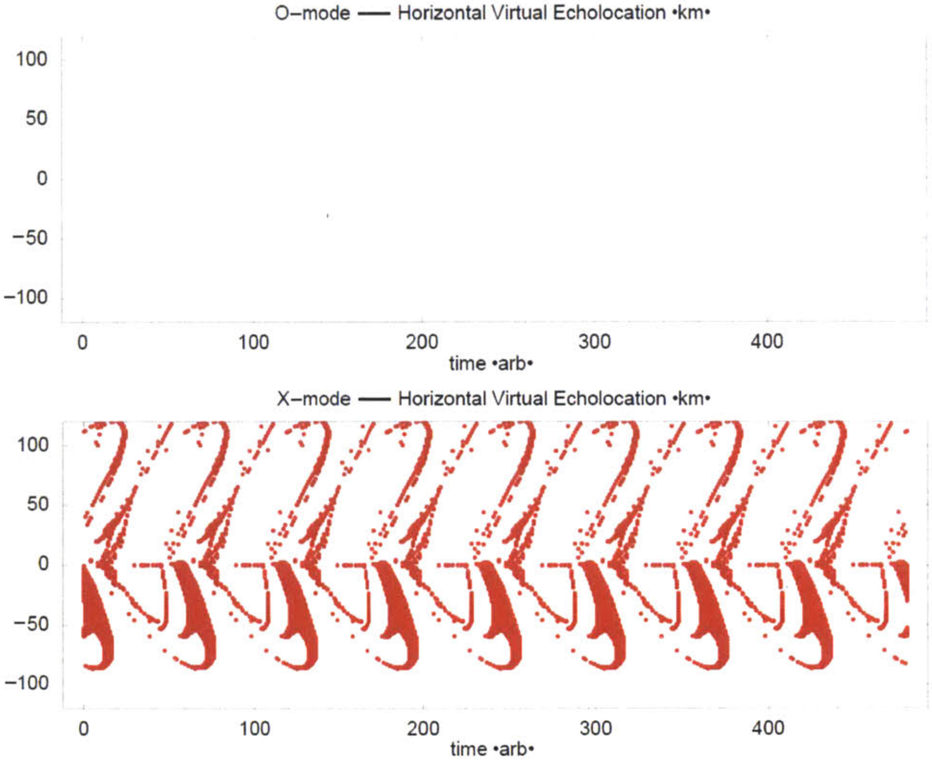

Point-source disturbance ($\lambda = 60$ km), sounding frequency 5.45 MHz:

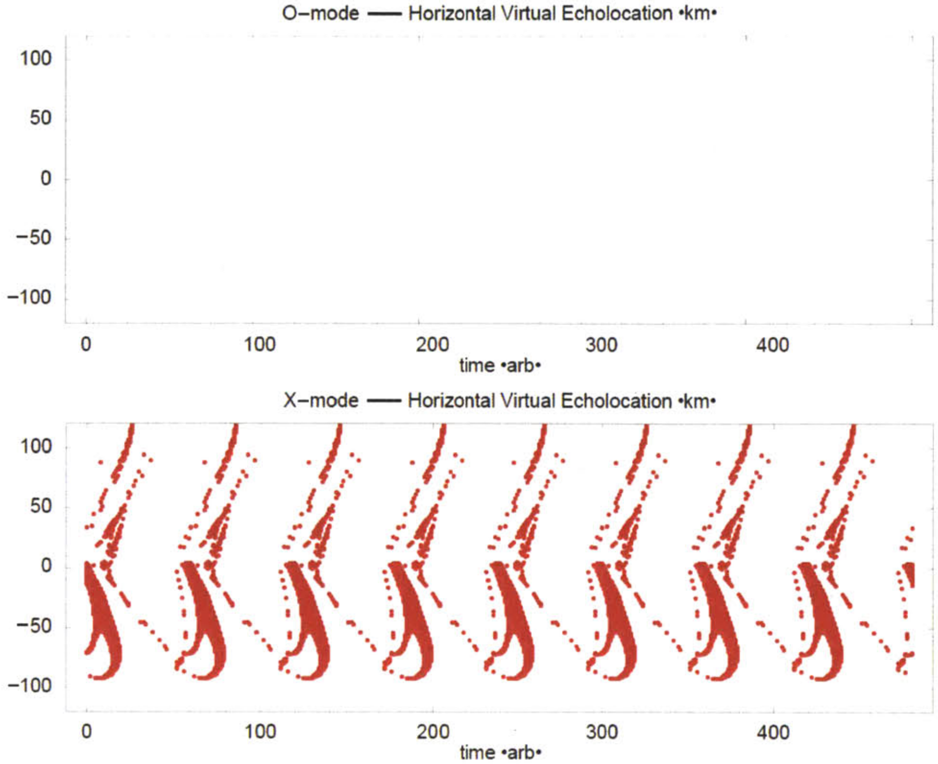

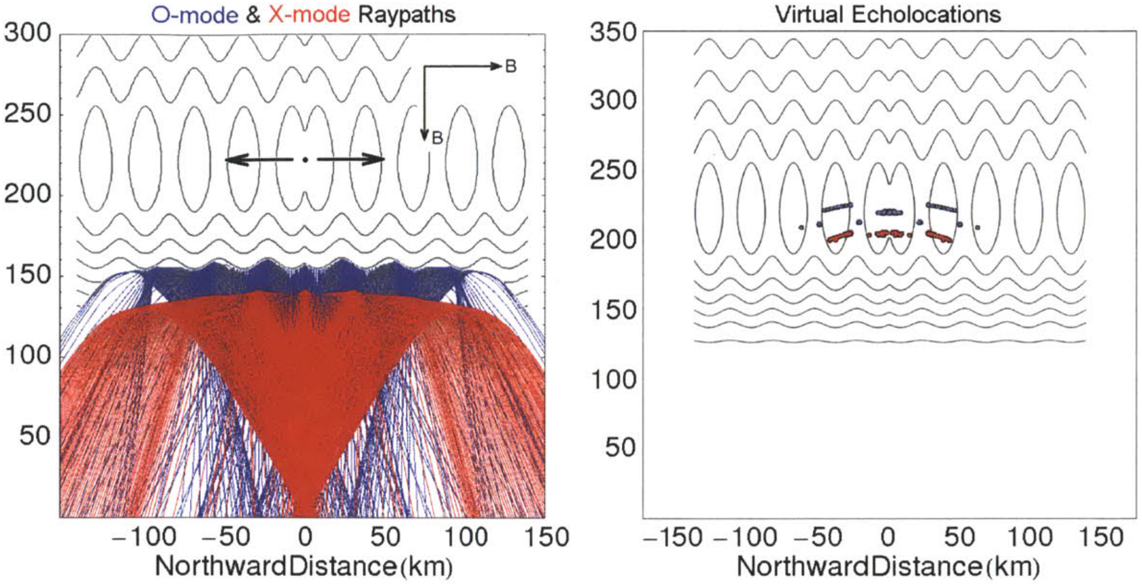

Figure E-4: The configuration of ionospheric plasma disturbance to be investigated in Part 4. The wavelength of these traveling disturbances is $\lambda = 30$ km. We set two separate cases of background magnetic field direction: one at 0° and another at 90° from horizontal direction. The peak plasma frequency we used in this ionospheric model is 4.9 MHz, and electron gyrofrequency is 1.0 MHz.

E.4 Ray Tracing Study: Part 4

In this part, we will set up a pattern of periodic disturbances that originate from a single point overhead. The disturbances will be generated continuously and spread out horizontally in both directions. The "digisonde" will launch both O-mode and X-mode radio diagnostic waves into the plasma layer, and then we will record their corresponding echolocations. We will have two distinct magnetic field configurations: (1) magnetic dip angle of 0° (equatorial extreme case), and also (2) magnetic dip angle of 90° (polar extreme case). For each respective magnetic field configuration, we are going to use the following sounding frequency values: 4.0, 4.4, and 4.8 MHz. All of the selected sounding frequencies are below the peak plasma frequency, so we will always have both O-mode and X-mode echoes in this case.

This setup is an extension to part 1 (magnetic dip angle of 50°). With an exactly horizontal or vertical B-field configuration, we finally recover a perfectly symmetric radial outward propagation pattern for *both* O-mode and X-mode echolocations.

Point-source disturbance, magnetic dip angle 0°, sounding frequency 4.0 MHz:

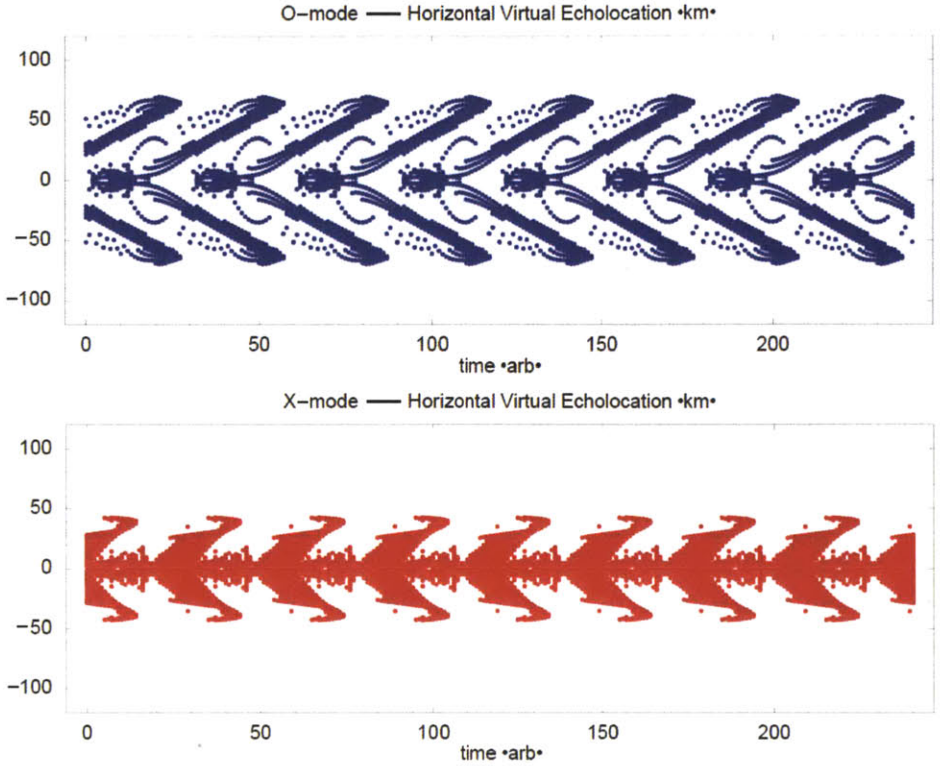

Point-source disturbance, magnetic dip angle 0°, sounding frequency 4.4 MHz:

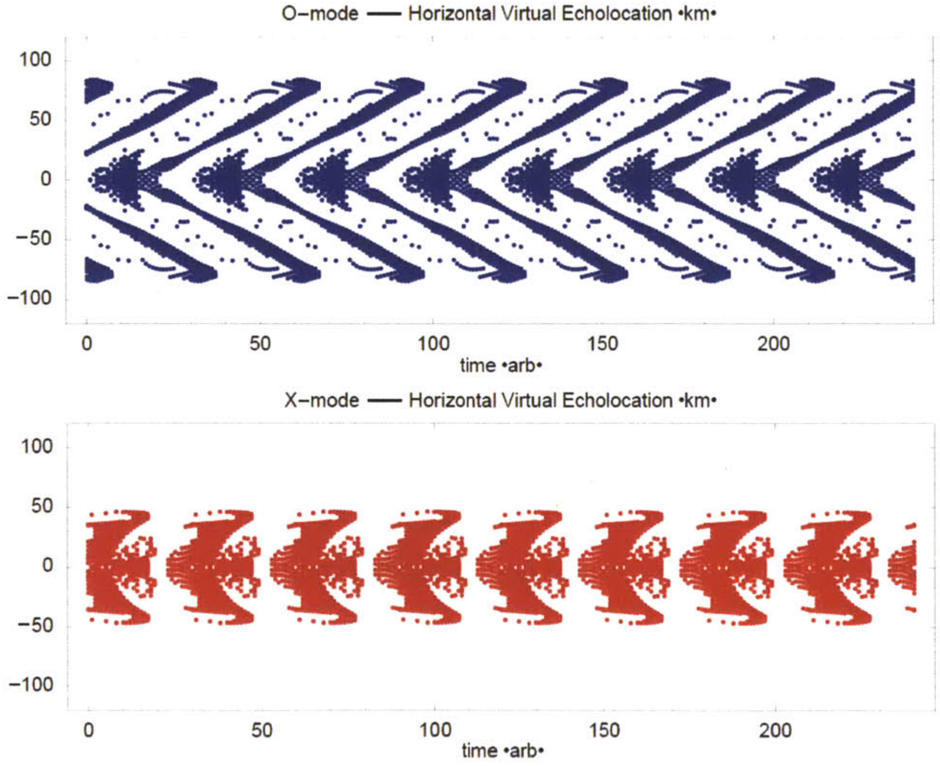

Point-source disturbance, magnetic dip angle 0°, sounding frequency 4.8 MHz:

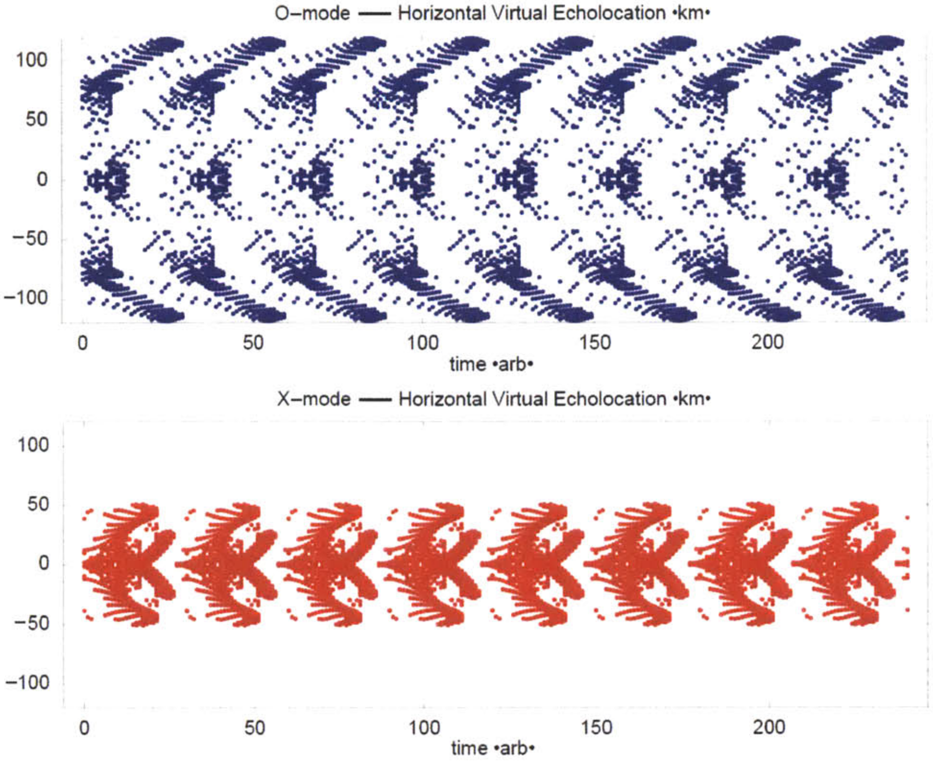

Point-source disturbance, magnetic dip angle 90°, sounding frequency 4.0 MHz:

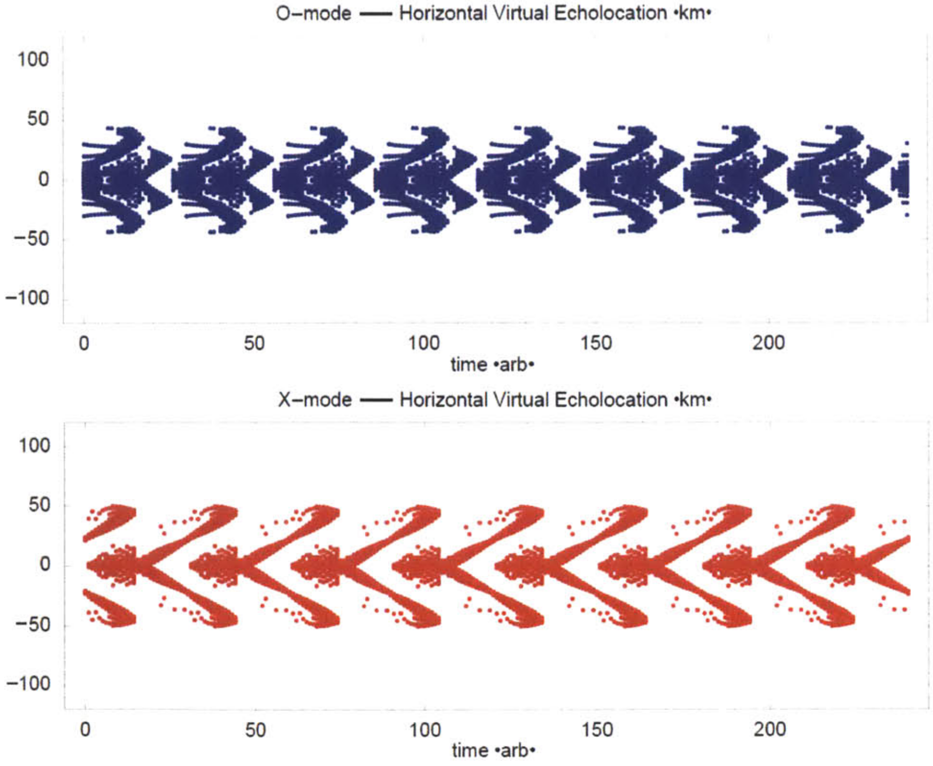

Point-source disturbance, magnetic dip angle 90°, sounding frequency 4.4 MHz:

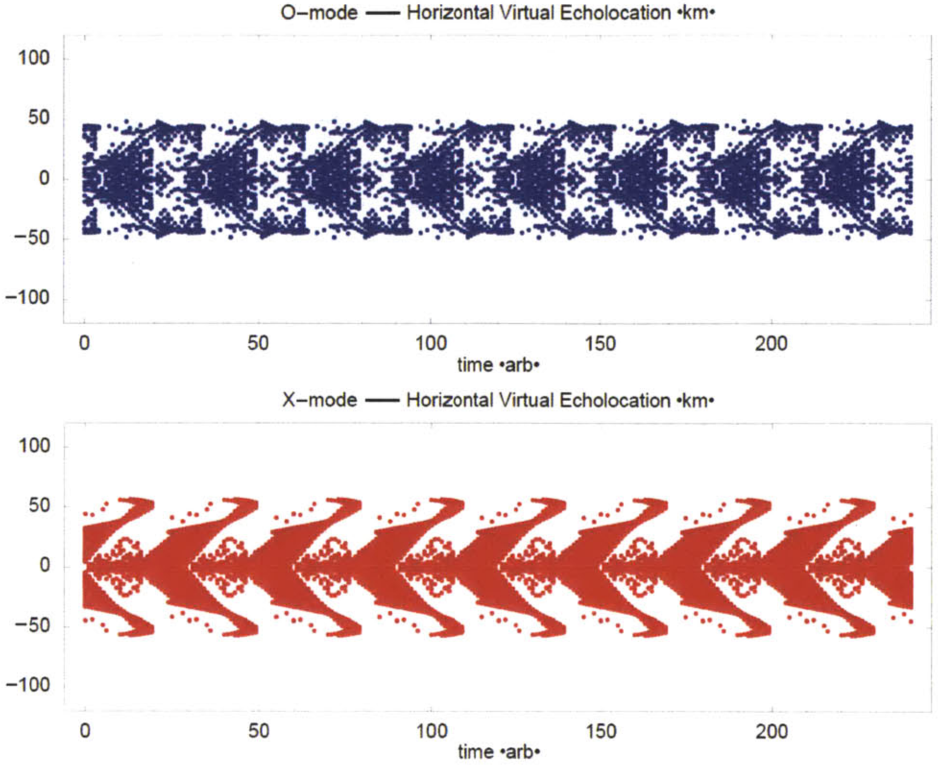

Point-source disturbance, magnetic dip angle 90°, sounding frequency 4.8 MHz:

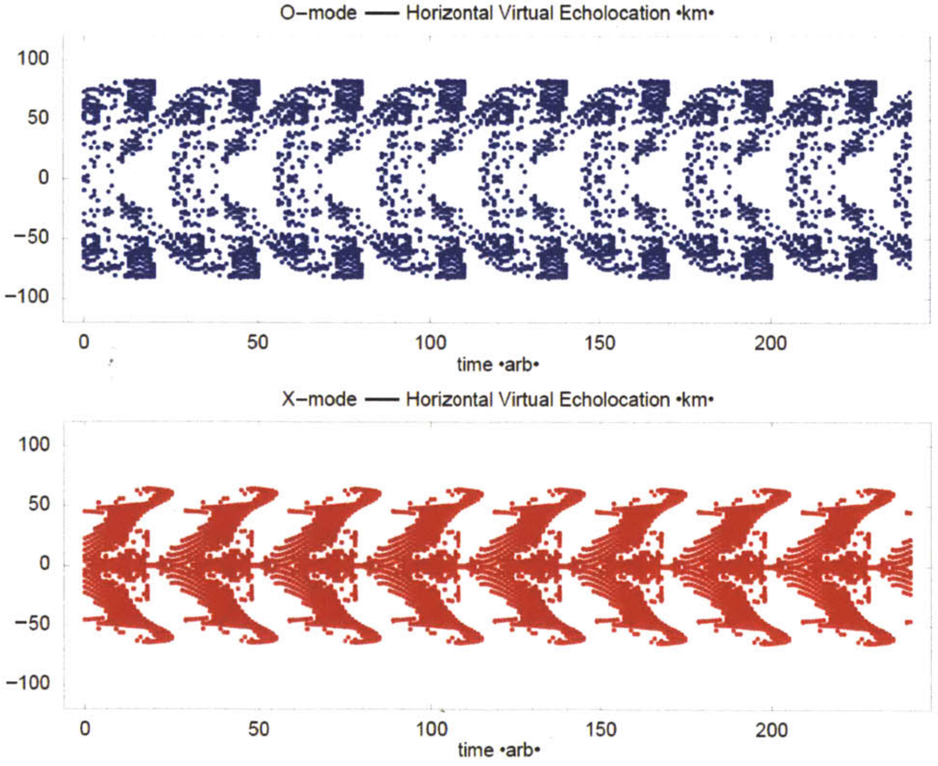

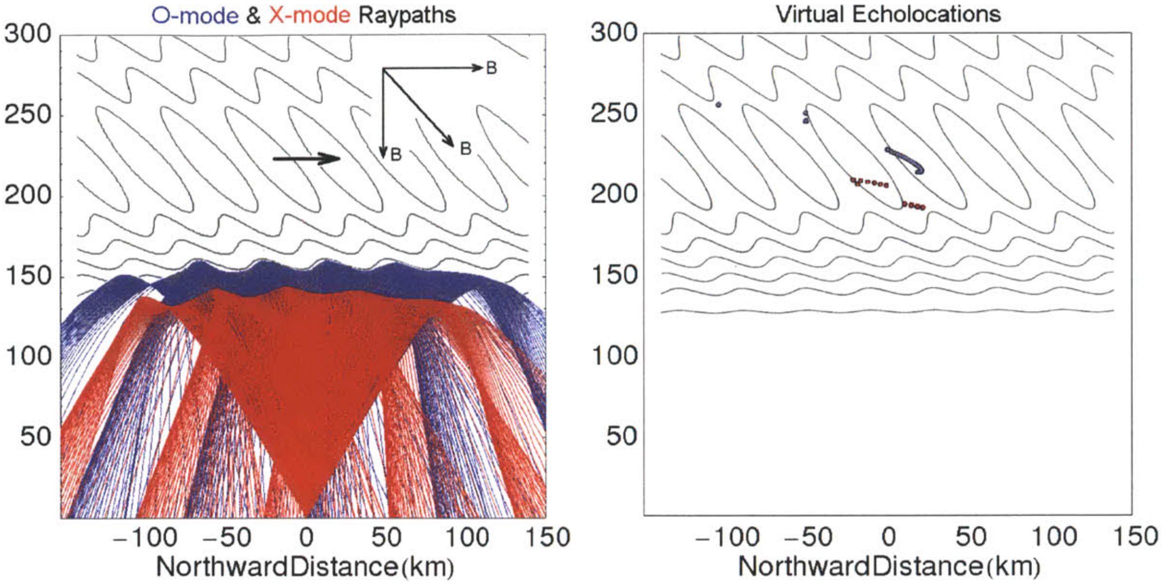

Figure E-5: The configuration of ionospheric plasma disturbance to be investigated in Part 5a. Along the horizontal axis, the periodic pattern repeats every ~39 km (the sheet separation is $\lambda_{\perp} = 30$ km). We set three separate cases of background magnetic field direction: at 0°, at 50° and at 90° from horizontal direction. The peak plasma frequency we used in the ionospheric model is 4.9 MHz, and electron gyrofrequency is set to 1.0 MHz.

E.5 Ray Tracing Study: Part 5a

In this part, we are going to set up a pattern of periodic disturbances that will simply pass by overhead and propagate horizontally in one direction only. The "digisonde" will launch both O-mode and X-mode radio diagnostic waves into the plasma layer, and then we will record their corresponding echolocations. With a fixed sounding frequency (4.0 MHz), we are going to vary the magnetic dip angle: 0°, 50°, and 90°. The pattern of periodic disturbances will stay slanted at 50° angle in all cases.

In this particular setup involving passing-by ionospheric disturbances with slanted plasma density striations, we have found that varying the magnetic dip angle only produced little effect on the skymap echolocations. In relative terms, the overall effect is more visible for the O-mode echolocations than the X-mode echolocations. In general, the spatial distribution of the skymap echolocations are skewed towards the south side. This skewness does not change as we vary the magnetic dip angle, suggesting that it has more to do with the tilting of the density striations.

Slanted passing-by disturbance, sounding frequency 4.0 MHz, magnetic dip angle 0°:

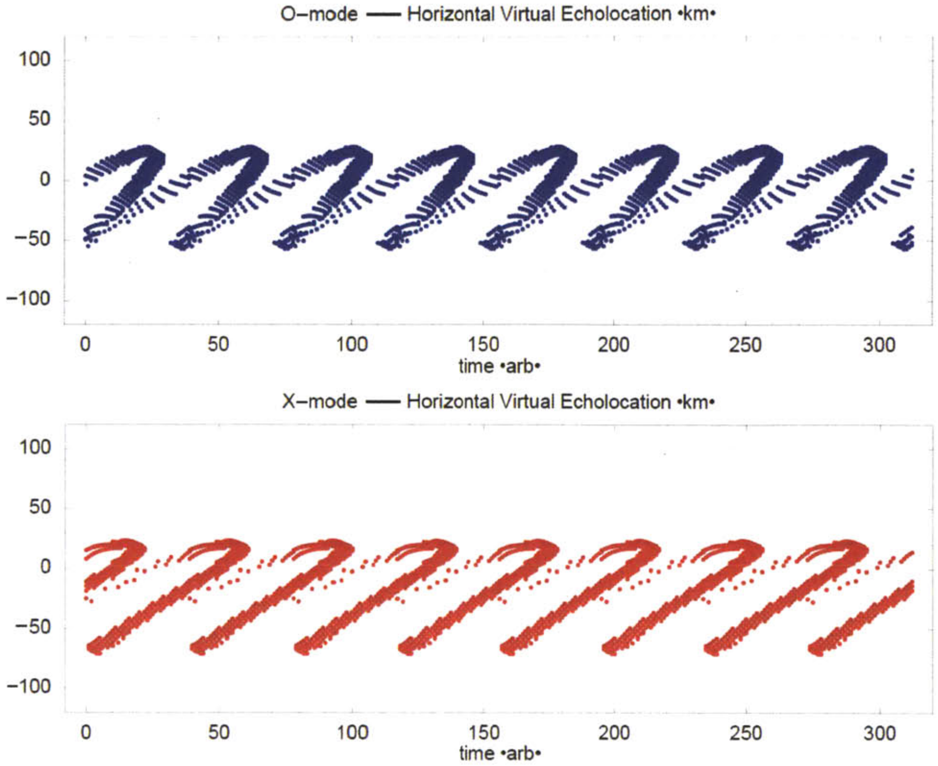
O–mode —— Horizontal Virtual Echolocation •km•

X–mode —— Horizontal Virtual Echolocation •km•

Slanted passing-by disturbance, sounding frequency 4.0 MHz, magnetic dip angle 50°:

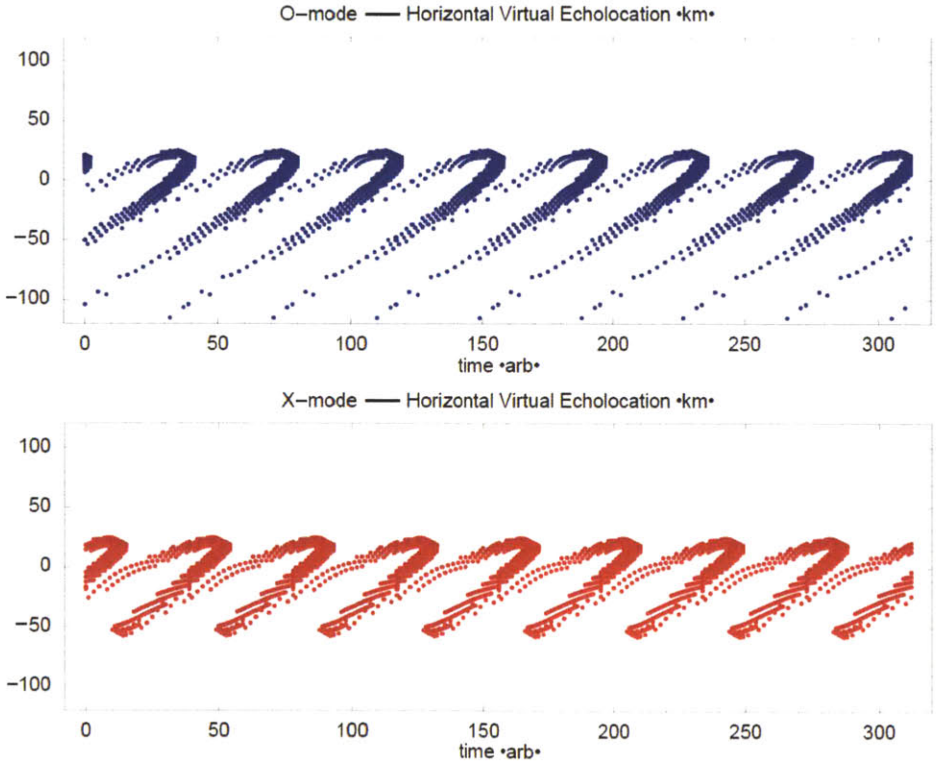
O–mode —— Horizontal Virtual Echolocation •km•

X–mode —— Horizontal Virtual Echolocation •km•

Slanted passing-by disturbance, sounding frequency 4.0 MHz, magnetic dip angle 90°:

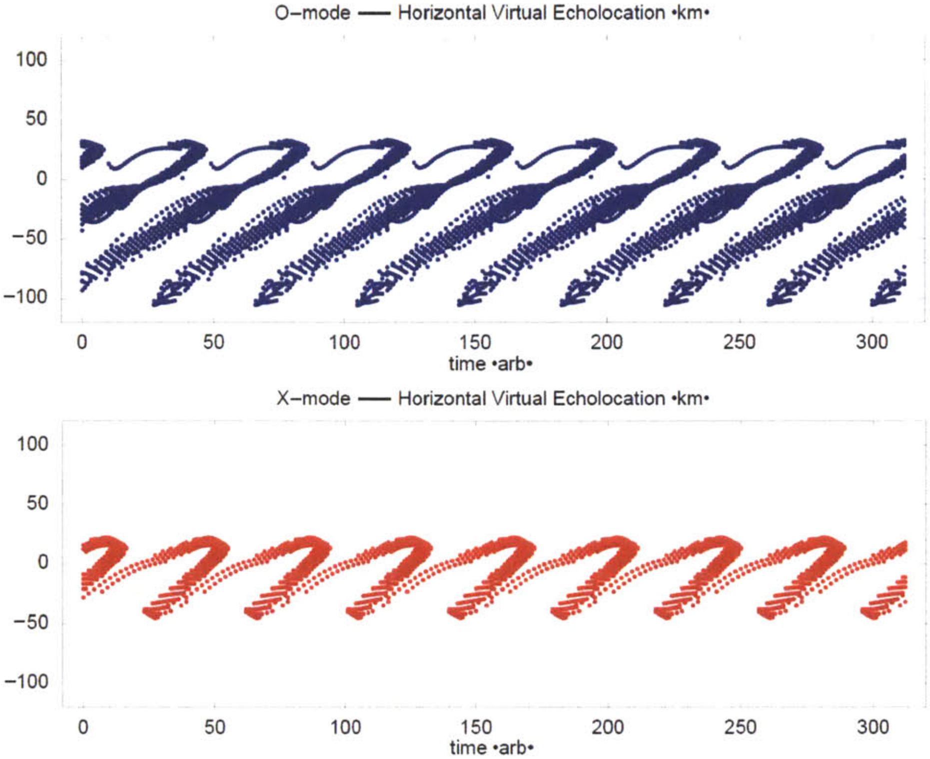

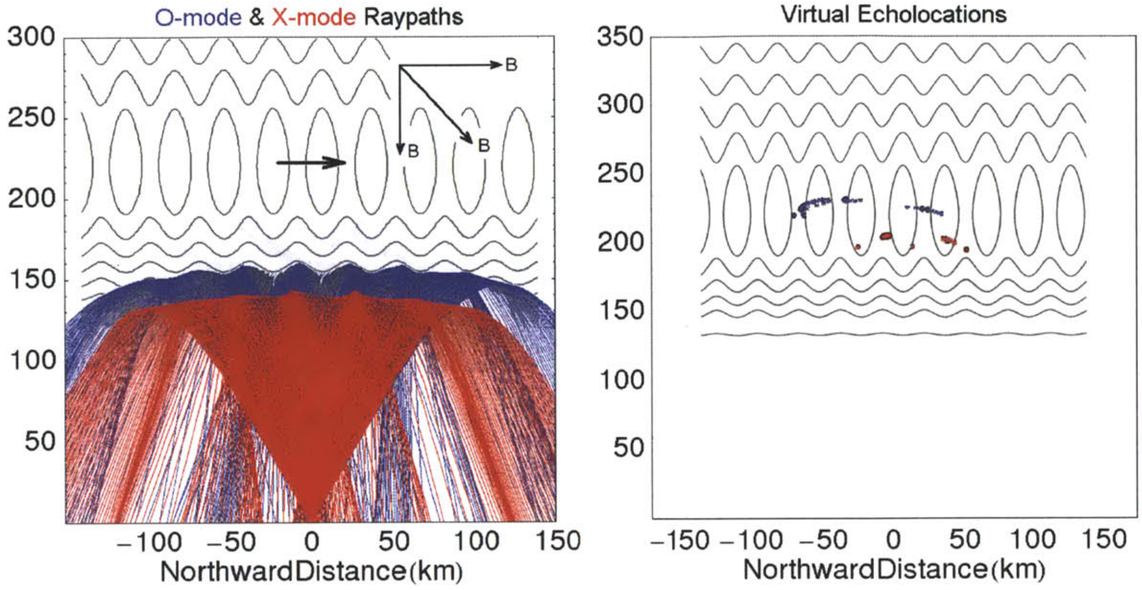

Figure E-6: The configuration of ionospheric plasma disturbance to be investigated in Part 5b. The wavelength of these traveling disturbances is $\lambda = 30$ km. We set three separate cases of background magnetic field direction: at 0°, at 50° and at 90° from horizontal direction. Peak plasma frequency in this ionospheric model is 4.9 MHz, and electron gyrofrequency is 1.0 MHz.

E.6 Ray Tracing Study: Part 5b

In this part, we are going to set up a pattern of periodic disturbances that will simply pass by overhead and propagate horizontally in one direction only. The "digisonde" will launch both O-mode and X-mode radio diagnostic waves into the plasma layer, and then we will record their corresponding echolocations. With a fixed sounding frequency (4.0 MHz), we are going to vary the magnetic dip angle: 0°, 50°, and 90°. The pattern of periodic disturbances will stay upright in all cases.

In this final setup where we have some passing-by ionospheric disturbances with an upright configuration for the density striations, we obtained skymap echolocations that are more evenly distributed north/south. As a result, in this case we can see the cluster of skymap echoes approaching and passing through the center point much more clearly. In general, we continue to observe the same pattern as we vary the magnetic dip angle. The only exception is with O-mode echolocations, which could still be unevenly distributed north/south for dip angle in between 0° or 90°.

Upright passing-by disturbance, sounding frequency 4.0 MHz, magnetic dip angle 0°:

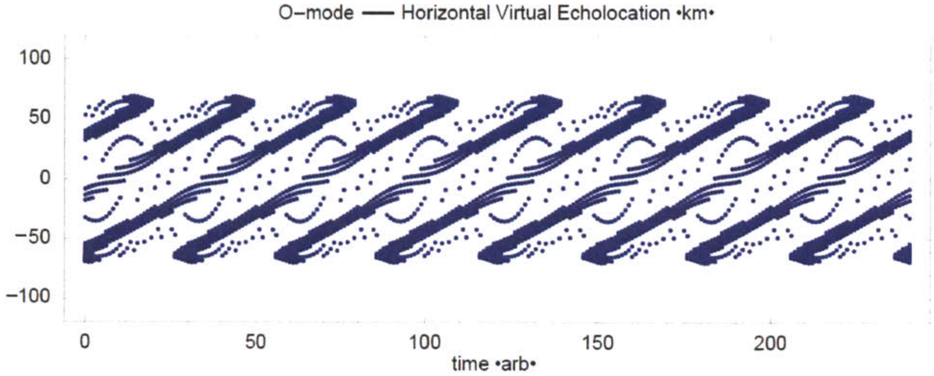

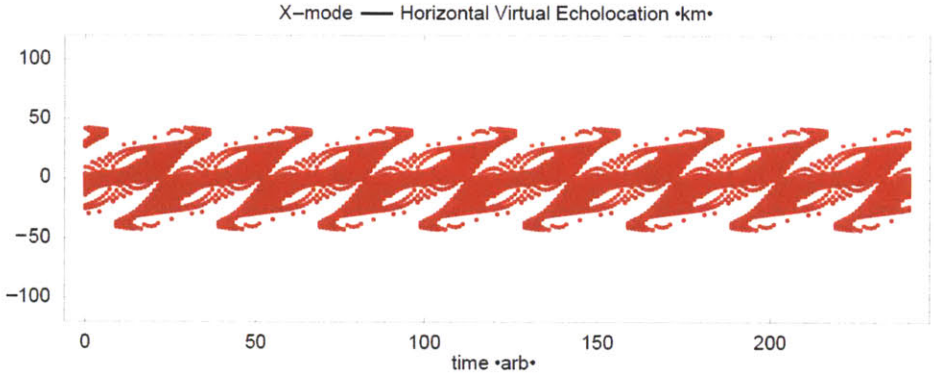

Upright passing-by disturbance, sounding frequency 4.0 MHz, magnetic dip angle 50°:

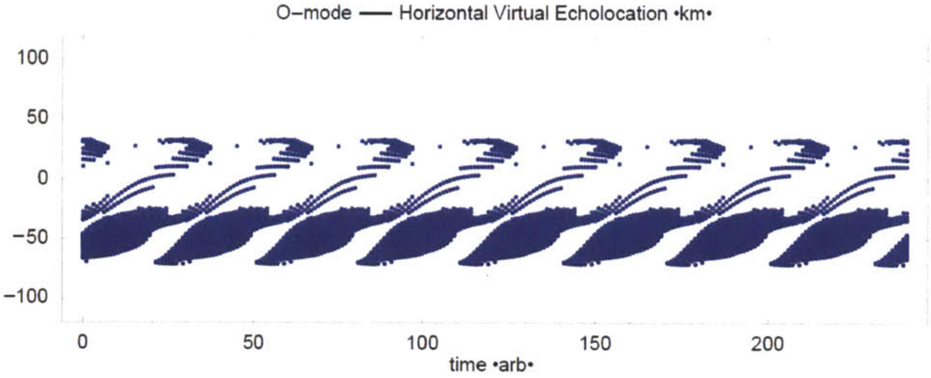

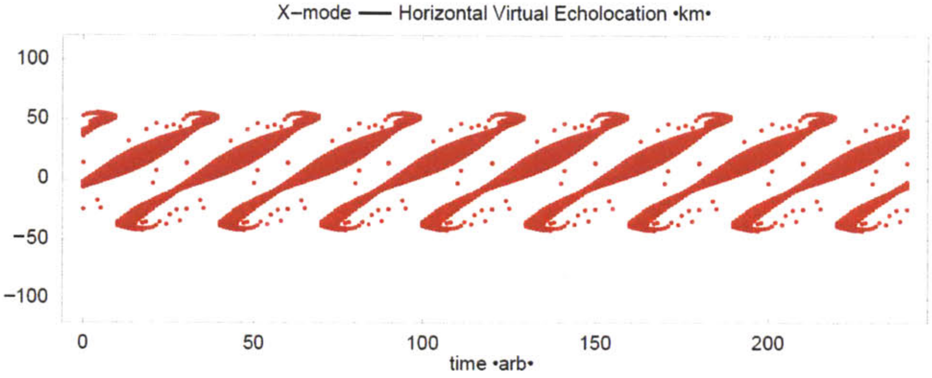

Upright passing-by disturbance, sounding frequency 4.0 MHz, magnetic dip angle 90°:

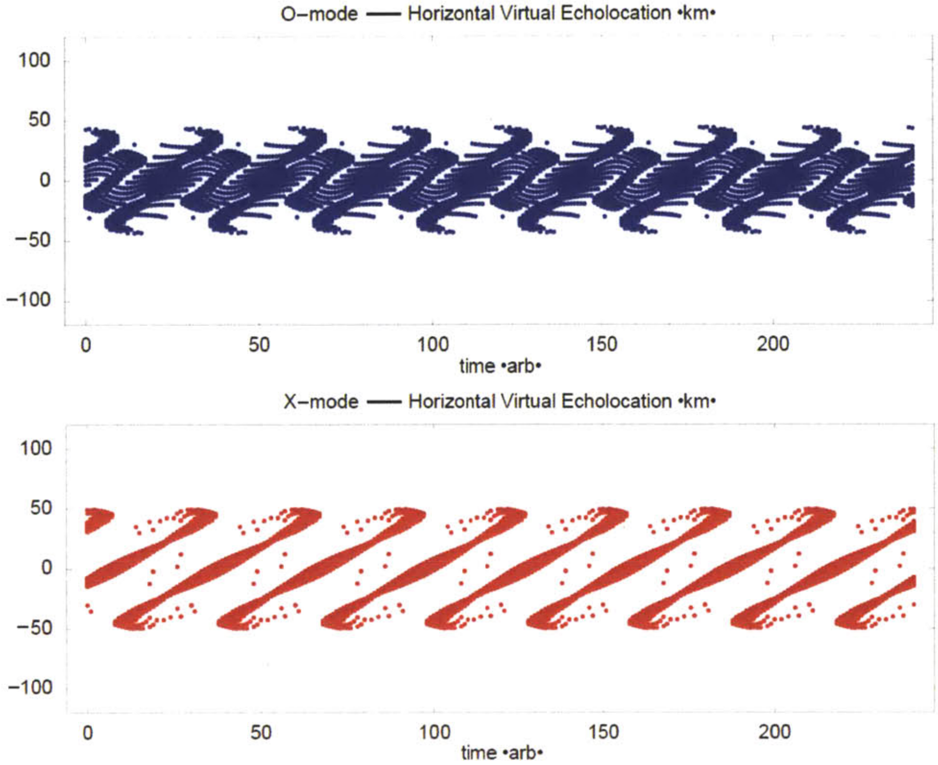

Bibliography

[1] J. Artru et al. (2005), *Ionospheric Detection of Gravity Waves Induced by Tsunamis*, Geophys. J. Int., **160**, 840.

[2] J. Artru, T. Farges, and P. Lognonne (2004), *Acoustic Waves Generated from Seismic Surface Waves: Propagation Properties Determined from Doppler Sounding Observation and Normal-modes Modeling*, Geophys. J. Int., **158**, 1067.

[3] T. Beer, *Atmospheric Waves* (John Wiley and Sons, 1974).

[4] W.J.G. Beynon and P.J.S. Williams (1978), *Incoherent Scatter of Radio Waves from the Ionosphere*, Rep. Prog. Phys., Vol. 41, 1978.

[5] N.F. Blagoveshchenskaya et al. (2005), *Phenomena in the Ionosphere-Magnetosphere System Induced by Injection of Powerful HF Radio Waves into Nightside Auroral Ionosphere*, Annales Geophysicae, 23:87–100, SRef-ID: 1432-0576/ag/2005-23-87.

[6] R.N. Bracewell, *The Fourier Transform and Its Applications* (McGraw-Hill, 1978).

[7] W.A. Bristow et al. (1994), *Identification of High-Latitude Acoustic Gravity Wave Sources Using the Goose Bay HF Radar*, Journal of Geophysical Research, **99**, A1, 319–331, doi:10.1029/93JA01470.

[8] W.A. Bristow and R. A. Greenwald (1995), *Estimating Gravity Wave Parameters from Oblique High-Frequency Backscatter: Modeling and Analysis*, Journal of Geophysical Research, **100**, A3, 36393648, doi:10.1029/94JA02704.

[9] K.G. Budden, *The Propagation of Radio Waves* (Cambridge University Press, 1985).

[10] P.F. Checcacci, *Measurements of Total Electron Content by Means of Satellite Radio Emissions*, Physics of the Upper Atmosphere (Editrice Compositori, 1970).

[11] N.E. Dalrymple (2001), *Simulation of Ionospheric Plasma Heating Experiments in the Versatile Toroidal Facility*, PhD Thesis (MIT).

[12] K. Davies, *Ionospheric Radio Propagation*, National Bureau of Standards Monograph 80 (US Government Printing Office, 1965).

[13] S.E. Dorfman (2005), *Intense Spreading of Radar Echoes from Ionospheric Plasmas*, BS Thesis (MIT).

[14] R.H. Eather et al. (1976), *Plasma Injection at Synchronous Orbit and Spatial Temporal Auroral Morphology*, Journal of Geophysical Research, **81**, 2805–2824.

[15] S.H. Francis (1973), *Acoustic-Gravity Modes and Large-Scale Traveling Ionospheric Disturbances of a Realistic, Dissipative Atmosphere*, Journal of Geophysical Research, **78**, 2278–2301.

[16] A. Gershunov, D.R. Cayan, and S.F. Iacobellis (2009), *The Great 2006 Heat Wave over California and Nevada: Signal of an Increasing Trend*, J. Climate, 22, 61816203, doi: http://dx.doi.org/10.1175/2009JCLI2465.1.

[17] S.A. Gonzalez et al. (2005), *An Energy Balance Study of the Lower Topside Ionosphere Using the Arecibo Incoherent Scatter Radar and Heating Facilities*, Journal of Geophysical Research, **110**, A11303, doi:10.1029/2005JA011154.

[18] G.I. Grigor'ev (1975), *Moving Ionospheric Disturbances which Develop during the Operation of Powerful Transmitters*, Translated from Izvestiya Vysshikh Uchebnykh Zavedenii, Radiofizika, Vol. 18, No. 12, pp. 1801-1805, December 1975.

[19] J. Hargreaves, *The Solar-Terrestrial Environment: An Introduction to Geospace*, Cambridge Atmospheric and Space Science Series (Cambridge University Press, 1992).

[20] L.S. He et al. (2004), *Studies of Medium Scale Travelling Ionospheric Disturbances Using TIGER SuperDARN Radar Sea Echo Observations*, Annales Geophysicae, 22:4077–4088, SRef-ID: 1432-0576/ag/2004-22-4077.

[21] C.O. Hines (1960), *Internal Gravity Waves at Ionospheric Heights*, Canadian Journal of Physics **38**, 1441–1481.

[22] R.D. Hunsucker and J.K. Hargreaves, *The High-Latitude Ionosphere and its Effects on Radio Propagation*, (Cambridge University Press, 2002).

[23] M.C. Kelley, *The Earth's Ionosphere: Plasma Physics and Electrodynamics* (Academic Press, 1989).

[24] M.C. Lee et al. (1998), *Ionospheric plasma bubble generated by Arecibo heater*, Geophysical Research Letters, **25**, 5, 579–582, doi:10.1029/98GL00327.

[25] M.C. Lee et al. (2008), *Did Tsunami-Launched Gravity Waves Trigger Ionospheric Turbulence over Arecibo?*, Journal of Geophysical Research, Vol. 113, A01302, doi:10.1029/2007JA012615.

[26] C.H. Liu et al. (1982), *Global Dynamic Responses of the Atmosphere to the Eruption of Mount St. Helens on May 18, 1980*, Journal of Geophysical Research, Vol. 87, No. A8, pp. 6281–6290.

[27] J.G. Luhmann (1983), *Ionospheric Disturbances Resulting from Ion-Neutral Coupling*, Space Science Reviews, **34**, 1983.

[28] R.J. Lunnen et al. (1984), *Detection of Radiation from a Heated and Modulated Equatorial Electrojet Current System*, Nature, vol. 311, 134–135, doi:10.1038/311134a0.

[29] G.A. Meehl et al. (2004), *More Intense, More Frequent, and Longer Lasting Heat Waves in the 21st Century*, Science, **305**, 994, doi:10.1126/science.1098704.

[30] G.M. Milikh et al. (2008), *Formation of Artificial Ionospheric Ducts*, Geophysical Research Letters, Vol. 35, L17104, doi:10.1029/2008GL034630.

[31] E. Mishin et al. (2012), *F2-Region Atmospheric Gravity Waves due to High-Power HF Heating and Subauroral Polarization Streams*, Geophysical Research Letters, Vol. 39, L11101, doi:10.1029/2012GL052004.

[32] NASA Earth Observatory Newsroom, *Heat Wave in North America and Western Europe*, National Aeronautics and Space Administration (August 2006).
(http://earthobservatory.nasa.gov/IOTD/view.php?id=6803)
last accessed 16 July 2012

[33] M.J. Nicolls and M. C. Kelley (2005), *Strong evidence for gravity wave seeding of an ionospheric plasma instability*, Geophysical Research Letters, **32**, L05108, doi:10.1029/2004GL020737.

[34] NOAA Web Documentation (2004), *Evidence for Precipitation of Energetic Particles by Ionospheric Heating Transmissions*, National Geophysical Data Center.
(http://www.ngdc.noaa.gov/stp/IONO/Dynasonde/SpEatHeating.htm)
last accessed 16 July 2012

[35] S.I. Oyama and B.J. Watkins (2007), *Artificial Ionospheric Irregularities Measured with MUIR (Modular UHF Ionospheric Radar) at HAARP (High Frequency Active Auroral Research Program)*, Journal of the National Institute of Information and Communication Technology, Vol. 54, Nos. 1/2.

[36] R. Pradipta (2007), *Could Global Warming Affect Space Weather? Case Studies of Intense Ionospheric Plasma Turbulence Associated with Natural Heat Sources*, MS Thesis (MIT).

[37] K. Rawer, *Wave Propagation in the Ionosphere*,
(Kluwer Academic Publishers, 1993).

[38] B.W. Reinisch et al. (1998), *Ionospheric Drift Measurements with Ionosondes*, Annali di Geofisica, Vol. 41, No. 5–6.

[39] W. Rideout and A.J. Coster (2006), *Automated GPS Processing for Global Total Electron Content Data*, GPS Solution, **10**, 219–228.

[40] Rietveld et al. (2003), *Ionospheric Electron Heating, Optical Emissions, and Striations Induced by Powerful HF Radio Waves at High Latitudes: Aspect Angle Dependence*, Journal of Geophysical Research, Vol. 108, No. A4, 1141, doi:10.1029/2002JA009543.

[41] D.H Roberts et al. (1982), *A Large-Amplitude Traveling Ionospheric Disturbance Produced by the May 18, 1980 Explosion of Mount St. Helens*, Journal of Geophysical Research, Vol. 87, No. A8, pp. 6291–6301.

[42] R.W. Schunk and A.F. Nagy, *Ionospheres: Physics, Plasma Physics, and Chemistry* (Cambridge University Press, 2000).

[43] A. Senior et al. (2006), *Effect of High-Latitude Atmospheric Gravity Wave Disturbances on Artificial HF Radar Backscatter*, Annales Geophysicae, **24**, 2347–2361.

[44] I.N. Sneddon, *Fourier Transforms* (McGraw-Hill, 1951).

[45] T.H. Stix, *Waves in Plasmas* (AIP Press — Springer-Verlag, 1992).

[46] P. Stubbe et al. (1982), *Ionospheric Modification Experiments in Northern Scandinavia*, Journal of Atmospheric and Terrestrial Physics, vol. 44, No. 12, pp. 1025–1041.

[47] T. Tsugawa et al. (2007), *Medium-Scale Traveling Ionospheric Disturbances Detected with Dense and Wide TEC Maps over North America*, Geophysical Research Letters, **34**, L22101, doi:10.1029/2007GL031663.

[48] S. Watada (2009), *Radiation of Acoustic and Gravity Waves and Propagation of Boundary Waves in the Stratified Fluid from a Time-Varying Bottom Boundary*, Journal of Fluid Mechanics, vol. 627, pp. 361–377, doi:10.1017/S0022112009005953.

[49] R.C. Whitten and I.G Poppoff, *Physics of the Lower Ionosphere* (Prentice-Hall, 1965).

[50] Wikipedia Article, *2006 North American heat wave.* (http://en.wikipedia.org/wiki/2006_North_American_heat_wave) *last accessed 16 July 2012*

[51] P.J.S. Williams (1996), *Tides, Atmospheric Gravity Waves and Traveling Disturbances in the Ionosphere*, in Modern Ionospheric Science, A Collection of Articles Published on the Occasion of the Anniversary: "50 Years of Ionospheric Research in Lindau", Editors: H. Kohl, R. Ruster & K. Schlegel (European Geophysical Society, Kathlenburg-Lindau FRG).

[52] K.C. Yeh and C.H. Liu, *Theory of Ionospheric Waves* (Academic Press, New York and London, 1972).

[53] E. Zauderer, *Partial Differential Equations of Applied Mathematics – 2nd Ed.* (John Wiley and Sons, 1989).